2020

Development of an Anatomically and Electrically Conductive Brain Phantom for Transcranial Magnetic Stimulation

Hamzah A. Magsood
Virginia Commonwealth University

Development of an Anatomically and Electrically Conductive Brain Phantom for Transcranial Magnetic Stimulation

A thesis submitted in partial fulfillment of the requirements for the degree of Doctor of Philosophy at Virginia Commonwealth University.

By: Hamzah Magsood

Master of Science

Department of Mechanical and Nuclear Engineering

College of Engineering

Advisor: Dr. Ravi L. Hadimani

Assistant Professor

Department of Mechanical and Nuclear Engineering

College of Engineering

Virginia Commonwealth University

Richmond, Virginia

December 2020

Acknowledgment:

I would like to express my immense gratitude and acknowledgment to everyone who helped me finish this work. My first and exceptional thanks go to my soulmate and most beloved person in my life, my wife Ghadeer. Without your pure-loving heart and faith in me, I would have not been where I am today. I am thankful to have such sweet and beautiful daughters, Eleen, and Sarah. They cherish my heart with joy and happiness that persist fueling my ambitions to reach the ultimate.

I am thankful to have loving and supporting parents and siblings—thanks for being in my life.

I am very grateful to my Ph.D. advisor, Dr. Ravi Hadimani, who relentlessly guided and supported me through my graduate school journey. Dr. Ravi was never late when I asked for his assistance or advice. Thank you, Dr. Ravi.

Thanks to my committee members, Dr. Kathryn Holloway, Dr. Karla Mossi, Dr. Reza Mohammadi, and Dr. Carrie Peterson, for being wonderful mentors and limitlessly kind people.

I am thankful to my friends in the Biomagnetics lab, who I enjoined every moment in their company. They made this journey joyful and full of laughter and beautiful discussions. Thanks to Farheen Syeda, Ivan Carmona, Ghali Aladwani, Shivakumar Hunagund, Ahmed El-Gendy, Shane Harstad, Ciro Serrate, Jennifer Mak, and Emily Cheng. Many thanks to undergraduate students who helped me in my thesis work. Thanks go to Brendan Quiroz, Cirro Serrate, and Youssif Al Kheder.

Abstract

Transcranial Magnetic Stimulation (TMS) is a non-invasive technique for diagnostics, prognostic, and treatments of various neurological diseases. However, the lack of anatomically realistic brain phantoms has made the experimental verification of stimulation strength in the form of induced electric fields/voltages in the brain tissues an impediment to developing new TMS coils, stimulators, and treatment protocols. There are significant technological, safety, and ethical limitations to test the potential TMS treatment procedures or develop enhancements and refine them on humans or animals. This work aims to bridge the gap by introducing and developing an innovative manufacturing and fabrications process to produce a geometrically and anatomically accurate head and brain phantom capable of being used in experimental evaluations of stimulation strengths in neuromodulation techniques and in particular in TMS. We developed a 3-D anatomically accurate brain phantom that can mimic the electrical conductivity of the brain by first developing a process of creating computational 3D models using patient-specific MRIs followed by the development of a polymer composite that mimics the brain's conductivity and finally, a process to covert computational 3D models to patient-specific anatomically accurate brain phantoms. We present the development and fabrication processes of the head and brain phantom in detail. The process is based on our novel technique called "the shelling method" that enables the production of highly intricate geometries like the brain. After that, we show an example of the current and immediate application of this research in which the brain phantom can play an essential role in developing new TMS treatment procedures for neurological disorders. We use the brain phantom to examine the safety of combing two of the prominent brain stimulation techniques, TMS and DBS. Our experiment on the phantom shows that It is unsafe to operate the TMS joined with the DBS when operated at maximum and proximal to the DBS leads. Moreover, we run a

series of experiments and measurements to assess and evaluate the brain phantom's stimulation strengths during TMS. We also present the measured magnetic fields generated by the TMS coils in the Biomagnetics Laboratory. We investigated the feasibility of mapping the electric field on the brain using anatomically accurate brain phantoms. Finally, we conclude our work and recommend future improvements to the patient-specific, anatomically accurate brain phantom.

Table of Contents

List of Figures:

This page intentionally left blank.

1 Introduction

One in five adults in the US has a diagnosable mental illness [1]. Alzheimer's and Parkinson's diseases are the most common neurodegenerative disorders in the US, accounting for half a million for the former [2] and 5.4 million for the latter [3]. Therefore, neuroscience and brain research has gained increasing attention in recent years [4]. TMS is an FDA approved treatment for depression [5], migraine [6], and obsessive-compulsive disorder (OCD) [7]. Researchers also investigate it extensively to be used as a promising treatment technique for other neurological disorders like Parkinson's [8,9], Alzheimer related cognitive impairments [10], and ischemic strokes recovery [11]. While computer modeling and simulation help calculate and predict the strength of stimulation of the TMS to design treatment protocols (dosage), it lacks aspects of the actual representation of real-world physics. Although there are extensive computational and clinical studies of the TMS, there is a lack of experimental and physical models for testing and examining the brain stimulation procedures and protocols. There are significant technological, safety, and ethical limitations to test the potential TMS treatment procedures or develop enhancements and refine them on humans or animals. The lack of anatomically realistic brain phantoms has made the experimental verification of stimulation strength in the form of induced electric fields/voltages in the brain tissues an impediment to developing new treatment protocols. Several papers report electrically conductive brain phantoms but lack the anatomical and geometrical features of the brain. [12–14]. The geometry of an electrically conducting material in the presence of a magnetic field can significantly influence the induced electric fields [15,16]. Wagner *et al.* (2004) state that "The induced field is entirely dependent upon the anatomical/geometrical structure and electrical tissue properties of the system and small perturbations can alter the field drastically" [17]. Therefore, it is crucial to consider the brain's

geometry, either numerically or experimentally, when studying the level of stimulation produced by external brain stimulation techniques.

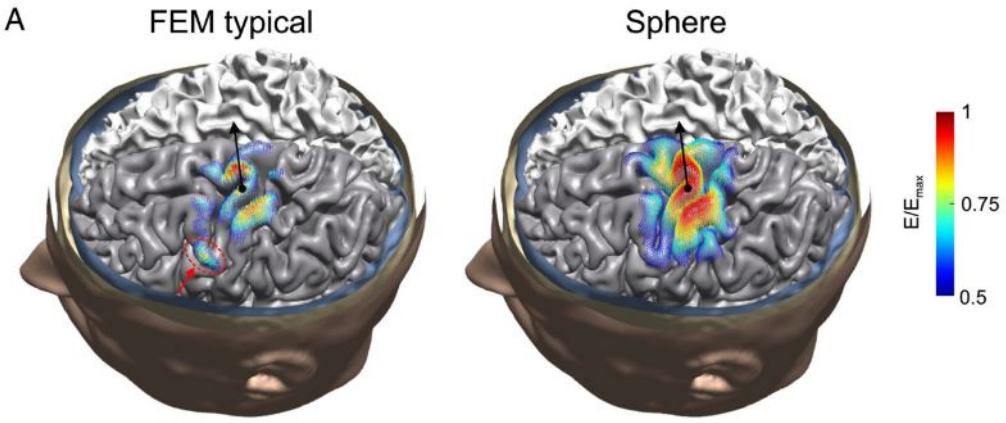

Figure 1 Electric field distribution and maxima change between FEM simulation that considers the geometry and heterogeneity in electrical conductivity compared to spherical models' projection.[15]

Advancement in the computational and modeling studies in TMS was achieved as researchers developed pipelines that can convert complex structural images of MRI into realistic models of the brain to investigate TMS's stimulation parameters further. For example, Thielscher et al. (2011) showed that the gyri's geometry in the brain, along with heterogeneity in conductivity, has a significant impact on the focality and target-ability. Figure 1 shows that the electric field distribution and maxima change between FEM simulation that considers the geometry and the heterogeneity in electrical conductivity compared to the projection of spherical models.

Previous modeling techniques were experimentally validated and verified with simple geometries like spheres or cubes [12,13,18]. Analogously, there is a need for experimental validation/verification of the computer modeling and simulation of complex and realistic brain models. This work aims to bridge the gap by introducing and developing an innovative manufacturing and fabrications process to produce a geometrically and anatomically accurate head

and brain phantom capable of being used in experimental evaluations of stimulation strengths in neuromodulation techniques and in particular in TMS.

This thesis consists of three main sections/chapters. In the first chapter, we present the processes involved in the development and fabrication of the head and brain phantom in detail. We present the novel method that we call the shelling method that we developed to obtain highly intricate and complex geometries like the brain. The other central part of chapter 1 is that we show the process of obtaining the “tissue" that mimics the brain's most relevant electrical property in such an application, namely, the electric conductivity.

In chapter 2, we show an example of the current and immediate application of this research in which the brain phantom can play an essential role in developing new TMS treatment procedures for neurological disorders. We use the brain phantom to examine the safety of combing two of the prominent brain stimulation techniques, TMS and DBS. We investigate the possible electromagnetic interference when using both modalities in this chapter. The alternating magnetic field generated by the TMS coils can induce unintended and excessive current on the DBS probe implanted in the head/brain. We present the brain and head phantom developed to host the DBS probe and exposed to the TMS's intense magnetic pulses. We measured the current in the DBS lead, and we show that the current is in the range of the unsafe limits when used at maximum coils power.

In chapter 3, we run a series of experiments and measurements to assess and evaluate the TMS and brain phantom environment. We present the measured magnetic field of the TMS coils in the Biomagnetics laboratory. We also investigated the feasibility of mapping the electric field on the brain using the oscilloscope probe. We measured the coils' induced voltages, on a conductive polymer sheet, and the brain phantom to reconstruct the electric field.

1.1 Brain anatomy and electrical properties

The central nervous system (CNS) consists of the brain and the spinal cord. The brain consists of three main parts: Cerebrum, cerebellum, and brainstem. The cerebrum is divided into left and right hemispheres that each hemisphere controls the opposite part of the human body. The cerebrum is comprised of different smaller regions and layers. The brain's outer layer is called the grey matter (GM) or the cortex, where the neural cells are mostly found. Going more in-depth than the cortex, we find the white matter (WM) made up of the neuron's axons or fiber tracts. The TMS work is substantially related to the brain's outer layer, the cortex because the effect of the magnetic field is mostly superficial [19]. Figure 2 shows some of the main parts of the CNS and the brain.

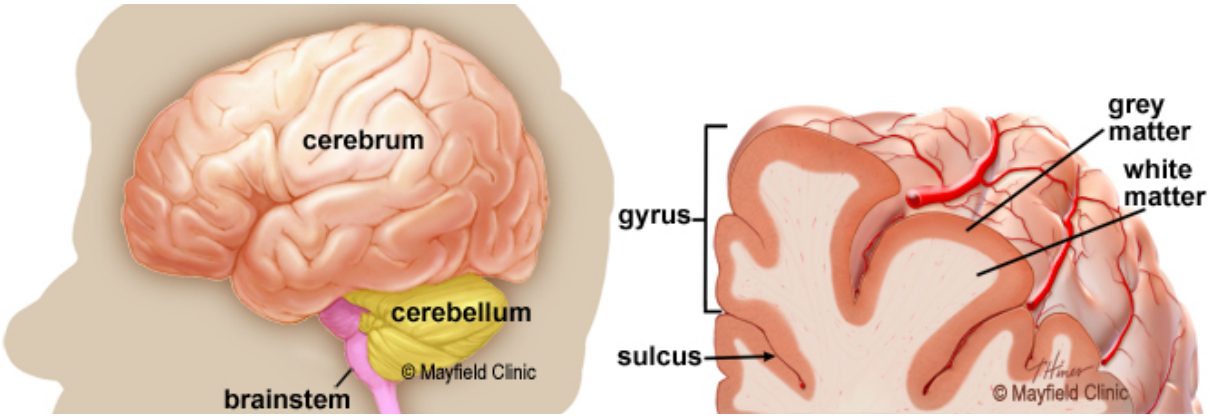

Figure 2 An illustration of some of the main parts of the central nervous system and the brain [20]

The electrical properties of the brain, especially the electrical conductivity, is of significant relevance to our work in the TMS and the fabrication of the brain phantom. Many researchers studied the brain's electrical properties over the past decades by various techniques and methodologies [21–30]. The first observation is that there is a wide range of variations in the reported electrical conductivity values. Such disparity could have resulted from the verity of the measuring techniques. Some of the techniques, for example, are based on direct measurements of the current form excised brain tissues of patient or cadavers, and some other techniques were based

on non-invasive means by evaluating the conductivity based on correlations to the MRI images information. We observed that in some cases, the conductivity of the grey matter is higher than the white matter and vice versa.

Moreover, the electrical properties like the conductivity and the permittivity are dependent on the frequency. For that reason, in table 1, we present some of the most relevant publications with values and measurements of electrical conductivity and permittivity (often referred to as the dielectric property). In general, these conductivity values (from 0.1 up to 2.5 S/m) are considered to fall in the low conductance values compared to the electrical conductivities of various materials, as in Figure 3.

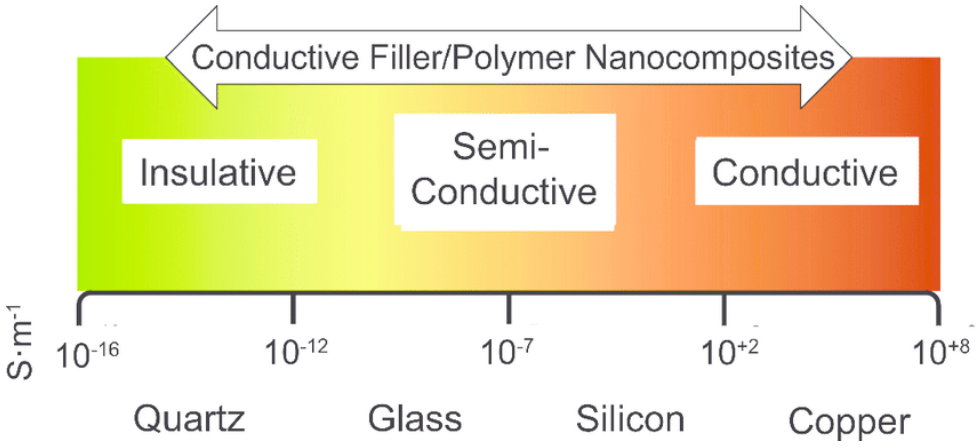

Figure 3 Spectrum of electrical conductivity of materials [32]

In this work, as we will show the process of manufacturing and fabricating the brain phantom, we chose to assign conductivity values that are averaged and within the range of the reported values.

Table 1. Relevant reported brain electrical properties in literature

Reference/ Author	**Method**	**Frequency**	**Conductivity (σ) and relative permittivity (ε_r) values**					
			GM		WM		CSF	
			σ[S/m]	ε_r	σ [S/m]	ε_r	σ [S/m]	ε_r
Gabriel. S (1996) [21,22,24]	Direct measurement	10 Hz - 20GHz (2.5 kHz)	0.05 - 10 (0.1)	10E+07 (10E+04)	-	-	-	-
Wagner. T	-	-	0.27	1.2E+07	0.12	1.2E+07	1.65	0.6E+07
Gabriel. C (2009) [27]	Direct measurement	less than 1 MHz	-	-	-	-	1.5	-
Akhtari. M (2016) [29]	Bulk measurements from excised brain tissues and dMRI analysis.	-	0.06-0.24	-	0.06-0.24	-	-	
Mickel. E. (2017) [30]	MRI T1-water content weighted acquisition	-	0.63	74.66	0.39	61.1	2.22	83.83

1.2 Neurons and action potential

The building blocks of the nervous system are the neuron cells and glial cells. The glia cells support the growth and development of the neurons by providing nourishment and protection.

Experts estimated that there are around 85 billion nerve cells in an adult human CNS [33]. The neuron consists of four main parts, cell body, axon, dendrites, and synaptic terminals, as shown in Figure 4.

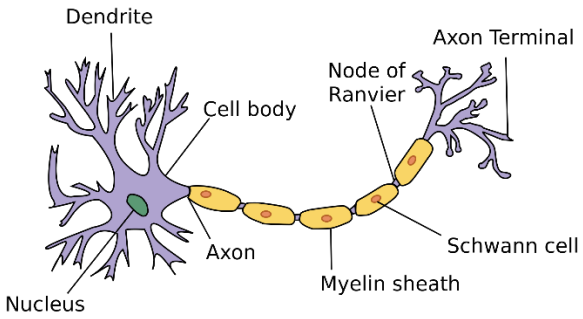

Figure 4 Depiction of the basic structure of the neurons [34]

There is tremendous connectivity between the neurons; there are trillion synaptic connections in one cubic centimeter of the cortex, and there are up to six levels of connections between some neurons in the brain. Therefore, the brain is highly interconnected, and any influence on one area of the brain will have a more considerable impact on the brain due to the connectivity. The neuron cells in the nervous system are divided into different groups according to their functions. Some are sensory; others are motor or a combination of the two. They also differ in terms of the geometrical structure like pyramidal, basket spindle, etc.

The neurons' activity and function are to process and transmit information around the nervous system and the body. Of the essential functions is the neural action potential shown in Figure 5. It is the transmission of electrical signals from one neuron to another in which the neuron membrane opens and exchange positively charged ions from outside the cell and negatively

charged ions inside and vice versa. This action potential happens when the neurons receive signals from other cells. The sum potential overcomes a threshold (around -55mV) that triggers the neuron to fire and start the ion exchange process. The cell always tries to maintain a resting potential of around -70 mV [35].

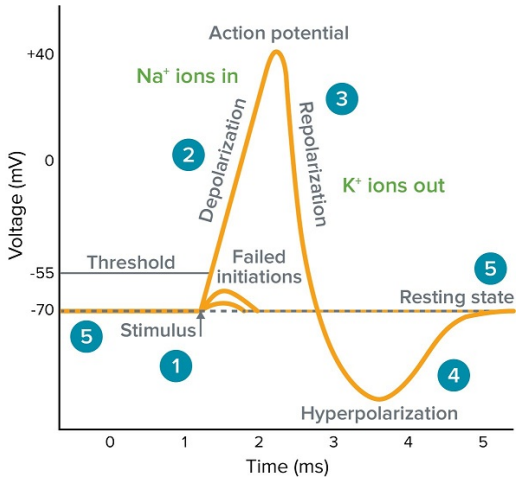

Figure 5 An illustration of the stages of the action potential of the neurons [36]

There are also other means of eliciting neural firing in neurons, such as applying an external alternating magnetic field similar to TMS, which induces an electric field that depolarizes axonal membrane and initiates action potentials in the neurons [37]. The amount of excitation depends on many factors like the length of the axons, the axons' orientation with respect to the rate of change of the electric field, electrical conductivity, and distance from the TMC coil [16,37,38].

There are two types of neuronal signals/responses, inhibitory and excitatory. The excitatory action is when the neurons firing extend to the next neuron by a class of chemicals called the neurotransmitters. The inhibitory action is the opposite, where the released neurotransmitters inhibit the firing of the next neurons.

The action potential is likely to occur when the electric field gradient is highest along and parallel to the axons and when bent as depicted in Figure 6.[39,40]

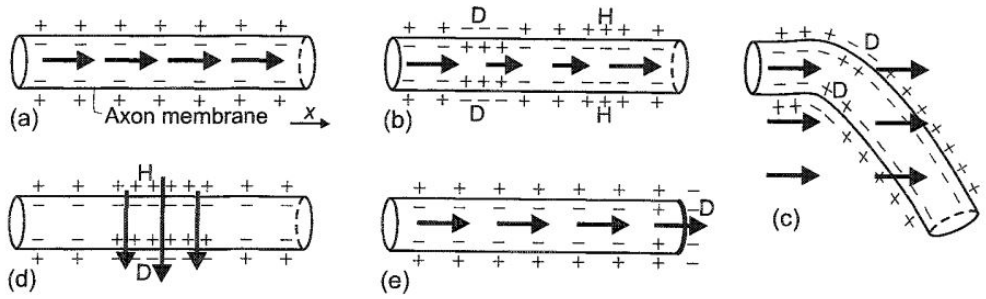

*Figure 6 An illustration of the likelihood of neural activation on axons with respect to the electric field. (a) Uniform **E** along axon showing no activation, (b) gradient activation, (c) bent axon in a uniform **E**, (d) transverse activation, (e) axon termination in a uniform **E.** D= depolarization, H= hyperpolarization.* [39]

That shows it is crucial to recognize the magnitude, directions, and gradient of the electric field to the treated neuron population during the brain stimulation.

1.3 Transcranial magnetic stimulation (TMS)

Transcranial Magnetic Stimulation (TMS) is a non-invasive technique for diagnostics and treatments of various psychiatric and neurological disorders [41–43]. TMS coils produce an intense and time-varying magnetic field on the brain that induces an electric field on the brain's conductive parts. The electric field works as a driving force on the neurons that will initiate an action potential when it exceeds specified limits (motor threshold). The alteration on the neuron synaptic in a controllable fashion will inhibit or excite these neurons' activity and, therefore, lead to a change in the brain and body functions. Figure 7 shows an illustration of the basic principle of the TMS.

There are many advantages of TMS that makes it very promising for researchers and clinicians. It is non-invasive, meaning that there is no need for any surgical interventions to modify the brain neural activity as opposed to techniques like the DBS. It is safe and relatively painless and has very little pain in some cases [44]. The most significant advantage of TMS is that it can be administered in an outpatient setting where the patient does not need to be hospitalized or

anesthetized. Patients can continue their day to day activities immediately after the TMS treatment [45].

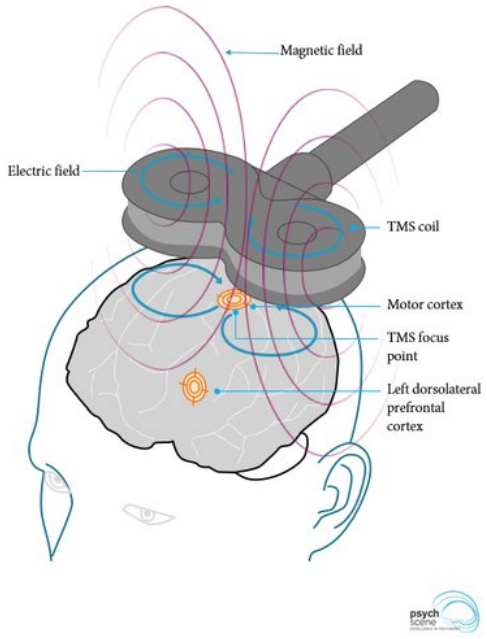

Figure 7 An illustration of the TMS, where coils produce a magnetic field which induces an electric field on the brain motor cortex. [46]

The TMS device consists of two main components, the power stimulator, and the coils, as in Figure 8. The power stimulator's function is to produce transient current form a charging system up 8000 A in less than 100ms (2-3kHz) and with voltages that reach up to 7500 V [47].

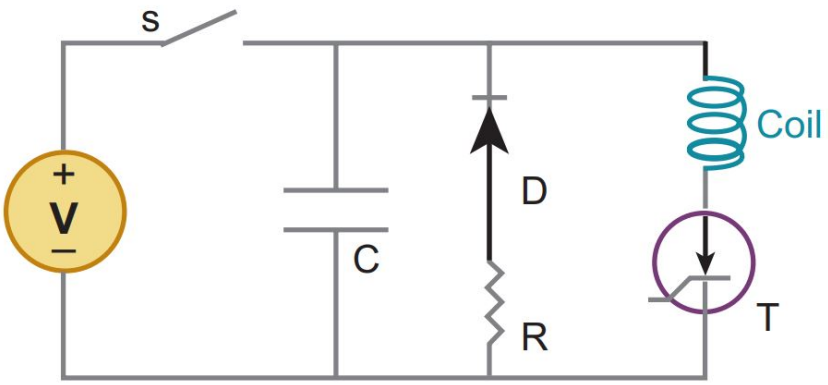

Figure 8 Simplified diagram of the single-pulsed TMS stimulator circuitry where V=voltage sources, s= switch, C= capacitor, D=diode, R= resistor, T= thyristor. [48]

The waveform of the current running in the coils is significant because it dictates the induced magnetic field's shape and the voltages, as illustrated in Figure 9.

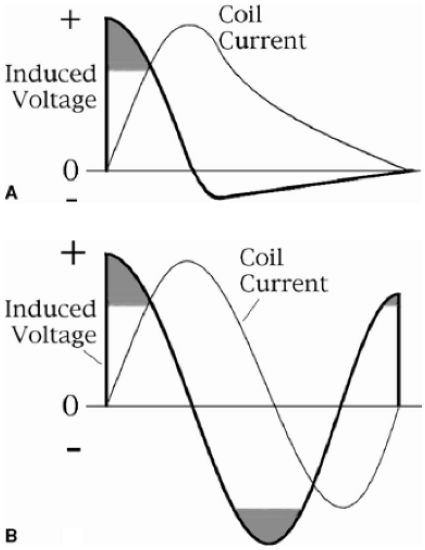

Figure 9 (A) monophasic and (B) biphasic pulses produced by the TMS coils [49].

1.4 Theoretical background

In electromagnetism, H is known as the magnetic field, and B is magnetic field flux density. They have the following relationship in the equation:

$$B = \mu_0 \mu_r H \quad \text{Eq. (1)}$$

Where B is the magnetic flux density, μ_0 is the permeability of the free space, μ_r is the relative permeability —the resultant multiplication of $\mu_0 \mu_r = \mu$.

After the magnetic field production in current-carrying coils, it penetrates the scalp and interacts with the brain tissue and generates an electric field in the conductive parts of the brain. This phenomenon is governed and expressed by the third law of Maxwell equations, Maxwell-Faraday's equation. Maxell's equations are shown in the following,

$$\nabla \cdot \mathbf{E} = \frac{\rho}{\varepsilon_0} \quad \text{Eq. (2)}$$

$$\nabla \cdot \mathbf{B} = 0 \quad \text{Eq. (3)}$$

$$\nabla \times \mathbf{E} = -\frac{\partial \mathbf{B}}{\partial t} \quad \text{Eq. (4)}$$

$$\nabla \times \mathbf{B} = \mu_0 \varepsilon_0 \frac{\partial \mathbf{E}}{\partial t} + \mu_0 \mathbf{j} \quad \text{Eq. (5)}$$

B is the amplitude of the magnetic flux density and **E** the electric field vectors. **ρ** is the charge density. **J** is the current density vector. The electric field in TMS can be found by the following equation [39]:

$$\vec{\mathrm{E}} = -\frac{\partial \vec{\mathrm{A}}}{\partial \mathrm{t}} - \nabla \Phi \quad \text{Eq. (6)}$$

$\vec{A}$ is the magnetic vector potential corresponds to current levels running in a coil, Φ is the electric scalar potential resulting from the charge accumulation on the conductor boundaries and discontinuities.

$$\vec{E} = -\nabla\Phi \qquad \text{Eq. (7)}$$

"ohm's law" is as follows,

$$\vec{J} = \sigma\vec{E} \qquad \text{Eq. (8)}$$

A special treatment to the Maxwell equations at lower frequency is called the Quasi-static approximation. Plonsey et at. (1969) [50] presented the derived equations in terms of the scalar and vector potentials. Heller et al. (1992) [51] expressed it in terms of the electric field directly and they are as follows:

$$\nabla \cdot J + \frac{\partial \rho}{\partial t} = 0 \qquad \text{Eq. (9)}$$

J can be decomposed into,

$$J = J^P + \sigma E \qquad \text{Eq. (10)}$$

J^P is the primary current and σE is the conduction or return current. In biological tissue, the effect of the dielectric current or the polarization current is negligible compared to the conduction current σE. When the conductivity is constant, the charge density decays fast following $e^{-\omega_0 t}$. Therefore, the charges appear at the surfaces when σ jumps in value. ω_0 is the characteristics frequency and it is giving by,

$$\omega_0 = \frac{\sigma}{\epsilon} \qquad \text{Eq. (11)}$$

The ratio of the conductor size to the skin-depth δ is of another consideration. δ is given by,

$$\frac{1}{\delta^2} = \frac{1}{2}\mu_0\sigma\omega \qquad \text{Eq. (12)}$$

When there is no electric charge density, the electric field equation is satisfied by,

$$\nabla^2 \mathrm{E} = -(i\mu_0\sigma\omega + \mu_0\epsilon\omega^2)E \qquad \text{Eq. (13)}$$

Assuming the brain conductivity $\sigma = 0.4\ S/m$ leads to

$$\delta^2 = \frac{2}{\mu_0\sigma\omega} = \ = 4.0\ X\ 10^5\ cm^5 \qquad \text{Eq. (14)}$$

For a frequency $\omega \approx 10^5$ and $D \approx 20\ cm$, $\left(\frac{D}{\delta^2}\right) \ll 1$. This shows that expansion of E in terms of ω will converge rapidly to a real solution, which is the principle of the quasi-static approximation. Inserting the expansion of E into Eq.13 yields,

$$\nabla^2 \mathrm{E} = 0 \qquad \text{Eq. (15)}$$

Now, to solve the problem for a magnetic source, the reciprocity theorem can be used, and it leads to,

$$\mathrm{p} \cdot \mathrm{E}_{(\mathrm{r1})} = \mathrm{i}\omega\mathrm{m} \cdot \mathrm{B}_{(\mathrm{r2})} \qquad \text{Eq. (16)}$$

where p is a current dipole at position r inside a conductor, m is a magnetic moment located at position r_2 outside the conductor. This equation is a direct relation between the magnetoencephalography and electromagnetic stimulation, and hence the reciprocity. The static B is given by Biot-Savart law,

$$\mathrm{B(r)} = \frac{\mu_0}{4\pi} \int d^3r' J(r') \times \nabla' \frac{1}{|r-r'|} \qquad \text{Eq. (17)}$$

Which can be converted into a surface integral

$$\mathrm{B(r)} = \frac{\mu_0}{4\pi}\,[\mathrm{P}\,\times\,\nabla_1\,\frac{1}{|r-r'|} - \Sigma_j\left(\sigma_j{}^{-}\,+\sigma_j{}^{+}\right)$$

$$\times \int ds'_j V(r')n(r') \times \nabla' \frac{1}{|r-r\prime|} \qquad \text{Eq. (18)}$$

Where V is the electric potential on the surface. Considering that the head is spherical and symmetrical, and the conductivity is only a variable of distance, the solution to the magnetic field is as follows,

$$\mathrm{B(r)} = \frac{\mu_0}{4\pi}\;\nabla_2\;\frac{\mathrm{p}\times r_1\cdot r_2}{F} = \frac{\mu_0}{4\pi F^2}\,[\,F\mathrm{p}\,\times \mathrm{r}_1 - (\mathrm{p}\,\times \mathrm{r}_1\cdot \mathrm{r}_2\,)\nabla^2 F] \qquad \text{Eq. (19)}$$

F is a function of the $\mathrm{r}_1$and r_2,

$$F = a(\mathrm{r}_2 a\,+\,\mathrm{r}_2\cdot\,a) \qquad \text{Eq. (20)}$$

And,

$$a = \mathrm{r}_2 - \mathrm{r}_1 \qquad \text{Eq. (21)}$$

To obtain E(r), $\mathrm{m}\cdot\mathrm{B(r)}$ is needed for the first term and as follows,

$$\mathrm{m}\cdot\mathrm{B(r)} = \frac{\mu_0}{4\pi}\,(m\cdot\nabla_2)\frac{\mathrm{p}\,\times \mathrm{r}_1\cdot \mathrm{r}_2}{F}$$

$$= \frac{\mu_0}{4\pi}\;\mathrm{p}\cdot(m\cdot\nabla_2)\frac{\mathrm{r}_1\times \mathrm{r}_2}{F} \qquad \text{Eq. (22)}$$

Comparing it to Eq.16 results in the electric field solution given by,

$$\mathrm{E}_{(\mathrm{r1})} = \mathrm{i}\omega\frac{\mu_0}{4\pi}\;\mathrm{p}\cdot(m\cdot\nabla_2)\frac{\mathrm{r}_1\times \mathrm{r}_2}{F}$$

$$= \mathrm{i}\omega\frac{\mu_0}{4\pi F^2}\,[F\mathrm{r}_1\times m - (m\cdot\nabla_2 f)\mathrm{r}_1\times \mathrm{r}_2] \qquad \text{Eq. (23)}$$

This page intentionally left blank.

2 Chapter1: Anatomically accurate and electrically conductive brain phantom

2.1 Introduction:

Mimicking human body organs is an exciting field in engineering and biomedical engineering in general [52,53]. Scientists, engineers, and researches have sought to manufacture, mimic, fabricate, replicate, and imitate specific properties and characteristics of physical objects since the dawn of the scientific method because it allows experimental methodologies to perform beside analytical and numerical solutions to apprehend the essences and principles of natural phenomena [54].

We have developed a geometrically accurate 3-D brain and head phantom [55] with the electrical conductivity matching the average electrical conductivity of the grey matter (GM) and white matter (WM) in the brain as well as the conductivity of the cerebrospinal fluid (CSF). In this study, we have mainly focused on GM and WM as they make up the cortex, which is the brain's main region that TMS procedures target in most neurological disorders' treatment. The phantom will enable the researchers and clinicians in the brain modulation to test and perform brain stimulations on the phantom before clinical studies of TMS treatment.

Manufacturing the geometry of the brain has been a challenge. Some groups successfully obtained the brain geometry but without imparting the electrical conductivity to the regions of the phantom material [12–14]. Therefore, the main challenge is to fabricate an electrically conductive and anatomical accurate brain phantom to validate the TMS's experimental side.

The principle of phantoms in medical imaging and health physics has been known for a long time [56]. For example, in medical physics, phantoms are used to assist in measuring the

absorbed dose of the X-ray of many X-ray machines modalities like conventional X-ray, computational tomography CT, mammography, etc. [57]. Also, they are utilized to calibrate other medical imaging modalities like the MRI machines [58]. The phantom, in this case, consists of many compartments. Each compartment is formed or created with a material that mimics the proton density of the different segments or parts of the human body.

The advancement in 3D printing techniques boosted the manufacturing processes for various applications [59,60]. There are many different techniques for 3D printing, including fused deposition modeling (FDM), powder bed, inject printing and contour crafting, stereo-lithography (SLA), selective laser sintering (SLS). There are also other emerging printing techniques where the printed materials consist of polymers enhanced with other composites to improve the performance and functionality (e.g., fiber-reinforced polymer composite, particle reinforced polymer composites, and nanocomposites).

The electrical conductivity values of any specific region of the brain vary between different sources of literature and also between subjects (see Table 1) [25,29,30,61]. For that reason, we chose an average conductivity of our brain phantom's constituent material (conductive polymer) to be approximately 0.25 Sm-1. This value is the average conductivity of the GM and WM from the literature. For the CSF, we chose a conductivity of about 1.4 Sm-1 made of saline water and injected inside the head phantom.

This chapter presents the process of creating the anatomically accurate electrically conductive brain phantom with an adjustable conductivity for brain stimulation applications.

2.2 Materials and Methods:

This section shows in detail the processes to produce the head and brain phantom. Nevertheless, first, I would like to give a brief summarized introduction of the entire process. To create an anatomically accurate and electrically conductive brain, we have to take it to step by step. Before imparting the conductivity to the brain phantom, we have to overcome manufacturing an intricate geometry such as the brain. We introduce a new approach that we call the shelling method, where we create shells/molds for the desired part of the brain to be built and used with as appropriate conductive composite to be cast into the molds. The process started with acquiring a magnetic resonance image (MRI) of the brain of an individual. The MRI images were segmented into 3D models in an stl file that is processed to create the shells. Shells were printed using a 3D printer with dual extrusion because the shells with the complex geometry need a support material that helps build up the shells and the surface finish. The advantage of using the shelling method is that those shells can be easily removed after the polymer's molding. After that, the shells were broken and dismantled using acetone and finally producing the phantom. We acquired SEM images of the conductive polymer composition to show the conductive filler's dispersion into the polymer. Finally, CT images of the physical phantom were acquired to confirm the brain's accurate reproduction of anatomical features compared to the original MRI segmented brain model. Each step is explained in detail in the following sub-sections. Figure 10 shows a summarized process chart of the brain phantom's creation and the related steps to validate it.

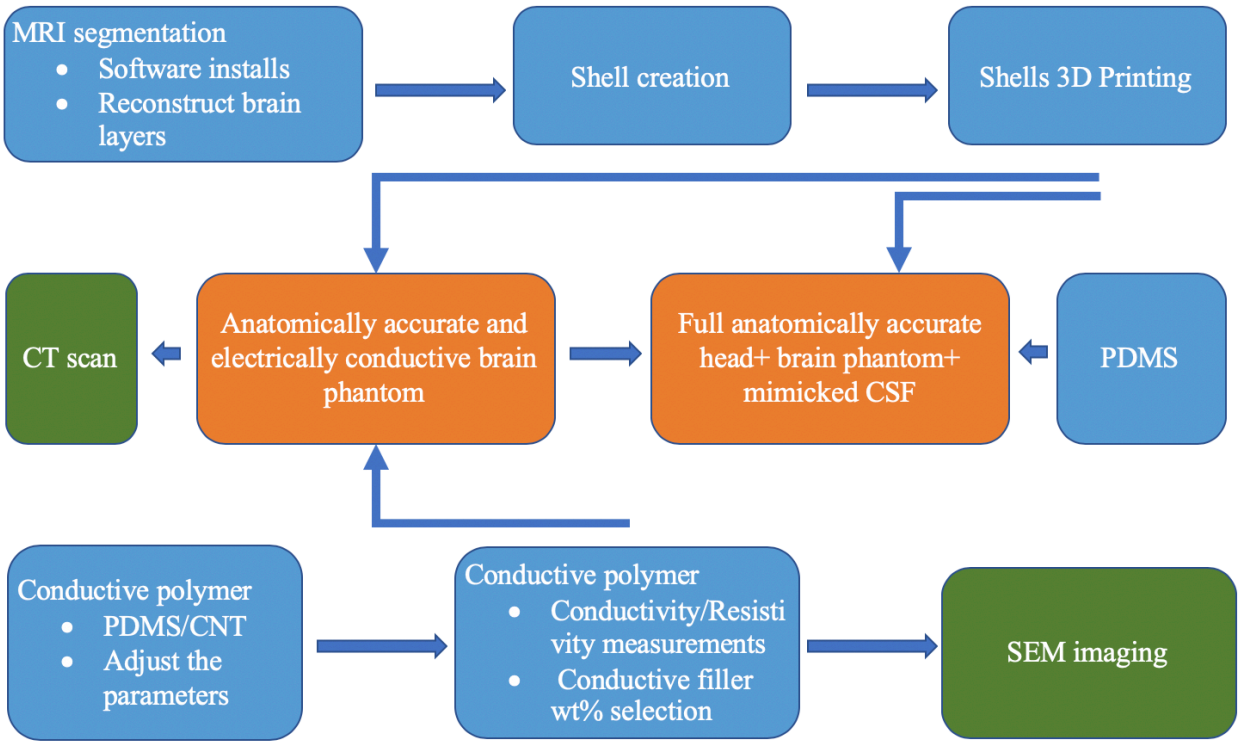

Figure 10 Process chart summarizing the steps related to the brain phantom creation and validation.

2.2.1 Segmentation: Reconstruction of the MRI images into 3D models.

There are many techniques for segmenting the 2-dimensional medical images into 3-dimensional models. For the brain segmentation, we used FreeSurfer (Athinoula A. Martinos Center for Biomedical Imaging, Charlestown, MA, United States), SimNIBS (Danish Research Centre for Magnetic Resonance (DRCMR), and FSL (Analysis Group, Oxford, UK) software. These software are used to segment the MRI images of the head into the skin, skull, CSF, and the main parts of the brain: Grey matter, white matter, ventricles, and cerebellum. In the following, we present the steps required to install the software to reconstruct the MRI images into brain models.

The process starts with installing the required software and ends by adjusting and handling the precision and characteristics of the brain models and simulation. These software are best to be installed on MAC and Linux systems.

First, very basic knowledge of how to use the Terminal on Mac is required, which is the equivalent of the Command window on Windows. That is because one will need to perform some tasks and commands on the terminal to complete either the installation, the configuration of the software, or in the later steps, the construction of the brain models and simulation.

Now, we open the terminal and make sure to work in the right shell environment. In our case, it is the ".bash" shell environment. In order to change the shell, go to the link (https://osxdaily.com/2007/02/27/how-to-change-from-bash-to-tcsh-shell/) and follow the steps. This is a crucial step because the installations will not complete as the variable required for installation will not be available on any shells other than the .bash environment. The terminal window should look like Figure 11.

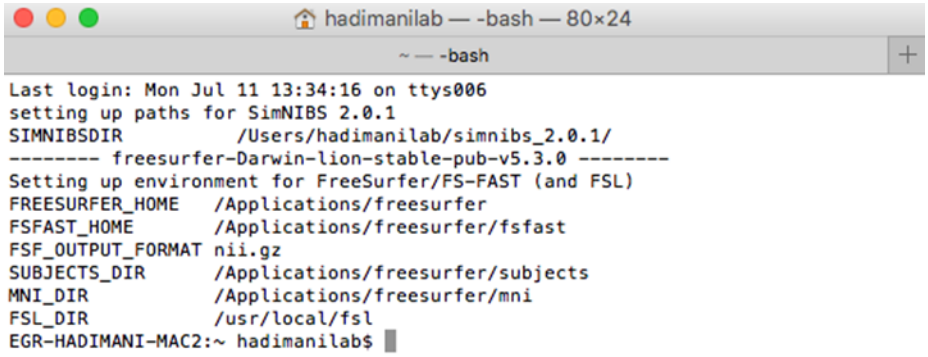

Figure 11 MAC terminal set on the Bash environment and ready for the software installation

We should note that the terminal's final set up as it appears in *Figure 11* will be achieved after completing the entire process. The following are the steps needed to install the three primary software (FreeSurfer, FSL, simNIBS):

1. FreeSurfer

I. We need to download and install the FreeSurfer from the following link (http://freesurfer.net/fswiki/DownloadAndInstall) and download the appropriate version for the MAC system.

II. After the download, simply we click on the .dmg file and complete the installation. We make sure that Mac OS X users: Mac OS X platform requires the installation of XQuartz for FreeSurfer to work correctly. Pre-Yosemite versions of OSX require XQuartz 2.7.5. Post-Yosemite versions of OSX require XQuartz 2.7.6) before going further in the installation.

III. Then, we open the Terminal and write the following configuration command:

```
$> export FREESURFER_HOME=/Applications/freesurfer

$> source $FREESURFER_HOME/SetUpFreeSurfer.sh
```

This simply means that the software is directly accessible and available to other software or whenever needed for recall.

2. FSL

I. For the installation of FSL, we go to the following link (https://fsl.fmrib.ox.ac.uk/fsl/fslwiki/FslInstallation) and download the FSL version for the MAC OS. Here also we need to register and create an account in order to be able to download.

II. Follow the steps in this link (http://fsl.fmrib.ox.ac.uk/fsl/fslwiki/FslInstallation/MacOsX) to complete the

installation. Then, we open the terminal and go to the download directory and type the following command,

python fslinstaller.py

3. simNIBS

I. After successfully installing FreeSurfer and FSL, we are ready to install simNIBS. Click on this link simNIBS (https://simnibs.drcmr.dk/) to go to the website where we can download the software. We need to register on the website and create an account. Then go to the download section and download SimNIBs latest version for MAC OS as in Figure 12.

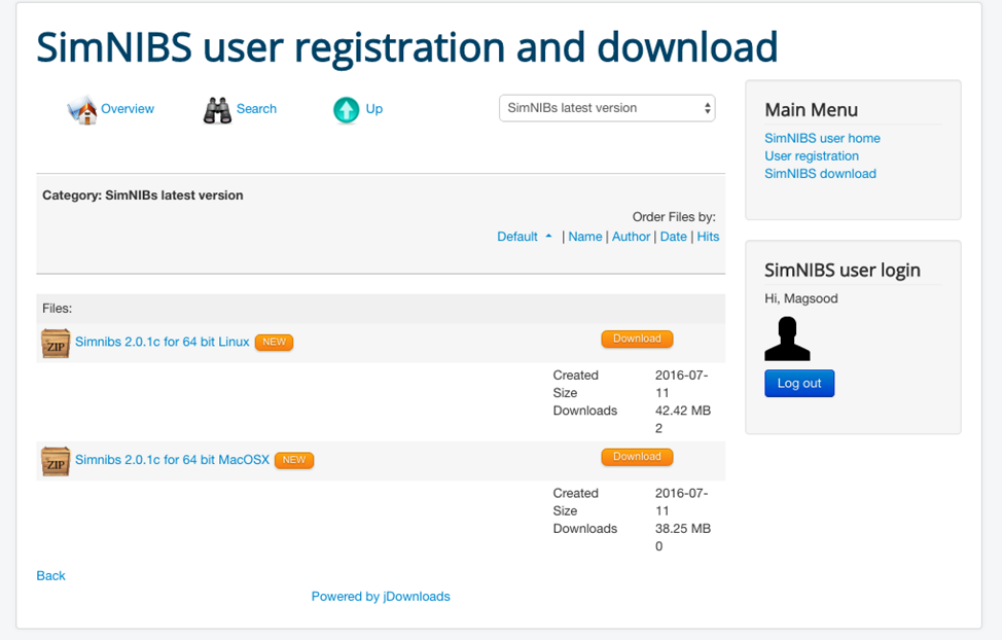

Figure 12 The webpage where simNIBS is downloaded from.

II. Now go to the following link and install simNIBS by the terminal. Or simply find the installation instructions from simNIBS website.

Now we are ready to create brain models with simNIBS. SimNIBS relies on FSL and FreeSurfer to perform the Segmentation. The segmentation is a process where the MRI images are analyzed based on the T1 and T2 relaxation time.

Now it is ready to use simNIBS to create models from MRI images that have the extension of nii.gz. We can find some of the reconstructed models as examples from the simNIBS website.

After downloading the example file, open the terminal instance to the directory to have the file downloaded. Type the following command:

mri2mesh --all simnibsExample almi5_T1.nii.gz almi5_T1fs.nii.gz almi5_T2.nii.gz almi5_T2fs.nii.gz

simNIBSExample is the model name. Change it accordingly if the file name is different.

Please allow about 12 hours of modeling. After that, to check up on the results, we can either do that through simNIBS_gui or the gmsh software.

In the terminal window, go to the directory where we have the files created after the modeling. The files should look like the following Figure 13:

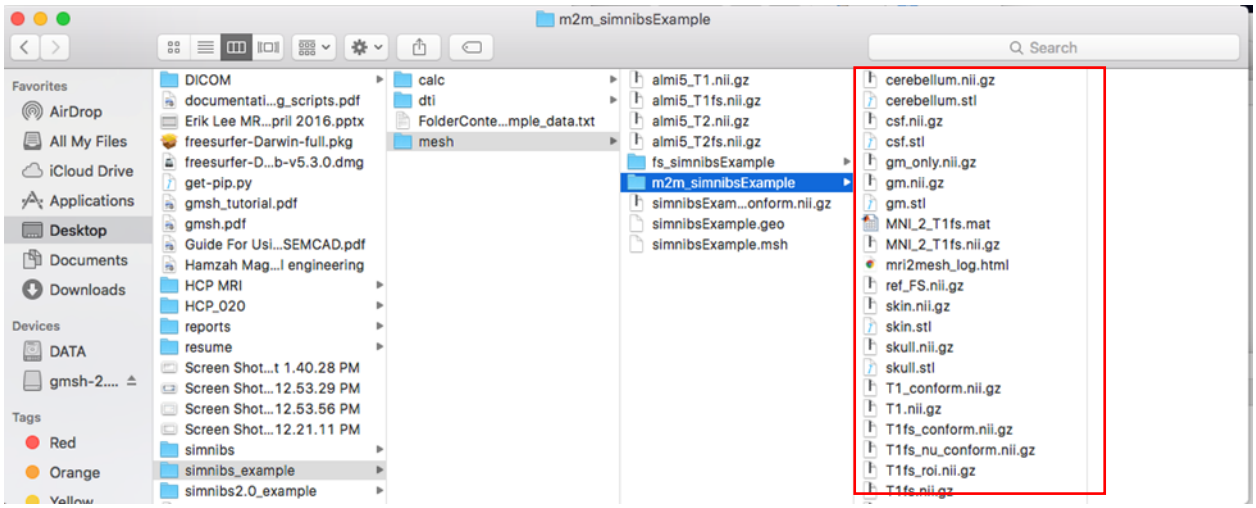

Figure 13 An example of the file window that contain the segmented files as stl extension

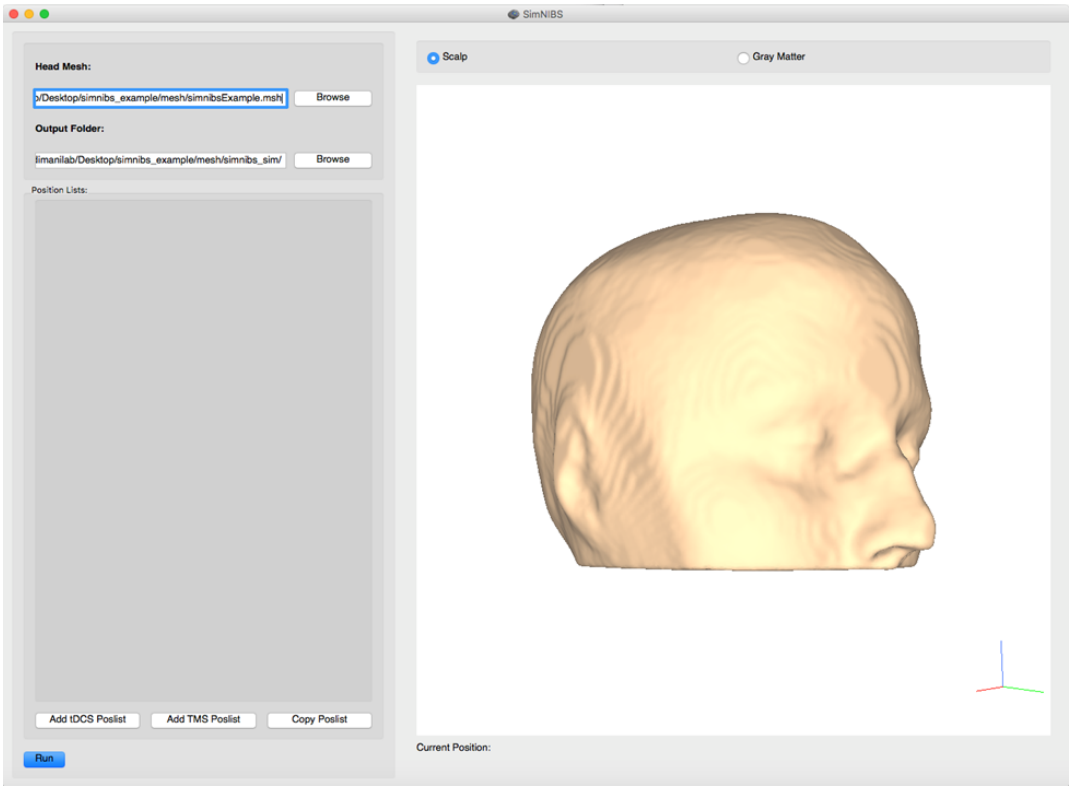

Figure 14 An example of a reconstructed model and ready for simulation in simNIBS

Now, we are ready to run a simulation on the created stl files of the brain model (Figure 14) and work on the shelling method developed to create and obtain the brain phantom's physical geometry. Figure 15 shows the separate regions of the reconstructed brain model in Meshmixer.

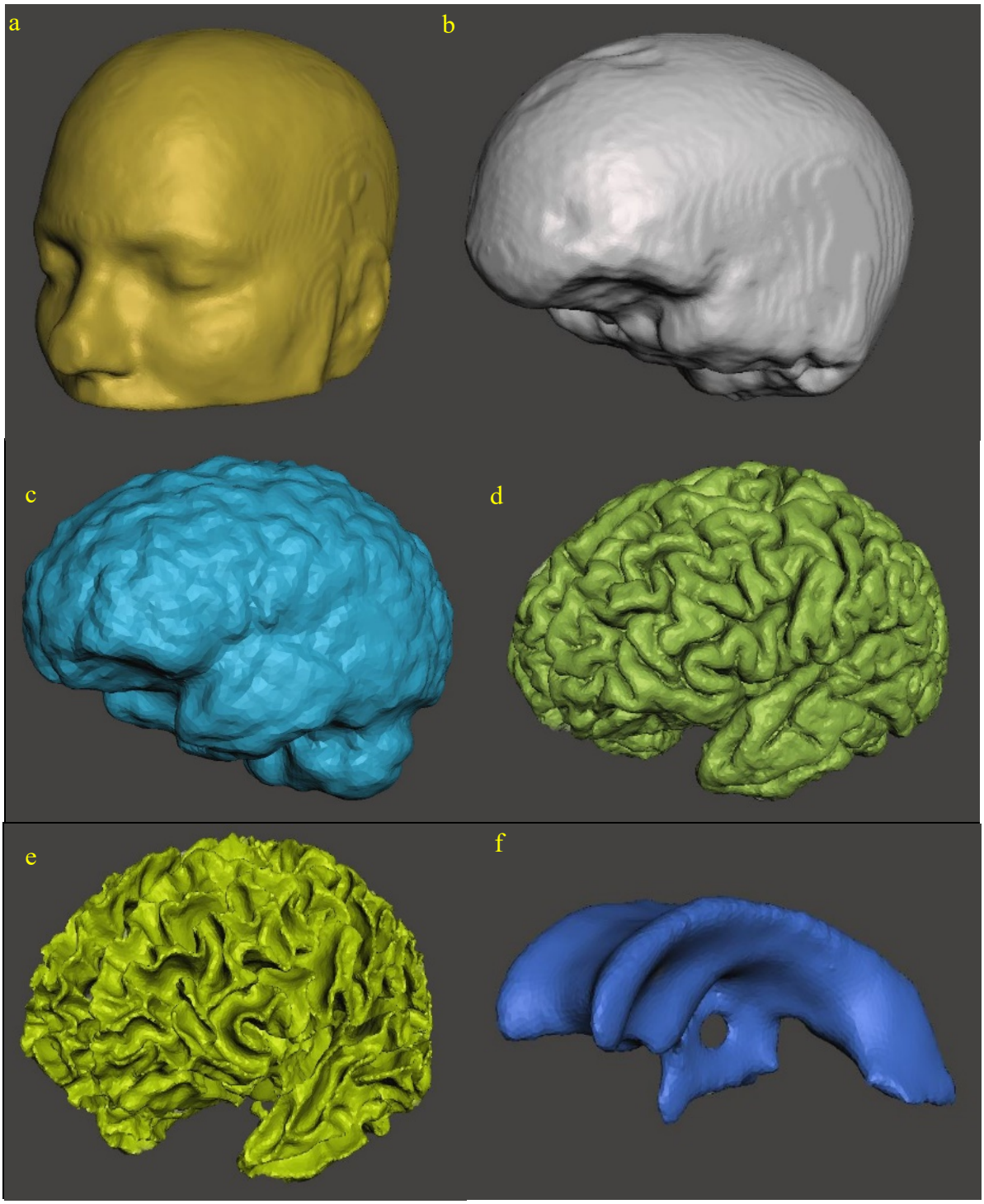

Figure 15 MRI image segmented into the (a) skin, (b) skull, (c) CSF, (d) grey matter GM, (e) white matter WM, and (f) ventricles. The scales of the segmented models are modified and do not reflect the actual scales

2.2.2 Shelling method and shells creation

We introduced the shelling method. The shelling method's main idea is that it is capable of producing the full geometry of the brain without losing any of its intricate features.

Following the segmentation of the brain parts, we imported the brain model into Meshmixer software. In Meshmixer, we worked on creating a shell of the brain's outer side by working on the Grey mater layer. One way to do that in Meshmixer is by creating a solid object out of the brain (GM) with a 1 mm offset thickness. Then, we subtract the original brain model from the solid brain. This will create the shell. The shell's inner side is nothing but the original geometry of the brain's surface (GM). There will be an overlap but only on the outer side of the shell, which is fine as long as the area of interest, inner side, is intact and has no overlap. In other words, the shell = 1 mm-additional-thickness brain model – original brain model.

After creating the shell, some refinement of the shell is needed as the post shell creation process results in tiny parts of the brain with undefined shapes due to the low mesh numbers in that region the thickness of the shell can vary depending on the 3D printing technique and material. In our work, we found that 1mm thickness is optimal between the shell's sturdiness and the dissolving/breaking of the shell time. This process can be applied to different parts of the segmented brain. For example, the white matter shell can be obtained by subtracting the white matter from the grey matter and then making a 1 mm thickness of the GM's inner side. Figure 16 shows a simplified illustration of creating the shell for any geometry of the brain.

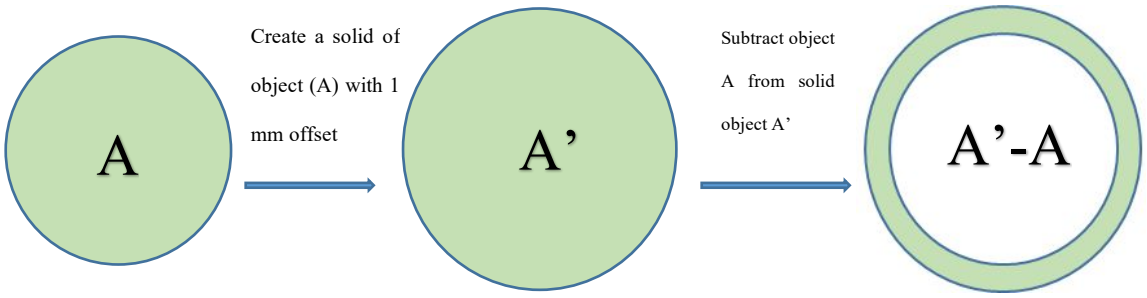

Figure 16 illustration of the shell creation with simplified geometry of the brain parts. This simple method can be applied to any part of the brain like GM, WM, or vertical. For example, considering the GM to be object A, we create a solid object in Meshmixer with 1mm offset distance to create object A'. Subtracting object A form A’ will result in a GM shell with thickness of 1mm.

To ease shell's printing, the brain shells were split into two shells, upper and lower shells, as in Figure 17. This way, we can cast the conductive polymer inside the shells, join them together, and then remove them.

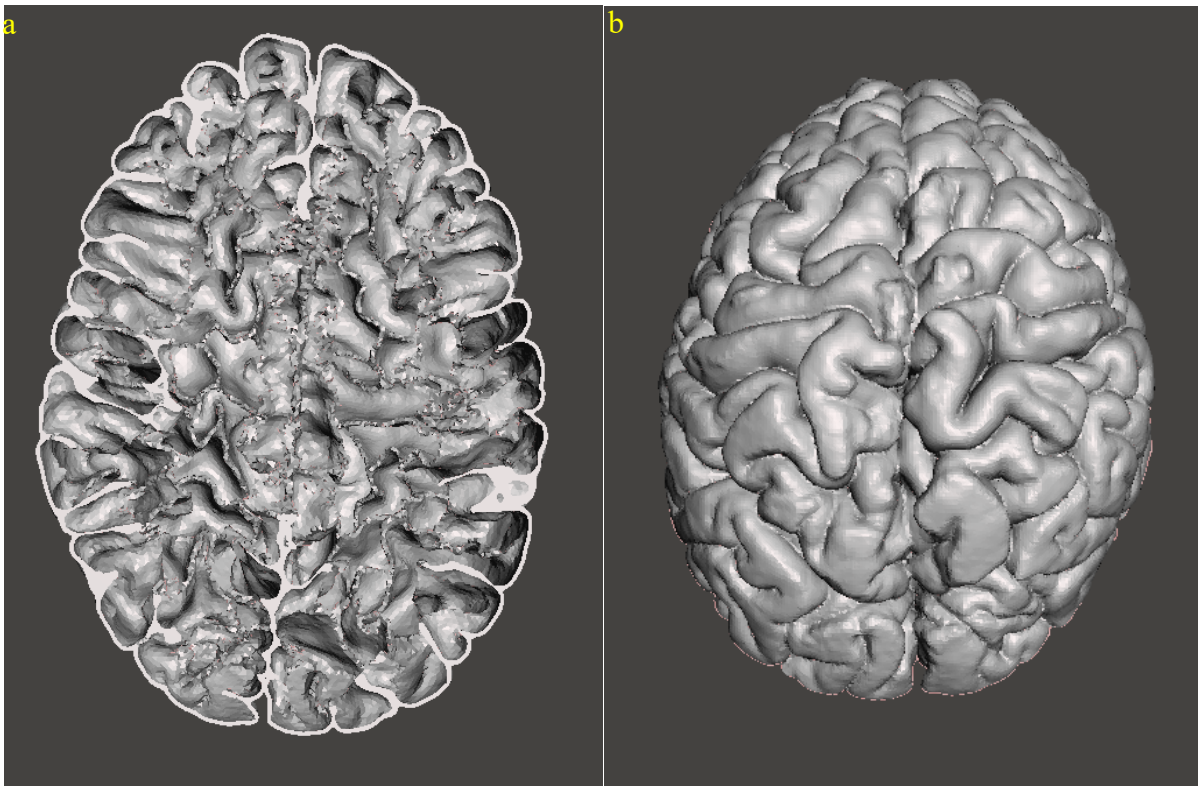

Figure 17 (a) inside and (b) outside views of the upper half of the grey matter shells created in Meshmixer and ready for 3D printing.

2.2.3 Shells 3-D printing

After the creation and refinement of the shells, the shell is ready to be printed. There are many different printing techniques. In this work, we used the filament deposition modeling FDM technique. We used Ultimaker3TM (Dual extrusion 3-D printer was obtained from Ultimaker Inc.) because it has dual extrusion and can print with Polylactic acid PLA and Polyvinyl alcohol PVA as support. The shell has an intricate geometry. Therefore, printing with one material will be troublesome to obtain the needed shell geometry with a fine surface finish. The surface finish is significant because it is a mold for to-become a phantom. So, we used a dual extrusion, one extruder to print the shell material. For that one, we used PLA because it becomes brittle when immersed in acetone. For the second extruder, we used PVA that is dissolvable in water to support the PLA to be built and help obtain a smoother surface finish. Figure 18 shows the setup of the

3D printing of the shell in open-access software Cura. One can adjust the printing parameters as needed, such as the filament deposition rate and temperature. There is no one setup of the parameters as it is an optimization process between time and quality.

Figure 19 shows the printing in the progress of the GM shells. After the printing is done, the entire printed object made of the PLA and PVA is immersed in water to dissolve the PVA and remain with the shell made of PLA, as shown in Figure 20. Now, the shell is ready to be cast with any polymer (e.g., conductive polymer). Figure 21 shows a flow chart summarizing the entire process of the shelling method. The process of preparing and imparting conductivity to the polymer is shown in the next section.

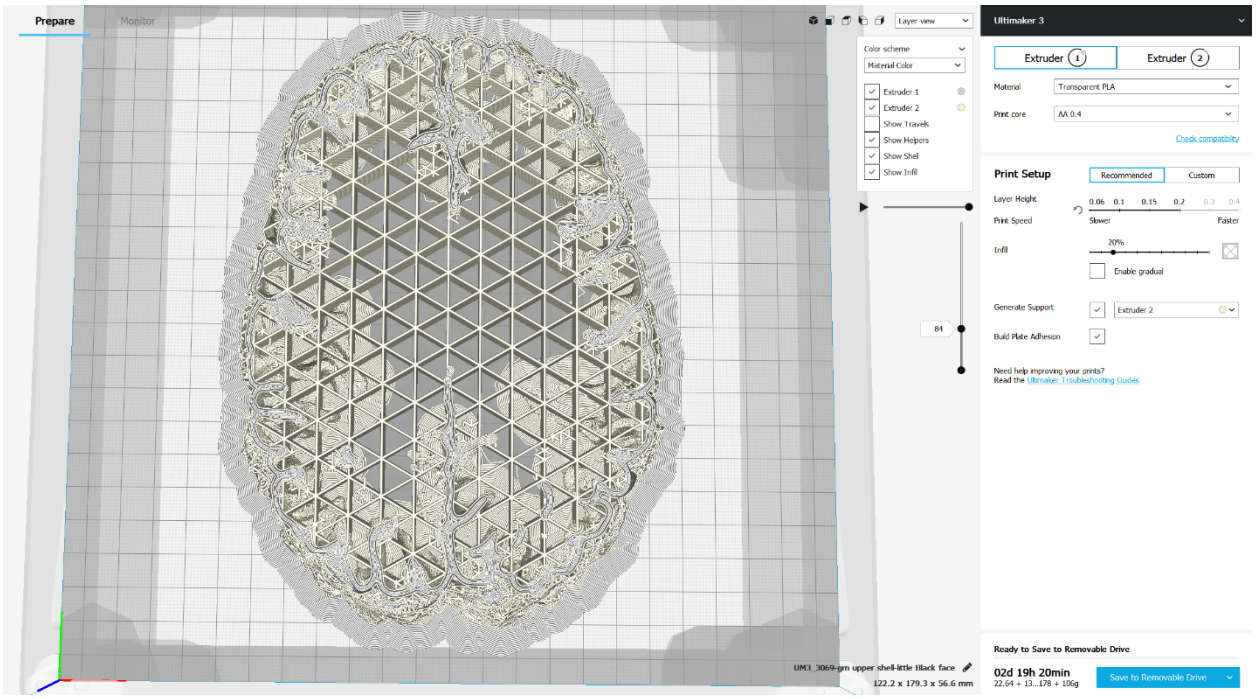

Figure 18 Shell printing preparation and setting in Cura software

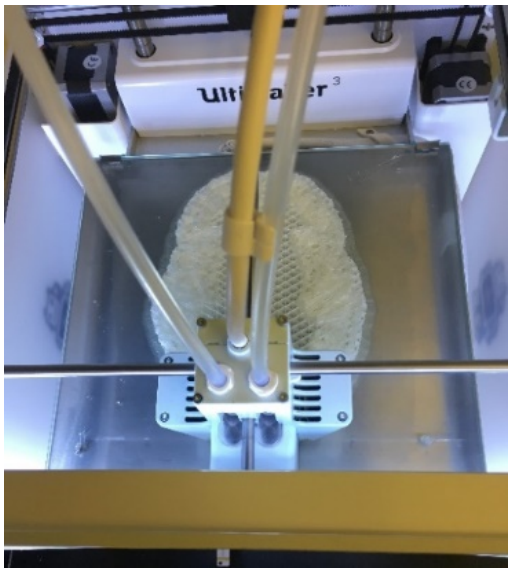

Figure 19 Showing the shells as they are in the printing process with the PLA as the main material and the PVA as a support

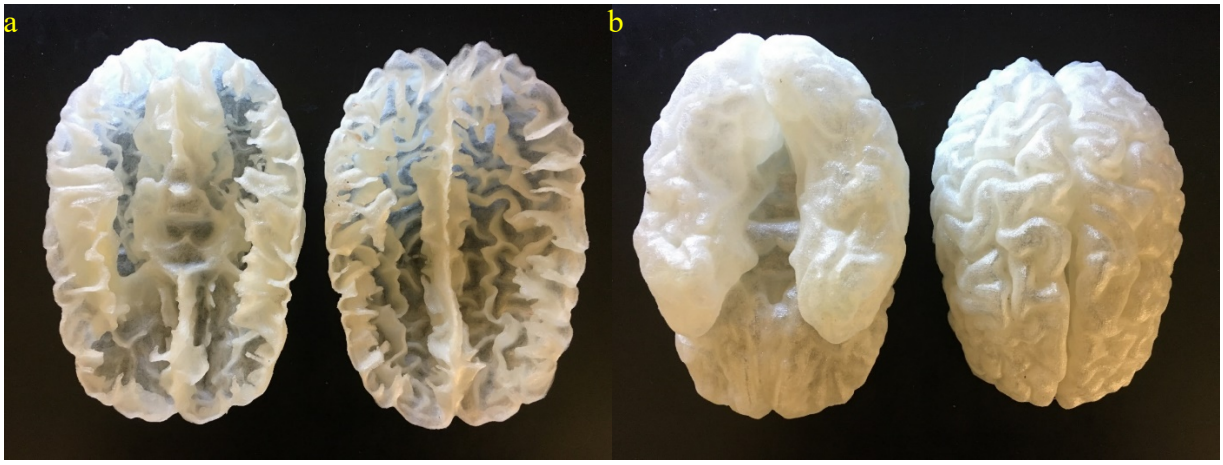

Figure 20 Upper and lower shells of the brain (GM) printed. We removed the supporting material PVA by washing and dissolving it in water. Now the shells are be casted with the conductive polymer

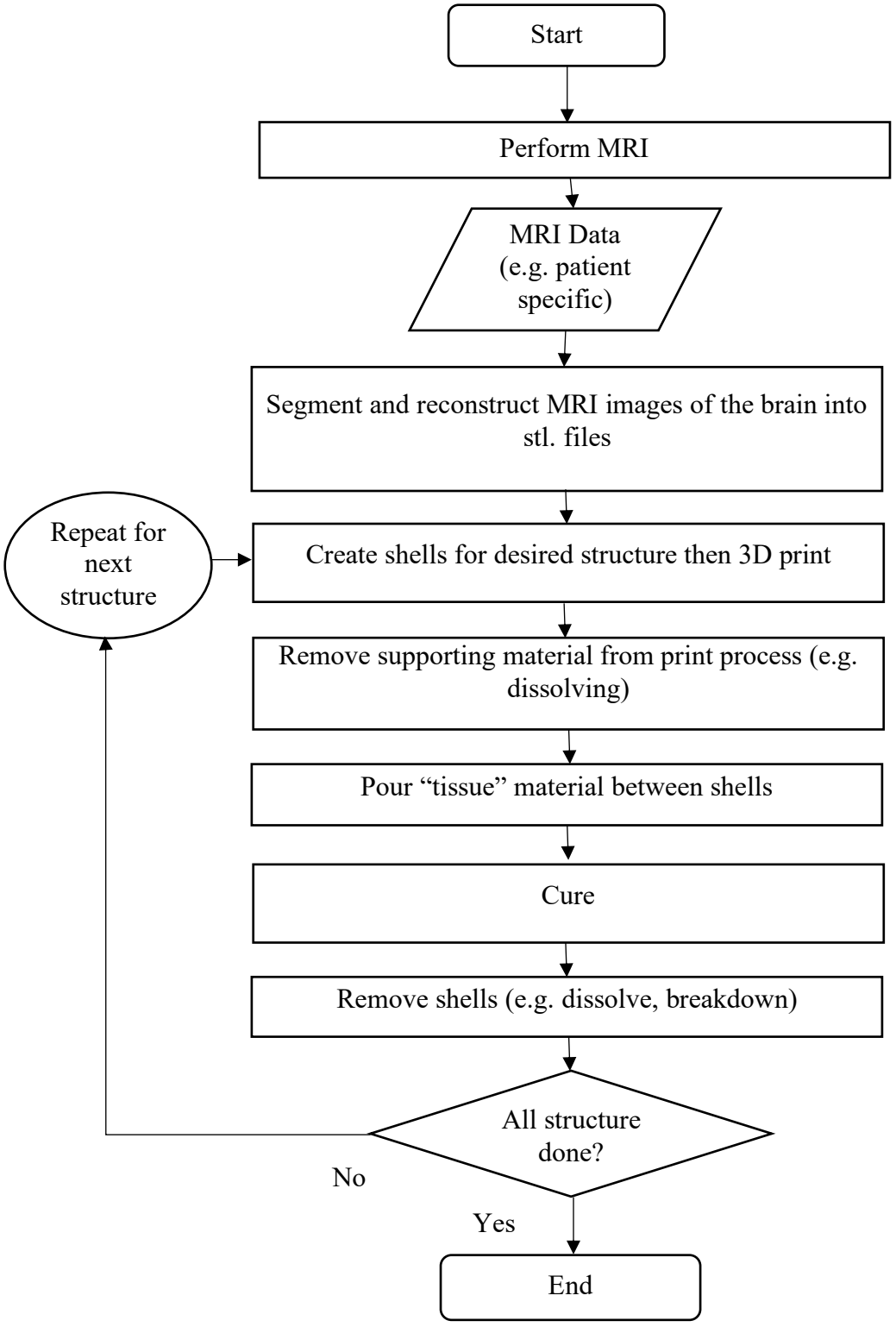

Figure 21 A flow chart showing summery of steps take in order to obtain the entire geometry of the brain and head phantom

2.2.4 Conductive polymer

The development of conductive polymers has been widely researched over the last decades for different applications [62–69]. In some applications, high electrical conductivity is needed regardless of the mechanical properties. In some other applications, elasticity is needed to be accompanied with the moderate conductivity. There are many ways to impart conductivity to the polymers. Some are achieved by chemical manipulation of the bonds of the polymer, and others are achieved by the addition of conductive material to the polymers. Some examples of the material used are single and multi-walled carbon nanotubes SWCNTs and MWCNTs, carbon black CB, copper flakes, and silver particles and nanowires. Some of the processes and techniques of producing the required conductive polymers include mixing, milling, and grinding processes.

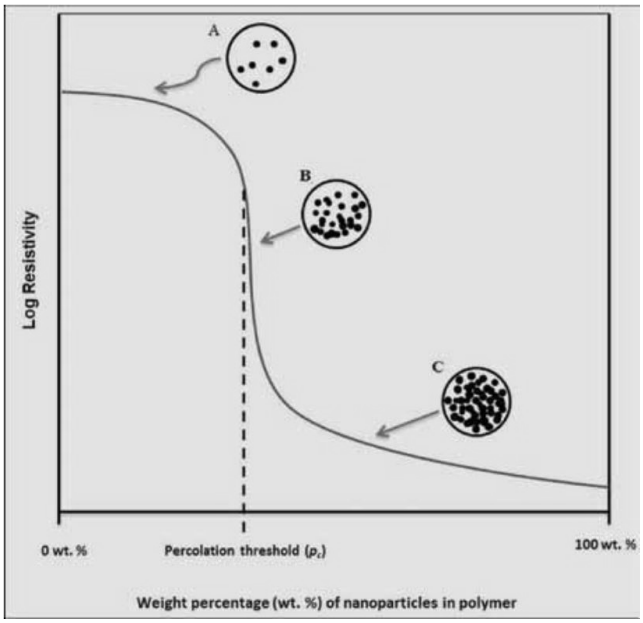

Figure 22 Overall trend of the resistivity reading compare to conductive nanoparticles filler in polymers [66]

Figure 22 shows the overall established resistivity relationship between the conductive filler loading/composition in the host polymer's weight percent. Our work attempted to impart the

conductivity to the host polymer and obtained a loading/composition vs. resistivity behavior similar to the one in Figure 22.

2.2.4.1 Conductive polymer preparation-criteria selection:

In our work on the conductive polymer, we aimed to match the brain's electrical conductivity closely. Table 1 shows the reported values of the electrical conductivity of different parts of the brain. Our targeted conductivity value for the brain lies in the range of about 0.1-0.5 S/m. These ranges cover the averaged conductivity value of the GM and WM in the brain. This conductivity range also is considered to be moderate when compared to other materials. Metals have a high conductivity of about 1E+06 to 1E+08 S/m.

Nevertheless, even though metals have high conductivity, they also have high permeability. We decided to work on additive material with high electrical conductivity but with low relative magnetic permeability of about 1. Magnetic permeability is the measure of how much a material will become magnetized in the presence of an externally applied magnetic field. Carbon allotropes like multi-walled carbon nanotubes MWCNT possess relatively low relative permeability μr of about 1 [70]. Imparting the electrical conductivity is achieved when the additive filler weight percentage wt% reaches a level where the electrical conductivity starts to increase rapidly. This threshold is known as the percolation limit. The percolation limit has been calculated and experimentally measured in the literature [71]. In our work, we show the conductive polymer's behavior and the increment of the conductivity to the wt% of the conductive filler/host polymer similar to Figure 23.

Our experiment examined the variations in resistance/conductance measurements for the following criteria: type of the hosting polymer, mixing time, mixing speed, filler addition rate, temperature exposure, and the sequence and order in which the components are mixed to form the

composite. Our goal was to test whether the conductivity is established, or passed percolation limits, in the samples or not. We used a multimeter to measure any resistance readings less about 100 kΩ. If the measurement is below 100 kΩ, it is considered that the method is valid in reducing the resistivity of the sample or lead to increasing the conductivity. In the following, we present the details of each consideration.

2.2.4.1.1 Type of host polymer:

We used two types of hosting polymers, commercial platinum-catalyzed silicone Ecoflex 00-20 and Polydimethylsiloxane (PDMS). The Ecoflex silicone consists of two parts mixed with a 1A:1B ratio. With Ecoflex, we could measure resistance values less than 100 kΩ, but because the Ecoflex is mixed with a 1:1 ratio, each part of the silicone needs to be prepared separately, and when joined together, they lost conductivity. Also, the Ecoflex silicone has relatively low capacitance for the additive conductive filler MWCNT. At about 13 wt% additive filler of the MWCNT, the Ecoflex parts A and B would not appropriately mix and cure. Also, the mechanical stiffness of the Ecoflex after mixing is very low. That could be a disadvantage because when the brain phantom is made, an acceptable level of stiffness is needed to be compatible with any future stimulation strength measurement on the phantom that might include some probe insertion. Based on these experiments, we believed that using Ecoflex is not reliable. Then we moved to work on the PDMS. PDMS's first advantage is that it has 10base:1curing agent mixing ratio. That means the addition of the curing agent to the based will not significantly affect the conductivity established in the PDMS base. Also, it is observed that the PDMS has more capacitance than Ecoflex to accept higher wt% of the additive conductive filler MWCNT. It can reach more than 16 wt% without affecting the conductivity established in the PDMS base.

2.2.4.1.2 Mixing speed:

Mixing speed is the stirrer's rotation per minute (rpm) used to mix the polymer and the conductive filler. It determines the shear force exerted on the mixture. Based on our experiments, mixing at speeds as high as 2500 rpm will result in a higher probability of losing established conductivity. When mixing at such high speed, we could establish the conductivity but then lose it before realizing it. That is because there might be a loss in the MWCNT aspect ratio due to the high shear force and breakage of the carbon tubes. Maintaining a higher aspect ratio is important because it will increase the connect-ability and network formation of the MWCNT within the hosting polymer and, therefore, increase the overall electrical conductivity of the composite. On the other hand, when mixing at speed around 600-700 rpm, we noticed that the conductivity is not established, especially for lower additive wt%. Therefore, we tested the mixing at 1000 rpm and found that it is optimal for establishing the conductivity, mixing time, and the weight percentage of the additive filler MWCNT.

2.2.4.1.3 Mixing time and conductive filler addition rate:

We noticed that imparting the conductivity to the polymer is obtained when the polymer becomes highly viscous and hard to mix. Each MWCNT percentage added to the polymer has different mixing timing. Reducing the filler weight's percentage results in a longer mixing time. It is logical. Since that with fewer MWCNT percentage, it takes longer mixing time to disperse the MWCNT within the polymer texture and create the connected network of the conductive MWCNTs. Therefore, the mixing time is variable depending on the MWCNT percentage. Also, for the same MWCNT percentage used, time varies based on the rate of addition of the MWCNT to the PDMS. When adding the MWCNT gradually, the mixing time increases, and vice versa.

For this reason, we made our main criterion is the observed viscosity and mixability. For example, the mixing time for 8.5 wt% MWCNT with a fast addition rate is about 10 mins, but the mixing time takes about 1 hour with gradual addition. Both cases result in conductivity establishment but not with an accurate reading. So, we decided to select the fast rate of conductive filler addition as the criterion for consistency.

2.2.4.1.4 Heat exposure:

The PDMS takes about 24 hours to cure after mixing the base with the curing agent thoroughly. However, one way to expedite the curing time is by exposing the composite to a heat source. When exposing the PDMS to a higher temperature, the curing time reduces to less than one hour. In our experiment on the conductive polymer creation, we noticed that exposing the conductive polymer to a heat source will lose the established conductivity. For that reason, we let the conductive polymer cure naturally and in the room temperature to avoid any modification or loss in the conductivity.

2.2.4.1.5 Components mixing order:

The conductive polymer components are the PDMS based, the curing agent, and the multi-walled carbon nanotubes MWCNT. The sequence of adding these components needs to be fixed and controlled to obtain consistent results and readings of the conductive polymer samples' resistivity. Our observation is that when adding all of the components together before the mixing, they result in inconsistent resistivity readings. That could be because as the curing agent was added to the mixture before mixing, the heat generated from the fast stirring modified the establishment of the sample's conductance. This is coherent with the experiments of heat exposure to the conductive polymer, where a loss in the conductivity was observed. For that reason, the curing agent is added to the mixture after the complete mixing of the PDMS based on the MWCNTs.

After adding the curing agent, the sample was mixed again with the stirrer but for a very brief and short time.

2.2.4.2 Conductive polymer preparation-final criteria selected:

Based on the experiments mentioned above, our final criteria for preparing the conductive polymers to establish a correlation between the weight percentage of the conductive filler MWCNT and the hosting polymer are as follows:

1) We used only PDMS base, curing agent, and multi-walled carbon nanotubes as the main components.
2) The mixing speed of the samples using the mechanical stirrer is 1000 rpm.
3) The conductive filler MWCNT must not be added at a gradual rate. The entire MWCNT patch should be added to the PDMS before the mixing.
4) The curing agent should be added after the mixing of the PDMS base with the MWCNT. It can then be mixed for a brief time (around 30s) to ensure that it is fully distributed through the mixture.
5) The prepared samples of the conductive polymer should not be exposed to a heat source to expedite the curing process. Otherwise, the conductive polymer might lose the established conductivity.

2.2.5 Conductive polymer samples preparation:

In this section, we show the steps of creating the conductive polymer samples (based on the criteria) to be tested and undergo resistivity measurements to establish a correlation between the weight percentage of the conductive filler MWCNT with the hosting polymer:

1) We prepare our sample components, polydimethylsiloxane PDMS base (SYLGARD 184 silicone elastomer base), curing agent (SYLGARD 184 silicone elastomer curing agent) and, Multi-walled carbon nanotubes MWCNT (Graphene supermarket, diameter: 50-85 nm length: 10-15µm) as seen in Figure 23. Measure each component's weight for the desired and targeted MWCNT wt% to the rest of the components.

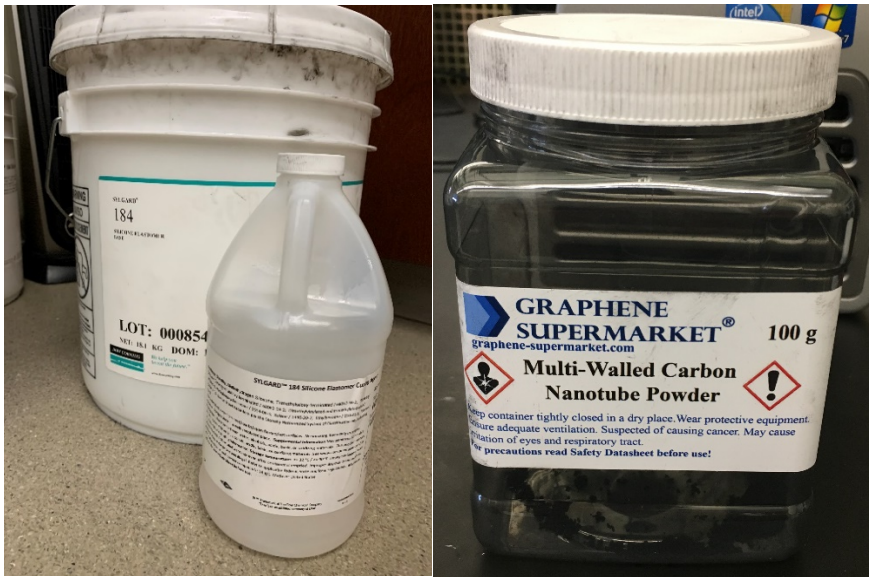

Figure 23 Main material components used to create the conductive polymer samples. a) PDMS base (SYLGARD 184 silicone elastomer base) and the curing agent (SYLGARD 184 silicone elastomer curing agent). b) Multi-walled carbon nanotubes MWMWCNTs (Graphene supermarket, diameter: 50-85 nm length: 10-15µm).

2) For all of the samples prepared, it is recommended that the PDMS base's weight and the curing agent are to be fixed. We used about 100 g PDMS based on 10 g curing agents (the mixing ratio of 10Base:1curing agent grams). Then the MWCNT weight is varied depending on the targeted weight percentage. The weight percentage calculated with the straightforward formula:

$$CNT\ wt\% = \frac{CNT\ weight\ (g)}{PDMS\ base\ wight\ (g) + curing\ agent\ weight\ (g) + \ CNT\ wt\ (g)}$$

3) We added the MWCNT to the PDMS based on a fast addition rate. Then the cup or container of the components is placed in a mechanical stirrer. Our experiment used the mechanical stirrer (Caframo, Ultra speed, model- BDC6015) with propeller and shaft (model A166), as seen in Figure 24.

Figure 24 The MWCNT is added to the PDMS base and mixed with the mechanical stirrer at 1000 rpm

4) After starting to mix the MWCNT with the PDMS, we will observe that the mixture's texture and outlook are changing over time. In Figure 25, we see that the mixture goes through three stages. The first is when the texture looks shinny and watery, low viscosity, and easy to be mixed entirely, as in Figure 25(a). The second is when we see that the texture becomes dimmer and starts to climb the blades rod, as in Figure 25(b). The third and final stage is when the mixture looks dimmer, has a texture of paste, and is harder to mix, meaning that the blades will rotate, but the mixture is no longer mixed thoroughly, as in Figure 25(c).

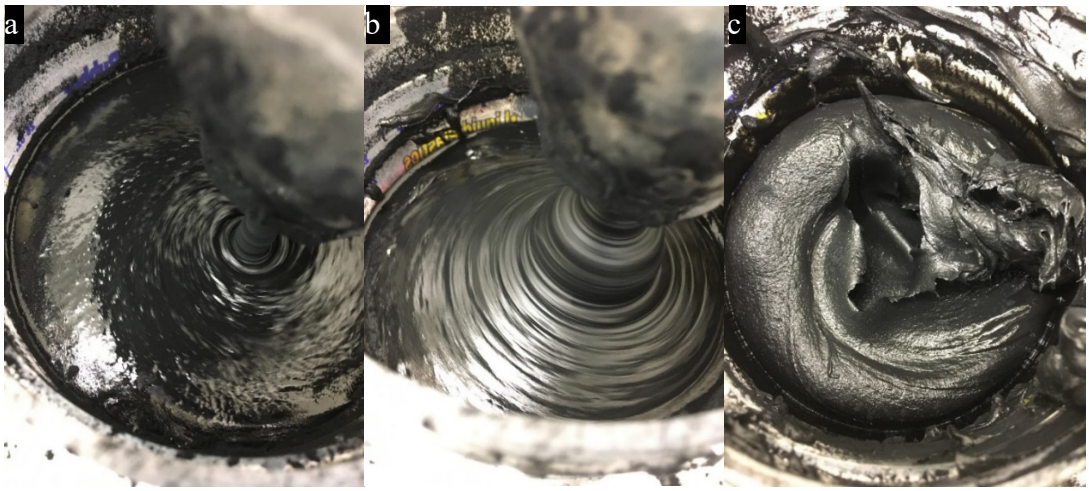

Figure 25 The main stages of the PDMS and MWCNT mixture over mixing time. (a) First stage where the texture looks shinny and watery, with low viscosity, and easy to be mixed entirely. (b) Second stage where we see that the texture becomes dimmer and starts to climb the blades rod. (c) The third and final stage is when the mixture looks dimmer, have a texture of paste, and harder to mix.

5) Now, we add the curing agent to the mixture and mix for no more than 30 s. We have to ensure that the curing agent is spread evenly through the entire sample for a better polymer curing process. Then, we leave the sample to cure for at least 24 hours. Some samples might take longer than 24 hours to cure. Therefore, we always need to check and make sure that the sample is fully cured.

2.2.6 Resistivity/ conductivity measurements of the conductive polymer

The conductivity σ (Sm-1) is the reciprocal of the resistivity ρ (Ω.cm) σ=1/ ρ. The resistivity is obtained by measuring the resistance R in (Ω) of the selected sample and convert it to Ω.cm based on the sample's dimensions. There are various methods to measure the resistivity of the sample. Some techniques, like 4-points probe methods, are more accurate than others. In our measurements, we were looking for a very close estimation and measurements of the resistivity. We examined the following MWCNT wt% 5.5, 6.5, 7.5, 8.5, 9.5, 10.5, 11.5, 12.5, 13.5, 14.5. For each MWCNT wt%, we made three samples, and for each sample, we cut three 1 cm3 pieces to perform the measurements. That means we performed nine reading for each wt% value. We used the multimeter contact probes and placed them on our conductive polymer samples. Also,

we used another method to confirm the readings of the first method. We simply added two metal plates with carbon conductive paste on both ends of the sample. The resistivity/conductivity measurements are shown in the results and discussion section of this chapter.

2.2.7 SEM images:

To understand our conductive polymer and observe the correlation between the conductive filler MWCNT wt% with the hosting polymer and the conductivity measured on the sample, we took scanning electron microscopy SEM images of four selected MWCNT wt% (5.5, 8.5.9.5 and 14.5). In the following, we show the preparation steps and parameters used to take the samples' images.

2.2.7.1 Sample preparation and scanning parameter:

We selected four samples to be scanned with the SEM and obtain images at the microscopic level to provide a better understanding of our conductive polymer and to observe the formation of the MWCNT and dispersion within the hosting polymer PDMS. In the following, we show the main steps we followed to obtain the SEM images:

We cut small pieces of the conductive polymers sample and place them on the stud with a double-side tape, as in Figure 26. It is recommended that the pieces be ripped off by a tweezer rather than cut with a razor. That will better show the roughness of the polymer concerning each MWCNT wt%. The sample on the stud then should be placed inside a coating spotter to gold-coat the sample to enhance the samples' SEM images.

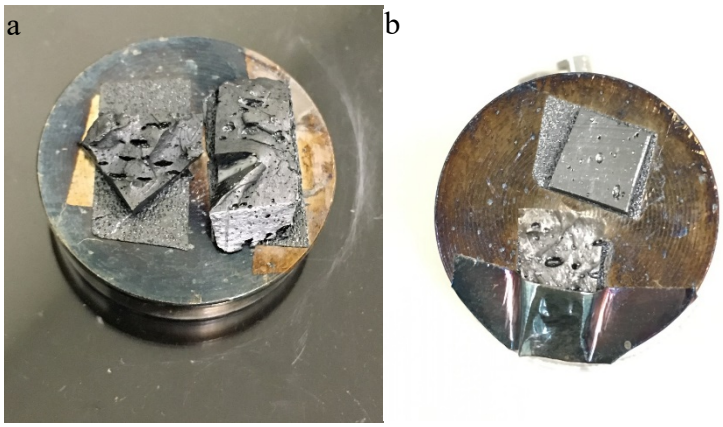

Figure 26 Conductive polymer samples prepared for scanning electron microscopy SEM. (a) the sample placed on the stud. (b) The sample after being gold coated by the coating spotter in order to enhance the quality of the images. It is recommended to work on 5 kV since we are working on a polymer-based texture. We obtained several images with several magnifications for each MWCNT wt% sample, and they are shown in the results and discussion section of this chapter.

2.2.7.2 Mimicked CFS conductivity:

To mimic the CFS, we used a saline solution with an adjustable concentration of sea salt. The targeted conductivity of CSF is in the range between 1-2.2 Sm-1, as in table 1. We mixed mineral sea salt with saline solution to increase its conductivity. The saline solution has an NaCl concentration of about 3.5 mg/ml to mimic the CSF's conductivity. The salt and minerals increase the water's conductivity because they introduce more free electrons and ions. Then, we measured the resistance at the ends of the narrow path we 3D printed depicted in Figure 27. Based on the dimension and measured resistance, we can obtain the resistivity and convert it to conductivity. The result of the obtain conductivity is shown in the results and discussion of this section.

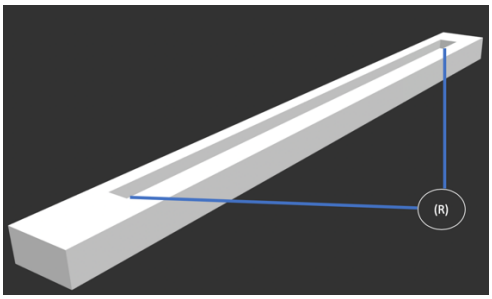

Figure 27 Depiction of the saline resistivity measurement process

2.3 Results and Discussion

Here, we show and discuss the results of the first and second part of this chapter. In the first part, we presented the method and steps required to obtain and manufacture the brain's intricate geometry. In the second part, we present the results of the conductive polymer resistivity measurements. Then we will show the result of the combination of the first and second parts where we select specified resistivity of the conductive polymer and fabricate the conductive brain based on the shelling method of the first part.

2.3.1 Brain phantom geometry obtained

Here, we show and discuss the results of the first of this chapter. In the first part, we presented the method and steps required to obtain and manufacture the brain's intricate geometry. The brain material is not electrically conductive at this point. Figure 28 shows the shelling method applied in order to obtain the GM layer only. In these shells, we printed the inner and outer layers of the GM. Then we injected the polymer (Silicone- Ecoflex) between the shells and let the polymer to cure as in Figure 29. After that, we placed and immersed the shells and the cured polymer in acetone for 24 hours. The acetone will make the shells softer and brittle. Then we removed the shells and obtained the geometry of the GM. This method is very useful in obtaining any complex geometry of the human body. There could be some cases in which some of the brain's mechanical aspects or any other organ of the human body need to be mimicked, replicated, or characterized. The used polymer can be selected based on different applications. One of the best advantages of this shelling method is that it can produce complex geometry to higher depth levels than some conventional molds and casting methods. That is because the shells are easy to be removed by dissolving them in acetone if the shells were printed with Acrylonitrile butadiene styrene ABS or they can be dismantled and break if they were printed with PLA. That is more

advantageous, primarily if the targeted material will be composed of hard polymers after they cure. In this work, as we will show in later sections of this chapter, we used the conductive polymer (PDMS/MWCNT composite) that becomes hard after the polymer gets cured. Therefore, dismantling the shells became much more comfortable when the shells were immersed in acetone. Figure 30 shows the shells after being removed from acetone, and they become easy to dismantle. The final production of the brain phantom's material is seen in Figure 31.

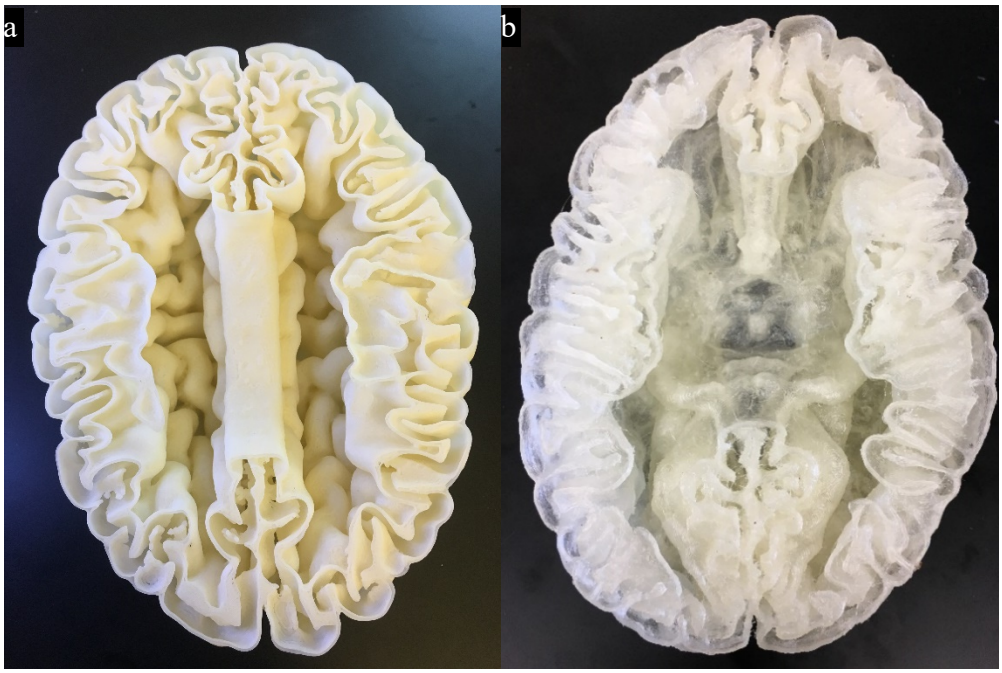

Figure 28 GM shells are printed and washed off from the support material. (a) Shows the shells printed with ABS material that dissolves in acetone. (b) Shows the GM shells printed with PLA that becomes brittle and softer when immersed in acetone.

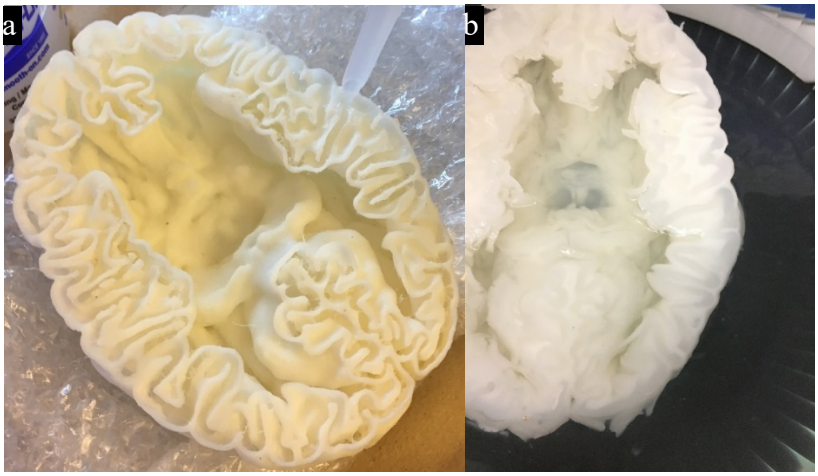

Figure 29 (a) the GM shells are being filled with polymer. (b)The polymer and shells after being cured and immersed in acetone

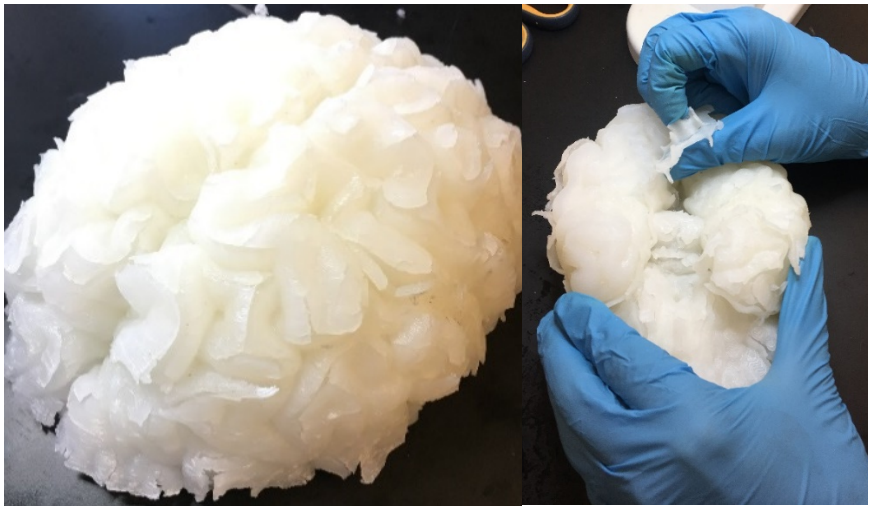

Figure 30 After removing from acetone, the shells became brittle and easy to dismantle.

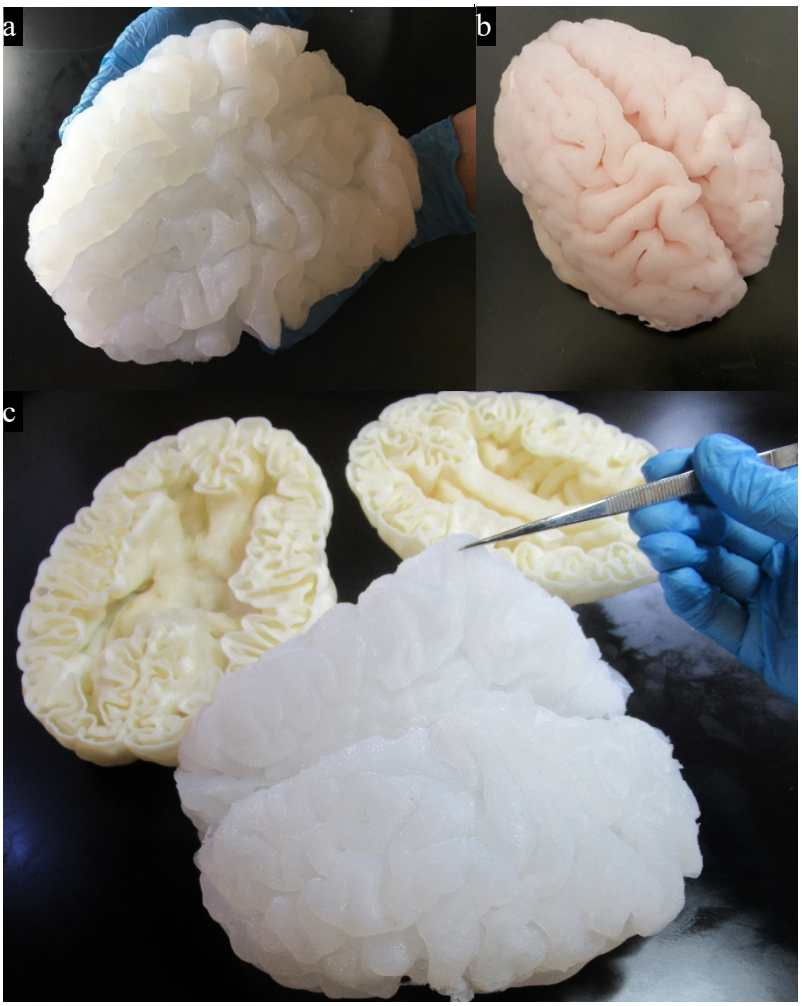

Figure 31 The brain phantom after removing the shells. (a) Shows the GM layer. (b) The GM was filled with another polymer to constitute for the WM. (c) the GM shells and the GM layer made of polymer

2.3.2 Conductivity/resistivity measurements of the conductive polymer

The conductive filler MWCNTs percentage plays a vital role in increasing and decreasing the polymer mixture's electrical conductivity. We measured the mixture's resistivity after it was cured to make sure that the formation of the carbon nanotubes inside the polymer is established, and the resistivity measurements are stable and reflect the actual resistivity of the mixture. One important observation when measuring the conductive polymer samples' resistance is that the resistance measured is not instantaneous, meaning that the resistance drops over time. The resistance measured decreases in exponential decay. After about three days of placing the multimeter probes on the conductive polymer samples, the resistance reading starts to stabilize. Figure 32shows the resistance readings on all of the conductive polymers to time with various conductive filler MWCNT wt% ranging from (6.45 wt% - 14.44 wt %). For better visualization and understanding of all of the sample's resistance with respect to time, Figure 33 shows the resistance behavior of all of the samples with different MWCNT wt% on a log scale. Figure 34 shows the final measured resistivity of the conductive polymer with different MWCNT wt%. For each sample of MWCNT wt%, we performed about nine measurements to approach the actual resistance measurements. In Figure 32 and Figure 33 , we can see that the stander deviation SD is high in almost all cases. However, the standard deviation decreases as the MWCNT wt % increases. This is evident and more explicit when calculating the coefficient of variance (CV = standard deviation /average*100) to see how close we are to obtain the targeted resistivity with each specific MWCNT wt%. For example, the resistance on day three for the 7.75 MWCNT wt% equals about 3.19 kΩ with a standard deviation of 1.78 Ω. Therefore, the coefficient of variance CV is about 55%. Nevertheless, with 8.85 MWCNT wt% and 11.40 MWCNT wt%, the CVs are about 30% and 12.65%. We attribute these variations to many factors; we observe very high

fluctuations in the initial readings of each measurement, and we record a very rough estimation of the resistance reading at t=0; the subsequent measurements were not performed at the same time of each day. Also, as mentioned in the method section, the resistance measurements can vary significantly with each mixing parameter. For that reason, we set the mixing criteria controlled as much as possible to avoid losses in the established conductivity or substantial variation in the measured resistivity.

Figure 34 shows the conversion of the resistance measured (Ω) to resistivity (Ω.cm) for each conductive polymer with different MWCNT wt%. In this figure, we can see some aspect or behavior of the resistivity of polymers with conductive fillers in the literature. On a log scale, we see that the resistivity decays over time and then start to stabilize around certain values with higher conductive filler weight percentage. In our Figure 34, we would have the same behavior at the higher resistivity if we added the pure PDMS polymer's resistivity and very low MWCNT wt%. However, since we started with 6.45 MWCNT wt%, we see the resistance's behavior as it is beyond the percolation threshold.

Figure 35 shows the resistivity conversion into conductivity for the conductive polymers samples with varying the MWCNTs wt%. The figure shows that the range of conductivities obtained covers the human brain's wide range of conductivities. For example, GM's conductivity is about 0.25 S/m. That can be achieved if we fabricate our brain phantom with about 8.50 MWCNTs wt%. The CSF has higher conductivity between (1.2-2.0 S/m); if we needed to fabricate a conductive polymer, we could achieve it with about 11.00 -11.50 MWCNTs wt%. The conductivity behavior, as seen in Figure 35 is not linear for the MWCNTs wt%. We can see a steep increment of conductivity between about 10.50 to 13.50 wt%. That means for any application in which the targeted conductivity lies within this region, the controlling parameters and criteria of

fabrication the conductive polymer might need to be more accurate and controlled. We should note that these measurements were carried on samples with about 100 g. In case we wanted to fabricate a conductive polymer on more massive scales like 1000-2000 g, there could be a little variation in the conductivity as the volume mixed is much larger than the sample we worked on. Therefore, more accurate and established methods and tools need to be used for better control. For example, the mechanical stirrer is better to be scaled up to match the container's size in which the conductive polymer components are mixed.

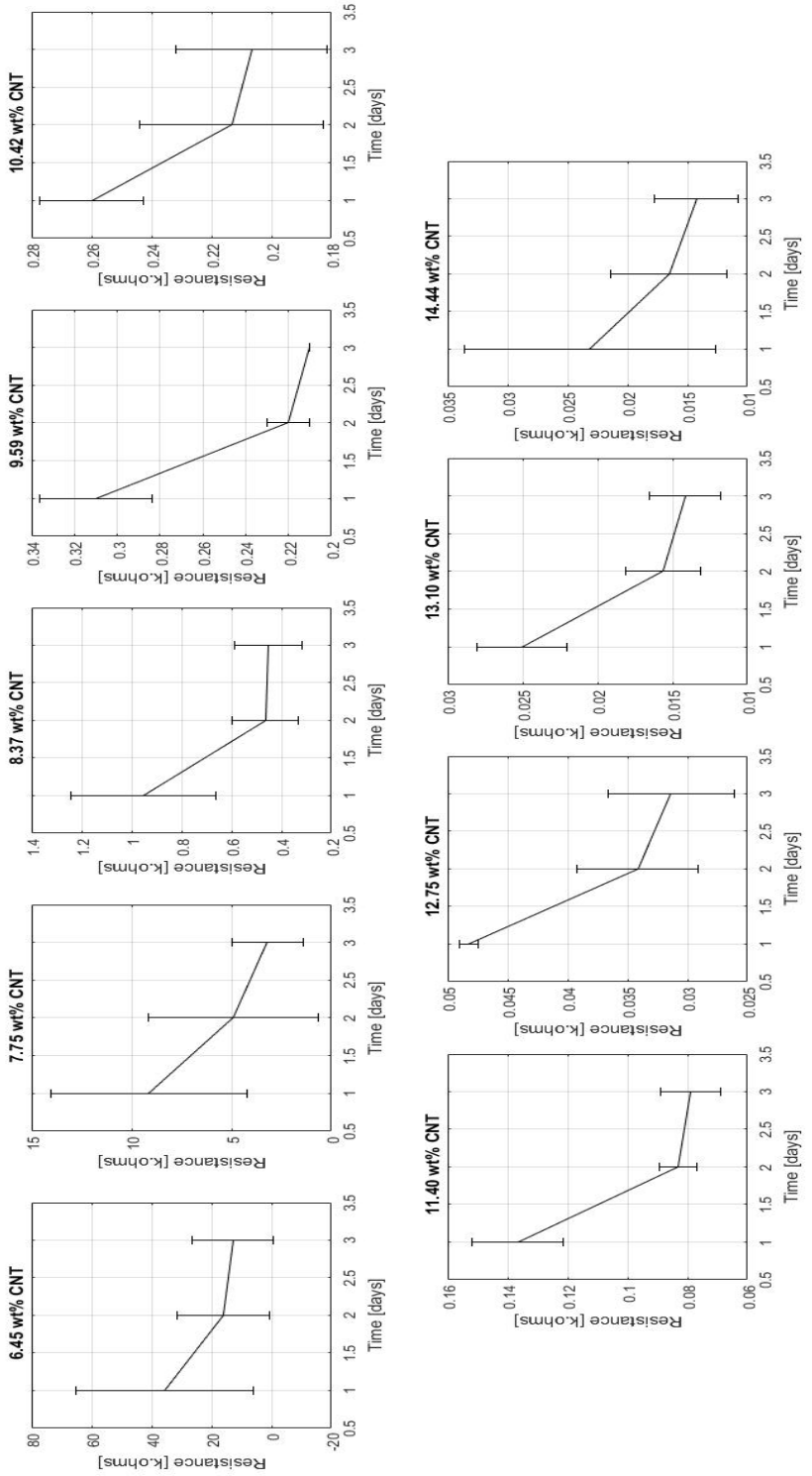

Figure 32 Resistance measurements of the conductive polymer samples reducing with respect to time with varying the conductive filler MWCNT wt%

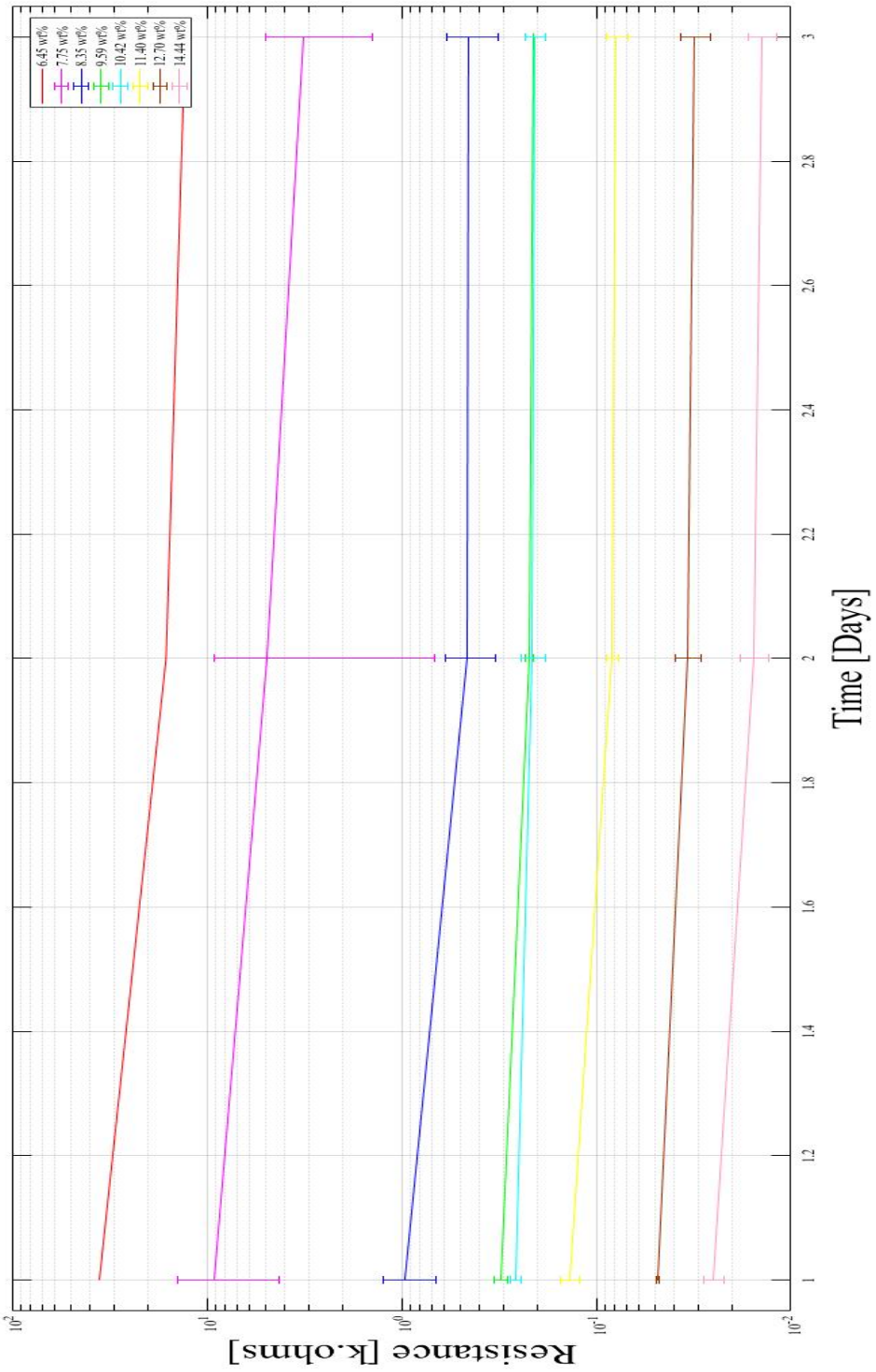

Figure 33 Resistance measurements of all the conductive polymer sample with respect to time with varying the conductive filer MWCNT wt% on a log scale

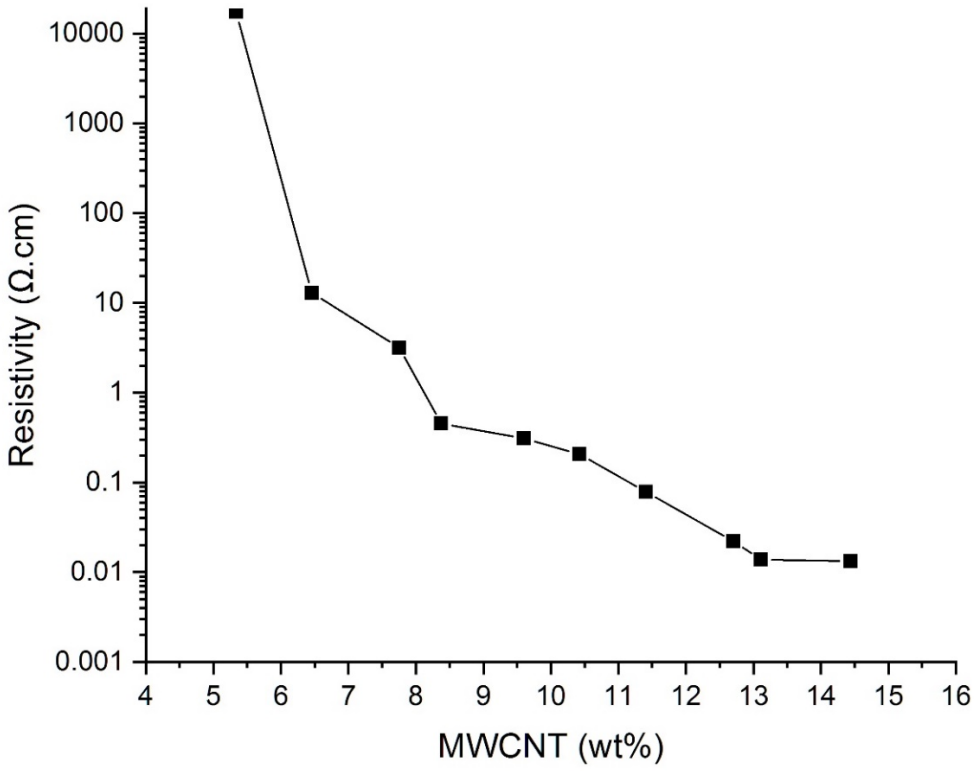

Figure 34 Resistivity of the conductive polymer sample with respect to varying the conductive filler MWCNT wt%

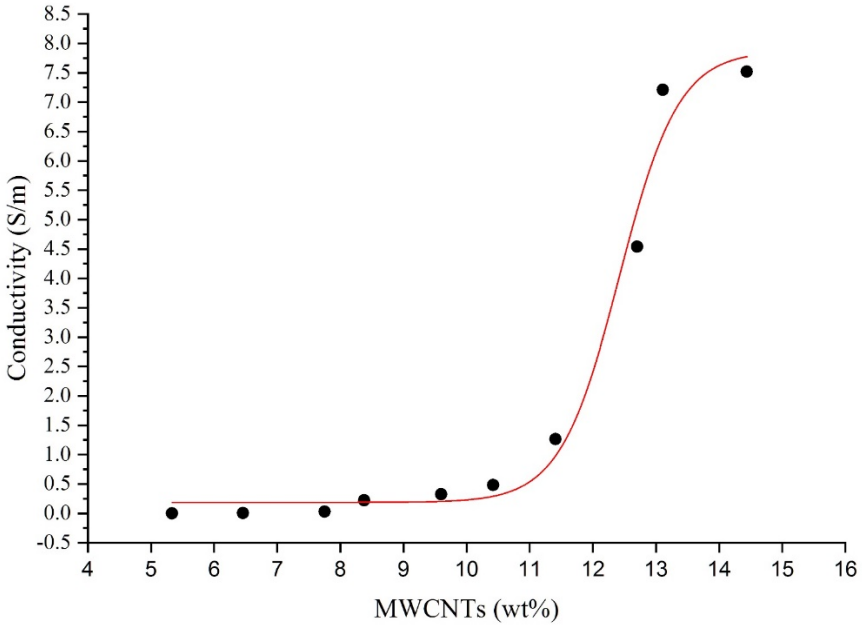

Figure 35 Conductivity of the conductive polymer samples with varying the MWCNTs wt%

2.3.3 SEM images of the conductive polymer with different MWCNT wt%

In this section, we present the SEM images of the conductive polymer with different levels of MWCNT wt% to show the dispersion of the MWCNTs within the PDMS. They are shown with different magnifications for each MWCNT wt% for better visualization of the overall dispersion and a smaller scale. These images are shown for four selected MWCNT wt%, 5.5, 8.5, 9.5, and 14.5 wt%. The difference can be seen clearly in the degree of dispersion. At lower concentrations 5.5 wt%, as in Figure 36MWCNTs are dispersed almost equally with some agglomerations. At 8.5 and 9.5 wt%, we can see the increased density of the MWCNTs with more bundles and agglomerations, as in Figure 37 and Figure 38. At 14.3 wt%, Figure 39, MWCNTs are well dispersed without agglomeration, but the resulting composite's texture is very rough.

Figure 40 shows the formation of the MWCNT on a microscopic scale (from 50-500 nm) and the actual size of the used MWCNTs in our work. The width of the MWCNTs is about 50 nm, and length is about 10 -20 μm which is within the claimed range by the manufacturer (50-85 nm width, 10-15 μm length). Therefore, the aspect ratio for the used MWCNTs is about 300:1.

We show in Figure 41 a correlation between higher and lower magnifications of each MWCNTs wt% to put these different concentrations into perspective. In Figure 42, we show the SEM images of selected MWCNT wt% (5.3, 8.3, and 14.3) in correspondence with each value of conductivity. We can see at the 8.5 wt%, where the conductivity starts to increase exponentially, the dispersed MWCNT throughout the PDMS texture as opposed to lower levels of MWCNT wt% (5.5) where the MWCNT is scarce between the MWCNT's bundle and agglomerations. This tells us that the dispersion of the MWCNT within the PDMS with preserving the same level of the aspect ratio is determinant in the electrical conductivity establishment and maintenance. Also, from the SEM figures, we can further improve the composite's conductivity for a given conductive

filler weight percentage inside the PDMS polymer. For example, the 0.25 Sm-1 that corresponds to 8.5 wt% can be achieved with lesser wt% conductive filler like 3-4 wt% by dispersing the agglomerated MWCNTs. These aggregations can be dispersed with better mixing techniques. MWCNTs can be first dispersed in a solution such as a heptane and sonicated before adding to the PDMS. Also, our PDMS polymer has few bubble formations within the composite. These bubbles can be removed by degassing the PDMS polymer after being molded by the brain shells. This can be because the polymer has a high viscosity and the shells on top, which may seal the polymer's air bubbles as they leave no openings for the gas to escape. Furthermore, using single-walled carbon nanotubes, SWCNTs, and a higher aspect ratio of the carbon nanotubes would further enhance the conductivity of any given conductive filler weight percent.

2.3.3.1 5.5 wt% MWCNT

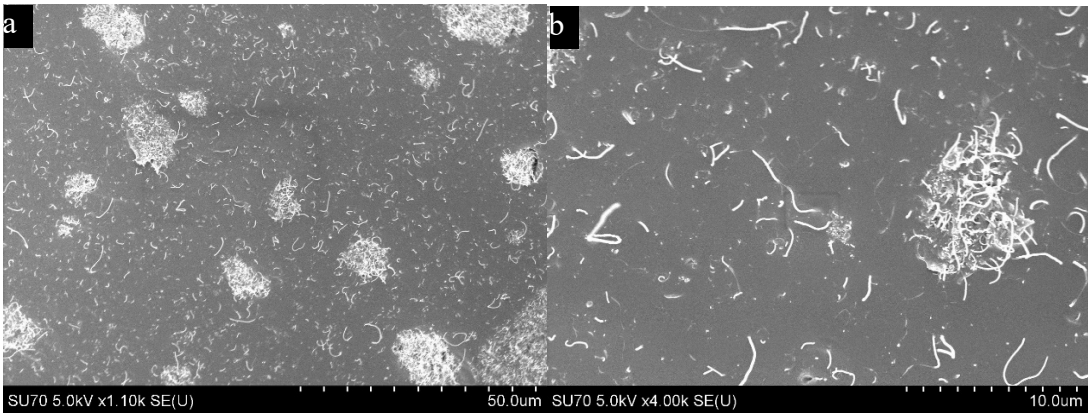

Figure 36 (a) & (b) SEM images of 5.5 MWCNT wt% showing the dispersion of the conductive filer MWCNT within the hosting polymer PDMS at different magnifications

2.3.3.2 8.5 wt% MWCNT

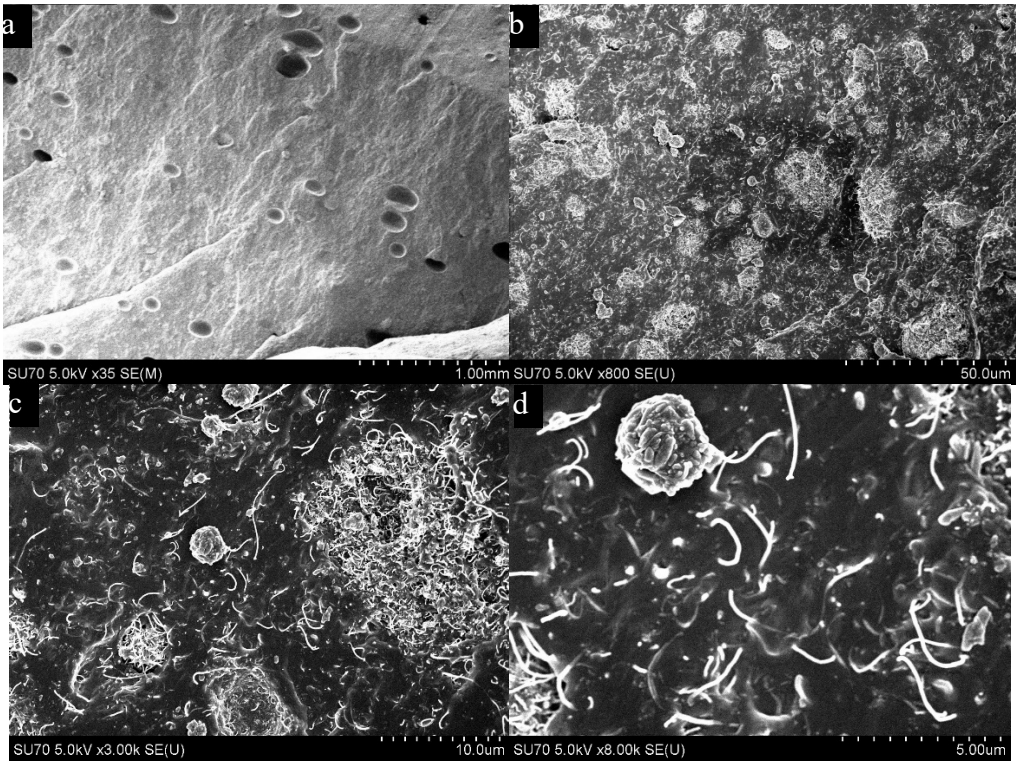

Figure 37 (a-e) SEM images of 8.5 MWCNT wt% showing the dispersion of the conductive filer MWCNT within the hosting polymer PDMS at different magnifications

2.3.3.3 9.5 wt% MWCNT

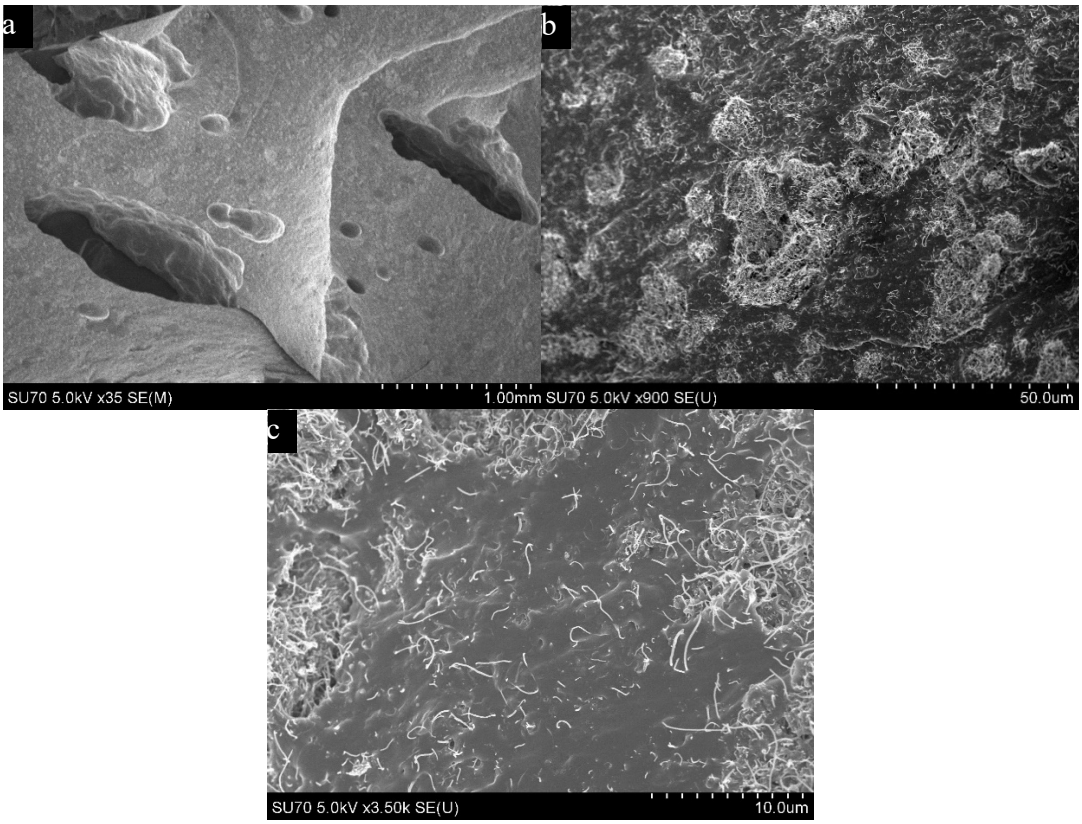

Figure 38 (a-c) SEM images of 9.5 MWCNT wt% showing the dispersion of the conductive filer MWCNT within the hosting polymer PDMS at different magnifications

2.3.3.4 15.5 wt% MWCNT

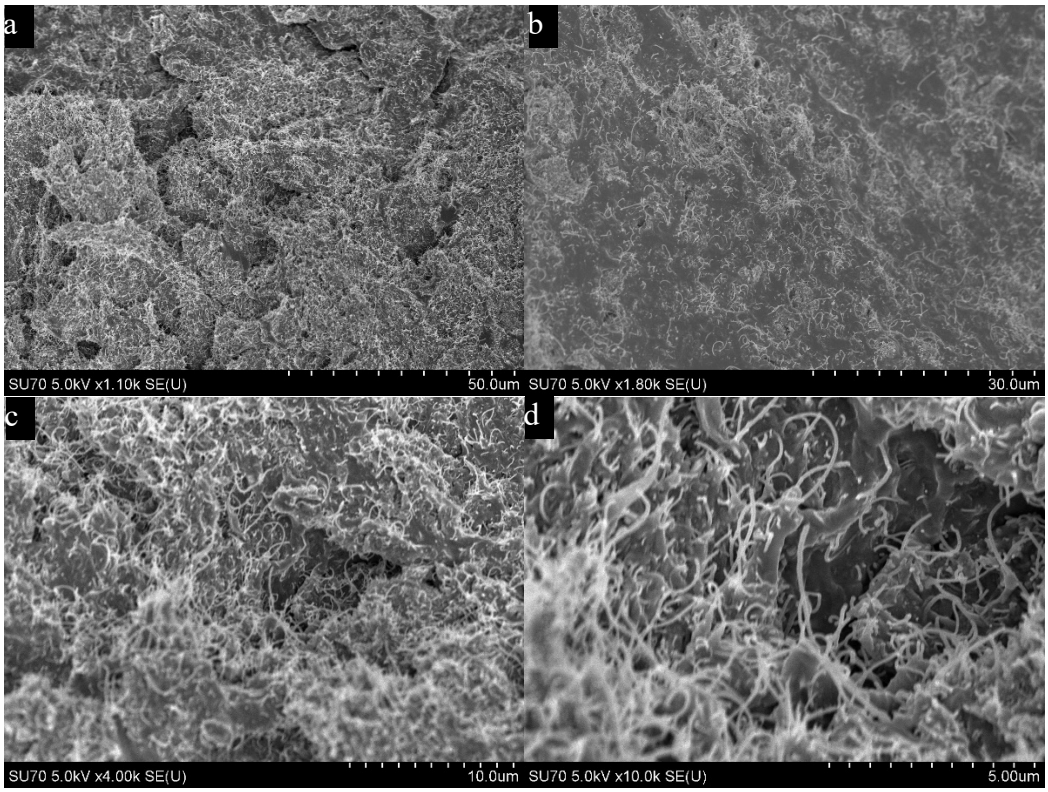

Figure 39 (a-d) SEM images of 14.5 MWCNT wt% showing the dispersion of the conductive filer MWCNT within the hosting polymer PDMS at different magnifications

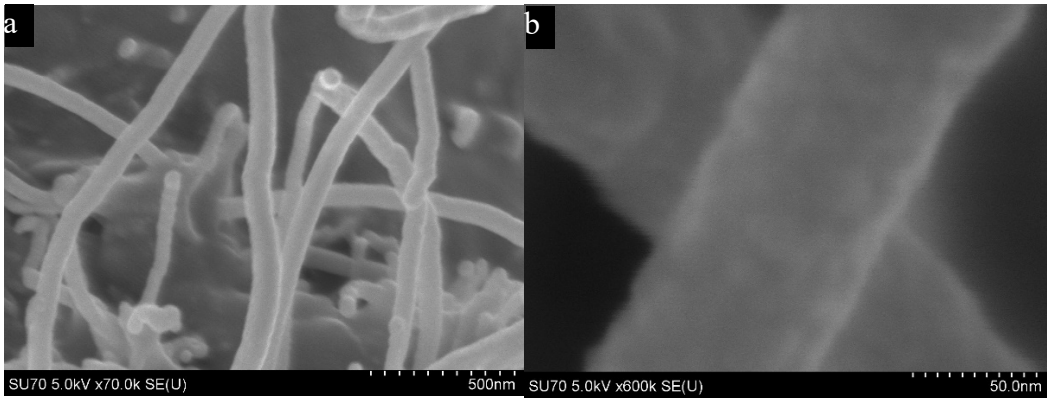

Figure 40 (a, b) SEM images MWCNT at higher magnification showing their size and formation

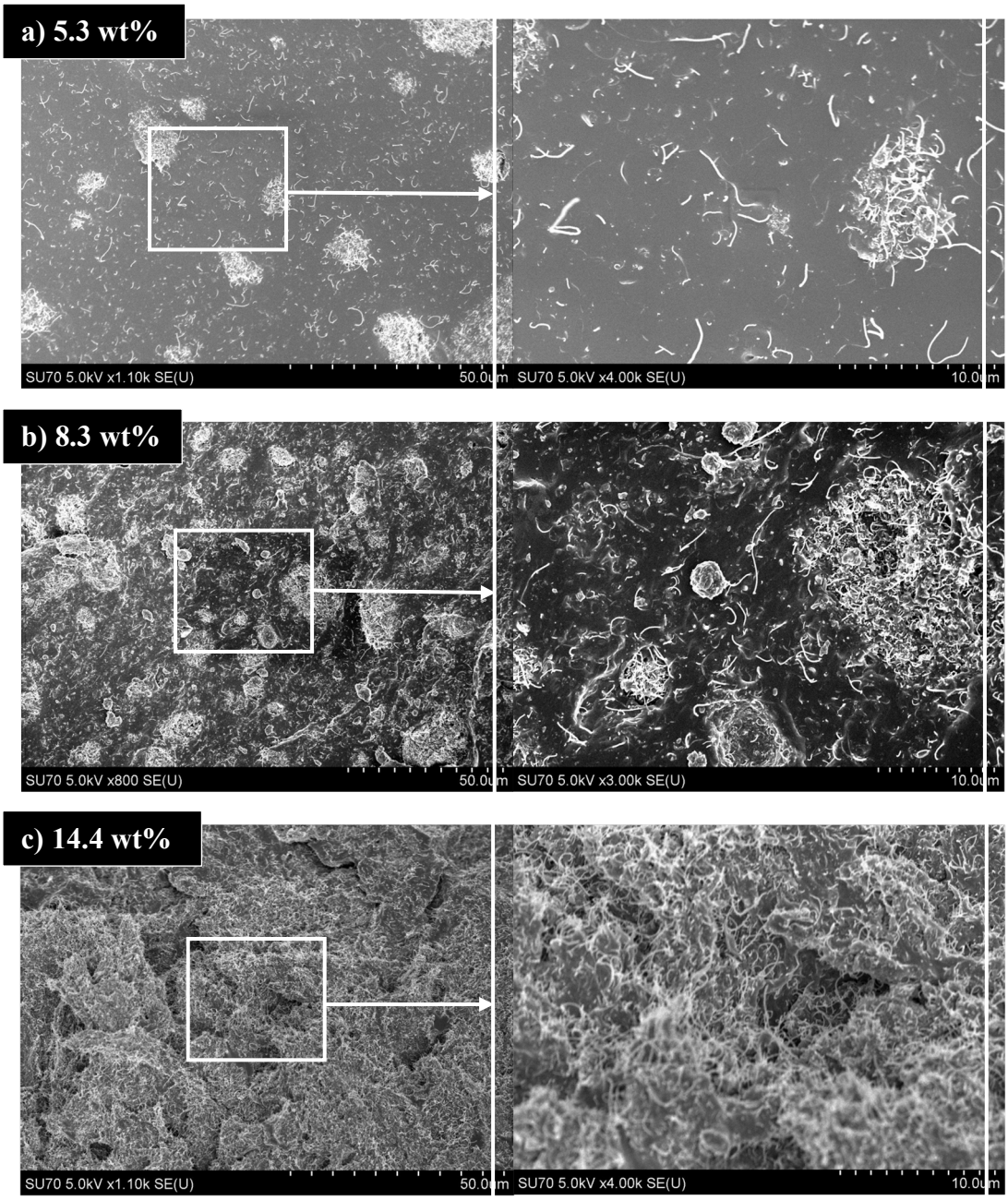

Figure 41 SEM images of the conductive polymer composite with varying conductive filler concentrations a) 5.3 wt% b) 8.3 wt% and c) 14.4%.

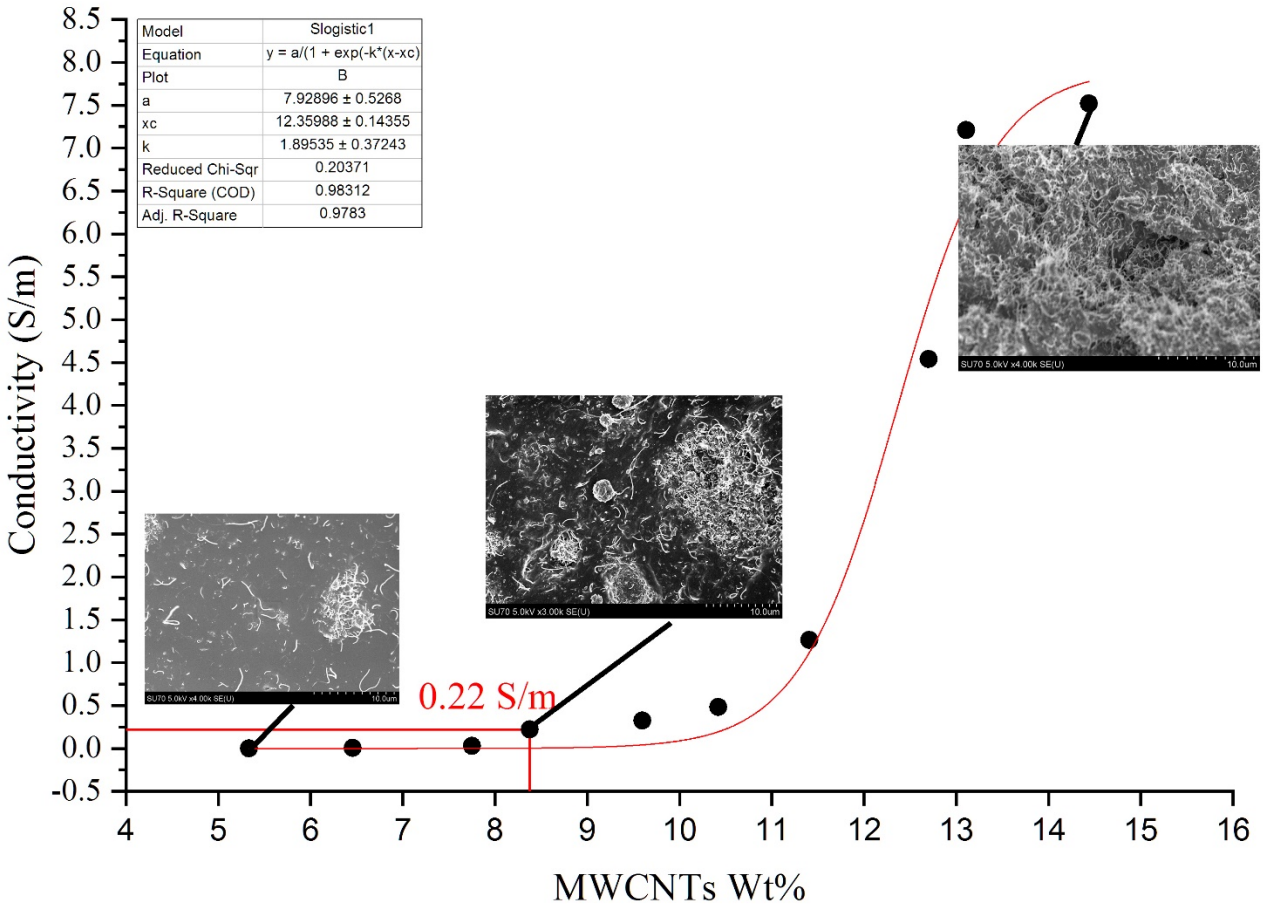

Figure 42 Conductivity measurements with non-linear regression curve acquired from 1 cm3 conductive polymer samples with MWCNT filling weight percentage ranging between 5.3-14.4% along with SEM images for the three selected concentrations 5.3%, 8.3% and 14.4%.

2.3.4 Anatomically accurate brain phantom with electrically conductive polymer

This is the third and last part of this chapter, where we show the results of combining the first and second parts. In the first part, we presented the manufacturing method and steps required to obtain and realize and physical geometry of intricate and complex materials like the brain. In the second part of the chapter, we presented the method of creating and fabricating the conductive polymer used as a constituent material for our brain phantom. We showed our method in adjusting and characterizing the electrical conductivity to match and mimic the brain's electrical conductivity. We show the steps needed to obtain the anatomically accurate brain phantom with the electrically conductive polymer in the following figures.

We targeted a conductivity of about 0.25 S/m to manufacture the brain because it is within the averaged value of the GM and WM conductivity values reported in the literature, as in table (1). This conductivity can be achieved with MWCNT wt% of about 8.5, as graphed in Figure 42.

Following the steps in Part 1, we printed the GM shells with PLA, as in Figure 20. Then, we made the conductive polymer but in a larger quantity. We used about 1200 g PDMS base, 120 g of the curing agent, and 120 g of the MWCNTs. That will equal about 8.5 wt%. We mixed the polymer with the conductive filler MWCNT following the previous section's criteria. Then, we poured the conductive polymer in the GM shells as. After pouring in the conductive polymer into the GM's upper and lower shells, joined the shells and placed it in a c-clamp to ensure a robust fixture of the shells and, therefore, accurately obtain the geometry, as in Figure 43.

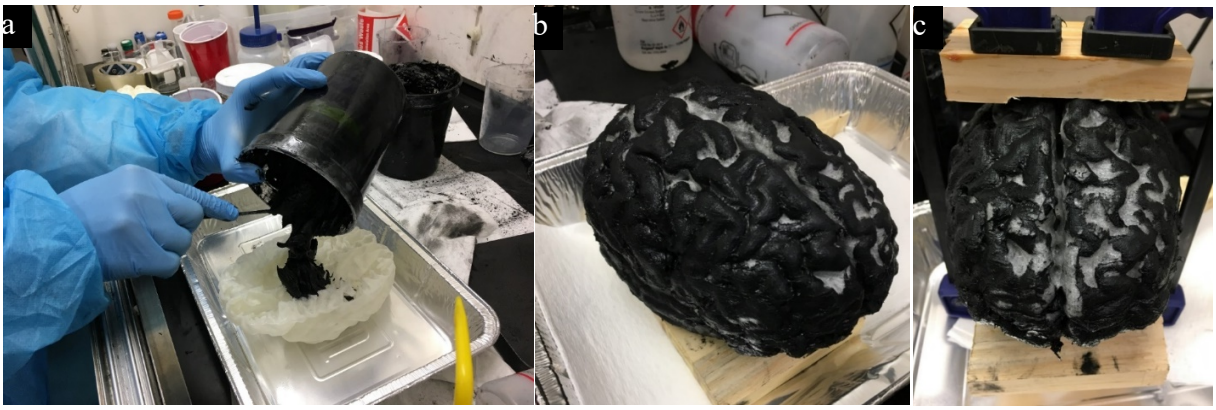

Figure 43 (a) The conductive polymer being poured into the GM shells in order to obtain the brain phantom (b) The brain phantom after the conductive polymer was poured into the upper and lower shells were joint and (c) put in a c-clamp to insure proper closure during polymer curing

The polymer needs to rest for about 48 hours before placing the entire brain in acetone for at least 24 hours. The acetone will make the PLA shells. We should be cautious when removing the shells not to tear the fabric of the brain phantom. If the shells are hard to be removed, they are recommended to put back in acetone to soften the shells more. After removing the shells, we will have the entire brain phantom as in Figure 44.

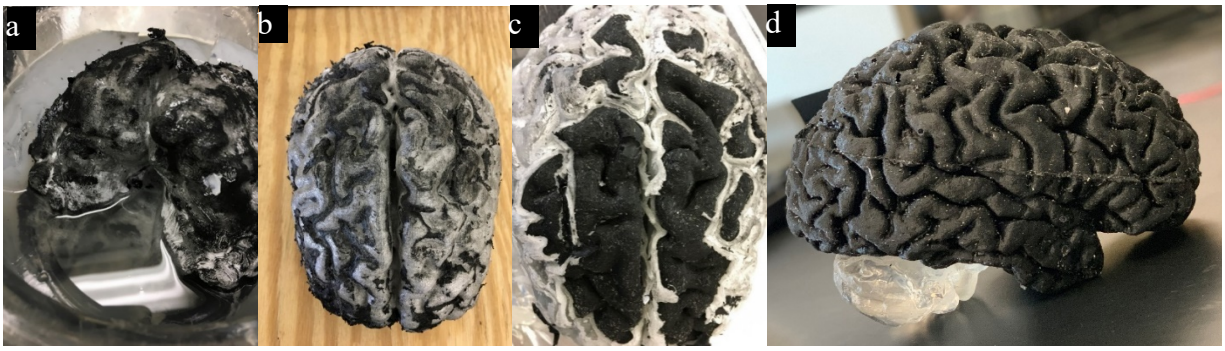

Figure 44 The brain phantom shells after being placed in acetone and removing the shells. (a) The brain phantom shells in the acetone for at least 24 hours. (b) The shells removed from the acetone. The shells became brittle and softer. (c) The shells are being removed and dismantled. (c) the shells are removed, and the brain phantom is realized

To summarize the entire process of the anatomically accurate brain phantom with the electrically conductive polymer using the shelling method, Figure 45 shows in images the major steps.

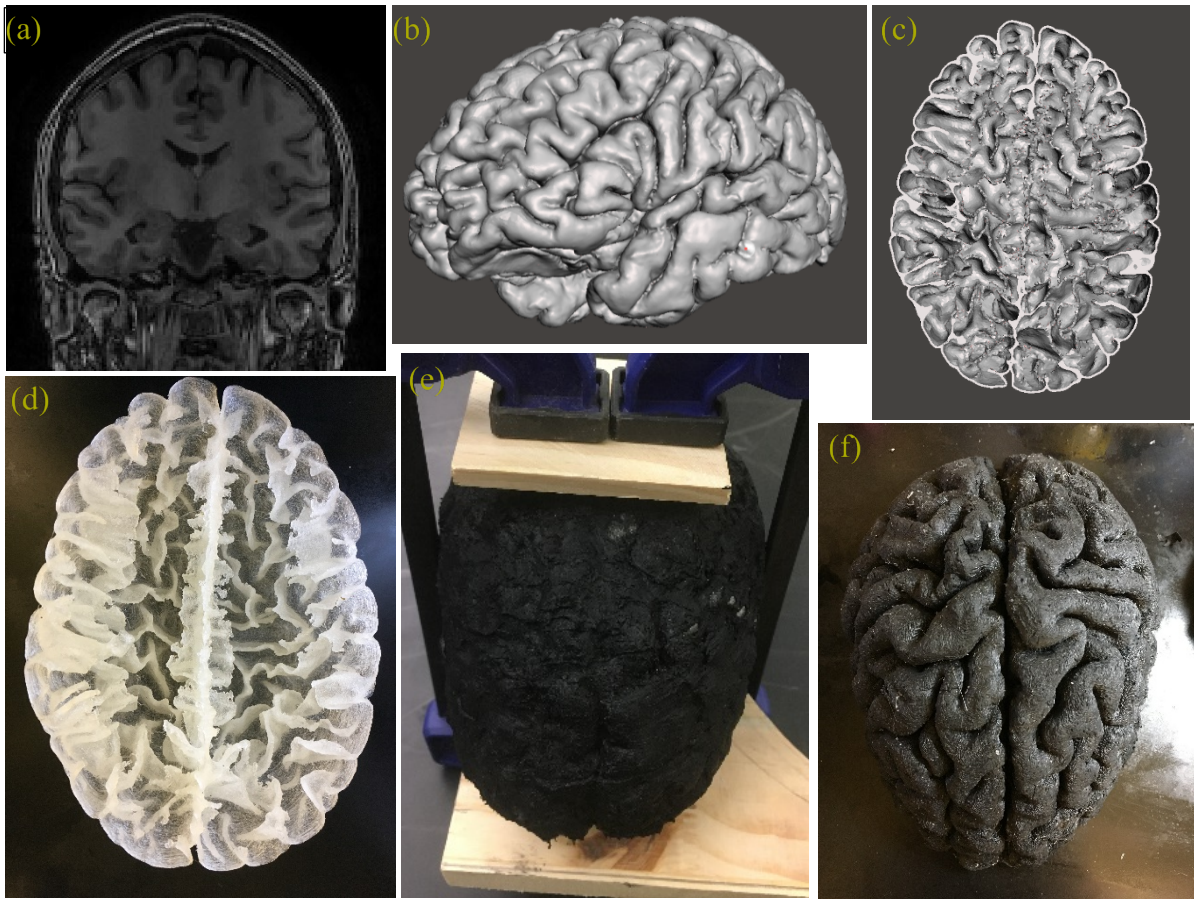

Figure 45 Summarization of the entire process starting from MRI images of the brain until the obtained brain phantom made of the conductive polymer. (a) MRI image in an nii format, (b) Reconstructed brain model in stl format, (c) Shell mold for the outer region of the brain/GM. Shown is the inner side of the upper s half shell, (d) Shell after printing and dissolving the support material, (e) Shells were filled with the conductive material and joined together and left to be cured, (f) Brain phantom after being immersed in acetone and the shells removed

2.3.5 Head phantom with the brain and CSF:

In our work on the development of the brain phantom, we also worked on obtaining the entire head geometry and mimicking the CSF conductivity. Following the same steps of the shelling method, we can obtain and create the geometry of the head's scalp and skull. Figure 46(a) shows the skull and scalp shells are being created and processed in Meshmixer based on the shelling method. The outer shell is the scalp's outer surface, and the inner shell is the structure surface of the CSF. We added four rods to fix the CSF structure because the gap area between the inner and outer shells will be built, filled, and printed with the supporting material PVA. After dissolving the support material with water, the CSF structure will have the supporting rods to fix them in place. After creating and then washed the PVA supporting material with water. In the scalp and skull, we used only PDMS because the conductivity of these layers is very low and does not interfere with the TMS coils' magnetic field. In this process, we used the vacuum to remove the PDMS bubble, as in Figure 46 (c).

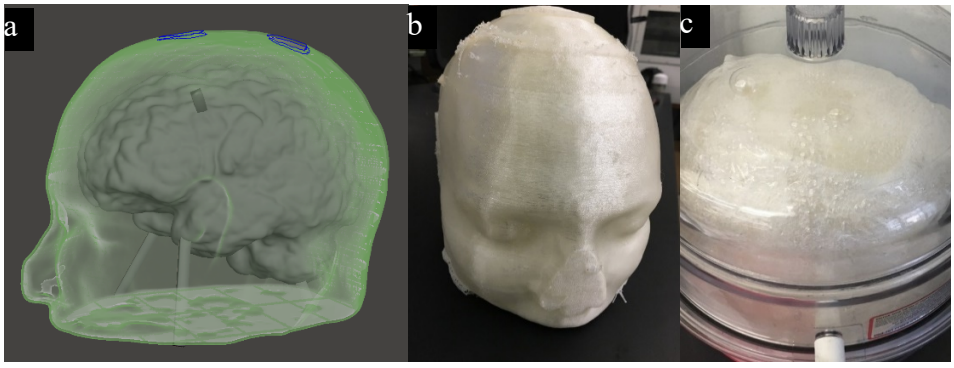

Figure 46 (a) skull and scalp shells are being created and processed to be ready for 3D printing (b) printing the scalp and skull shells with PLA and supporting material PVA. (c)

We let the PDMS cure, and then the outer shell was removed, as in Figure 47(a). At this stage, the inner shell (CSF structure) can be seen inside the PDMS head. We need to cut the PDMS and remove the inner shell. For best placement of the brain phantom inside the head, we also

created the cerebellum structure made with the PDMS and placed it inside the head after that, we placed the brain inside the head phantom as in Figure 47(b) &(c). The final step is to close and sealed the head phantom and inject the saline solution with the match conductivity to the CSF, as in Figure 48.

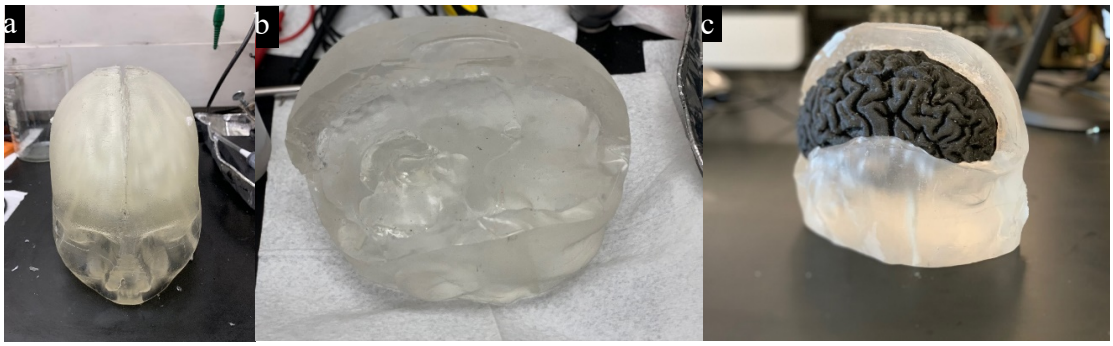

Figure 47 (a) outer shell of the skin and skull after being removed the PDMS is cut and the inner shell is removed. (b) We created the cerebellum and put it inside the head to ensure a good placeman of the brain (c) the brain phnatoim placed inside the head.

Figure 48 The mimicked CFS is being injected isside the head.

2.3.6 CT scans for the brain and head phantom

The brain phantom, shown in Figure 45 (f) was imaged using a CT scan to confirm that the anatomical features in the MRI/stl files match the phantom's anatomical features, as shown in Figure 49. There are seemingly small deviations of the cortex's anatomical features from the original MRI image due to the placement and orientation offsets of the phantom inside the CT scanner. Due to this misalignment, the CT scan slices are challenging to overlap on the original MRI slices. This can be corrected by using an accurate fixture to hold the phantom in the CT scanner.

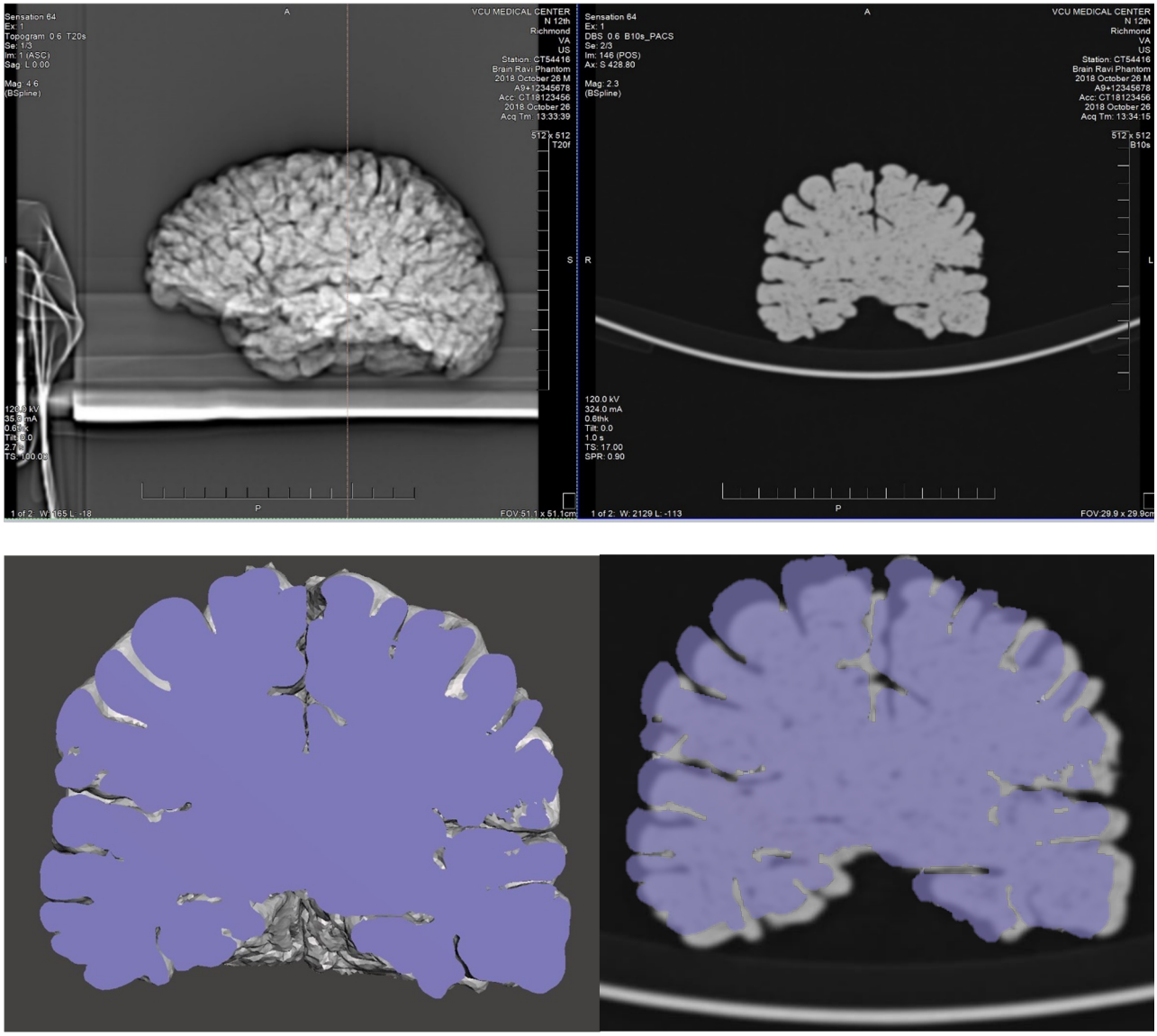

Figure 49 Brain phantom CT images compared to the brain model confirming anatomical features matching. Top) CT images for the brain phantom. Bottom left) cross section of the brain model from Meshmixer. Bottom right) an approximate overlap between cross section C

2.4 Conclusion:

This chapter showed our work on the innovative method of manufacturing and fabricating an anatomically accurate and electrically conductive brain and head phantom with mimicked CSF based on the shelling method. The process started form downloading MRI images form the Human connectome project. The images were segmented in stl models. From the stl brain model, we created shells printed with a 3D printer to serve as molds for the brain phantom material or tissue. The brain phantom material is fabricated of a conductive polymer that consists of PDMS and MWCNT. We showed that the conductivity varies to the concentration and weight percentage of the MWCNT with respect to the host polymer PDMS. We established the conductivity curve and selected a particular concentration to match the conductivity of the brain. Moreover, we took SEM images for the conductive polymer to understand the relation between the MWCNT wt%, conductivity, and dispersion. We also image the brain phantom with CT to show that the brain phantom geometry is very accurate to the brain in the stl file based on the MRI images.

This page intentionally left blank.

3 Chapter 2: Safety Study of Combination Treatment: Deep Brain Stimulation and Transcranial Magnetic Stimulation

3.1 Introduction:

Deep brain stimulation (DBS) is a medical technique using one or more electrodes surgically inserted deeply into specific regions in the brain to mitigate and alleviate motor symptoms in patients with Parkinson's diseases [72], such as slowed movement (bradykinesia), and resting tremor and rigid muscles [73,74]. However, patients also suffer from other hampering symptoms like hypophonic speech and difficulties in swallowing (dysphagia) [75–77]. Since those symptoms are not treatable with the DBS, an introduction of other modalities like repetitive Transcranial Magnetic Stimulation (rTMS) is proposed as an option in the treatment or alleviation of such symptoms [41,76,78–81]. rTMS is a non-invasive treatment where time-varying magnetic fields are produced by current running in coils to induce electric fields in the patient and therefore stimulating neurons in the targeted region [79,82]. Combining the two methods of treatment might risk the safety of the patient with implanted DBS because the high-intensity magnetic field produced by the TMS will elicit high levels of electrical current that might travel down the path into the deeper regions of the brain and cause burn or damage. Therefore, there is a need to accurately study the prospected effects by including all of the parameters involved without risking patients with implanted DBS. Some previous studies have underestimated and oversimplified the geometrical complexities of the lead and biological tissue [83]. Besides, we are not aware of any studies as of yet which have used physical models with accurate head, and brain geometry and impedances to study the effects of TMS on full implanted DBS leads [14,83–87]. Kumar et al. (1999) measured the induced currents by TMS at 100% intensity from a homogenous phantom.

They found that the induced currents in the range of microampere, which is lower than the operating range of conventional DBS treatment. Kuhn et al. (2011) investigated the effect of the TMS on the DBS internal power generator IPG. They measured the voltages induced on the leads and found that the voltages did not exceed the operating limit. Both studies concluded that the combination of the two modalities would not result in unsafe levels of induction on the DBS leads. On the contrary, Shimojima et al. (2010) and Deng et al. (2011) drew a different conclusion that the combination of the two techniques will produce high levels of induction. Deng et al. measured the induced voltages, and current on a hollow mannequin phantom with a full configuration of the DBS leads and extensions. They reported very high levels of induced currents that reached up to 82 mA. Shimojima et al. did a similar investigation, but in a head phantom that is filled with gelatin of similar conductivity to the brain. They measured charge density that reached up to 20 μC/cm2 /phase, which is considered to be in the unsafe levels. We also found other clinical investigations done by Kuhn (2002) and Hidding (2006) of the combination treatments in which the TMS was applied to patients with implanted DBS. The investigators measured the motor evoked potentials MEP on the patients and did not report any adverse reactions or complications post the application of the TMS on the volunteered patients.

In this study, we experimentally measure an anatomically accurate head and brain phantom fabricated based on MRI images, the induced voltages, and current form such combination. With an accurate physical model mimicking the impedances and geometries, we can account for any energy interference of displacement currents with the induced current in the DBS lead.

We fabricated the head and brain phantom based on MRI images developed into the brain model using FreeSurfer, simNIBS, and FSL pipelines. The head phantom is fabricated with

electrical conductivities matching cerebrospinal fluid and averaged conductivity of grey and white matter. Induced current on an implanted DBS probe in the brain phantom was measured.

.

3.2 Materials and Methods

We realized that based on the literature and discussions with our collaborator from VCU medical campus, Dr. Kathryn Holloway, that there are different configurations for the DBS in terms of the number of leads used (unipolar or bipolar), number of windings of DBS probe, and its extensions, and the overall circuitry involved. Since this is a safety study, we aimed to simplify the experiment and configurations to the least complicated setup. We used the unipolar configuration, meaning that we used only one DBS lead inserted. Also, surgeons usually tuck the DBS wire under the skin on top of the skull. Sometimes they make loops or windings that we posit might increase the level of induction based on Ampere's law. For that reason, we decided to use only one loop. DBS probes are connected to the internal pulse generator IPG. The IPG could be set on "ON" or "OFF" state. In our experiment and to take a more simplistic approach, assumed that the IPG is set on an "OFF" state so that we would not have any additional current or voltage that might interfere with the initial induction by the alternating magnetic field of the TMS on the DBS probes and brain phantom.

We fabricated an anatomically accurate head/brain phantom with an implanted DBS probe at the hypothetical STN location. The head model consists of four main parts.1) the brain phantom 2) skull, skin, and scalp 3) cerebrospinal fluid, and 4) implanted DBS probe. The process of creating the brain and head phantom can be found in detail in chapter 1 and in our published patent, where we show the detailed steps for creating each part of the head phantom [88,89]. There are some additional steps in the fabrication process to place the DBS probes inside the phantom properly. In the following sections, we briefly show a general procedure to obtain each part of the head phantom with an implanted DBS.

3.2.1 Brain phantom

The brain phantom was fabricated using a healthy subject's MRI images downloaded from the online database of human connectome project HCP, Parkinson's Progression Marker Initiative PPMI [90]. The MRIs were segmented, and a 3D brain model was developed into an stl format using FreeSurfer (Athinoula A. Martinos Center for Biomedical Imaging, Charlestown, MA, United States), SimNIBS (Danish Research Centre for Magnetic Resonance (DRCMR), and FSL (Analysis Group, Oxford, UK) software. From the model, we created shells to serve as molds for the segments of the brain. For example, to create the grey matter, we used the head model and created the outer shells of the grey matter. These shells were 3-D printed and were used as molds for the constituent material of the brain phantom. In parallel, a conductive polymer composite was prepared to mimic the electrical conductivity of the brain. The conductive polymer composite is composed of multi-walled carbon nanotubes (MWCNT) and polydimethylsiloxane (PDMS). The addition of the MWCNT to the PDMS imparts an electrical conductivity dependent on the concentration of the MWCNT. The conductive polymer is poured into the molds and left to solidify. After the solidification, the molds are immersed in acetone to be removed and to obtain the accurate anatomy of the brain matching the MRI. The brain phantom was fabricated with a measured impedance of 450-500 Ω that matches the average impedance of the human brain [24,25,29,30,91].

3.2.2 Skin, scalp and skull

Skin, scalp, and the skull were built as a single layer with the shelling method used to obtain the brain phantom, as in Figure 50. Nevertheless, in this case, we used only PDMS as the constituent material because the electrical conductivities of these regions are low and similar to

PDMS. The figure shows the PDMS after It cured, and the outer shell was removed. We can still see the inner shell through the opaque PDMS polymer.

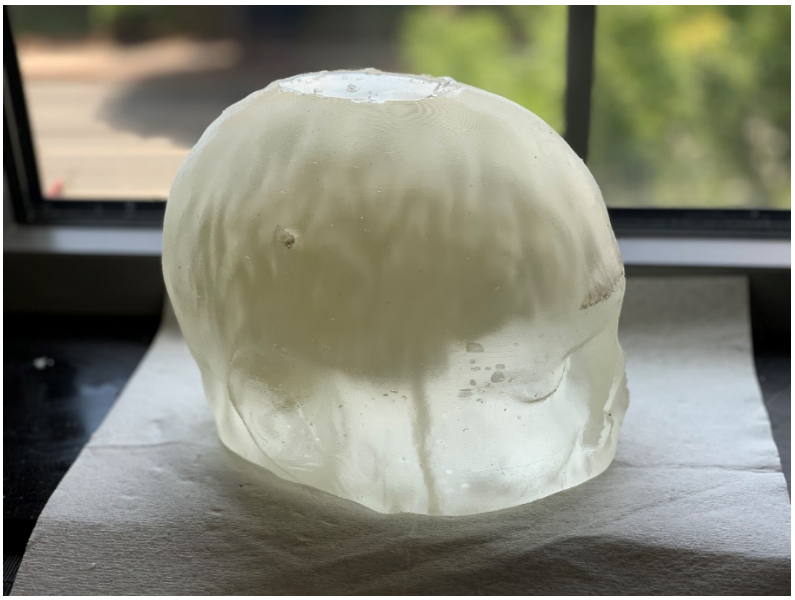

Figure 50 Anatomically accurate skin and scalp made of PDMS

3.2.3 Cerebrospinal fluid

The gap between the brain and the skull is the CSF space. We filled this space with a saline solution that has an electrical conductivity similar to the CSF conductivity in humans, which is about 1.0-1.2 Sm^{-1}.

3.2.4 Implanted DBS probe

DBS leads are comprised of four electrodes which lie at the site of stimulation, with four separate wires capable of delivering current to each contact. Each wire is wrapped in insulation to avoid interference with the other wires, and there is further insulation that comprises the entirety of the probe body. We used a commercial FDA-approved DBS lead (Medtronic 3387 lead) shown in Figure 51 that is commonly used in DBS surgeries (Medtronic Lead Kit for DBS Stimulation, 2016).

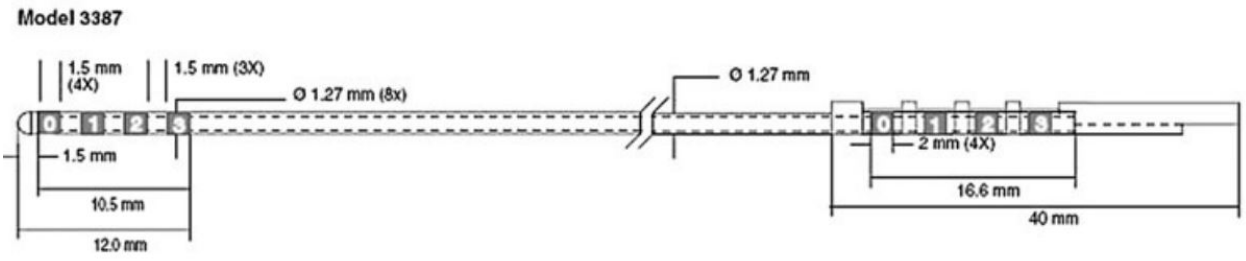

Figure 51 Schematic depiction of the Medtronic DBS lead model 3387 [72]

To accurately determine the location of the hypothetical STN in the brain phantom, we measured as Figure 52 in the distances and dimensions from the skin to the targeted location so that we can print shells with a guided opening designed for the DBS lead insertion.

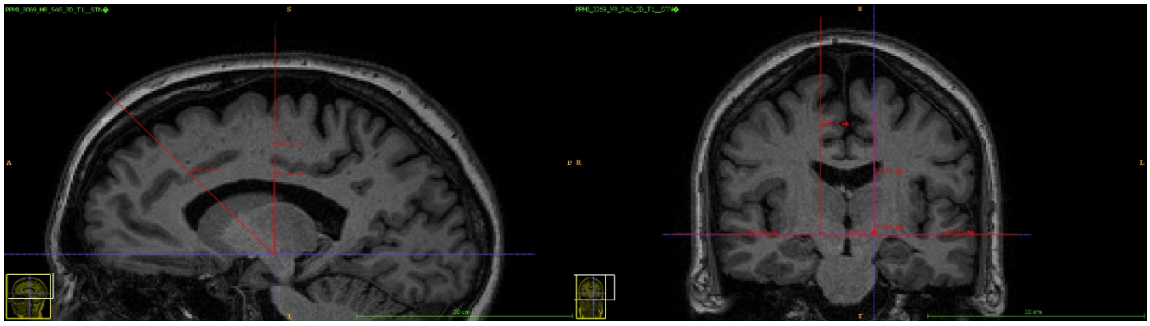

Figure 52 Measuring the dimension of the STN to help in building the brain shells with guided opening

Next, we added the guided opening on the shell, and 3D printed the shells with PLA Figure 53. The DBS probe was inserted into the conductive polymers during the curing and solidification period and through a guided opening on the brain phantom shell. After the solidification of the brain phantom, the molds were removed.

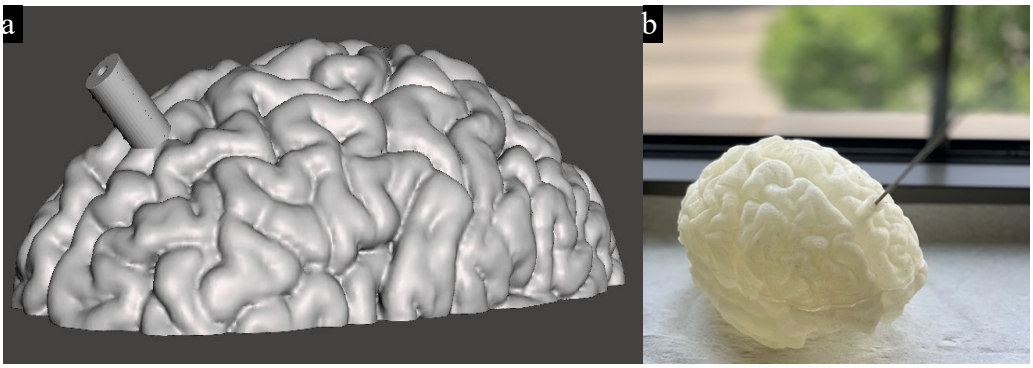

Figure 53 (a) the brain shells with the guided opening being processed in Meshmixer. (b) The shell after printing. We can see that a narrow rod can slide into the opening with certain angel.

We should note that we kept the stylet, supporting material, of the DBS probe in order to protect the integrity and structure of the wires inside the probe from damage. The DBS probes are very delicate and prone to damages, as reported by the FDA [93] . We believe that the presence of stylet has a negligible effect on the induced current in the lead wires as it is electrically isolated from the rest of the probe structure. The inside volume of the helical coils of the probe undergoes Faraday's cage effect, and hence the stylet will experience no induced electric field [94].

The final realization of the brain phantom that includes the realistic brain phantom and mimicked CSF with implanted DBS probe in the hypothetical STN is seen in Figure 54(c).

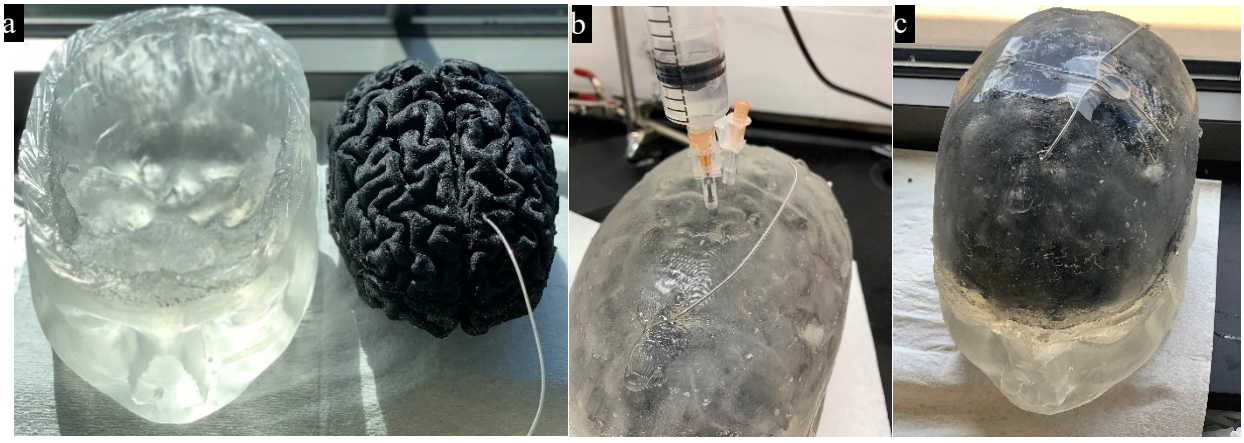

Figure 54 (a) Head model with skin, scalp and skull (left) and brain phantom with the implanted DBS probe (right). (b) Head phantom is enclosed and the saline solution that mimics the CSF is being injected into the head phantom. (c) Final realization of the anatomically accurate head phantom with the implanted DBS probe

3.2.5 Experimental set up and measurement of the induced current:

An FDA-approved TMS device, Magstim (model: Rapid 2 with Magstim AirFilm coils), was used to apply TMS to the physical head phantom. TMS coils were placed about 1 cm on top of the DBS lead. The magnetic field was applied from 50-100% TMS coil's current intensity with a single pulse and signal frequency of 2500Hz. The probe has one loop winding on top of the phantom. Then, we measured the induced voltage by measuring the voltage difference between the lead contacts and converted them into induced currents. The experimental setup is shown in Figure 55, and the circuital diagram is shown in Figure 56.

Figure 55 Experimental set-up where time-varying magnetic field by the transcranial magnetic stimulator is applied on the physical head phantom.

In Figure 56, we show a schematic diagram of the circuit used to measure the induced voltage/current on the DBS. The circuit consists of two main parts A and B. Part A represents the equivalent impedance Z_{eq} of the brain phantom. In a real patient, this impedance would be the impedance of the neighboring regions of the inserted DBS leads. Part B represents the DBS probe

and DBS pulse generator's internal resistance, and it is typically about 100 Ω [95]. The resultant voltage waveform is shown in Figure 57, and the voltage values corresponding to coils' intensities 50-100% are shown in Figure 58.

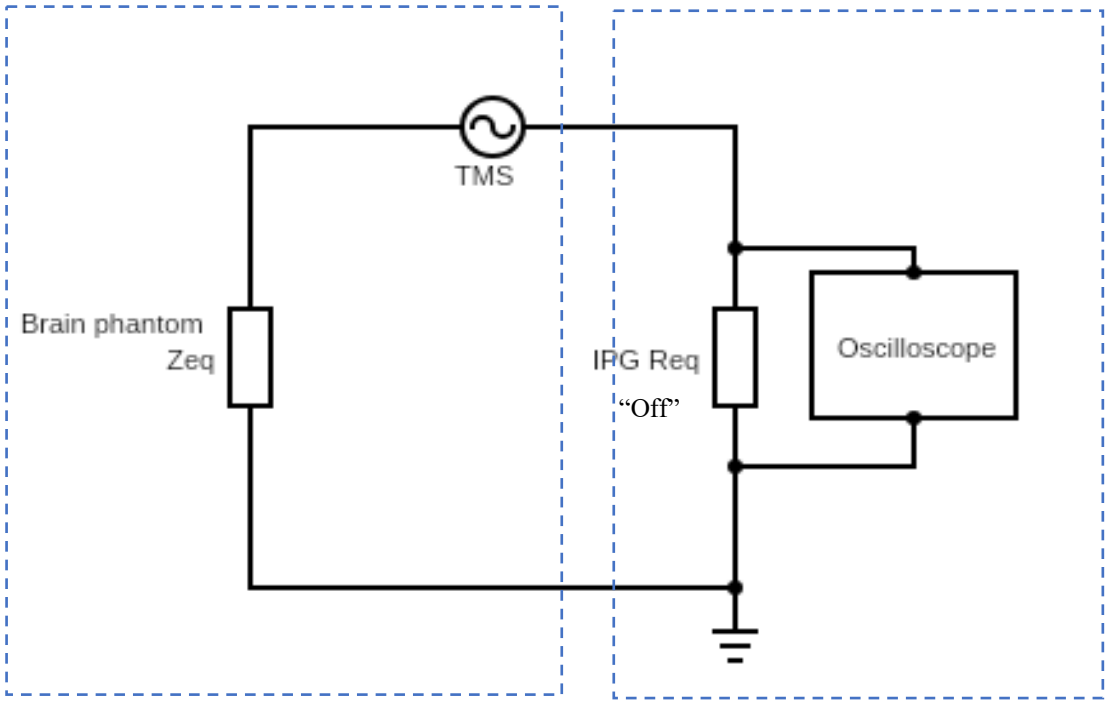

Figure 56 Schematic diagram of the circuit used to obtain the induced electric current on the DBS probe in the presence of the time-varying magnetic field.

3.3 Results:

Figure 57 shows the bi-phasic waveforms obtained during the measurements. The waveform shown here corresponds to the measured induced voltage at 100% coils intensity. The waveform obtained with minor artifacts at the ends potentially due to an abrupt transition of the original pulse of the magnetic field, and the artifact in the middle is a result of minor variations in the electric field due to switching off the power transistor inside the TMS stimulator. Figure 58 shows the

currents induced for changing the magnetic field strength produced by the TMS coils. The induced voltages are converted directly to induced current by dividing the voltage drop by the value of Req=100 Ω.

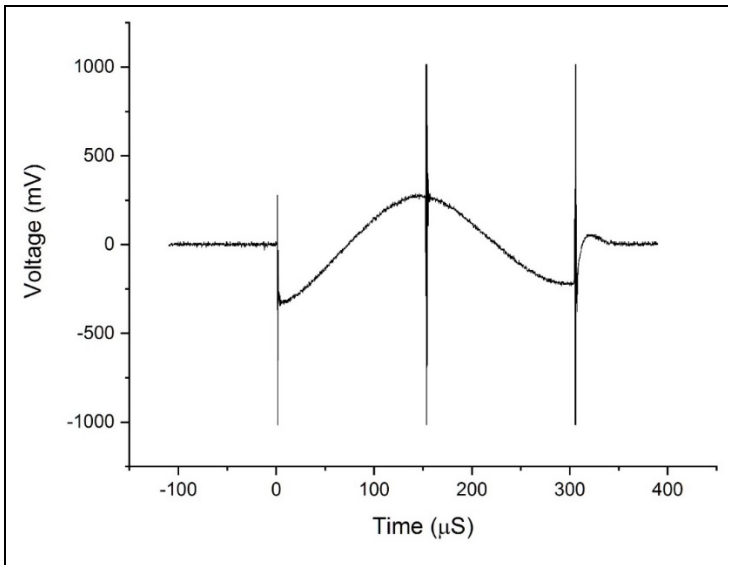

Figure 57 The waveforms obtained from the voltage measurements on the DBS probe during TMS.

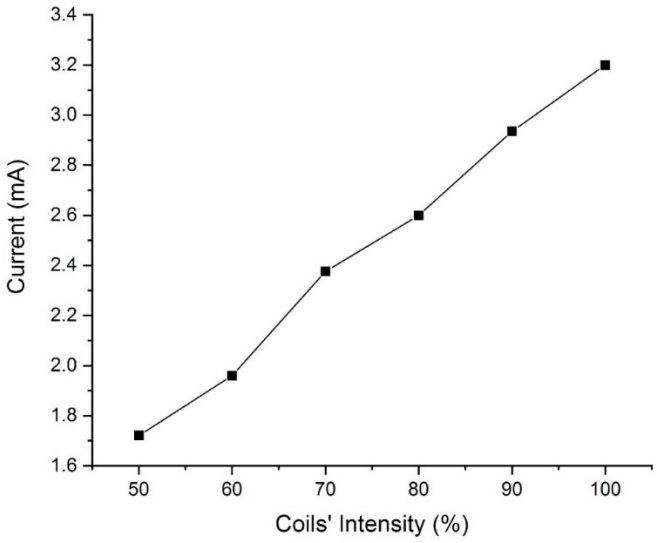

Figure 58 Induced currents with respect to TMS coil's intensities.

3.4 Discussion

From the results of the experiments on the physical head phantom, the induced current values are of the order of mA (1.71-3.20 mA), which are in the range of current values used in DBS (3.2-4.5 mA) [96]. They are higher than values reported by Kumar *et al.* (1999), where they reported induced current in the range of 70-120 μA. However, [83] reported higher values in the range of 12.75-83 mA, and [14] reported a current density of 20 $\mu C/cm^2$ /phase, which is considered to be exceeding the safety threshold). Therefore, our measured values are consistent with Deng *et al.* and Shimogima *et al.* We theorize that the variation in the results may be due to several factors, the accuracy of the real DBS probe geometry, the medium in which the DBS probe is implanted, and the design and values of the electrical components of the complete circuit. ***We have experimentally measured the induced voltages and currents in the widely used Medtronic DBS lead. We accounted for the complexity of brain anatomy and geometry. In our experimental model, we used our novel anatomically accurate brain and the head phantom that mimics the impedance/conductivity of the brain as well as the CFS.*** Previous studies either lack geometrical accuracy of the medium in which the DBS probes were inserted in, DBS probe and lead design, or accurate impedance values. The geometry and impedance of the medium are essential because they determine the magnitude of the electric field produced and, in turn, contribute to the current induced in the DBS probe. Such considerations will help to expand the study to include other DBS configurations and TMS coil orientations and placement. Thus, considering the prior work in the literature of TMS and DBS safety, our study is an improved analysis considering a more accurate brain phantom, actual DBS probe with accurate impedance. Previous studies showed that with the increased number of loops, the induced current would increase proportionally. Our work shows that even with a single loop, the current induced is on the

range of unsafe limits. Moreover, Figure 4 shows that even at lower coil intensities, the induced current is noticeable and is in the mA range.

Lorentz forces are other potential sources of risk in such combination techniques. However, previous work by Shimogima *et al.* showed that there are no detectable movements on the DBS lead inserted in a gelatin phantom, and therefore the risk from Lorentz forces is negligible. For that reason, and since our results show that it might be unsafe to combine DBS with TMS, we did not investigate other possible risks such as Lorentz forces in our study.

3.5 Conclusion

In this work, we investigated the safety of combining DBS with TMS treatments. We developed an accurate physical model with commercially used DBS lead. Our measurements show that using a time-varying magnetic field applied by 100% TMS intensity in the presence of DBS will induce currents that are higher than the safe limits (3.2-4.5 mA), which may result in over-stimulation. These results are in agreement with previous studies that considered the safety of the combination of TMS with DBS. We attempted to minimize the sources of errors that might result in higher variation in the result. The majority of the induction on the DBS lead is primarily due to the effect of the magnetic field on the DBS lead. However, we should note that there are several reasons we considered such an experimental setup. Based on previous reports related to safety studies cited in this chapter, we found conflicting conclusions about whether it is safe to combine the TMS with the DBS. Some of those experiments lacked the details and complexities in the physical head models. In our lab, we work on the development of the brain and head models to bridge the gap on the experimental side of TMS. We have mimicked the physical environment where the TMS and other brain-stimulating methods are performed would be beneficial toward

approaching such studies. We acknowledge that one major downside is the difficulty of adjusting and replicating the setup.

Nevertheless, we believe that we can minimize if we did our experimental work carefully, the sources of errors by providing such a physical environment. The configuration of the DBS lead to parameters like the TMS coils intensity and orientations, and also with respect to the brain, and the head model is quite simple. We used only one lead, one loop, and a single orientation. There is a variety of other configurations that are much complex and might be harder to track the source of errors. Our goal is to prepare the physical environment and then extend the test to different combinations and configurations of the combined TMS and DBS treatment. We only used a simple configuration with one loop on the wire and used an accurate brain, and the head phantom that matches the geometry and an averaged electrical conductivity. Our results suggest that even with the simplified setup, the level of induction is above the unsafe limits. Therefore, we recommend that the TMS should not be applied at 100% intensity directly over the implanted DBS leads in the STN area.

This page intentionally left blank.

4 Chapter3: Measurements of stimulation strength

4.1 Introduction

The brain phantom described in the previous chapters are intended to be validated with the measurements of stimulation strength such as induced voltages on the phantom, magnetic field strength produced by the figure-of-eight coils of the TMS, the induced reference voltages and on the oscilloscope probes. The measurements are then used in mapping the electric field on the brain phantom.

Ever since the introduction of the TMS, many groups have attempted to evaluate the level of induced electric field that the TMS can produce on the brain cortex. Many analytical studies aimed to establish the correlation between the intensity, frequency, and time variability of the magnetic field and its effect on a biologically conductive material like the brain that has specific values of conductive and permittivity [12,13,17,18,97–100].

With the rapid development of fast and powerful computers, the field of computational calculations and numerical simulations expanded and flourished. The computational TMS research has thrived to a point where highly accurate brain models with variable and anisotropic conductivities are used to study the stimulation [38,101–104].

It is vital to measure and evaluate the magnitude and strength of the electric field because it is directly correlated to neural excitation and firing. Many factors determine the likelihood of neural firing when influenced by an electric field. The directionality and magnitude of the electric field are the two major contributors to the neural firing ignition.

These measurements presented in this chapter are an effort to evaluate the electric field on complex geometry formed by conductive polymer. We are not aware of any group that

made such an attempt. This is because it is not a trivial task, and the brain phantom that we developed in the Biomagnetics Lab is the first to account for the geometry of the brain. Previous techniques have been developed by other groups to measure the electric field techniques like the loaded probe, long rectangular loop, and triangular loop, etc. [105–107]. These techniques are developed to measure the electric field in air or saline with simple geometry. Therefore, there is a need to develop a new or an existing technique to measure the electric field on complex and with relatively low conductivity materials and with minimal interference between the induced field and the measuring probes.

The work presented here is divided into four sets of measurements: 1) voltage measurements on the brain phantom with respect to distance and compared to e-field calculations from FEM simulation, 2) Magnetic field measurements, 3) electric field measurements in air, and 4) electric field measurement on a conductive sheet and conductive brain phantom. The purpose of the first task in that we validate and confirm that the brain phantom we fabricated is responsive to the magnetic stimulation. In this case, we measure the voltages. Then we compared the change of the voltages to the change of the electric field calculated from simulation software. The magnitude of the stimulation is not of a concern at this point as we are only interested in showing that the brain phantom is being stimulated and that the stimulation is a result of the time-varying magnetic field form the TMS coils. Therefore, we will show the stimulation strength and behavior on the brain phantom as the distance from the coils and the intensity of the current change. The same parameters (coil distance, current in the coil) will be applied in the simulation for comparison. The remaining tasks of this chapter aim to map the electric field in air, conductive sheet, and the brain phantom to show the effect of the geometry and measuring techniques on the electric field mapping.

4.2 Materials and methods

4.2.1 Voltage measurement and E-field calculation on the brain vs. distance

The phantom was examined by measuring stimulation strength (voltage) under different TMS parameters and compared with FEM of the induced electric field. For the measurement of voltage, we positioned the TMS coils on the brain phantom, and an oscilloscope probe is placed just underneath the surface of the phantom in order to measure the voltage (phantom probe). Also, we placed another probe at the same distance (from the coils) of the first probe, but it was placed outside the phantom to measure the voltage induced on the probe just from the TMS coils as a reference probe. Then, we applied the magnetic field from the TMS coils at four distances 1, 2, 3, and 4 cms and four different power intensities 25%, 50%, 75%, and 100% at each distance. The brain phantom and experimental setup are shown in Figure 59(a).

Also, we replicated the same setting of the experimental work with FEM simulation where the TMS coils in the software were placed at four distances 1, 2, 3, and 4 cm from the surface of the brain model and with four intensities 25%, 50%, 75%, and 100% at each distance Figure 59 (b); the maximum intensity is based on 5000 A. Moreover, the assigned conductivity of the brain model is 0.25 S/m, grid size 2mm, and the frequency of the stimulating magnetic field was 2.5 kHz.

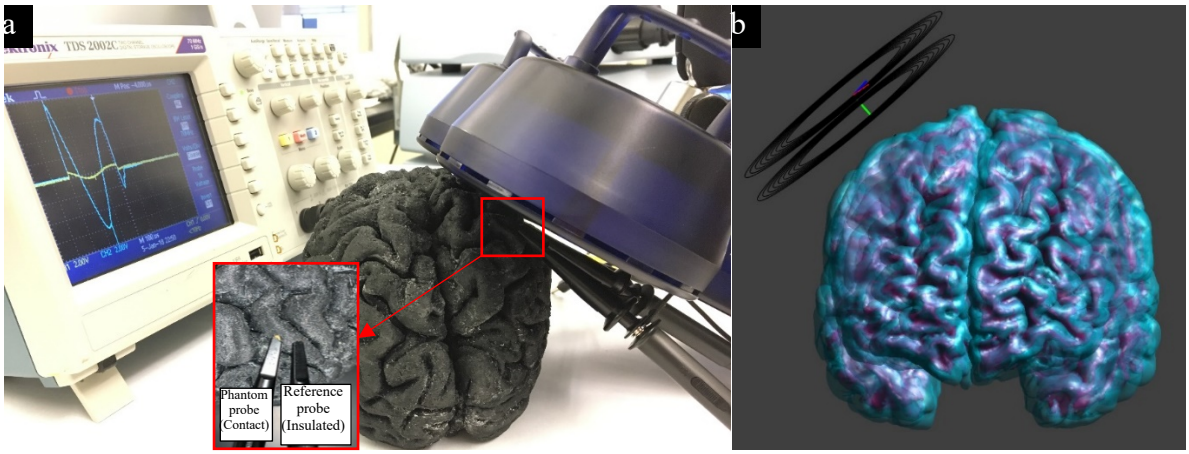

Figure 59 (a) the experiment set up to measure the voltages as a function of varying the distance coils-surface distance and coils current intensity. (b) The simulation set up to calculate the electric field as a function of varying the distance coils-surface distance and coils current intensity

4.2.2 Magnetic field measurements

We must familiarize ourselves with the magnetic field produced by the TMS coils and its strength and distribution. That will provide insight and prediction of what would the voltages and electric field behave. I used a Gaussmeter (Lakeshore Cryotronics model 475, Westerville, OH, USA) with a transverse Hall probe (Lakeshore Cryotronics model HMNT-4E04-VR). The Hall probe is a solid-state sensor that proportionally relates the induced output voltage to the magnetic flux density. The probe is placed on the x-y plane at z=0 cm of the coils, as in Figure 60 where the sensor is perpendicular to the surface of the coil. The Hall probe readings of the magnetic flux density are sensitive to the angle of the surface normal and the flux lines. Therefore, the magnetic field reading along the plane will only capture the perpendicular component. The Gaussmeter is set on the Peak mode designated to measure the pulsed magnetic field. The distance between each measurement point is 1 cm.

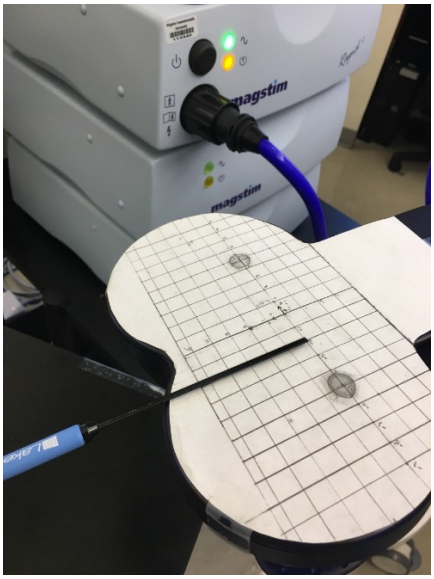

Figure 60 Hall probes positioned on the XY-plane of the TMS coils and at z=0 to measure the magnetic flux density.

4.2.3 Electric field measurements in air

Similar to the magnetic field measurements, we placed the oscilloscope probe on the surface of the coils and measured the magnitudes of the voltages. According to the equation (7), the electric field is the spatial derivation of the voltage. Therefore, we directly measured the voltages on the XY-plane and at z=0 cm from the surface of the TMS coils. The results section shows the voltages readings and the electric field derived from the voltages. The resolution of the measurement is 1 point/cm, same as in the magnetic field flux measurements.

4.2.4 Electric field measurement on the conductive sheet

After measuring the voltages on the surface of the coils, we measured the voltages induced on the surface of a conductive sheet that has the same conductivity as the brain phantoms fabricated in our lab (average of grey and white matter conductivities). The reason to map the electric field on the conductive sheet is that the measurements will take place on simple 2-D geometry. The only complication with such measurements is that the probe, in this case, will interfere with and perturb the induced electric field on the conductive sheet. The conductive sheet has an average thickness

of about 1.5 mm. The sheet was placed on a fixture at about z=1 cm, as close as possible to the surface of the coils. In this case, we increased the measurement resolution to 2 points/cm in order to enhance the mapping of the electric field.

Moreover, in order to reduce the interference of the oscilloscope probe with the magnetic field, the probe was positioned on the sheet on the opposite side of the coils. We believe that the small thickness of the sheet will have a minimal impact on the voltages measured and the electric field propagation. The conductive sheet and the experimental set up is shown in Figure 61

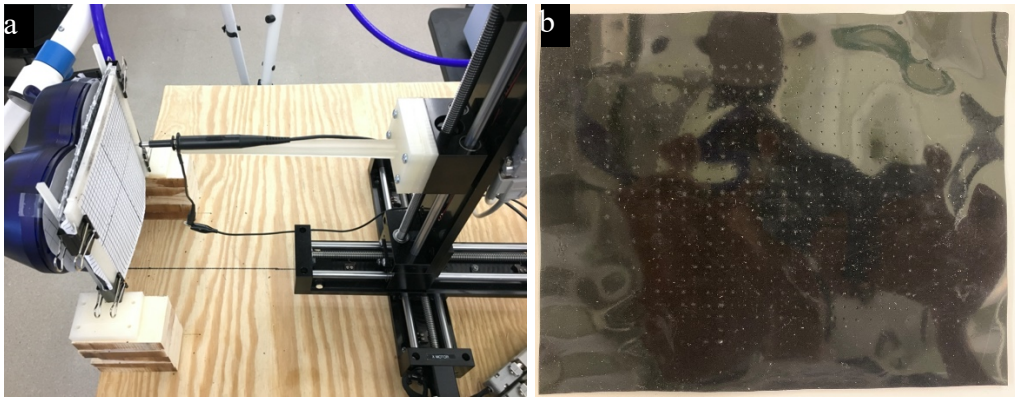

Figure 61 (a) Conductive sheet with conductivity similar to the brain phantom used in the voltage measurement and electric field mapping. (b) The experimental set up where the conductive sheet is placed on a fixture and the voltage measurements were taken from the opposite side of the sheet.

4.2.5 Electric field measurements on the brain phantom (M1 area)

The last step is to map the electric field on the brain phantoms, specifically on the primary motor cortex, M1 area. Clinicians usually stimulate this area before TMS treatment to establish the evoked motor threshold EMT so that the treatment dose is suitable to the patients. The measurement points are spread along the surface of the M1 area, as shown in Figure 62 with a resolution of 2 points/cm. The TMS coil was placed parallel to the upper surface of the brain and at about z=3 cm. We increased the distance because it was challenging to place the oscilloscope probe at a smaller distance. Since we are interested in the electric field mapping (behavior) rather

than the electric field magnitude, we thought that should not have a significant impact on the measurements except the fact that the probes can interfere with the magnetic and electric field.

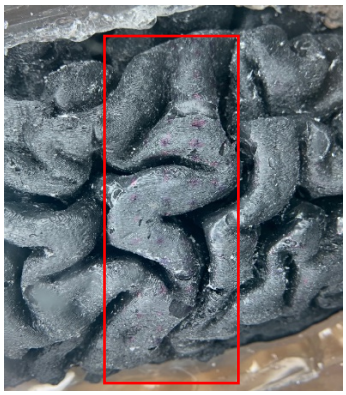

Figure 62 The M1 area of the brain phantom where the voltage measurements were acquired

4.3 Results and discussion

4.3.1 Voltage measurement and E-field calculation on the brain Vs. distance

Figure 63 shows the biphasic signal of the voltage that is expected and established in the literature. As seen in the Figure 63, the reference probe has a lower magnitude of the induced voltage. This induced voltage is a result of the induction of the time-varying magnetic field on the oscilloscope probe. This indicates that there is a noticeable induced electric field in the phantom due to the applied magnetic field from the TMS coils. We subtracted the induced voltage on the reference probe from the induced voltage measured on the brain phantom, as presented in Figure 64.

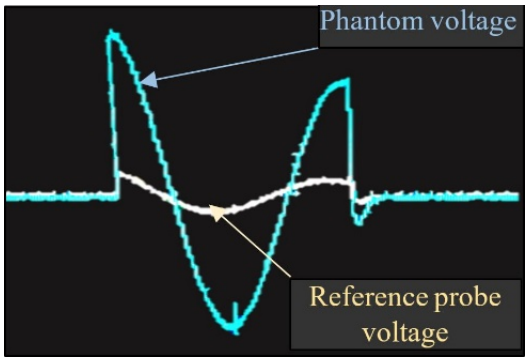

Figure 63 Voltage signals from the phantom and the reference probe

In the simulation part, we show the induced electric field as a stimulation strength because we could not find a method in sim4life to show the local induction of the voltage. We believe presenting the electric field is sufficient in this case because we are interested in comparing the effect of distance and coil's intensity on the level and behavior of the stimulation. The electric field magnitude is shown in Figure 65.

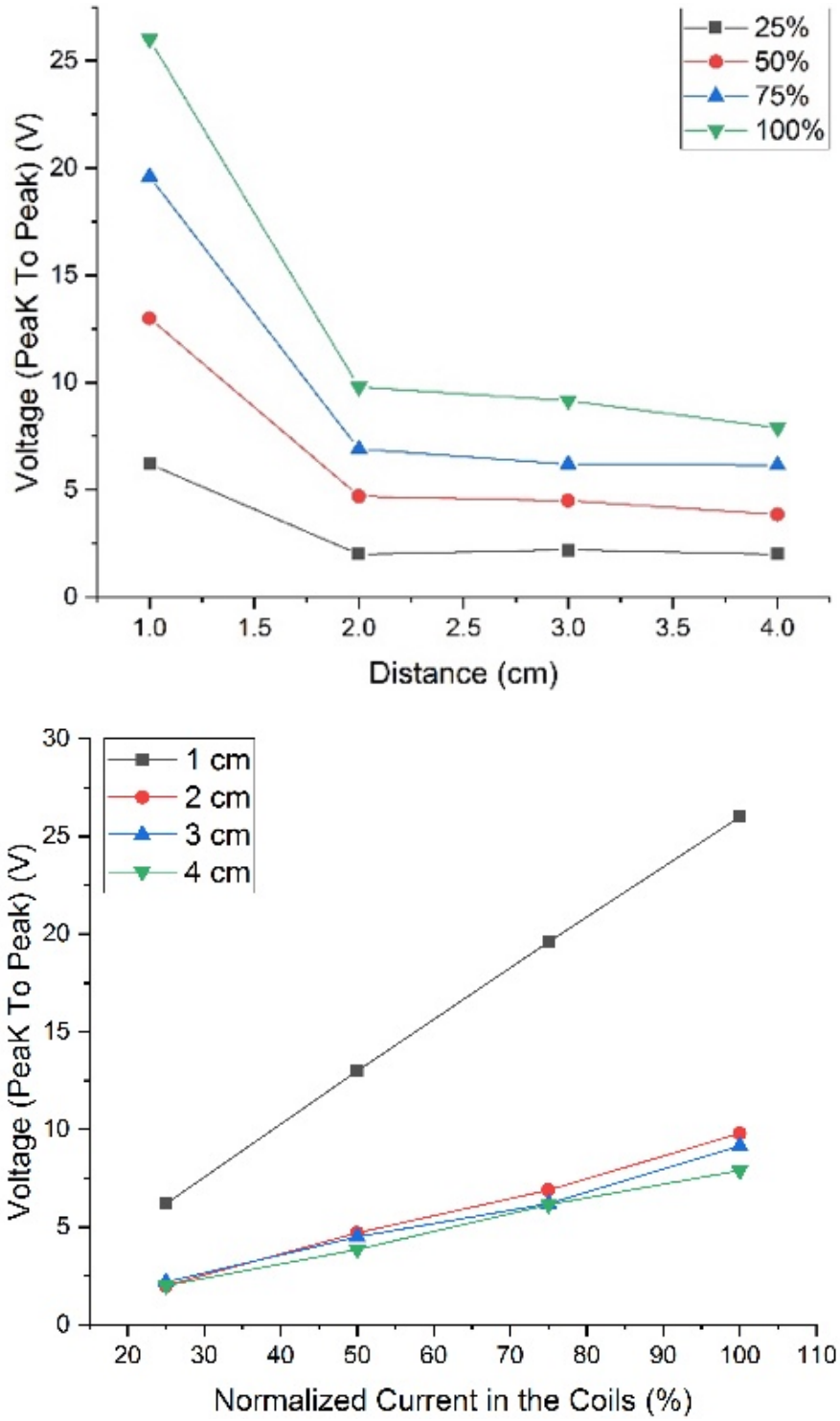

Figure 64 Voltage measurements from the brain phantom with varying distances (1, 2, 3, and 4cm) and TMS coils' intensities (25, 50, 75, and 100%)

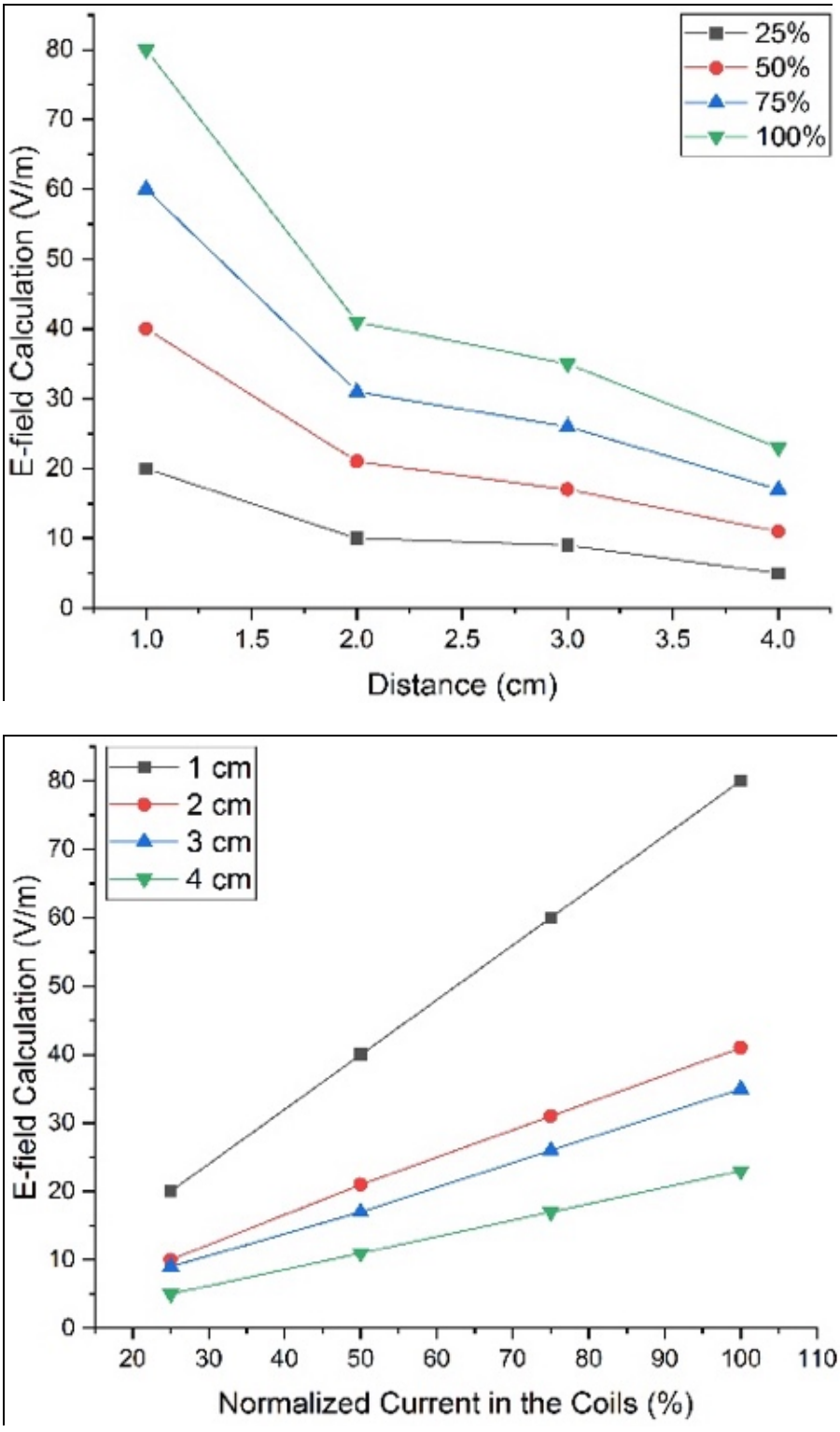

Figure 65 Electric field calculation from sim4life on the brain model for varied distances (1, 2, 3, and 4cm) and TMS coils' intensities (25, 50, 75, and 100%)

Comparing Figure 64 between Figure 65, measurements, and simulation, it can be seen that there is similar overall behavior. The voltage measurements and e-field readings are linearly dependent on intensity in both figures. Also, the induced voltage decreases rapidly with the distance. However, the gap between the 1cm and 2cm is larger in the experimental results than it is in the simulation. This can be due to the complexity of the experimental setup. For example, there could be some discontinuities within the phantom due to the tear in the polymer caused by the repeated probe insertion. Also, the magnetic field is sensitive to the distance from the source; therefore, there might be a slight difference between the intended and the actual distances from the probes to the coils. As stated above that the purpose of the study is just to demonstrate that the brain phantom, since it is electrically conductive, can be stimulated. The presented figures indeed show that the phantom is responsive. Finally, even though the phantom is fabricated to be globally homogenous but, there could be some local inhomogeneity within the phantom that result in slightly deviated voltage readings.

4.3.2 Magnetic field measurements

As mentioned in the materials and methods section of this chapter, the Gaussmeter used to acquire the magnetic field flux measurements has a pulse mode that captures the positive and negative peaks of the recorded signal. In Figure 66 we present the averaged magnitude of the two peaks. Figure 66 shows the measurement profile of magnetic flux density along the centerline of the TMS coils. The highest magnitude of magnetic induction is seen at the center of each coil that reaches up to 0.77 T, where the region between the two coils has about 0.43 T.

For better visualization of the instantaneous magnetic field flux density, we need to consider the polarity of each coil. For that reason and because we know that the current running in each coil of the figure-of-eight coil is opposite to the other, the magnetic flux must follow the polarity and directionality. We assumed that the polarity of one of the coils is opposite to the other one, as we can see in Figure 67 and Figure 68.

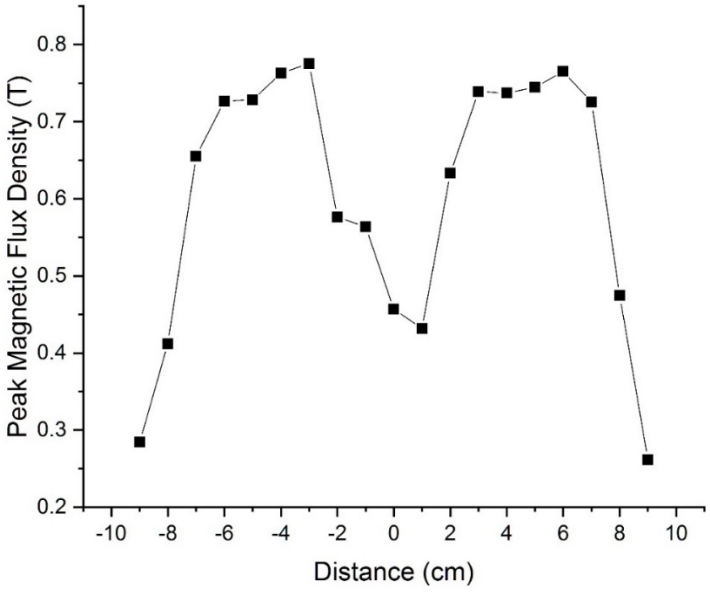

Figure 66 Peak magnetic flux density profile at the center of the XY-plane along the surface of the Magstim rapid TMS coils

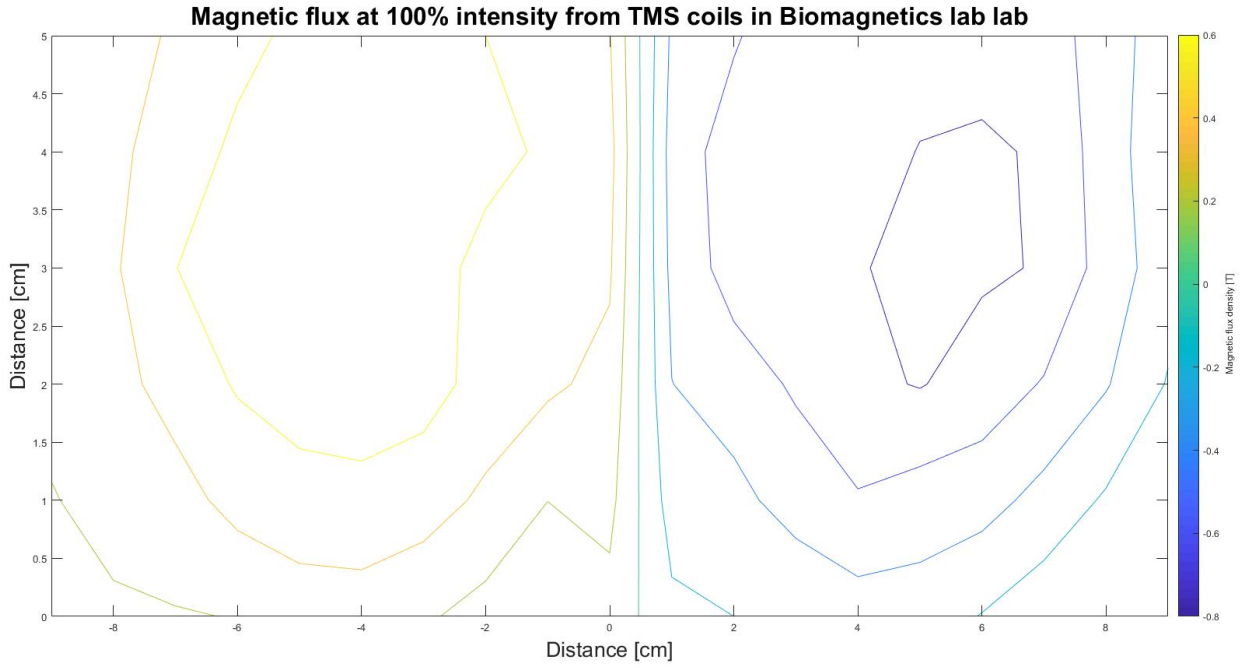

Figure 67 Contour of the magnetic flux density from at the surface of the TMS coils with consideration of the polarity

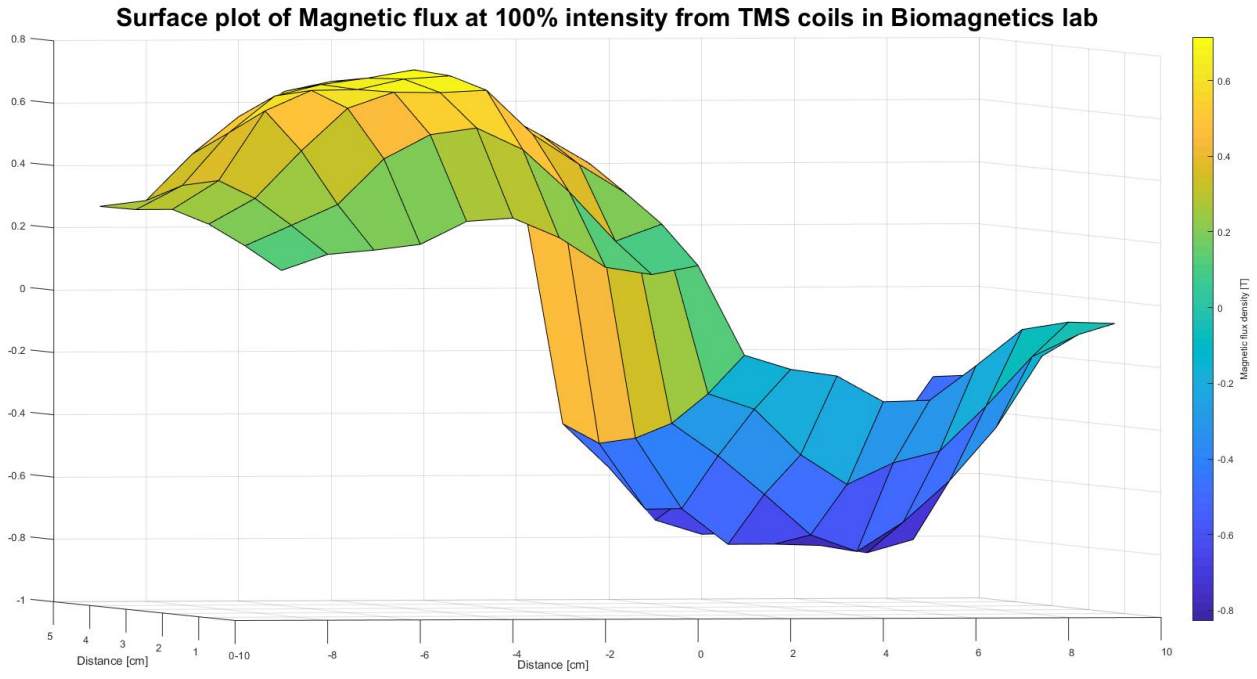

Figure 68 Magnetic flux density on the surface of the TMS coils with consideration of the polarity

4.3.3 Electric field measurements in air

In order to map the electric field on the surface of the coil, we need to measure the voltages and then map and reconstruct the electric field. The electric field is the first spatial derivative of the voltage. In the TMS, the current is running in the coils follows a sine wave. The magnetic field generated will follow the same wave function. However, the time varying magnetic field, according to Maxwell-Faraday's law, will induce an electric field which is a cosine wave. We confirm this in Figure 69. We can notice the waveform is not symmetrical, and it appears that the TMS produces a damped cosine wave. For that reason, whenever we want to determine the magnitude of the voltage, we take the averaged peak value.

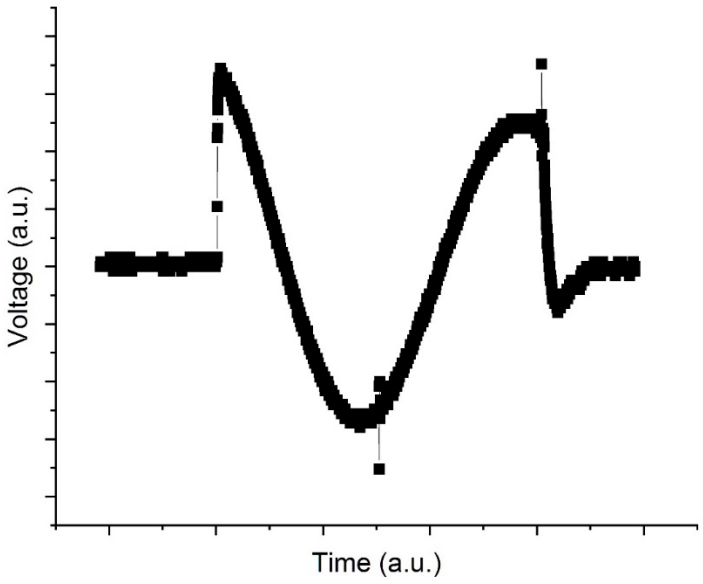

Figure 69 Bi-phasic voltage induced by the time-varying magnetic field of the TMS coils

Figure 68 shows the voltages measured on the surface of the TMS coils. We can see that the voltage magnitude follows the pattern seen in the measured magnetic flux density, where the highest voltage magnitudes are produced in the center of each coil. However, the voltages' values are graphed without the consideration of the polarity difference between the coils, therefore, would result in a wrong reconstruction of the electric field, as in Figure 71. We realized that mapping the

electric field is not correct because the essential purpose of the figure of eight coils design is to produce a high electric field magnitude (hot spot) in the region in between the coils. What we see in this figure is that the electric field is following an opposite behavior as it is showing a rather cold spot in that region. This dictated that we had to consider the polarity of the voltages measured as we did with the magnetic flux density. Figure 72 shows the voltages as the polarity difference between the coils were considered. This is confirmed from the literature as by Meng et al. (2018), where they show a voltage polarity in their measurement of the voltages and electric field produced by TMS coils [100]. Now the electric field with the consideration of the polarity is mapped in Figure 73. The figure shows clearly that the electric field is highest in the center regions between the coils as expected. The magnitude of the electric field in the center reaches up to 600 V/m for 100% power rating of the stimulator (5000A).

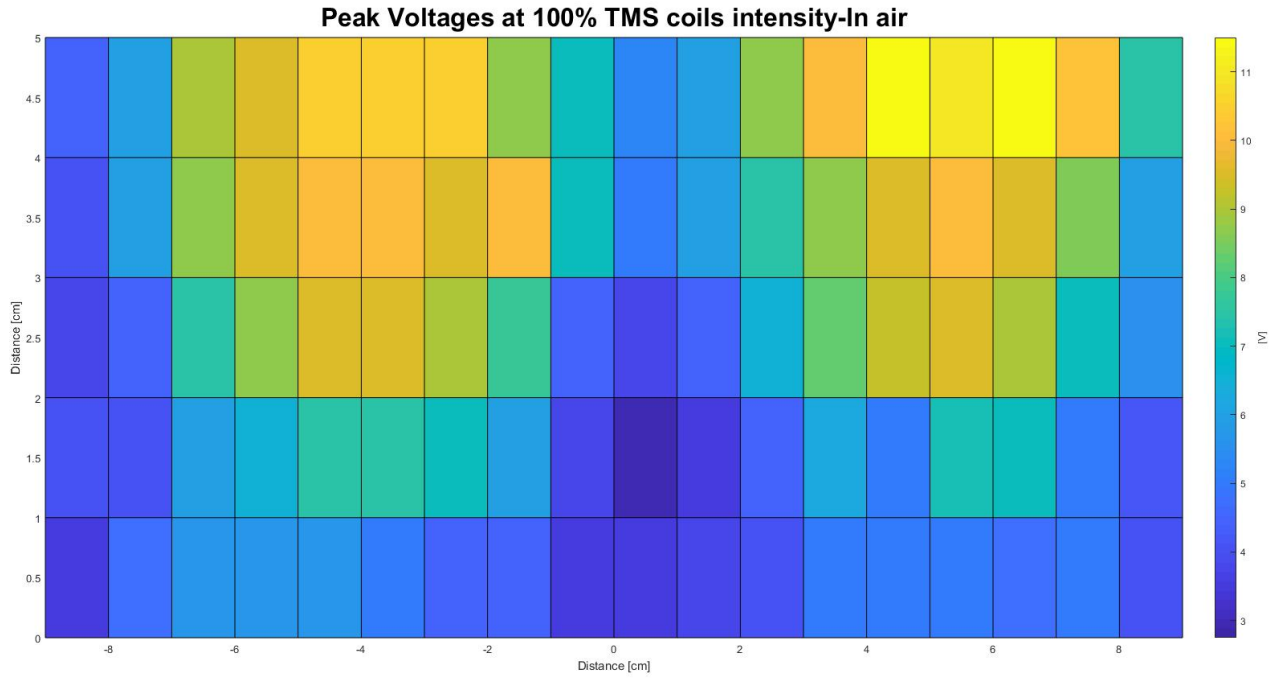

Figure 70 Voltage measurements of the TMS coils on the XY-plane and z=0. The TMS coils set on 100% intensity, with no consideration of the polarity.

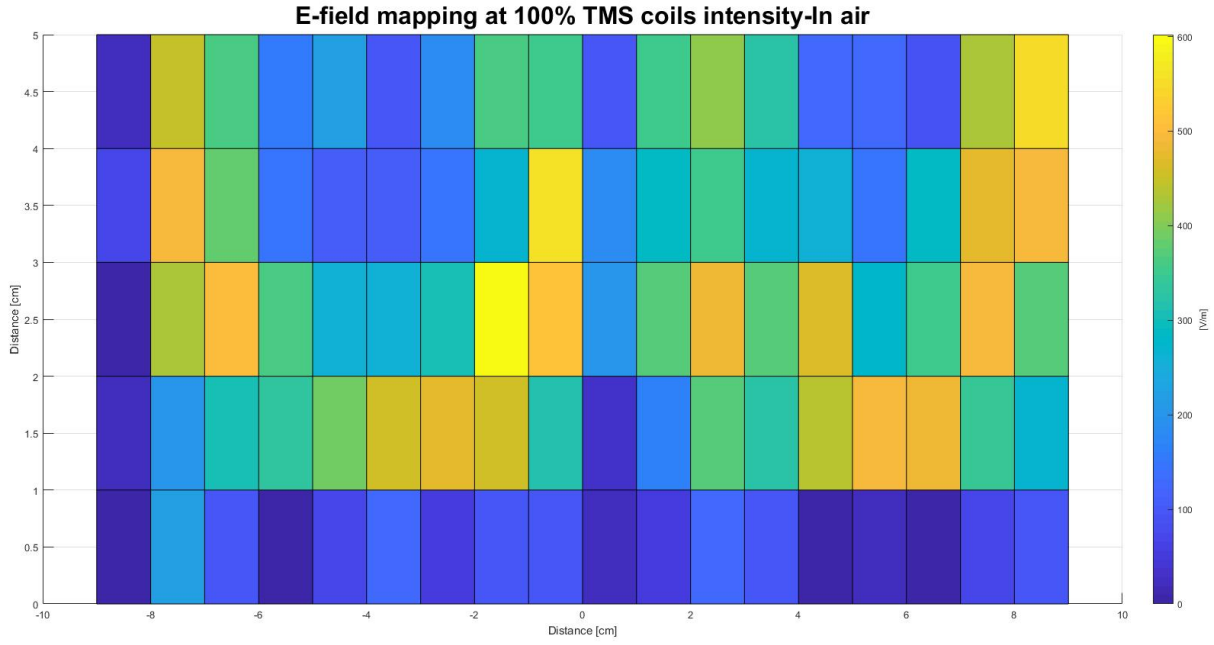

Figure 71 Electric field mapping from the Voltage measurements of the TMS coils on the XY-plane and z=0. The TMS coils set on 100% intensity, with no consideration of the polarity.

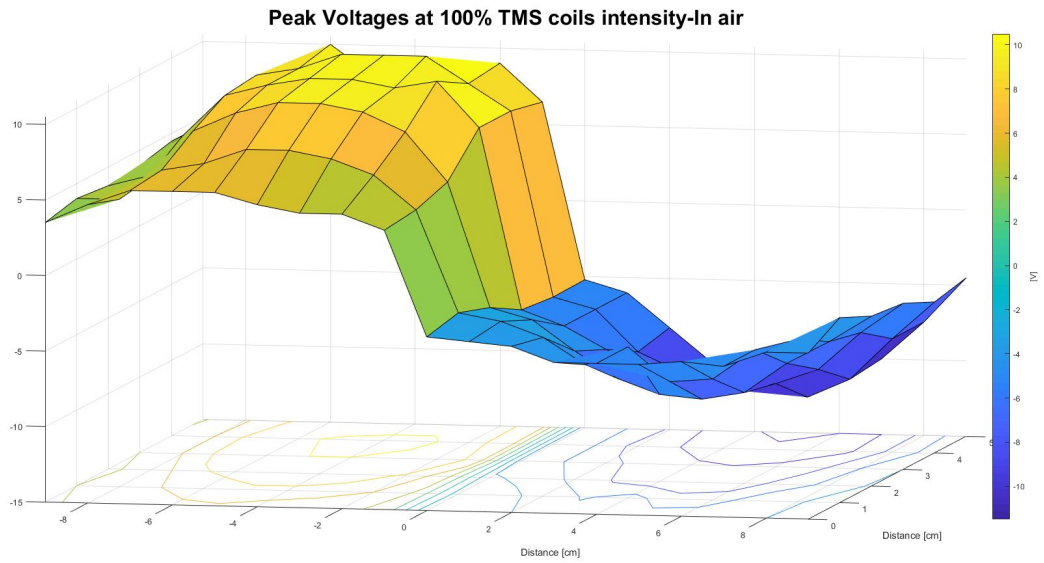

Figure 72 Surface view of the Voltage measurements and contour projection of the TMS coils on the XY-plane and z=0. The TMS coils set on 100% intensity, with consideration of the polarity.

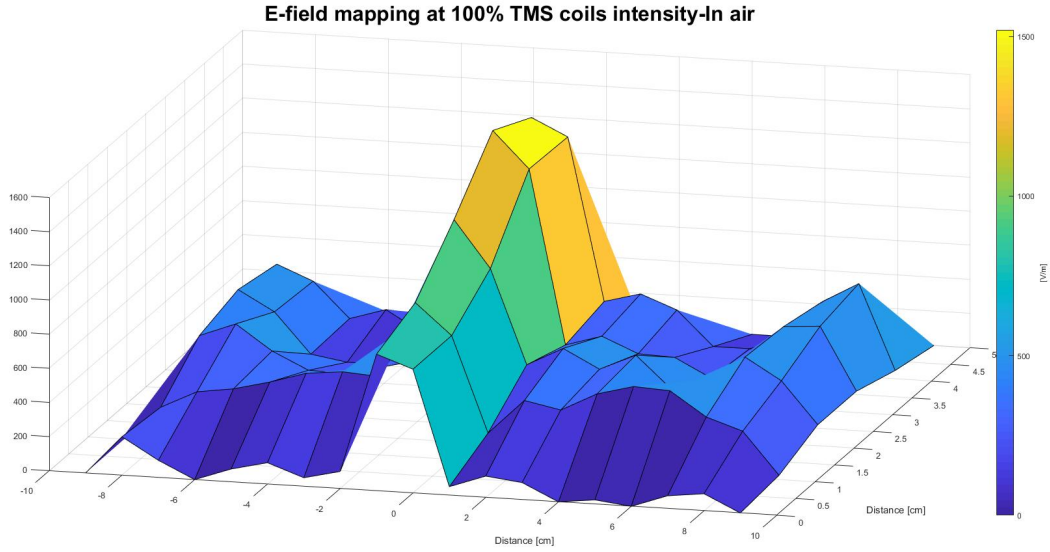

Figure 73 Surface view of the electric field mapping from the voltage measurements of the TMS coils on the XY-plane and z=0. The TMS coils set on 100% intensity, with consideration of the polarity.

4.3.4 Electric field measurement on the conductive sheet

In this section, the voltage measurement and electric field mapping from the conductive sheet is presented. We applied the same polarity consideration here. The resulted measured

voltages are shown in Figure 74 and the corresponding electric field mapped is shown in Figure 75. We can notice that the electric field has the highest magnitude in the middle that extends up to 30,000 V/m, and the voltages measured reach up to 150 V. The typical values of the electric field seen in the FEM simulation range between (100-300 V/m). The high electric field when measured on the conductive sheet can be attributed to many factors. First, the distance in which the measurement was carried out was close to the surface of the coils, which might exponentially increase the induction with respect to the distance. The FEM simulation considers the distance between the coils and the brain surface, which is around 2-3 cm. Therefore, the magnitude of the electric field should fall steeply as the distance increases. Second, since we measured the voltages from a material that is relativity low in electrical conductivity, there could be a stronger and dominant influence from other properties of the material in which the measurements are carried on. The electric permittivity of the material could be a significant contributor to the measured voltage. Even though Porzig et al. (2013) show that when considering the effects of polarization in biological tissues, the polarization current increases to high magnitudes but then attenuates rapidly when compared to the induced conduction currents [108]. It could be the case that even though the polarization currents were very brief, they were captured in the measurements and therefore amplified the induced voltages. On the other hand, there could also be a perturbation and distortion of the electric field when the oscilloscope probes are inserted in the conductive sheet resulting in faulty readings of the voltages and, therefore, incorrect mapping of the electric field.

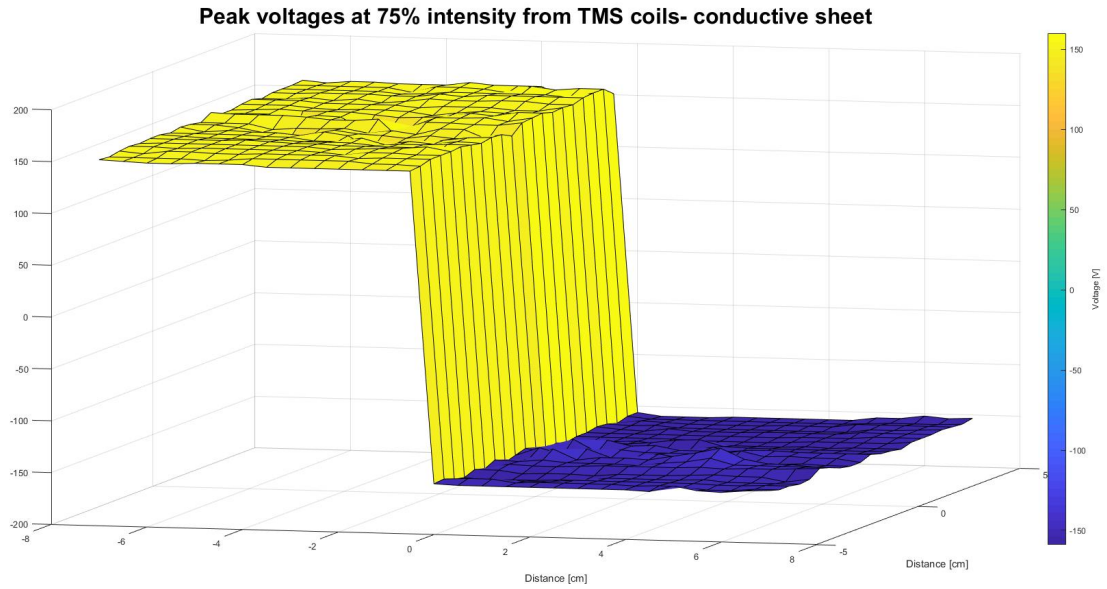

Figure 74 Surface view of the voltage measurements and the TMS coils on the conductive sheet. The TMS coils set on 75% intensity, with consideration of the polarity.

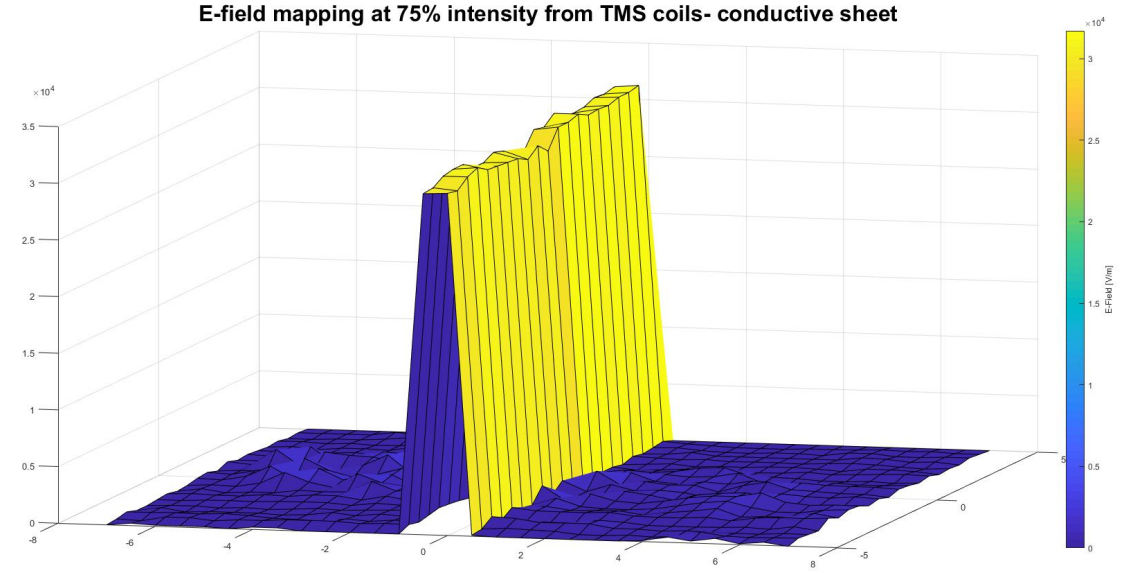

Figure 75 Electric field mapping from the voltage measurements of the TMS coils on the conductive sheet. The TMS coils set on 75% intensity, with consideration of the polarity.

4.3.5 Electric field measurements on the brain phantom (M1 area)

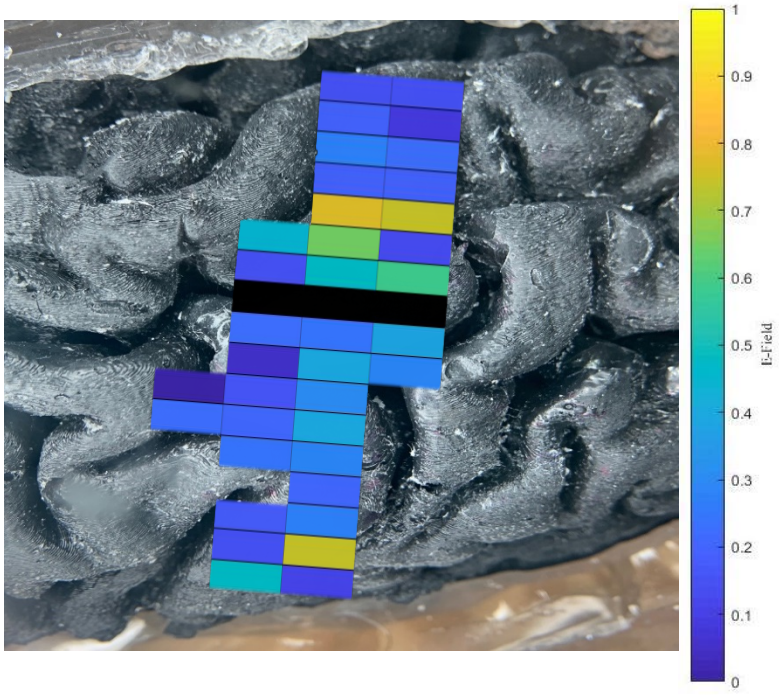

Figure 76 Normalized electric field mapping from the voltage measurements of the TMS coils on the Brian phantom. The TMS coils set on 75% intensity, with no consideration of the polarity.

Since the electric field magnitudes measured are very high, we thought to examine the electric field distribution on the brain phantom regardless of the actual magnitudes. In Figure 76, we can see that the electric field distribution does not follow a recognizable pattern. There are several reasons for that. The first influence comes from the fact that the geometry of the conductor determines the measured electric field. The measurements could be highly distorted to the point where the variation in the potential is lost, and as a result, the electric field reconstruction is incorrect. Many researchers attempted to capture and measure the electric field without distorting the electric field. This group [109], for example, shows the process and development of such devices utilized to detect the electric field in the air without distortion. There is a need to develop

such devices in TMS field, especially with the emergence of physical models and phantoms of the brain.

4.4 Conclusion:

In this chapter, we demonstrated that the brain phantom with the assigned conductivity is responsive to an external alternating magnetic field. The phantom showed a recognizable induction of voltages when stimulated by the TMS coils. We ultimately attempted to reconstruct and map the electric field on the brain phantom. Given the fact that the electric field mapping on a complex geometry is a challenging one, we broke down the work on four main tasks. First, we measured the magnetic field flux density produced by the TMS coils. We detected strength of about 0.8 Tesla at the highest peak right at the center of the coils. Second, we mapped the electric field on the surface of the coils (on air) by measuring the induced voltages. The voltages induced showed a behavior similar to the magnetic field. Right at the center of the TMS figure-of-eight coils, we detected the highest spatial variation of the voltages, which directly indicated the presence of the focal and hot spot of the electric field produced by coils. Third, we mapped the electric field on a conductive sheet that has the same conductivity as the brain phantom. The magnitude of the electric field on the conductive sheet was very high (up to $3x10^4$ V/m), which is two orders of magnitudes higher than the electric field measured on the surface of the coils (on air). Fourth and last, we mapped the electric field on the surface of the M1 area of the phantom. The results showed a distorted electric field pattern with very high magnitudes. There is an interference between the electric field induced on the conductive polymer and the oscilloscope probe. Also, there could be charges accumulation on the contact point of measurements that resulted in high spiked in the voltages and, in turn, result in distorted mapping to the electric field. We concluded that such a task is very challenging, and a much better understanding of the theoretical background of the

measurement theory of the electric field in composite polymer media, such as PDMS-CNT, is needed.

5 Conclusions, contributions, and future work recommendations

This thesis's main focus was to overcome what was seemingly an insurmountable task, creating a physical model that emulates anatomy and the electrical conductivity of the brain. We presented a novel manufacturing method capable of producing geometries complex and intricate like the brain with an imparted electrical conductivity. We used the innovative method that we call "shelling method," where we used 3D printers to prints molds of the brain based on reconstructed models of MRI images. We developed a conductive polymer with tunable conductivity to be cast into the 3D printed shells. We established a conductivity vs. filler/composite wt% chart to serve as a reference for any desired or targeted conductivity that reach up to 8 S/m. The shelling method that we developed now protected by a pending patent.

We further developed the phantom to include the head and the CSF. It is an important step. It leads to a more reliable representation of the physical environment for the experimentations and measurements because it has been demonstrated in the literature that the CSF has a significant impact on the induced electric field on the GM.

There are many potentials applications of the manufacturing process of the brain phantom and the fabrication of the conductive polymer. Our brain phantom is primarily designed to mimic the conductivity of the brain. However, the relative permittivity of the real brain can reach up to 70. Even though the impact of the brain's dielectric property might be minimal at low frequencies, it still could be considered in the future development of the brain phantom where the conductivity and the permittivity are tuned to account for both conduction and polarization effects.

Moreover, mapping the electric field on the brain phantom would be the next major and essential step towards a complete understanding of the brain's stimulation effects. Such a task is

non-trivial because the very act of measurement of the electric field using conductive probes will distort and perturb the electric field, especially on a complex geometry like the brain and the externally application alternating magnetic field. Researchers recently developed a non-distortion electric field microelectromechanical (MEMS) sensor for applications like high-voltage power or atmospheric electrostatic electric field mapping [109]. Similar sensors or probes are needed to be incorporated in the brain phantom's future development and for measurement of the electric field. With further development of the measurement theory on such anatomical phantoms, one can correlate and verify those measurements using TMS simulation similar to recent work on the transcranial direct current stimulation (tDCS) [110–112]. Furthermore, the phantom can further be developed for other brain stimulation techniques such as tDCS. In such a case, the manufacturing process needs to account for skin conductivity.

We used the brain, and the head phantom to experimentally study the safety of combining two brain stimulations treatments, TMS and DBS. The brain and head phantom was utilized to account for the DBS probe inside the brain phantom to replicate the DBS's real surgical configuration. Based on preceding work in this subject, we attempted to represent the problem most realistically and simplistically. For instance, we used simple configuration to the DBS probe with only one winding and simple and accurate circuital components like the impedance of the brain and internal pulse generator of the DBS. We measured the currents induced on the leads, and we concluded that the current magnitudes were in the unsafe limits when the TMS is operated on the maximum intensity and right on top of the DBS windings.

This study can be extended to consider further the IPG location inside a chest pocket with the inclusion of mimicked resistivity of the entire path between the IPG and the DBS leads inside the brain. With the proper replication of such a problem, we can even introduce possible solutions

to minimize the induced and unintended currents and, therefore, make it possible to combine the two treatments to benefit the patient who needs such combinatory treatment.

In the last chapter, we ran a series of measurements aiming to understand and evaluate the magnetic and electric fields produced by the commercial figure-of-eight TMS coils. We show that it is imperative to consider each coil's polarity when mapping the magnetic and electric fields. Furthermore, mapping the electric field in the air is a straightforward task compared to electric field mapping in a material like the conductive polymer developed in this thesis. The electric field seems to get distorted without a recognizable pattern in general, except right below the coils. It could have resulted from the interference of the measurement probes with the induced electric field in the material. Therefore, there is a need for a less invasive and no distortive techniques for measuring the electric field in materials like conductive polymers.

6 Publications based on this thesis work:

6.1 Peer-reviewed journals publications

[1] Safety Study of Combination Treatment: Deep Brain Stimulation and Transcranial Magnetic Stimulation

Magsood, H., Syeda, F., Holloway, K., Carmona, I.C. and Hadimani, R.L., 2020. Safety Study of Combination Treatment: Deep Brain Stimulation and Transcranial Magnetic Stimulation. Frontiers in Human Neuroscience, 14, p.123.

[2] Effect of anatomical variability in brain on transcranial magnetic stimulation treatment

Syeda. F, **Magsood. H**, Lee, E. G., El-Gendy, A. A., Jiles, D. C., & Hadimani, R. L. (2017). "Effect of anatomical variability in brain on transcranial magnetic stimulation treatment". AIP Advances, 7(5), 056711.

[3] [Under review] Development of Brain Phantoms for Experimental Verification of Stimulation Strengths during TMS

H. Magsood, R. L. Hadimani" Development of Anatomically Accurate Brain Phantoms for Experimental Verification of Stimulation Strengths during TMS", Material science and Engineering: C. submitted Feb 2019.

6.2 Patent (Pending)

Hamzah Magsood, Ciro Serrate, Ahmed El-Gendy, Ravi Hadimani, "ANATOMICALLY ACCURATE BRAIN PHANTOMS AND METHODS FOR MAKING AND USING THE SAME", Declared for patent application on Aug 2018, US20190057623A1.

6.3 International Conference Presentations based on this thesis:

1. **H. Magsood**, R. L. Hadimani, "Development of a procedure for experimental mapping of electric field induced by TMS in an anatomically accurate brain phantom" **MMM 2019**, Las Vegas, November 2019.
2. **H. Magsood**, F. Syeda, and R. L. Hadimani, "Anatomically Accurate Brain Phantom for Transcranial Magnetic Stimulation" **IEEE EMBS Neural Engineering**, San Francisco, March 2019.
3. **H. Magsood**, A. Elgendy, and R. L. Hadimani, "Experimental Verification of Transcranial Magnetic Stimulation Using Newly Developed Brain Phantom," **APS March Meeting**, Los Angeles, March 2018.
4. **H. Magsood**, F. Syeda and R. L. Hadimani "Experimental Verification of Transcranial Magnetic Stimulation Using Anatomically Accurate Brain Phantom," **INTERMAG 2018**, Singapore, Jan. 2018
5. F. Syeda, C. H. Serrate, **H. Magsood**, K. Holloway and R. L. Hadimani, "Simulation of Cortical Transcranial Magnetic Stimulation in Motor Pathway for Treatment of Parkinson's Disease" **INTERMAG 2018**, Singapore, Jan. 2018.

6. F. Syeda, **H. Magsood**, E. Lee, A. El-Gendy, D. Jiles, and R. Hadimani, "Effect of Anatomical Variability in Brain on Transcranial Magnetic Stimulation Treatment," **American Physical Society SEAPS**, November 10-12, 2016.
7. F. Syeda, **H. Magsood**, E. Lee, A. El-Gendy, D. Jiles, and R. L. Hadimani, "Effect of Parkinson's Disease in Transcranial Magnetic Stimulation Treatment" **American Physical Society March Meeting**, New Orleans, March 13-17, 2017.
8. F. Syeda, **Hamzah Magsood**, E. G. Lee, D. C. Jiles, P. Rastogi, R. L. Hadimani, "Effect of Varying MRI Data on Volume Stimulated in Brain during Transcranial Magnetic Stimulation" **61st MMM,** New Orleans, USA, November 2016.

7 References:

[1] N. National Institute Of Mental Illness, Mental Illness, (n.d.). https://www.nimh.nih.gov/health/statistics/mental-illness.shtml.

[2] A. Alzheimer Association, Alzheimer disease, (n.d.). https://www.alz.org/alzheimers-dementia/facts-figures.

[3] N. National Institute of Neurological Disorders and Stroke, Parkinson's Disease, (n.d.). https://report.nih.gov/nihfactsheets/ViewFactSheet.aspx?csid=109.

[4] S. Science daily, Rapid growth in neuroscience research, (n.d.). https://www.sciencedaily.com/releases/2017/04/170420093736.htm.

[5] M.S. George, S.H. Lisanby, D. Avery, W.M. McDonald, V. Durkalski, M. Pavlicova, B. Anderson, Z. Nahas, P. Bulow, P. Zarkowski, P.E. Holtzheimer, T. Schwartz, H.A. Sackeim, Daily Left Prefrontal Transcranial Magnetic Stimulation Therapy for Major Depressive Disorder, Arch. Gen. Psychiatry. 67 (2010) 507. https://doi.org/10.1001/archgenpsychiatry.2010.46.

[6] D.W. Dodick, C.T. Schembri, M. Helmuth, S.K. Aurora, Transcranial magnetic stimulation for migraine: A safety review, Headache. 50 (2010) 1153–1163. https://doi.org/10.1111/j.1526-4610.2010.01697.x.

[7] USFDA, Press Announcements - FDA permits marketing of transcranial magnetic stimulation for treatment of obsessive compulsive disorder, U.S. Foood Drugs. (n.d.). https://www.fda.gov/newsevents/newsroom/pressannouncements/ucm617244.htm (accessed January 28, 2019).

[8] F. Fregni, D.K. Simon, A. Wu, A. Pascual-Leone, Non-invasive brain stimulation for Parkinson's disease: A systematic review and meta-analysis of the literature, J. Neurol. Neurosurg. Psychiatry. 76 (2005) 1614–1623. https://doi.org/10.1136/jnnp.2005.069849.

[9] D. Georgiev, F. Lange, C. Seer, B. Kopp, M. Jahanshahi, Movement-related potentials in Parkinson's disease, Clin. Neurophysiol. 127 (2016) 2509–2519. https://doi.org/10.1016/j.clinph.2016.04.004.

[10] W.Y. Hsu, Y. Ku, T.P. Zanto, A. Gazzaley, Effects of noninvasive brain stimulation on cognitive function in healthy aging and Alzheimer's disease: A systematic review and meta-analysis, Neurobiol. Aging. 36 (2015) 2348–2359. https://doi.org/10.1016/j.neurobiolaging.2015.04.016.

[11] L.G. Richards, K.C. Stewart, M.L. Woodbury, C. Senesac, J.H. Cauraugh, Movement-dependent stroke recovery: A systematic review and meta-analysis of TMS and fMRI evidence, Neuropsychologia. 46 (2008) 3–11. https://doi.org/10.1016/j.neuropsychologia.2007.08.013.

[12] T. Swiontek, C. Kurakami, Magnetically Induced Current Density in Saline and, (1989) 1167–1168.

[13] K. Yunokuchi, R. Koyoshi, G. Wang, T. Yoshino, Y. Tamari, H. Hosaka, M. Saito, Estimation of focus of electric field in an inhomogeneous medium exposed by pulsed magnetic field, Conf Proc IEEE Eng Med Biol Soc. 1 (1999) 467. https://doi.org/10.1109/IEMBS.1999.802545.

[14] Y. Shimojima, H. Morita, N. Nishikawa, M. Kodaira, T. Hashimoto, S. ichi Ikeda, The safety of transcranial magnetic stimulation with deep brain stimulation instruments, Park.

Relat. Disord. 16 (2010) 127–131. https://doi.org/10.1016/j.parkreldis.2009.09.006.

[15] A. Thielscher, A. Opitz, M. Windhoff, Impact of the gyral geometry on the electric field induced by transcranial magnetic stimulation, Neuroimage. 54 (2011) 234–243. https://doi.org/10.1016/j.neuroimage.2010.07.061.

[16] A. Opitz, M. Windhoff, R.M. Heidemann, R. Turner, A. Thielscher, How the brain tissue shapes the electric field induced by transcranial magnetic stimulation, Neuroimage. 58 (2011) 849–859. https://doi.org/10.1016/j.neuroimage.2011.06.069.

[17] T. Wagner, M. Gangitano, R. Romero, H. Théoret, M. Kobayashi, D. Anschel, J. Ives, N. Cuffin, D. Schomer, A. Pascual-Leone, Intracranial measurement of current densities induced by transcranial magnetic stimulation in the human brain, Neurosci. Lett. 354 (2004) 91–94. https://doi.org/10.1016/S0304-3940(03)00861-9.

[18] J.O. Nieminen, L.M. Koponen, R.J. Ilmoniemi, Experimental characterization of the electric field distribution induced by TMS devices, Brain Stimul. 8 (2015) 582–589. https://doi.org/10.1016/j.brs.2015.01.004.

[19] K. Miller, Biomechanics of the brain, 2011. https://doi.org/10.1007/978-1-4419-9997-9.

[20] Mayfield Brain & Spine, (n.d.). https://mayfieldclinic.com/pe-anatbrain.htm.

[21] S. Gabriel, R.W. Lau, C. Gabriel, The dielectric properties of biological tissues: III. Parametric models for the dielectric spectrum of tissues., Phys. Med. Biol. 41 (1996) 2271–93. https://doi.org/10.1088/0031-9155/41/11/003.

[22] A. Peyman, A.A. Rezazadeh, C. Gabriel, S. Gabriel, R.W. Lau, The dielectric properties of biological tissues: I. Literature survey Dielectric properties of rat tissue as a function of age

The dielectric properties of biological tissues: III. Parametric models for the dielectric spectrum of tissues, Phys. Med. Biol. 41 (1996). http://iopscience.iop.org/0031-9155/41/11/001 (accessed February 24, 2017).

[23] E.A. Rashed, J. Gomez-Tames, A. Hirata, Deep Learning-Based Development of Personalized Human Head Model with Non-Uniform Conductivity for Brain Stimulation, IEEE Trans. Med. Imaging. (2020) 1–1. https://doi.org/10.1109/tmi.2020.2969682.

[24] S. Gabriel, R.W. Lau, C. Gabriel, The dielectric properties of biological tissues: {II}. {M}easurements in the frequency range 10 {H}z to 20 {GH}z, Phys Med Biol. 41 (1996) 2251–2269.

[25] J.A. Latikka, J.A. Hyttinen, T.A. Kuurne, H.J. Eskola, J.A. Malmivuo, The conductivity of brain tissues: Comparison of results in vivo and in vitro measurements, Annu. Reports Res. React. Institute, Kyoto Univ. 1 (2001) 910–912. https://doi.org/10.1109/IEMBS.2001.1019092.

[26] N.K. Logothetis, C. Kayser, A. Oeltermann, In Vivo Measurement of Cortical Impedance Spectrum in Monkeys: Implications for Signal Propagation, Neuron. 55 (2007) 809–823. https://doi.org/10.1016/j.neuron.2007.07.027.

[27] C. Gabriel, A. Peyman, E.H. Grant, Electrical conductivity of tissue at frequencies below 1 MHz, Phys. Med. Biol. 54 (2009) 4863–4878. https://doi.org/10.1088/0031-9155/54/16/002.

[28] M.A. Kandadai, J.L. Raymond, G.J. Shaw, Comparison of electrical conductivities of various brain phantom gels: Developing a “brain gel model,” Mater. Sci. Eng. C. 32 (2012) 2664–2667. https://doi.org/10.1016/j.msec.2012.07.024.

[29] M. Akhtari, D. Emin, B.M. Ellingson, D. Woodworth, A. Frew, G.W. Mathern, Measuring the local electrical conductivity of human brain tissue, J. Appl. Phys. 119 (2016). https://doi.org/10.1063/1.4941556.

[30] E. Michel, D. Hernandez, S.Y. Lee, Electrical conductivity and permittivity maps of brain tissues derived from water content based on T1-weighted acquisition, Magn. Reson. Med. 77 (2017) 1094–1103. https://doi.org/10.1002/mrm.26193.

[31] H. McCann, G. Pisano, L. Beltrachini, Variation in Reported Human Head Tissue Electrical Conductivity Values, Springer US, 2019. https://doi.org/10.1007/s10548-019-00710-2.

[32] M. Arjmand, S. Sadeghi, Nitrogen-Doped Carbon Nanotube/Polymer Nanocomposites Towards Thermoelectric Applications, Thermoelectr. Power Gener. A Look Trends Technol. (2016) 323.

[33] S. Herculano-Houzel, The human brain in numbers: a linearly scaled-up primate brain, Front. Hum. Neurosci. 3 (2009) 1–11. https://doi.org/10.3389/neuro.09.031.2009.

[34] Neuron, (n.d.). https://simple.wikipedia.org/wiki/Neuron#/media/File:Neuron.svg.

[35] B.P. Bean, The action potential in mammalian central neurons, Nat. Rev. Neurosci. 8 (2007) 451–465. https://doi.org/10.1038/nrn2148.

[36] M. Devices, No Title, (n.d.). https://www.moleculardevices.com/applications/patch-clamp-electrophysiology/what-action-potential#gref.

[37] H.R. Siebner, G. Hartwigsen, T. Kassuba, J.C. Rothwell, How does transcranial magnetic stimulation modify neuronal activity in the brain? Implications for studies of cognition, Cortex. 45 (2009) 1035–1042. https://doi.org/10.1016/j.cortex.2009.02.007.

[38] P.I. Petrov, S. Mandija, I.E.C. Sommer, C.A.T. Van Den Berg, S.F.W. Neggers, How much detail is needed in modeling a transcranial magnetic stimulation figure-8 coil: Measurements and brain simulations, PLoS One. 12 (2017) 1–20. https://doi.org/10.1371/journal.pone.0178952.

[39] R.J. Ilmoniemi, J. Ruohonen, J. Karhu, Transcranial magnetic stimulation - A new tool for functional imaging of the brain, Crit. Rev. Biomed. Eng. 27 (1999) 241–284.

[40] M.S. George, R.H. Belmaker, Transcranial magnetic stimulation in clinical psychiatry, American Psychiatric Pub, 2007.

[41] M. Kobayashi, A. Pascual-Leone, Transcranial magnetic stimulation in neurology, Lancet. 2 (2003) 145–156.

[42] E.M. Wassermann, S.H. Lisanby, Therapeutic application of repetitive transcranial magnetic stimulation: a review, Clin. Neurophysiol. 112 (2001) 1367–1377. https://doi.org/10.1016/S1388-2457(01)00585-5.

[43] S.H. Lisanby, B. Luber, T. Perera, H. a. Sackeim, Transcranial magnetic stimulation: applications in basic neuroscience and neuropsychopharmacology., Int. J. Neuropsychopharmacol. 3 (2000) 259–273. https://doi.org/10.1017/S1461145700002005.

[44] P.M. Rossini, S. Rossi, Transcranial magnetic stimulation Diagnostic, therapeutic, and research potential, Neurology. 68 (2007) 484–488.

[45] Johons Hopkins medicine, Brian stimulation, (2019). https://www.hopkinsmedicine.org/psychiatry/specialty_areas/brain_stimulation/tms/faq_tms.html.

[46] Transcranial Magnetic Stimulation for Depression - Review of the Evidence, (n.d.). https://psychscenehub.com/psychinsights/transcranial-magnetic-stimulation-for-depression/ (accessed February 21, 2019).

[47] A. Rotenberg, J.C. Horvath, A. Pascual-Leone, Transcranial Magnetic Stimulation, Neuromethods, vol. 89, 2014. https://doi.org/10.1007 /978-1-4939-0879-0.

[48] T. Wagner, A. Valero-Cabre, A. Pascual-Leone, Noninvasive Human Brain Stimulation, Annu. Rev. Biomed. Eng. 9 (2007) 527–565. https://doi.org/10.1146/annurev.bioeng.9.061206.133100.

[49] C.M. Epstein, R. Michelucci, M. Hallett, Neupsy Key, (2020). https://neupsykey.com/transcranial-magnetic-stimulation/#F2-88.

[50] R. Plonsey, D.B. Heppner, Considerations of quasi-stationarity in electrophysiological systems, Bull. Math. Biophys. 29 (1967) 657–664. https://doi.org/10.1007/BF02476917.

[51] L. Heller, D.B. van Hulsteyn, Brain stimulation using electromagnetic sources: theoretical aspects, Biophys. J. 63 (1992) 129–138. https://doi.org/10.1016/S0006-3495(92)81587-4.

[52] F.-M. Chen, X. Liu, P. Polym, S. Author, Advancing biomaterials of human origin for tissue engineering HHS Public Access Author manuscript, Prog Polym Sci. 53 (2016) 86–168. https://doi.org/10.1016/j.progpolymsci.2015.02.004.

[53] J.J. Green, J.H. Elisseeff, Mimicking biological functionality with polymers for biomedical applications, Nature. 540 (2016) 386–394. https://doi.org/10.1038/nature21005.

[54] F. Guala, Models, Simulations, and Experiments, Model. Reason. (2011) 59–74. https://doi.org/10.1007/978-1-4615-0605-8_4.

[55] H. Magsood, C.H.A. Serrate, A.A. El-Gendy, M.R.L. Hadimani, Anatomically accurate brain phantoms and methods for making and using the same, US Pat. US20190057623A1. (2019). https://patents.google.com/patent/US20190057623A1/en.

[56] D. Robinson, The Phantoms of Medical and Health Physics, Med. Phys. 43 (2016) 5264.

[57] B.W. Pogue, M.S. Patterson, Review of tissue simulating phantoms for optical spectroscopy, imaging and dosimetry, J. Biomed. Opt. 11 (2006) 041102. https://doi.org/10.1117/1.2335429.

[58] K.E. Keenan, M. Ainslie, A.J. Barker, M.A. Boss, K.M. Cecil, C. Charles, T.L. Chenevert, L. Clarke, J.L. Evelhoch, P. Finn, D. Gembris, J.L. Gunter, D.L.G. Hill, C.R. Jack, E.F. Jackson, G. Liu, S.E. Russek, S.D. Sharma, M. Steckner, K.F. Stupic, J.D. Trzasko, C. Yuan, J. Zheng, Quantitative magnetic resonance imaging phantoms: A review and the need for a system phantom, Magn. Reson. Med. 79 (2018) 48–61. https://doi.org/10.1002/mrm.26982.

[59] T.D. Ngo, A. Kashani, G. Imbalzano, K.T.Q. Nguyen, D. Hui, Additive manufacturing (3D printing): A review of materials, methods, applications and challenges, Compos. Part B Eng. 143 (2018) 172–196. https://doi.org/10.1016/j.compositesb.2018.02.012.

[60] X. Wang, M. Jiang, Z. Zhou, J. Gou, D. Hui, 3D printing of polymer matrix composites: A review and prospective, Compos. Part B Eng. 110 (2017) 442–458. https://doi.org/10.1016/j.compositesb.2016.11.034.

[61] C. Gabriel, A. Peyman, E.H. Grant, Electrical conductivity of tissue at frequencies below 1 MHz, Phys. Med. Biol. 54 (2009) 4863–4878. https://doi.org/10.1088/0031-9155/54/16/002.

[62] J.N. Coleman, S. Curran, A.B. Dalton, A.P. Davey, B. Mccarthy, W. Blau, R.C. Barklie, Percolation-dominated conductivity in a conjugated-polymer-carbon-nanotube composite, (1998). https://journals.aps.org/prb/pdf/10.1103/PhysRevB.58.R7492 (accessed July 13, 2017).

[63] X. Niu, S. Peng, L. Liu, W. Wen, P. Sheng, Characterizing and patterning of PDMS-based conducting composites, Adv. Mater. 19 (2007) 2682–2686. https://doi.org/10.1002/adma.200602515.

[64] W. Zhang, A.A. Dehghani-Sanij, R.S. Blackburn, Carbon based conductive polymer composites, (2007). https://doi.org/10.1007/s10853-007-1688-5.

[65] A. Saleem, L. Frormann, A. Soever, Fabrication of Extrinsically Conductive Silicone Rubbers with High Elasticity and Analysis of Their Mechanical and Electrical Characteristics, Polymers (Basel). 2 (2010) 200–210. https://doi.org/10.3390/polym2030200.

[66] K.-Y. Chun, Y. Oh, J. Rho, J.-H. Ahn, Y.-J. Kim, H.R. Choi, S. Baik, Highly conductive, printable and stretchable composite films of carbon nanotubes and silver, (2010). https://doi.org/10.1038/NNANO.2010.232.

[67] J. Ozhikandathil, A. Khosla, M. Packirisamy, Electrically Conducting PDMS Nanocomposite Using In Situ Reduction of Gold Nanostructures and Mechanical Stimulation of Carbon Nanotubes and Silver Nanoparticles, ECS J. Solid State Sci. Technol. 4 (2015) S3048–S3052. https://doi.org/10.1149/2.0091510jss.

[68] S. Wu, J. Zhang, R.B. Ladani, A.R. Ravindran, A.P. Mouritz, A.J. Kinloch, C.H. Wang, Novel Electrically Conductive Porous PDMS/Carbon Nanofiber Composites for

Deformable Strain Sensors and Conductors, ACS Appl. Mater. Interfaces. 9 (2017) 14207–14215. https://doi.org/10.1021/acsami.7b00847.

[69] S.S. Hassouneh, L. Yu, A.L. Skov, A.E. Daugaard, Soft and flexible conductive PDMS/MWCNT composites, J. Appl. Polym. Sci. 134 (2017) 1–9. https://doi.org/10.1002/app.44767.

[70] W. Zhang, H. Xiong, S. Wang, M. Li, Y. Gu, Electromagnetic characteristics of carbon nanotube film materials, Chinese J. Aeronaut. 28 (2015) 1245–1254. https://doi.org/10.1016/j.cja.2015.05.002.

[71] M. Weber, M.R. Kamal, Estimation of the volume resistivity of electrically conductive composites, Polym. Compos. (1997). https://doi.org/10.1002/pc.10324.

[72] R.J. Coffey, Deep brain stimulation devices: A brief technical history and review, Artif. Organs. 33 (2009) 208–220. https://doi.org/10.1111/j.1525-1594.2008.00620.x.

[73] J.S. Perlmutter, J.W. Mink, Deep brain stimulation., Annu. Rev. Neurosci. 29 (2006) 229–257. https://doi.org/10.1146/annurev.neuro.29.051605.112824.

[74] R.J. Coffey, Deep Brain Stimulation Devices: A Brief Technical History and Review, Artif. Organs. 33 (2009) 208–220. https://doi.org/10.1111/j.1525-1594.2008.00620.x.

[75] K.R. Chaudhuri, D.G. Healy, A.H. V Schapira, Non-motor symptoms of Parkinson{\textquotesingle}s disease: diagnosis and management, Lancet Neurol. 5 (2006) 235–245. https://doi.org/10.1016/s1474-4422(06)70373-8.

[76] L. Hartelius, P. Svensson, Speech and Swallowing Symptoms Associated with Parkinson's Disease and Multiple Sclerosis: A Survey, Folia Phoniatr. Logop. 46 (1994) 9–17.

https://doi.org/10.1159/000266286.

[77] J. Jankovic, Parkinson's disease: clinical features and diagnosis., J. Neurol. Neurosurg. Psychiatry. 79 (2008) 368–376. https://doi.org/10.1136/jnnp.2007.131045.

[78] S.C. Blank, Speech production: Wernicke, Broca and beyond, Brain. 125 (2002) 1829–1838. https://doi.org/10.1093/brain/awf191.

[79] M.S. George, Z. Nahas, M. Molloy, A.M. Speer, N.C. Oliver, X.-B. Li, G.W. Arana, S.C. Risch, J.C. Ballenger, A controlled trial of daily left prefrontal cortex {TMS} for treating depression, Biol. Psychiatry. 48 (2000) 962–970. https://doi.org/10.1016/s0006-3223(00)01048-9.

[80] A. Pascual-Leone, J. Valls-Solé, E.M. Wassermann, M. Hallett, Responses to rapid-rate transcranial magnetic stimulation of the human motor cortex, Brain. 117 (1994) 847–858. https://doi.org/10.1093/brain/117.4.847.

[81] A. Pascual-Leone, D. Nguyet, L.G. Cohen, J.P. Brasil-Neto, A. Cammarota, M. Hallett, Modulation of muscle responses evoked by transcranial magnetic stimulation during the acquisition of new fine motor skills, J. Neurophysiol. 74 (1995) 1037–1045. https://doi.org/10.1152/jn.1995.74.3.1037.

[82] M.S. George, S.H. Lisanby, H.A. Sackeim, Transcranial Magnetic Stimulation: Applications in Neuropsychiatry, JAMA Psychiatry. 56 (1999) 300–311. https://doi.org/10.1001/archpsyc.56.4.300.

[83] Z.-D. Deng, S.H. Lisanby, A. V Peterchev, Transcranial magnetic stimulation in the presence of deep brain stimulation implants: Induced electrode currents, in: 2010 Annu. Int.

Conf. {IEEE} Eng. Med. Biol., IEEE, 2010. https://doi.org/10.1109/iembs.2010.5625958.

[84] R. Kumar, R. Chen, P. Ashby, Safety of transcranial magnetic stimulation in patients with implanted deep brain stimulators, Mov. Disord. 14 (1999) 157–158. https://doi.org/10.1002/1531-8257(199901)14:1<157::aid-mds1027>3.3.co;2-l.

[85] A.A. Kühn, J. Huebl, Safety of transcranial magnetic stimulation for the newer generation of deep brain stimulators, Parkinsonism Relat. Disord. 17 (2011) 647–648. https://doi.org/10.1016/j.parkreldis.2011.05.007.

[86] U. Hidding, T. Bäumer, H.R. Siebner, C. Demiralay, C. Buhmann, T. Weyh, C. Moll, W. Hamel, A. Münchau, MEP latency shift after implantation of deep brain stimulation systems in the subthalamic nucleus in patients with advanced Parkinson's disease, Mov. Disord. 21 (2006) 1471–1476. https://doi.org/10.1002/mds.20951.

[87] A.A. Kühn, T. Trottenberg, A. Kupsch, B.-U. Meyer, Pseudo-bilateral hand motor responses evoked by transcranial magnetic stimulation in patients with deep brain stimulators, Clin. Neurophysiol. 113 (2002) 341–345. https://doi.org/10.1016/s1388-2457(01)00731-3.

[88] H. Magsood, C.H.A. Serrate, A.A. El-Gendy, M.L.R. Hadimani, Anatomically accurate brain phantoms and methods for making and using the same, (2019).

[89] H. Magsood, R.L. Hadimani, Development of Anatomically Accurate Brain Phantoms for Experimental Verification of Stimulation Strengths during TMS, Mater. Sci. Eng. C. (2019).

[90] Human connectome project HCP, Parkinson's progression marker initiative, (2018).

https://ida.loni.usc.edu/login.jsp?project=PPMI#.

[91] C. Gabriel, a Peyman, E.H. Grant, Electrical conductivity of tissue at frequencies below 1 MHz., Phys. Med. Biol. 54 (2009) 4863–4878. https://doi.org/10.1088/0031-9155/54/16/002.

[92] Medtronic Lead Kit for {DBS} Stimulation, Biomed. Saf. Stand. 46 (2016) 157. https://doi.org/10.1097/01.bmsas.0000508150.05478.86.

[93] FDA, Class 1 Device Recall Deep Brain Stimulation Lead Kit, (2013). https://www.accessdata.fda.gov/scripts/cdrh/cfdocs/cfres/res.cfm?id=116147.

[94] S.J. Chapman, D.P. Hewett, L.N. Trefethen, Mathematics of the faraday cage, SIAM Rev. 57 (2015) 398–417. https://doi.org/10.1137/140984452.

[95] Zhi-De Deng, S.H. Lisanby, A. V. Peterchev, Transcranial magnetic stimulation in the presence of deep brain stimulation implants: Induced electrode currents, in: 2010 Annu. Int. Conf. IEEE Eng. Med. Biol., IEEE, 2010: pp. 6821–6824. https://doi.org/10.1109/IEMBS.2010.5625958.

[96] F.R. de Noriega, R. Eitan, O. Marmor, A. Lavi, E. Linetzky, H. Bergman, Z. Israel, Constant Current versus Constant Voltage Subthalamic Nucleus Deep Brain Stimulation in Parkinson's Disease, Stereotact. Funct. Neurosurg. 93 (2015) 114–121. https://doi.org/10.1159/000368443.

[97] A. Zolj, Electrically Small Dipole Antenna Probe for Quasi- static Electric Field Measurements, (2018).

[98] T. Swiontek, Mapping of current densities induced, 13 (1991) 851–852.

[99] S.H. Lisanby, B. Luber, C. Schroeder, M. Osman, D. Finck, R. Jalinous, V.E. Amassian, J. Arezzo, H.A. Sackeim, 333. Intracerebral measurement of rTMS and ECS induced voltage in vivo, Biol. Psychiatry. 43 (1998) S100. https://doi.org/10.1016/S0006-3223(98)90781-8.

[100] Q. Meng, M. Daugherty, P. Patel, S. Trivedi, X. Du, E. Hong, F. Sen Choa, High-sensitivity and spatial resolution transient magnetic and electric field probes for transcranial magnetic stimulator characterizations, Instrum. Sci. Technol. 46 (2018) 502–518. https://doi.org/10.1080/10739149.2017.1401547.

[101] Z. De Deng, S.H. Lisanby, A. V. Peterchev, Electric field depth-focality tradeoff in transcranial magnetic stimulation: Simulation comparison of 50 coil designs, Brain Stimul. 6 (2013) 1–13. https://doi.org/10.1016/j.brs.2012.02.005.

[102] A. Thielscher, T. Kammer, Electric field properties of two commercial figure-8 coils in TMS: Calculation of focality and efficiency, Clin. Neurophysiol. 115 (2004) 1697–1708. https://doi.org/10.1016/j.clinph.2004.02.019.

[103] G.M. Kroch, S.M. Goetz, J.M. Bernabei, Z. De Deng, W.H. Lee, A. V. Peterchev, Field Distribution Model of Transcranial Static Magnetic Stimulation, Neuromodulation Technol. Neural Interface. 6 (2014) 2014. https://doi.org/10.1111/ner.12699.

[104] S. Zhang, K. Cui, X. Zhang, X. Shi, M. Ge, M. Zhao, G. Xu, W. Yan, Effect of Transcranial Ultrasonic-Magnetic Stimulation on Two Types of Neural Firing Behaviors in Modified Izhikevich Model, IEEE Trans. Magn. 54 (2018). https://doi.org/10.1109/TMAG.2017.2773086.

[105] P.M. Glover, R. Bowtell, Measurement of electric fields due to time-varying magnetic field gradients using dipole probes, Phys. Med. Biol. 52 (2007) 5119–5130.

https://doi.org/10.1088/0031-9155/52/17/001.

[106] Q. Meng, P. Patel, S. Trivedi, X. Du, E. Hong, F.-S. Choa, Sensor probes and phantoms for advanced transcranial magnetic stimulation system developments, Smart Biomed. Physiol. Sens. Technol. XII. 9487 (2015) 94870W. https://doi.org/10.1117/12.2177014.

[107] J.E. Smith, A. V. Peterchev, Electric field measurement of two commercial active/sham coils for transcranial magnetic stimulation, J. Neural Eng. 15 (2018). https://doi.org/10.1088/1741-2552/aace89.

[108] K. Porzig, H. Brauer, H. Toepfer, Biological tissues dispersivity and power loss density in transcranial magnetic stimulation, 2013 21st Int. Conf. Software, Telecommun. Comput. Networks, SoftCOM 2013. (2013). https://doi.org/10.1109/SoftCOM.2013.6671857.

[109] A. Kainz, H. Steiner, J. Schalko, A. Jachimowicz, F. Kohl, M. Stifter, R. Beigelbeck, F. Keplinger, W. Hortschitz, Distortion-free measurement of electric field strength with a MEMS sensor, Nat. Electron. 1 (2018) 68–73. https://doi.org/10.1038/s41928-017-0009-5.

[110] Y. Huang, A.A. Liu, B. Lafon, D. Friedman, M. Dayan, X. Wang, M. Bikson, W.K. Doyle, O. Devinsky, L.C. Parra, Measurements and models of electric fields in the in vivo human brain during transcranial electric stimulation, Elife. 6 (2017) 1–26. https://doi.org/10.7554/eLife.18834.

[111] O. Puonti, G.B. Saturnino, K.H. Madsen, A. Thielscher, Value and limitations of intracranial recordings for validating electric field modeling for transcranial brain stimulation, Neuroimage. 208 (2020) 116431. https://doi.org/10.1016/j.neuroimage.2019.116431.

[112] Y. Huang, A. Datta, M. Bikson, L.C. Parra, Realistic volumetric-approach to simulate transcranial electric stimulation - ROAST - a fully automated open-source pipeline, J. Neural Eng. 16 (2019). https://doi.org/10.1088/1741-2552/ab208d.

[113] M. Hallett, Transcranial magnetic stimulation and the human brain., Nature, 406, 147-150 . 406 (2000) 147–150.

[114] M. Kobayashi, A. Pascual-Leone, Transcranial magnetic stimulation in neurology, Lancet Neurol. 2 (2003) 145–156. https://doi.org/10.1016/s1474-4422(03)00321-1.

[115] A. V. Peterchev, T.A. Wagner, P.C. Miranda, M.A. Nitsche, W. Paulus, S.H. Lisanby, A. Pascual-Leone, M. Bikson, Fundamentals of transcranial electric and magnetic stimulation dose: Definition, selection, and reporting practices, Brain Stimul. 5 (2012) 435–453. https://doi.org/10.1016/j.brs.2011.10.001.

[116] L.J. Crowther, R.L. Hadimani, A.G. Kanthasamy, D.C. Jiles, Transcranial magnetic stimulation of mouse brain using high-resolution anatomical models, J. Appl. Phys. 115 (2014) 17B303. https://doi.org/10.1063/1.4862217.

[117] S.D. March, S. McAtee, M. Senter, K. Spoth, D.R. Stiner, L.J. Crowther, R.L. Hadimani, D.C. Jiles, Focused and deep brain magnetic stimulation using new coil design in mice, in: 2013 6th Int. {IEEE}/{EMBS} Conf. Neural Eng., IEEE, 2013. https://doi.org/10.1109/ner.2013.6695887.

[118] P. Rastogi, R.L. Hadimani, D.C. Jiles, Investigation of Coil Designs for Transcranial Magnetic Stimulation on Mice, IEEE Trans. Magn. 52 (2016) 1–4. https://doi.org/10.1109/TMAG.2015.2514064.

[119] G. Tay, M. Chilbert, J. Battocletti, A. Sances, T. Swiontek, C. Kurakami, "Measurement of magnetically induced current density in saline in vivo., Ieee Eng. Med. Biol. Soc. 11H Annu. Int. Conf. (1989) 1167–1168. https://doi.org/10.1109/IEMBS.1989.96142.

[120] A. Opitz, M. Windhoff, R.M. Heidemann, R. Turner, A. Thielscher, How the brain tissue shapes the electric field induced by transcranial magnetic stimulation, Neuroimage. 58 (2011) 849–859. https://doi.org/10.1016/j.neuroimage.2011.06.069.

[121] Y. Wang, C. Zhu, R. Pfattner, H. Yan, L. Jin, S. Chen, F. Molina-Lopez, F. Lissel, J. Liu, N.I. Rabiah, Z. Chen, J.W. Chung, C. Linder, M.F. Toney, B. Murmann, Z. Bao, A highly stretchable, transparent, and conductive polymer, (n.d.). http://advances.sciencemag.org/content/advances/3/3/e1602076.full.pdf (accessed June 10, 2017).

[122] G.B. Saturnino, O. Puonti, J.D. Nielsen, D. Antonenko, K.H. Madsen, A. Thielscher, SimNIBS 2.1: A Comprehensive Pipeline for Individualized Electric Field Modelling for Transcranial Brain Stimulation, Brain Hum. Body Model. (2019) 3–25. https://doi.org/10.1007/978-3-030-21293-3_1.

[123] M.W. Woolrich, S. Jbabdi, B. Patenaude, M. Chappell, S. Makni, T. Behrens, C. Beckmann, M. Jenkinson, S.M. Smith, Bayesian analysis of neuroimaging data in FSL., Neuroimage. 45 (2009) S173–S186. https://doi.org/10.1016/j.neuroimage.2008.10.055.

[124] M.F. Glasser, S.N. Sotiropoulos, J.A. Wilson, T.S. Coalson, B. Fischl, J.L. Andersson, J. Xu, S. Jbabdi, M. Webster, J.R. Polimeni, D.C. Van Essen, M. Jenkinson, The minimal preprocessing pipelines for the Human Connectome Project, Neuroimage. 80 (2013) 105–124. https://doi.org/10.1016/j.neuroimage.2013.04.127.

[125] J. Germick, Y. Alkheder, P. Rastogi, R.L. Hadimani, A. Pandurangi, D.C. Jiles, Development of Focused Transcranial Magnetic Stimulation Coils for Treating Schizophrenia, IEEE Trans. Magn. 54 (2018) 1–5. https://doi.org/10.1109/TMAG.2018.2850328.

[126] E.G. Lee, P. Rastogi, R.L. Hadimani, D.C. Jiles, J.A. Camprodon, Impact of non-brain anatomy and coil orientation on inter- and intra-subject variability in TMS at midline, Clin. Neurophysiol. 129 (2018) 1873–1883. https://doi.org/10.1016/j.clinph.2018.04.749.

[127] E.G. Lee, W. Duffy, R.L. Hadimani, M. Waris, W. Siddiqui, F. Islam, M. Rajamani, R. Nathan, D.C. Jiles, Investigational Effect of Brain-Scalp Distance on the Efficacy of Transcranial Magnetic Stimulation Treatment in Depression, IEEE Trans. Magn. 52 (2016) 1–4. https://doi.org/10.1109/TMAG.2015.2514158.

[128] F. Syeda, H. Magsood, E.G. Lee, A.A. El-Gendy, D.C. Jiles, R.L. Hadimani, Effect of anatomical variability in brain on transcranial magnetic stimulation treatment, AIP Adv. 7 (2017) 056711. https://doi.org/10.1063/1.4974981.

[129] P. Rastogi, E.G. Lee, R.L. Hadimani, D.C. Jiles, Transcranial Magnetic Stimulation-coil design with improved focality, AIP Adv. 7 (2017) 056705. https://doi.org/10.1063/1.4973604.

[130] G.B. Saturnino, A. Thielscher, K.H. Madsen, T.R. Knösche, K. Weise, A principled approach to conductivity uncertainty analysis in electric field calculations, Neuroimage. 188 (2019) 821–834. https://doi.org/10.1016/j.neuroimage.2018.12.053.

8 Appendices

8.1 Appendix I: Paper 1 (**Materials Science and Engineering C**: Accepted with revisions)

Development of Anatomically Accurate Brain Phantom for Experimental Validation of Stimulation Strengths during TMS

Hamzah Magsood[1]*and R. L. Hadimani[1, 2]*

[1]Department of Mechanical and Nuclear Engineering, Virginia Commonwealth University, Richmond VA 23284, USA

[2]Department of Biomedical Engineering, Virginia Commonwealth University, Richmond VA 23284, USA

Key Words: Transcranial Magnetic Stimulation; TMS, Neuromodulation; Brain Phantoms

Abstract: Transcranial magnetic stimulation (TMS) is a non-invasive technique for diagnosis and treatment of various neurological conditions. However, the lack of realistic physical models to test the safety and efficacy of stimulation from magnetic fields generated by the coils has hindered the development of new TMS treatment and diagnosis protocols for several neurological conditions. We have developed an anatomically and geometrically accurate brain and head phantom with an adjustable electrical conductivity matching the average conductivity of white matter and grey matter of the human brain and the cerebrospinal fluid. The process of producing the phantom starts with segmenting the MRI images of the brain and then creating shells from the segmented and reconstructed model ready for 3-D printing and serving as a mold for the conductive polymer. Furthermore, we present SEM images and conductivity measurements of the conductive polymer composite as well as confirmation of the anatomical accuracy of the phantom with computed tomography (CT) images. Finally, we show results of induced voltage measurements obtained from TMS on the brain phantom.

* Corresponding authors: Hamzah Magsood: magsoodha@vcu.edu, Dr. Ravi Hadimani: rhadimani@vcu.edu

1. Introduction

Transcranial Magnetic Stimulation (TMS) is a non-invasive technique for diagnostics and treatments of various neurological diseases [1]–[5]. TMS is an FDA approved treatment for depression [5], migraine [6], and obsessive-compulsive disorder (OCD) [7] . It is also investigated extensively to be used as a promising treatment technique for other neurological disorders like Parkinson's [8,9], Alzheimer related cognitive impairments [10] and ischemic strokes recovery [11]. Although there are extensive computational and clinical studies of TMS, there is a lack of an experimental and physical model for testing and examining the brain stimulation procedures and protocols. There are significant technological, safety and ethical limitations to test the potential TMS treatment procedures or develop enhancements and refine them on humans or animals. The lack of anatomically and geometrically realistic brain phantoms has made the experimental verification of induced electric fields in the brain tissues an impediment to the development of new treatment protocols. There is also a lack of animal studies of TMS due to lack of animal phantoms [116–118]. Several papers report electrically conductive brain phantoms but lack the anatomical and geometrical features of the brain [119]-[14]. The geometry of an electrically conducting material in the presence of a magnetic field can significantly vary and alter the induced electric fields [15,120]. Therefore, it is important to mimic the conductivity and the geometry of the physical model used in the experimental verification in brain stimulation applications such as TMS.

We have developed a geometrically accurate 3-D brain and head phantom [55] with the electrical conductivity matching the average electrical conductivity of the grey matter (GM) and white matter (WM) in the brain as well as the conductivity of the cerebrospinal fluid (CSF). In this study, we have mainly focused on GM, WM, and CSF as they make up the cortex and the interface

of the GM/CSF in which the main regions of the brain are targeted in most of the TMS procedures for treating various neurological disorders. The manufacturing process presented in here will help researchers in the biomedical field to mimic and develop complex geometries of the human body with imparted adjustable electrical conductivity. The phantom, with appropriate experimental verifications, will help the researchers and clinicians in the field of the brain modulation to test and approve new coil designs or new treatments protocols

The brain is made of a conductive polymer. The development of conductive polymers has been widely researched over the last decades for different applications [62–68]. In some applications, high electrical conductivity is needed along with a rigid constraints on mechanical properties [121]; in some other applications, elasticity is needed to be accompanied with moderate conductivity [69]. There are many methods to impart conductivity to the polymers; some are achieved by chemical manipulation of the bonds of the polymer and other are achieved by the addition of conductive material to the polymers. Some examples of the material that can be used are single and multi-walled carbon nanotubes (MWCNTs), carbon black, copper flakes, silver particles and silver nanowires. Some of the processes and techniques of producing the required conductive polymers include mixing, milling, and grinding processes.

In this paper, we present a process of creating an anatomically accurate and electrically conductive brain phantom with an adjustable conductivity for brain stimulation applications. The process started with acquiring magnetic resonance image (MRI) of the brain of an individual. Then the images were segmented and reconstructed into three-dimensional model in an .stl format. The 3-D model was processed to create shells/molds that were ready for 3-D printing and then for casting the conductive polymers. After that, the shells were broken and dismantled using acetone and finally producing the phantom. We then showed experimental results of induced voltages on

the brain phantom by TMS coils. We also acquired scanning electron microscopy (SEM) images of the conductive polymer composition to show the dispersion of the conductive filler into the polymer. Finally, CT images of the physical phantom were acquired to confirm the accurate reproduction of anatomical features of the brain compared to the original MRI segmented brain model.

2. Material and Methods

2.1 Materials:

To prepare the conductive polymer of the brain phantom, we used Multi-walled carbon nanotube (MWCNT) (diameter: 50-85 nm length: 10-15μm) mixed with polydimethylsiloxane polymer (PDMS). A mechanical stirrer (Ultra speed, model- BDC6015) was used to mix the PDMS polymer with MWCNT. The conductive polymer was casted and poured into shells that were printed using Ultimaker3^{TM} Dual extrusion 3-D printer obtained from Ultimaker Inc. We used polylactic acid (PLA) as the shell building material and polyvinyl alcohol (PVA) as a support material for PLA. The MRI images were segmented using FreeSurfer (http://surfer.nmr.mgh.harvard.edu/, Athinoula A. Martinos Center for Biomedical Imaging, Charlestown, MA, United Sates), SimNIBS [122] (Danish Research Centre for Magnetic Resonance DRCMR) and FSL [123] software (Analysis Group, Oxford, UK). MRI data used in the preparation of this work were obtained from the Human Connectome Project (HCP) database [124].The shell creation and modifications were performed using Meshmixer. The scanning electron microscopy (SEM) images of the conductive polymer were acquired using Hitachi SU-70. Voltage measurements acquired using oscilloscope (Tiktronic, TDS20002C). TMS applied on the brain phantom using Magstim (model Rapid 2^{TM} stimulator with Magstim AirFilm^{TM} coils).

2.2 Reconstruction of the MRI images into 3D models:

For the development of heterogeneous head models, we used FreeSurfer, SimNIBS and FSL software. The three software packages operate together to segment the T1 and T2 weighted MRI images of the head into the skin, skull, cerebrospinal fluid (CSF) GM, WM, ventricles and cerebellum and construct a 3D volumetric heterogeneous head model. We have reported this procedure of developing head models in our previous publications [125–127]. The final segmented and reconstructed brain model from MRI is shown in Figure 1.

2.3 Shell creation:

Following the segmentation of the brain parts, we imported the brain model into Meshmixer software. In Meshmixer, we worked on creating a shell of the outer side of the brain by working on the GM surface, which is the surface of the brain. The shell was created by creating a solid brain model with 1mm offset thickness. Then, we subtract the original brain model from the solid brain. This will create the shell with 1mm thickness. The additional 1mm thickness is the shell of the brain and should not be confused with the brain itself. The inner side of the shell is the original geometry of the brain surface (GM). There is an overlap but only on the outer side of the shell, which is fine as long as the area of interest, inner side, is intact and has no overlap. In other words, the shell = 1 mm-additional-thickness solid brain model – original brain model. Furthermore, the shell thickness needed for the job can vary depending on the 3D printing technique and the material used. Since we used PLA, 1mm thickness is optimal between the toughness and dissolvability/breakage of the shell. That is because the 3D printed shell will be immersed in acetone. Acetone makes PLA brittle and breakable. This process is the last step done in order to remove the shells from the conductive polymer.

To ease the process of printing the shells, we split the brain shell in two, upper and lower shells. This way we could cast the conductive polymer inside the shells, join them together, and then remove the shells. Figure 2 shows the upper and lower shells and a view of the inside and outside surfaces of the upper half.

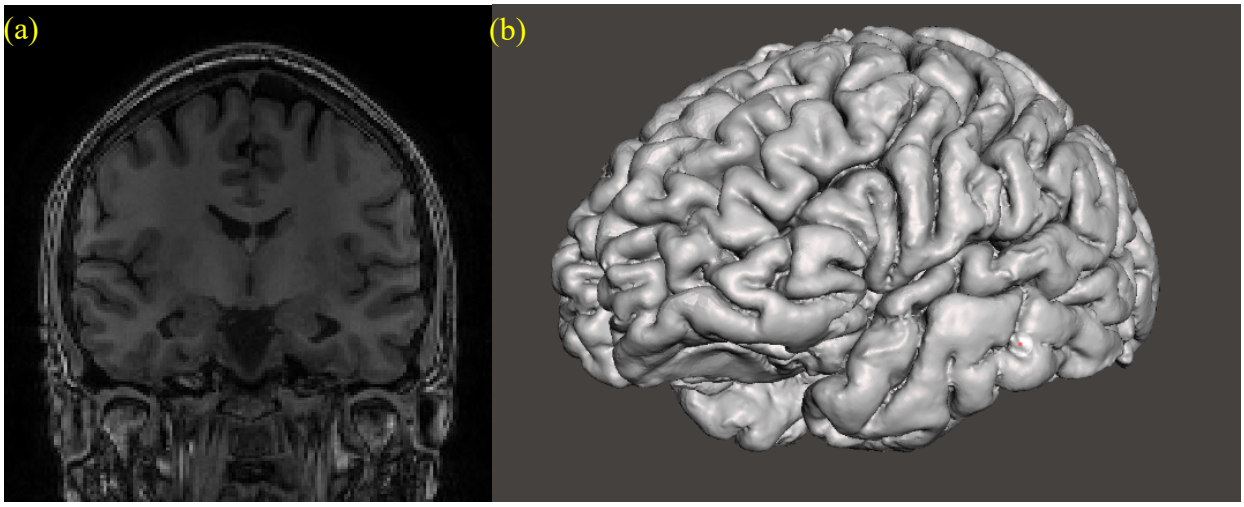

Figure 1. Brain model after the completion of segmentation and reconstruction of MRI. a) MRI images before

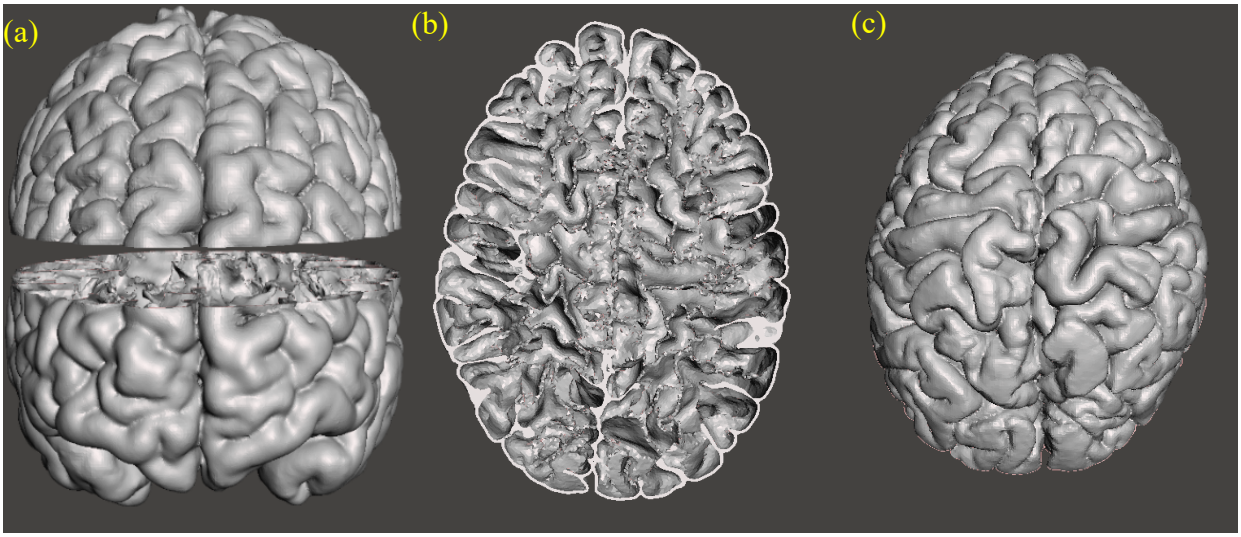

Figure 2. Upper and lower shells (a) with view to the inner (b) and outer (c) surfaces of the upper half of the grey

2.4 The 3-D shell printing:

We used a filament deposition modeling FDM 3-D dual extrusion printer, Ultimaker3^{TM}. It is capable of printing with PLA and compatible PVA as a support. A 3D-printer with dual extrusion is essential because for printing such intricate geometry, a compatible support material that is easy to remove will ensure best support for the main material. For the first extruder we used PLA as main material to build the shells. PLA is selected because it becomes brittle when immersed in acetone. For the second extruder, we used PVA as a support material that is dissolvable in water. The printing preparation and support material rendering was done in an open-source software Cura provided by Ultimaker Inc. Shell material, PLA was printed with 100% infill (without voids) and layer thickness 0.12 mm. Support material PVA was printed with standard pattern by Cura. After the printing, the shells configuration that is made of the PLA and PVA is immersed in water to dissolve the PVA; then, the shells are ready to be casted with the conductive polymer. Figure 3 shows an overview of the printing with the support and the shell after it was cleaned from the support.

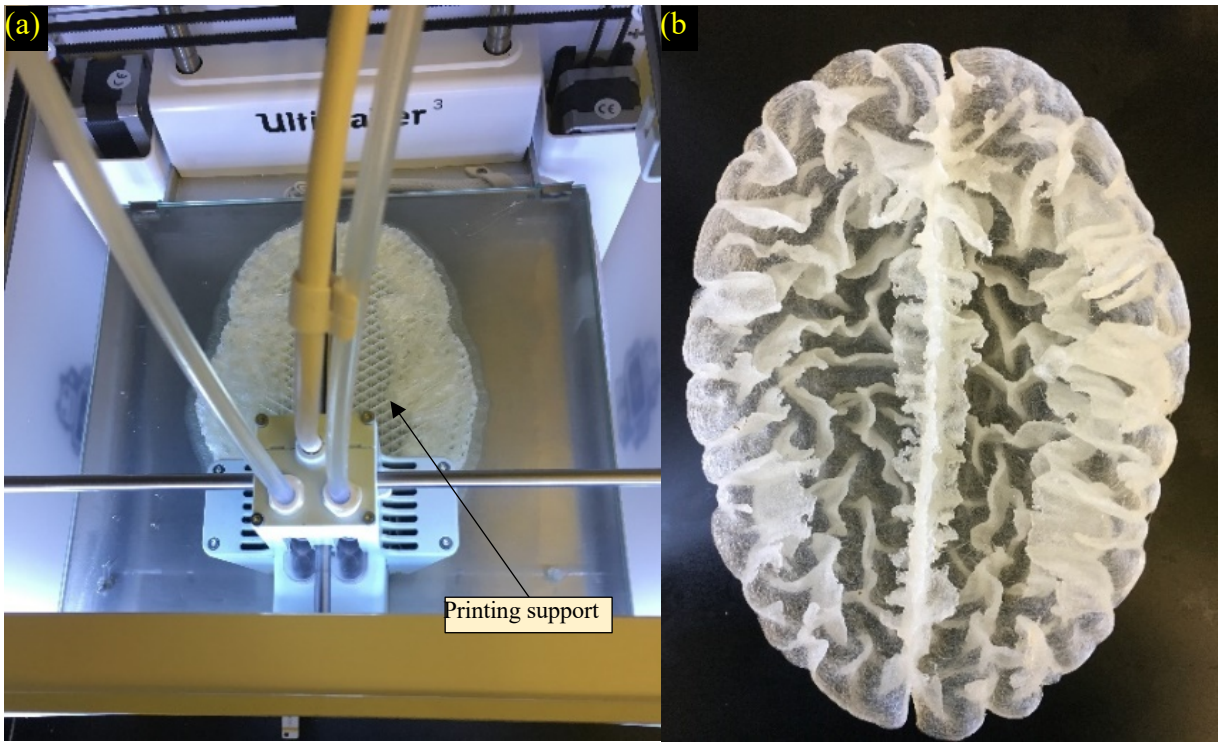

Figure 3. (a) Shells as they are being printed PLA as main material and with PVA as a support.

2.5 Electrically conductive polymer:

The electrical conductivity of specific regions of the brain varies between different sources of literature and also between subjects [25,29,30,61]. For that reason, we chose an average conductivity of our brain phantom's constituent material (conductive polymer) to be approximately 0.25 Sm^{-1}. This value is within the average conductivity of the GM and WM from the latest literature [23,31]. For the CSF, we chose a conductivity of about 1.4 Sm^{-1} made of a saline water and injected inside the head phantom.

For our phantom, we chose the PDMS as the hosting polymer and the MWCNT as the conductive filler. The PDMS was chosen because it is flexible even with loading of more than 10% wt. of MWCNTs which is essential for insertion of electrodes in the phantom. It is also widely used in research and development of conductive polymers [21-28]. A high-speed stirrer was used to disperse MWCNT into PDMS. The process of imparting conductivity to the polymer is an optimization process between the mixing time, mixing speed and percentage of conductive filler to the polymer. The criterion used in our work was by adding the targeted percentage of the MWCNT to the PDMS and then mixing with 1000 rpm until it becomes paste-like; then added the PDMS curing agent to the mixture and stir it thoroughly. This mixing speed was chosen because when applying higher than 1000 rpm, the MWCNTs break down to lower aspect ratio and therefore reduce their ability to conduct electricity; and mixing speed lower than 1000rpm is not effective for thorough dispersion of MWCNTs within the polymer matrix. Furthermore, mixing time depends on the percentage of the conductive filler in the polymer. The higher the filler percentage, the longer the mixing time. It was mixed until the mixture becomes thick and no longer blend into itself by the stirrer blades.

2.6 Induced voltage measurements:

Stimulation strengths inside and on the surface of the phantom were measured under different TMS parameters. TMS coils were positioned on the brain phantom and an oscilloscope probe was placed just underneath the surface of the phantom in order to measure the voltage (phantom probe). Also, we placed another probe at the same distance (from the coils) of the first probe but it was placed outside the phantom to measure the voltage induced on the probe just from the TMS coils as a reference probe. Then, we applied a biphasic magnetic field from the TMS coils at four distances 1, 2, 3, and 4 cm and at four different current coil intensities 25%, 50%, 75%, and 100% at each distance. The amplitude of 100% current pulse in the TMS coil is approximately 5000A. The brain phantom and experimental setup is shown in Figure 4.

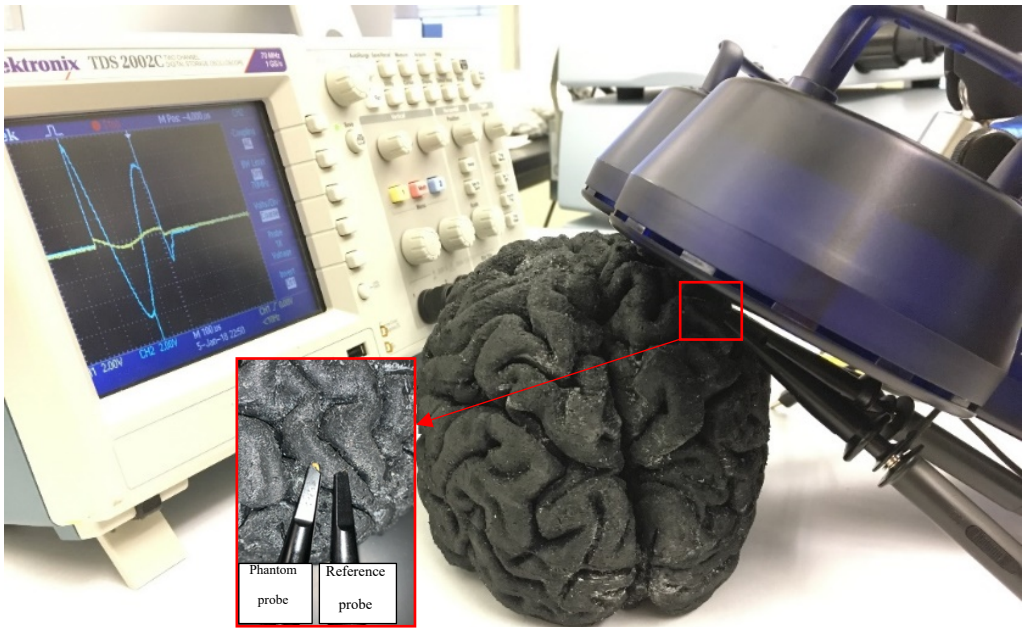

Figure 4. Experiment setup with applied time-varying magnetic field with TMS coils at four distances 1, 2, 3, and 4cm and at four different current coil intensities 25, 50, 75, and 100% at each distance

3. Results

3.1 Resistivity/conductivity measurement of the conductive polymers:

The conductive filler CNTs weight percentage play an important role in increasing and decreasing the imparted electrical conductivity to the polymer mixture. Figure 5 shows the conductivity measurement of the conductive polymer samples with weight percentage of CNT in PDMS ranging from 5.3 to 14.4% (with addition of SEM images for 3 concentrations, 5.3%, 8.3% and 14.4%). Resistivity measurements were acquired from 1 cm^3 samples and then converted to conductivity by the relationship ($\sigma = 1/\rho$) where σ is the conductivity in Sm^{-1} and ρ is the resistivity

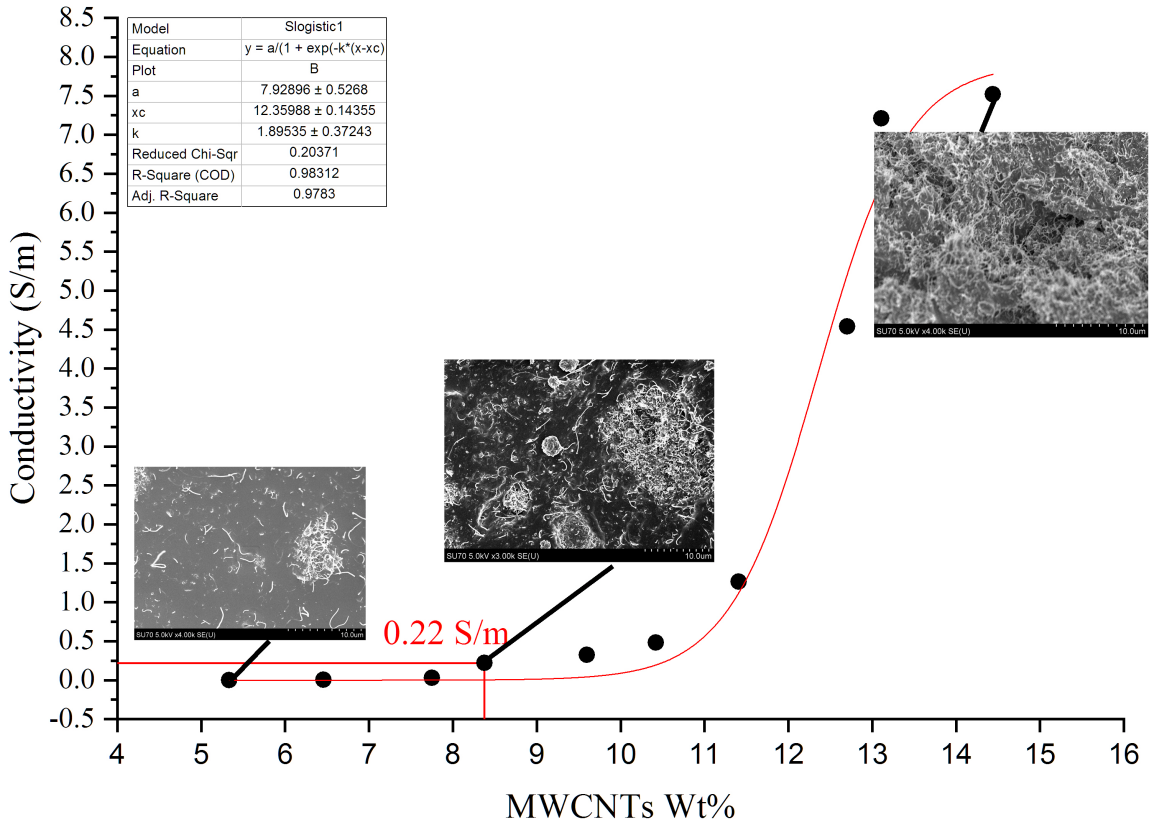

Figure 5. Conductivity measurements with non-linear regression curve acquired from 1 cm^3 conductive polymer samples with MWCNT filling weight percentage ranging between 5.3-14.4% along with SEM images for the three

Ω.m. Resistivity of the mixture was recorded after the composite was cured so that the resistivity values had settled to nearly constant values.

3.2 SEM Images of the conductive polymer:

SEM images in Figure 6 show the dispersion of the MWCNTs within the PDMS with increasing MWCNT concentration. The difference can be seen clearly in the degree of dispersion. At lower concentrations, MWCNTs are dispersed almost equally with some agglomerations. At 14.3 wt% (Figure 6 (c)), MWCNTs are well dispersed without agglomeration and the texture of the resulting composite is rough. We chose to show three concentrations; the minimum and maximum loading concentration, 5.3wt% (Figure 6(a)) and 14.4 wt% (Figure 6(c)), and at the concentration used for the brain phantom material 8.3 wt% (Figure 6(b)).

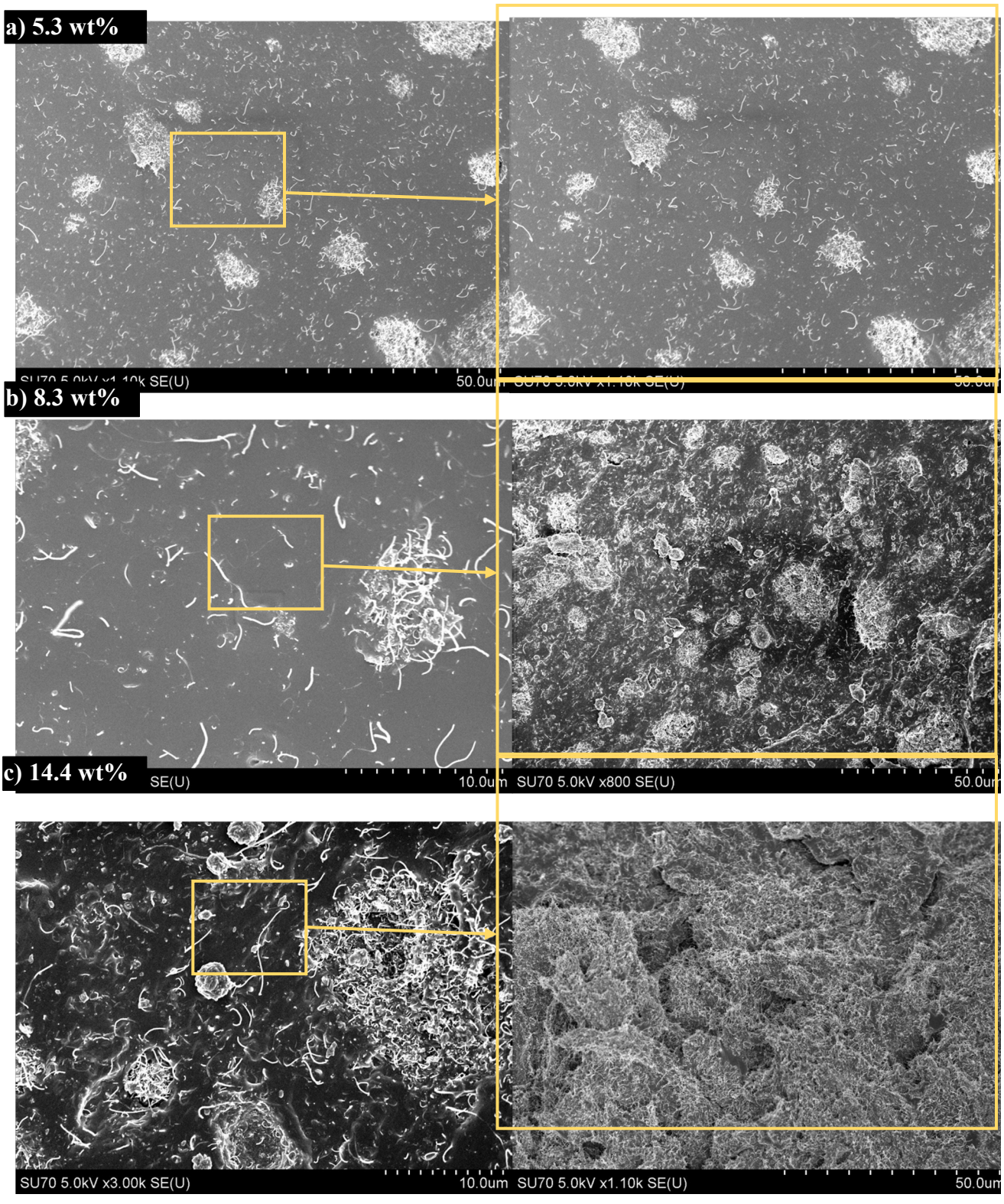
a) 5.3 wt%
b) 8.3 wt%
c) 14.4 wt%
SE(U)
10.0um
SU70 5.0kV x800 SE(U)
50.0um
SU70 5.0kV x3.00k SE(U)
10.0um
SU70 5.0kV x1.10k SE(U)
50.0um

3.3 Brain phantom:

After choosing the targeted conductivity of 0.25 Sm^{-1} for our polymer, the upper and lower grey matter shells were filled with the conductive polymer, securely joined, and left for around 72 hours to cure. Then, the phantom was immersed in acetone. The acetone made the shell material PLA brittle and breakable, which made it easier to remove the shells and finally expose the PDMS-MWCNT composite brain phantom as shown in Figure 7. Also, a summarization of the entire process of the phantom creation is shown in Figure 8 and a flow chart is shown in Figure 10.

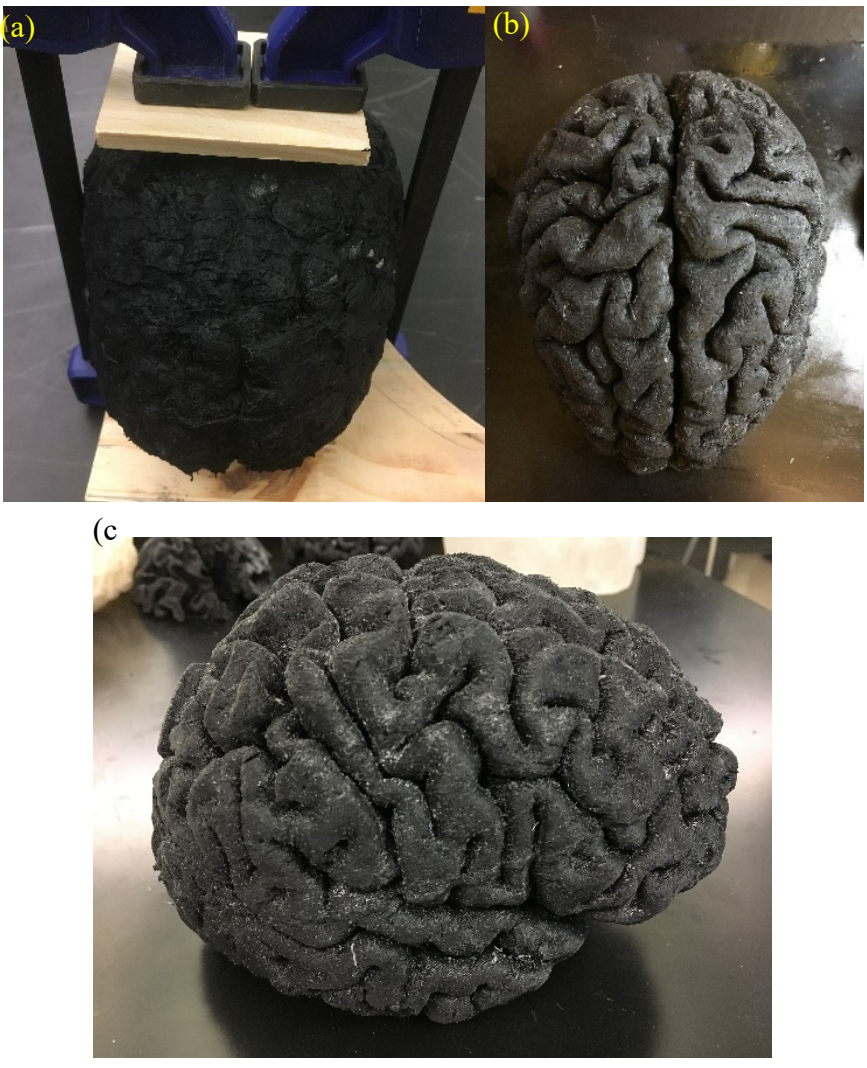

Figure 7. Final steps of the phantom creation. (a) The shells were filled with the conductive material and joined

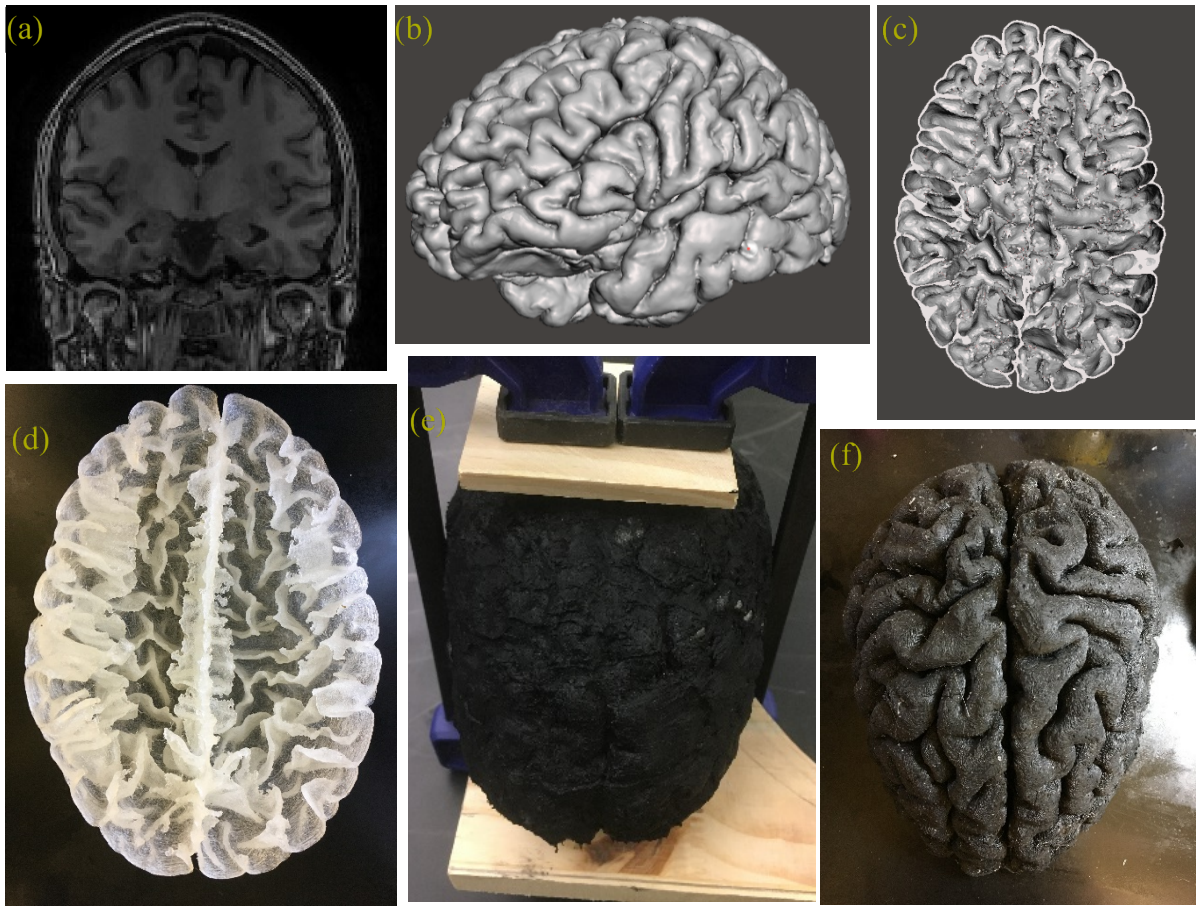

Figure 8. Summarization of the entire process starting from MRI images of the brain until the obtained brain phantom made of the conductive polymer. (a) MRI image in an nii format, (b) Reconstructed brain model in stl format, (c) Shell mold for the outer region of the brain/GM. Shown is the inner side of the upper half shell, (d) Shell after printing and dissolving the support material, (e) Shells were filled with the conductive material and joined together and left to be cured, (f) Brain phantom after being immersed in acetone and removing the shells

3.4. Head phantom and CSF

The head model consists of, the skin, scalp, skull, CSF and the brain phantom (grey matter, white matter and ventricles). In the phantom, the skin, scalp, and skull are joined in one layer and are made of non-conductive PDMS because these regions (except for the skin) exhibit very low and negligible electrical conductivities compared to the brain and CSF. Since the skull has very low conductivity where it impedes current flow, we can join the skin with the skull to be made non-conductive polymer. The CSF is made of a saline solution with adjustable conductivity. Figure 9 shows the steps of creating the layer of the skin, scalp, and skull using the same shelling method with the brain phantom. We 3-D printed the outer shell of the skin and the inner layer of the scalp. Then the supporting material of the printing was dissolved, and we poured the PDMS in between the shells to form the layer. After that, the shells were removed and we remained with the desired layer. After that, we placed the brain phantom inside the head. The gap in between the inner side of the head and the outer side of the brain is the CSF region. We injected the conductive saline solution in the gap. The saline solution has an NaCl concentration of about 3.5 mg/ml to mimic the CSF's conductivity. The final realization of the head and brain is shown in Figure 9(e).

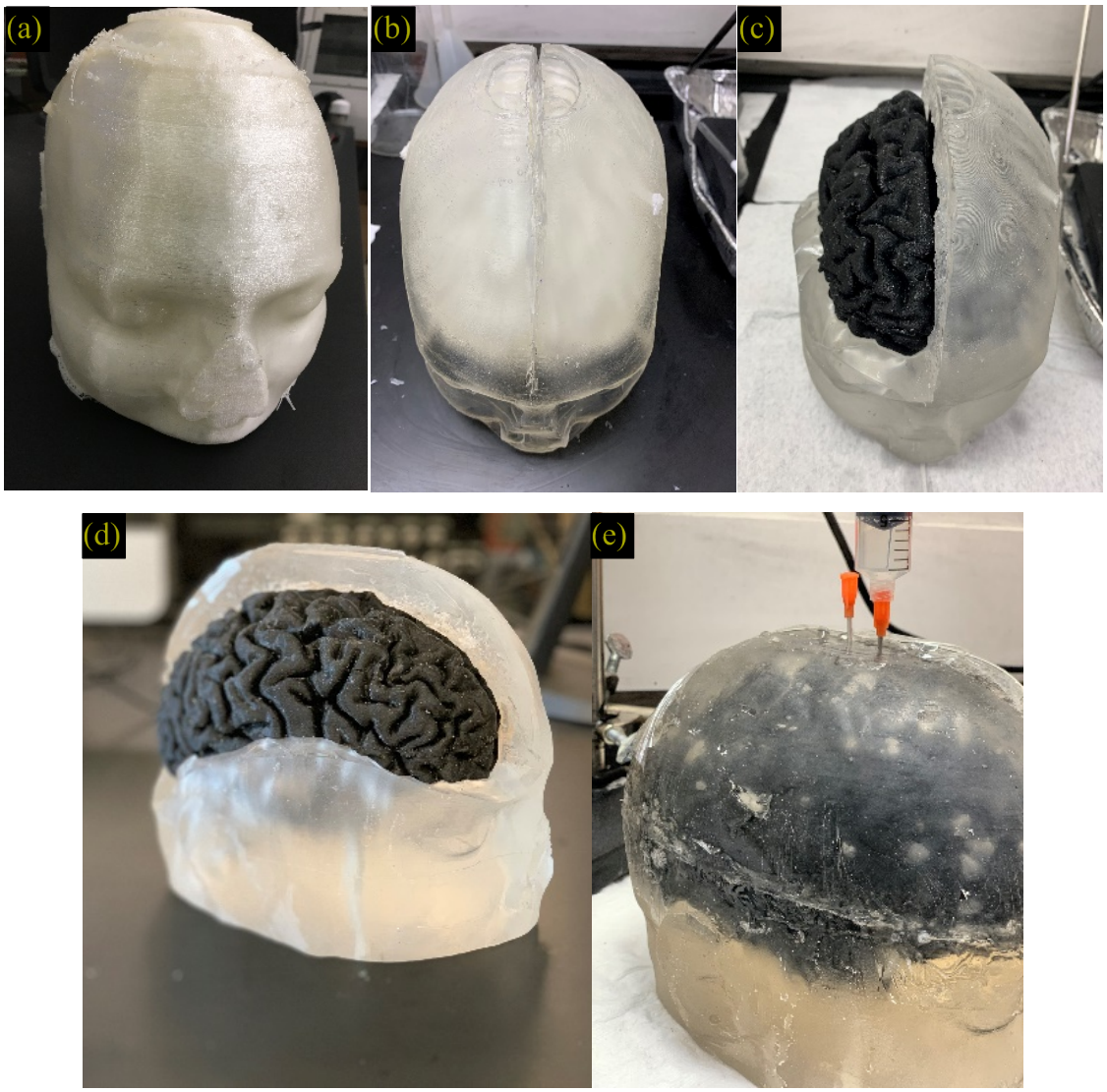

Figure 9. Fabrication of anatomically accurate head phantom using scalp, skull, CSF and the brain phantom. (a) The head shells after printing. (b) The head after the PDMS was poured and the outer shells was removed (the inner shell is not removed yet and can be seen through the fabric of the head phantom. (c, d) the brain phantom is placed inside the head. (e) The head phantom after being sealed and the conductive saline is being injected to mimic the CSF.

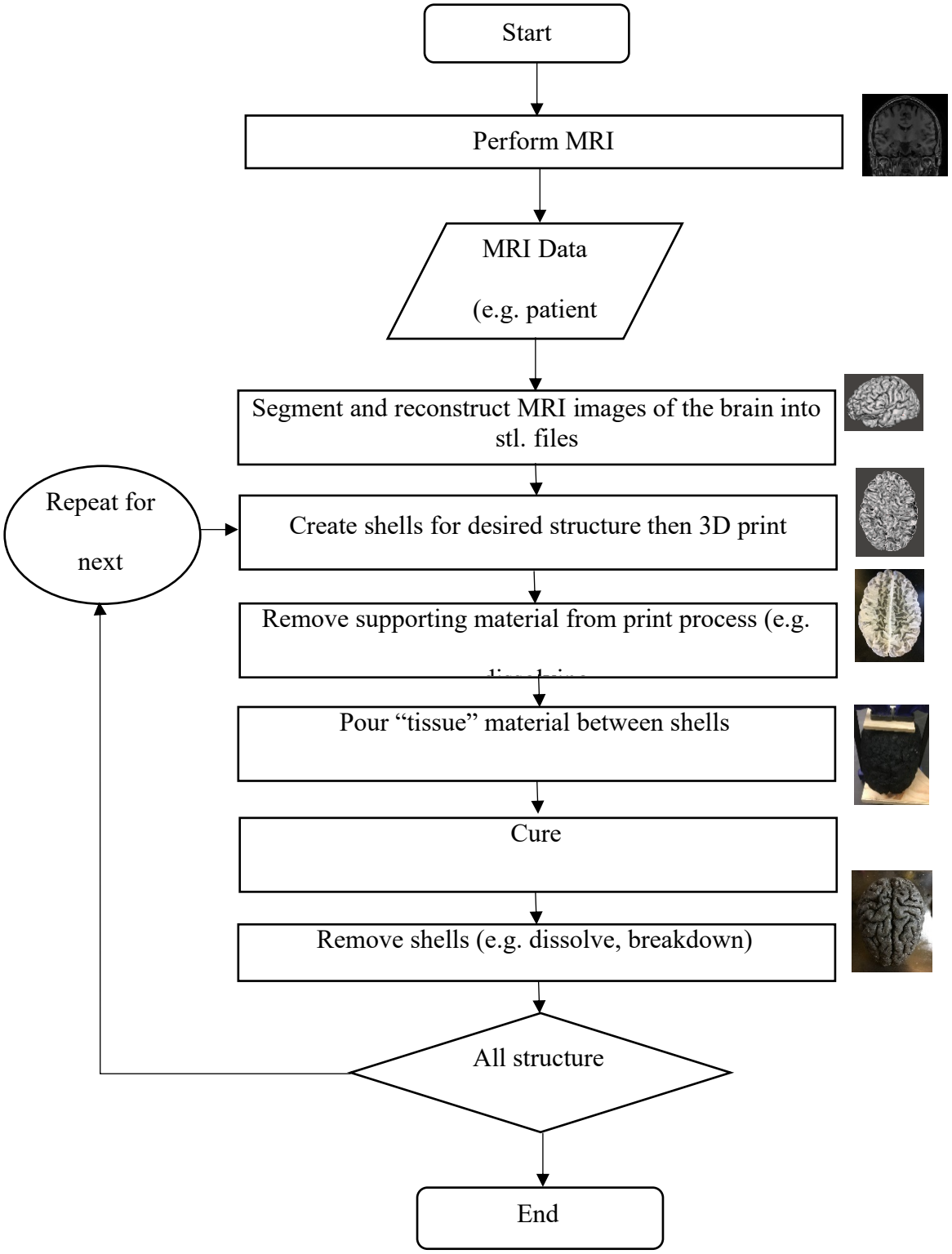

Figure 10. A flow chart showing summery of steps take in order to obtain the entire geometry of the brain and head phantom

3.5 Computed tomography (CT) images of the brain phantom:

The brain phantom shown in Figure 8 (c) was imaged using CT scan to confirm that the anatomical features in the MRI/stl files match the anatomical features of the phantom as shown in Figure 11. There are seemingly small deviations of anatomical features of the cortex of the phantom from original MRI image due the placement and orientation offsets of the phantom inside the CT scanner. Due to this misalignment, the CT scan slices are difficult to overlap on the original MRI slices. This can be corrected by using an accurate fixture to hold the phantom in the CT scanner.

3.6 Induced voltage measurements:

The voltage measurements at 1, 2, 3 and 4 cm distance are shown in Figure 12. Voltage readings shown in Figure 12 (a) and (b) represents the difference between the voltages induced on phantom probe and the reference probe; and they demonstrate different relationship between the measured voltages, distances, and current in the coil's intensities. Figure 12 (a) demonstrates a linear behavior between the induced voltages in the phantom vs. current intensities in the TMS coil at different distances from the phantom. Figure 12 (b) demonstrates a rapid decrease in the induced voltage in the phantom as a function of distances between the phantom and the coil at different current intensities in the TMS coil.

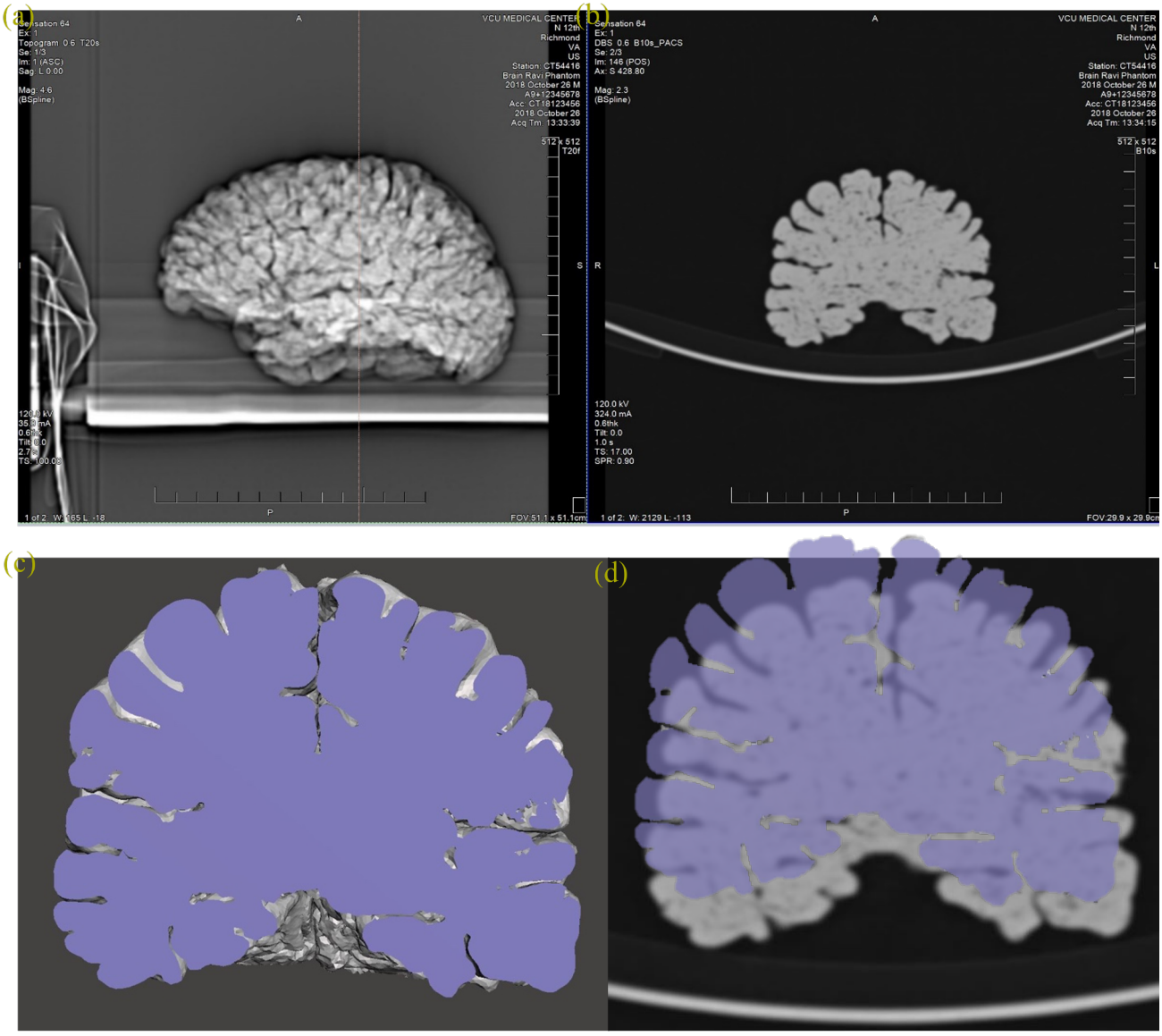

Figure 11. Brain phantom CT images compared to the brain model confirimg antomical features matching. (a, b) CT

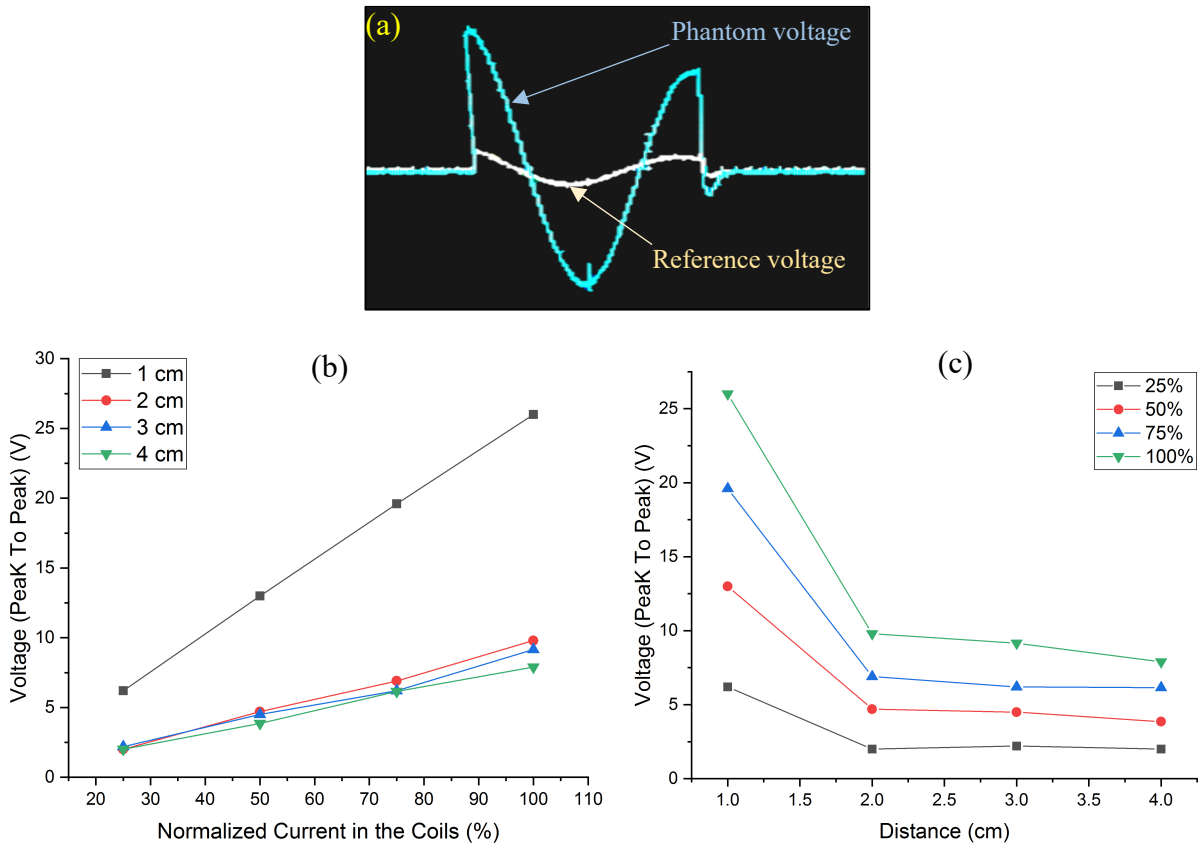

Figure 12. Measured voltages with varied distances (1, 2, 3, and 4cm) and intensities (25, 50, 75, and 100%) of the TMS coil. (a) Illustration of the measured voltage signals from the phantom and the probe with a biphasic TMS device. (b) Demonstration of a linear behavior for measured voltages vs intensities at different distances. (c)

4. Discussion

The brain phantom was created by a process that started with brain MRIs being segmented and reconstructed into three-dimensional brain model. Shells were created out of the brain model to be 3-D printed to serve as a mold for the conductive polymer. The shells were removed after immersing the PDMS-MWCNT polymer filled mold in acetone to obtain the brain phantom. The brain phantom created with above process is anatomically accurate as seen in Figure 9 where the CT scan of the phantom is compared with the .stl file of the MRI of the brain. It is important to consider the geometry and anatomy of the brain accurately when studying the effect of induced electric field with the application of external magnetic field such as TMS. The geometry has a crucial impact on the distribution of the induced electric field because the orientation of the magnetic field with respect to the surface of the brain it interacts with can change the amount of induction on these specific points of the surface significantly. Therefore, using spherical conductive brain phantoms to investigate the induced electric field distribution by TMS will result in inaccurate results. Our brain phantom takes accurate anatomical features of the brain into considerations and provides an important and essential feature for experimental study of stimulation strengths and field profiles generated by TMS in human brain.

The conductivity of the polymer that constitutes the brain phantom was selected based on the average conductivity of WM and GM 0.25 Sm^{-1}. We studied the change in the electrical conductivity when using MWCNT as a conductive filler with the hosting polymer PDMS. We chose a concentration of MWCNT of 8.3wt% to be used in our phantom because it approximately matches the average conductivity of GM and WM of a healthy adult human brain reported in the literature [17-20].

The conductivity of the composite can be further improved for a given conductive filler weight percentage inside the PDMS polymer. For example, the 0.25 Sm^{-1} that correspond to 8.5 wt% can be achieved with lesser wt% conductive filler like 3-4 wt% by dispersing the agglomerated MWCNTs. This is evident from the SEM images shown in Figure 6 (b). These aggregations can be dispersed with better mixing techniques. MWCNTs can be first dispersed in a solution such as heptane and sonicated before adding to the PDMS. Also, our PDMS polymer has some bubble formations within the composite. These bubbles can be removed by degassing the PDMS polymer after being molded by the brain shells. This can be challenging because the polymer has high viscosity and also the shells on top, which may seal the air bubbles inside the polymer as they leave no openings for the gas to escape. Furthermore, using single walled carbon nanotubes, SWCNTs and a higher aspect ratio of the carbon nanotubes would enhance the conductivity further for any given conductive filler weight percent.

Figure 12 shows induced voltage as a function of coil current intensity and distance, it can be seen that the voltage is linearly dependent on coil current intensity and decrease rapidly with the distance. The variation in induced voltage is significantly higher between the 1cm and 2cm coil distances compared to other distances. This is due to rapid decrease in the magnetic field with the distance from the source of magnetic field which results in rapid decrease in the induced voltage with the distance. This is seen in both Figure 12 (a) and (b) which align with previous literature [128][129].

This brain phantom can be used in many applications related to brain stimulation techniques such as TMS and deep brain stimulation (DBS). It can be used to test safety of combination treatment of the TMS and the DBS. The DBS probe can be inserted into the brain

phantom and the TMS applied to measure the amount of induced currents and determine the safety of the combined treatment.

The brain phantom can be improved to be fabricated with different conductivities for the GM and WM. The electric filed stimulated in the GM is influenced by the conductivity of the WM [130]. Therefore, separate conductivities insure a better and more accurate measurements of the induced electric field on the brain surface. However, our brain phantom with homogenous conductivity can still provide a rigorous insight into stimulation procedures because it is geometrically and anatomically matching the human brain.

Moreover, mapping the electric field on the brain phantom would be a next major and important step toward complete understanding of the stimulation effects on the brain. Such task is non-trivial because the very act of measurement of the electric field using conductive probes will distort and perturb the electric field especially on a complex geometry like the brain and with the application of externally alternating magnetic field. Researchers recently developed a non-distortion electric field microelectromechanical (MEMS) sensor for applications like high-voltage power or atmospheric electrostatic electric field mapping [109]. Similar sensors or probes are needed to be incorporated in the future development of the brain phantom and for measurement of electric field. With the further development of the measurement theory on such anatomical phantoms, one can correlate and verify those measurements with computer simulation of TMS similar to recent work on the transcranial direct current stimulation (tDCS) [110–112]. Furthermore, the phantom can further be developed for other brain stimulation techniques such as tDCS. In such case, manufacturing process needs to account for the skin conductivity.

5. Conclusion

In this work, we presented a process of creating an electrically conductive anatomically and geometrically accurate brain phantom used for experimental validation of neuromodulation techniques such as TMS and tDCS. The process started with converting MRIs into 3-D brain models. The models used for shell creation are 3D printed and served as molds for electrically conductive polymer. The conductive polymer consists of PDMS as host polymer and MWCNT as conductive filler. Also, stimulation strengths induced by TMS parameters were measured as induced voltages on the phantom. The results showed an expected linear behavior for the measured voltages vs. coil's current intensity and a rapid decrease behavior for the measured voltages vs. distances between the phantom and the coils. This phantom with average conductivity of GM and WM can work for cortical TMS applications. However, further development of the phantom with varying conductivities of GM and WM is needed for better evaluation and measurement of the stimulation strength of the TMS.

Acknowledgements

Authors would like to thank Dr. Kathryn Holloway of Department of Neurosurgery for useful discussions and assistance in getting CT scans of the brain phantom. Also, special thanks to Dr. Ahmed El-Gendy for useful discussion and assistance on the conductive polymer creation, and to Ciro Serrate and Brendan Quiroz for their help during the process of the phantom creation. The project is in part funded by NSF SBIR Phase I #1622060 and Saudi Arabian Ministry of Higher Education Scholarship Program.

Vitae

Hamzah Magsood, M.S.: Received his bachelor degree in nuclear engineering with a major in medical physics from King Abdul-Aziz University KAU, Jeddah, Saudi Arabia in 2010. He received his M.S. in mechanical and nuclear engineering form Virginia Commonwealth University VCU, Richmond, USA in 2015. He is currently pursuing his PhD degree in the mechanical and nuclear engineering in the BioMagnetics lab at VCU.

Ravi Hadimani, Ph.D.: has first a class honors degree in Mechanical Engineering from Kuvempu University, India, MS in Mechatronics from the University of Newcastle, UK and PhD in Electrical Engineering from Cardiff University, UK. He has served as a Project Scientist at the Institute of Materials Research and Innovation of the University of Bolton, UK. He was an Adjunct Assistant Professor at Iowa State University and was also an Associate of Ames Laboratory, US Dept. of Energy. Dr. Hadimani's research focus is on magnetic materials and devices for biomedical applications, magnetocaloric refrigeration and energy harvesting. He has developed a hybrid piezoelectric and photovoltaic energy harvester which is capable of harvesting electrical energy from solar, wind and rain energy.

8.2 Appendix II: Paper 2:

frontiers in Human Neuroscience

ORIGINAL RESEARCH
published: 03 April 2020
doi: 10.3389/fnhum.2020.00123

Safety Study of Combination Treatment: Deep Brain Stimulation and Transcranial Magnetic Stimulation

Hamzah Magsood[1]*, *Farheen Syeda*[1], *Kathryn Holloway*[2,3,4], *Ivan C. Carmona*[1] *and Ravi L. Hadimani*[1,2]*

[1]Department of Mechanical and Nuclear Engineering, Virginia Commonwealth University, Richmond, VA, United States, [2]Department of Biomedical Engineering, Virginia Commonwealth University, Richmond, VA, United States, [3]McGuire Research Institute, Hunter Holmes McGuire Veterans Affairs (VA) Medical Center, Richmond, VA, United States, [4]Department of Neurosurgery, Virginia Commonwealth University Health System, Richmond, VA, United States

OPEN ACCESS

Edited by:
Laleh Golestani Rad,
Northwestern University,
United States

Reviewed by:
Sergey N. Makarov,
Worcester Polytechnic Institute,
United States
Sunder Rajan,
Center for Devices and Radiological Health (CDRH), United States
Lucia Navarro De Lara,
Massachusetts General Hospital,
Harvard Medical School,
United States

***Correspondence:**
Hamzah Magsood
magsoodha@mymail.vcu.edu
Ravi L. Hadimani
rhadimani@vcu.edu

Specialty section:
This article was submitted to Brain Imaging and Stimulation, a section of the journal Frontiers in Human Neuroscience

Received: 30 October 2019
Accepted: 17 March 2020
Published: 03 April 2020

Citation:
Magsood H, Syeda F, Holloway K, Carmona IC and Hadimani RL (2020) Safety Study of Combination Treatment: Deep Brain Stimulation and Transcranial Magnetic Stimulation.
Front. Hum. Neurosci. 14:123.
doi: 10.3389/fnhum.2020.00123

Patients with advanced Parkinson's disease (PD) often receive deep brain stimulation (DBS) treatment, in which conductive leads are surgically implanted in the brain. While DBS treats tremor and rigidity, patients often continue to suffer from speech and swallowing impairments. There is preliminary evidence that transcranial magnetic stimulation (TMS) of the cortex may be beneficial for these symptoms. However, the potential electromagnetic interactions of the strong magnetic fields from TMS on the conductive leads is unknown, and the combination therapy has not been approved for use. In this article, we report an experimental study of the safety of combining DBS and TMS. We fabricated an anatomically accurate head and brain phantom with electrical conductivities matching cerebrospinal fluid and averaged conductivity of gray and white matter. Induced current on an implanted DBS probe in the brain phantom was measured. Our results show that TMS will induce current values in the range or higher than typical DBS stimulation current. Thus, the combination of TMS/DBS treatment might cause over-stimulation in the brain when stimulated directly over the DBS lead with 100% TMS current intensity.

Keywords: DBS, TMS, Parkinson's, safety study, combined treatment, experimental, head models

INTRODUCTION

Patients with Parkinson's disease (PD) suffer from debilitating symptoms, including bradykinesia, resting tremor, shuffling gait, and rigidity as well as hypophonic speech and swallowing difficulties (Hartelius and Svensson, 1994; Chaudhuri et al., 2006; Jankovic, 2008). Although the symptoms initially respond to Levodopa, a dopaminergic medication, the symptoms often become refractory or side effects of the medications can cause additional symptoms (Marsden and Parkes, 1976, 1977; Melamed, 1979). In these cases, physicians recommend deep brain stimulation (DBS) surgery, in which one or two electrical leads are inserted into the subthalamic nucleus (STN) or globus pallidus internus (GPi), and an electrical current is continuously delivered to these nuclei from a battery pack inserted into a chest pocket as it is on an "On" state (Perlmutter and Mink, 2006; Coffey, 2009; Lozano and Lipsman, 2013). DBS has been shown to effectively

improve motor symptoms in patients of both PD as well as essential tremor (Koller et al., 2001; Perlmutter and Mink, 2006; Coffey, 2009). However, one of the more crippling symptoms of PD that is not treated by DBS is hypophonic speech and swallowing difficulty (dysphagia). Not surprisingly, hypophonia and dysphagia can seriously deteriorate the quality of life and cause complications such as weight loss, isolation, and depression (Schrag et al., 2000; Plowman-Prine et al., 2009; Crary et al., 2012). Importantly, these symptoms typically present well after the other motor symptoms have become problematic, thus most patients with speech and swallowing symptoms will have received DBS by the time of onset. The mouth motor area of the primary motor cortex is thought to play a role in the pathophysiology of these symptoms, and manipulation of this cortex through repetitive Transcranial Magnetic Stimulation (rTMS) has been proposed as a treatment option (Hartelius and Svensson, 1994; Pascual-Leone et al., 1994, 1995; Fox et al., 2001; Blank et al., 2002; Kobayashi and Pascual-Leone, 2003). rTMS is a non-invasive neuromodulation therapy that utilizes time-varying magnetic fields to induce electric fields in the patient's brain, thus stimulating neurons in the targeted region (George et al., 1999, 2000). However, the potential for electromagnetic interference from the magnetic fields of rTMS with the conductive leads of DBS has precluded clinical implementation of the combination therapy. Primarily, there is concern regarding eddy currents, which are induced on conductive surfaces caused by time-varying magnetic fields. It is hypothesized that B-fields from rTMS may induce such currents on the surface of any conductive part of the lead, and this current would travel along the lead down to the contacts, in turn stimulating the deep brain nuclei which the contacts target. We posit that this issue has yet to be studied with accurate models and parameters. In the past, studies have considered the implications of combining DBS with rTMS, but we argue that these studies are quite limited. Some have underestimated and oversimplified the geometrical complexities of the lead and biological tissue (Deng et al., 2010). Besides, we are not aware of any studies as of yet which have used physical models with accurate head and brain geometry and impedances to study the effects of TMS on full implanted DBS leads (Kumar et al., 1999; Deng et al., 2010; Shimojima et al., 2010; Kühn and Huebl, 2011). The consideration of the accurate impedances and geometries account for any energy couplings of displacement currents with the induced current in the DBS lead. A brief literature review outlining differences between these publications and our present work, including general methods and findings, is presented in **Table 1**.

We have previously studied the effects of TMS on a conductive cylinder and individual lead contacts in deep brain regions. We focused on the E-field induced in the brain tissues surrounding the conductive probe and found that although there was a slight increase in E-field in the tissues surrounding the lead, E-field values did not come close to the stimulation threshold (Syeda et al., 2017). However, that study did not include the geometrical complexities of DBS wires within the lead; these model details would enable a more comprehensive study of TMS-induced current inside the lead body. While E-field at the contact locations may not have reached the stimulation threshold, it is crucial to determine the current induced in the conductive wires, as this current would potentially lead to deep brain stimulation. In our previous study, we did not consider a closed loop and the simulation was applied at motor threshold instead of 100% TMS power. In this article, we report an experimental study of the safety of combining DBS and TMS in a realistic head phantom. We fabricated an anatomically accurate head and brain phantom based on MRI images developed into the brain model using FreeSurfer, simNIBS, and FSL pipelines. The head phantom is fabricated with electrical conductivities matching cerebrospinal fluid and averaged conductivity of gray and white matter. Induced current on an implanted DBS probe in the brain phantom was measured.

rTMS is currently FDA-approved for the treatment of a drug-resistant major depressive disorder but has shown beneficial effects for symptoms of other neurological conditions (George et al., 1999; Klein et al., 1999; Wassermann and Lisanby, 2001; Khedr et al., 2005). During TMS, alternating current is run through a figure-of-8 coil, which causes a time-varying magnetic field. This B-field then propagates through the patient's skull and onto the brain cortex, where an electric field is induced and neurons in the targeted cortical region are depolarized (Chen et al., 1997; George et al., 1999; Wassermann and Lisanby, 2001). rTMS in the mouth area of the primary motor cortex may help relieve hypophonia and dysphagia by similarly induced plasticity (Pascual-Leone et al., 1994, 1995; Kobayashi and Pascual-Leone, 2003).

Because TMS induces a time-varying magnetic field, it is important to consider the effects of TMS on conductive DBS leads. From Faraday's law of induction, it is clear that any time-varying magnetic field will induce an electric field on a conductive substance and a subsequent eddy currents on the conductive surfaces of the lead wires. In this study, we explore factors that mediate the intensity of this current. Furthermore, the location of the lead tip is typically at similar sites in each patient, at the GPi or STN. However, it is also important to note that the course of the additional lead body lying on the surface of the skull is closest to the TMS coil. Therefore, it is important to consider the distance between the lead and TMS coil.

MATERIALS AND METHODS

Generally, clinicians use either bipolar configuration or unipolar configuration of DBS. In the bipolar configuration, the current is delivered to one contact such that the voltage difference between the contact and its neighboring contact creates a sphere of potential at the stimulation location. In the unipolar configuration, the generator case is positive and a single contact is negative (McIntyre et al., 2004; Butson and McIntyre, 2005; Wei and Grill, 2005). The current induced in either of these configurations, on the order of mA, must be compared against current-induced due to TMS B- fields. Therefore, we have tested these leads in the "OFF" position, with no direct current applied to the leads.

TABLE 1 | Previous publications studying the safety of combination transcranial magnetic stimulation/deep brain stimulation (TMS/DBS) treatments.

Publication	Methods	Current Induced in DBS Leads	Results/Notes
Kumar et al. (1999)	Homogeneous phantom head model. TMS at 100% intensity performed 1 cm above leads. Voltage measured between contacts.	70–125 μA	Induced current lower than DBS stimulation.
Shimojima et al. (2010)	Homogeneous phantom head model. TMS applied at various locations along head model Impedance used: 1,162 Ω	>20 $\mu C/cm^2$/phase	Current too high for stimulation to be performed safely.
Kühn and Huebl (2011)	TMS at 100% intensity with DBS ON at 4V. Voltage measured between contacts.	0.2–2.8 V	Voltage does not exceed DBS stimulation and TMS duration is too short to cause stimulation.
Deng et al. (2010)	Created full circuit from contacts to chest IPG. Did not use full DBS lead geometry.1.2 kΩ resistor with contacts.	Up to 83 mA. If DBS is OFF, current is only possible at V >5V.	Induced current too high for stimulation to perform safely.
Kühn et al. (2002)	Clinical investigation of five patients with bilateral DBS and TMS in the Motor Cortex.	N/A	Contralateral and ipsilateral motor-evoked potentials were induced in 3/5 patients from TMS. No other complications reported.
Hidding et al. (2006)	Clinical investigation of eight Parkinson's patients with DBS, and mono pulse TMS in the Motor Cortex.	N/A	MEP latencies were significantly shortened, possibly due to current induced from TMS. No other complications reported.
Current work	Anatomically accurate head phantom. TMS at 100% intensity	(1.71–3.20 mA)	Induced current higher than DBS stimulation.

Moreover, we have assumed that the surgeon has tunneled the lead directly posteriorly towards the vertex so that the subgaleal lead is relatively medial, while the TMS coils are placed laterally and inferiorly to access the ipsilateral mouth motor cortex.

Anatomically Realistic Head Phantom With Implanted DBS Preparation

We fabricated an anatomically accurate head/brain phantom with an implanted DBS probe at the hypothetical STN location. The head model consists of four main parts: (1) the brain phantom; (2) skull, skin, and scalp; (3) cerebrospinal fluid; and (4) implanted DBS probe. The process of creating the brain and head phantom can be found in detail in our published patent where we show the detailed steps for creating each part of the head phantom (Magsood et al., 2019; Magsood and Hadimani, Under Review). In the following sections, we briefly show a general procedure to obtain each part of the head phantom with an implanted DBS.

Brain Phantom

The brain phantom was fabricated using a healthy subject's MRI images downloaded from the online database of human connectome project HCP, Parkinson's Progression Marker Initiative (PPMI; Human Connectome Project HCP, 2018). The MRIs were segmented and a 3D brain model was developed into an stl format using FreeSurfer (Athinoula A. Martinos Center for Biomedical Imaging, Charlestown, MA, United States), SimNIBS (Danish Research Centre for Magnetic Resonance, DRCMR), and FSL (Analysis Group, Oxford, UK) software. From the model, we created shells to serve as molds for the segments of the brain. For example, to create the gray matter we used the head model and created the outer shells of the gray matter. These shells were 3-D printed and were used as molds for the constituent material of the brain phantom. A conductive polymer composite was prepared to mimic the electrical conductivity of the brain. The conductive polymer composite is composed of multi-walled carbon nanotubes (MWCNT) and polydimethylsiloxane (PDMS). The addition of the MWCNT to the PDMS imparts an electrical conductivity depending on the concentration of the MWCNT. The conductive polymer is poured into the molds and left to solidify. After the solidification, the molds are immersed in acetone to be removed and to obtain the accurate anatomy of the brain matching the MRI. The brain phantom was fabricated with a measured impedance of 450–500 Ω that matches the average impedance of the human brain (Gabriel et al., 1996, 2009; Latikka et al., 2001; Akhtari et al., 2016; Michel et al., 2017).

Skin, Scalp and Skull

Skin, scalp, and the skull were built as a single layer with the shelling method used to obtain the brain phantom. But in this case, we used only PDMS as the constituent material because the electrical conductivities of these regions are low and similar to PDMS.

Cerebrospinal Fluid

The gap between the brain and the skull is the CSF space. We filled this space with a saline solution that has an electrical conductivity similar to the CSF conductivity in human which is about 1.0–1.2 Sm^{-1}.

Implanted DBS Probe

DBS leads are comprised of four electrodes which lie at the site of stimulation, with four separate wires capable of delivering current to each contact. Each wire is wrapped in insulation to avoid interference with the other wires, and there is further insulation that comprises the entirety of the probe

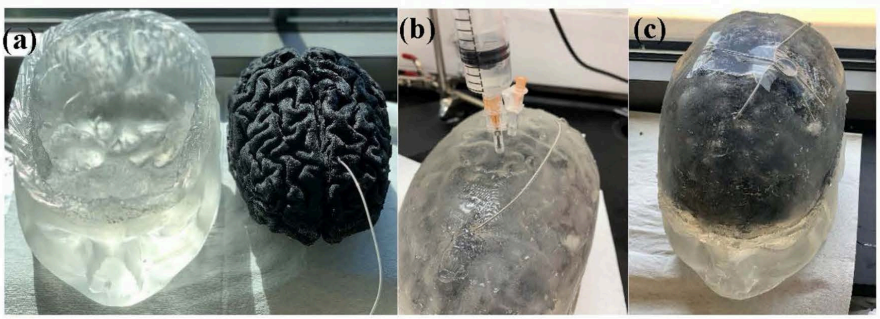

FIGURE 1 | (A) Head model with skin, scalp and skull (left) and brain phantom with the implanted deep brain stimulation (DBS) probe (right). **(B)** Head phantom is enclosed and the saline solution that mimics the cerebrospinal fluid (CSF) is being injected into the head phantom. **(C)** Final realization of the anatomically accurate head phantom with the implanted DBS probe.

FIGURE 2 | Experimental set-up where time-varying magnetic field by the transcranial magnetic stimulator is applied on the physical head phantom.

body. We used a commercial DBS lead (Medtronic 3387 lead) commonly used in DBS surgeries (Medtronic Lead Kit for DBS Stimulation, 2016).

The DBS probe was inserted into the conductive polymers during the solidification and through a guided opening on the brain phantom molds. After the solidification of the brain phantom, the molds were removed. We should note that we kept the stylet, supporting material, of the DBS probe to protect the integrity and structure of the wires inside the probe from damage. The DBS probes are very delicate and prone to damages as reported by the FDA (FDA, 2013). We believe that the presence of stylet has a negligible effect on the induced current in the lead wires as it is electrically isolated from the rest of the probe structure. The inside volume of the helical coils of the probe undergoes Faraday's cage effect and hence the stylet will experience no induced electric field (Chapman et al., 2015).

The final realization of the brain phantom that includes the realistic brain phantom and mimicked Cerebrospinal fluid (CSF) with implanted DBS probe in the hypothetical STN is seen in **Figure 1C**.

Experimental Setup and Measurement of the Induced Current

An FDA-approved TMS device, Magstim (model: Rapid 2 with Magstim AirFilm coils) was used to apply TMS to the physical head phantom. TMS coils were placed about 1 cm on top of the DBS lead. The magnetic field was applied from 50% to 100% TMS coil's current intensity with a single pulse and signal frequency of 2,500 Hz. The probe has one loop winding on top of the phantom. Then, we measured the induced voltage by measuring the voltage difference between the lead contacts and converted them into induced currents. The experimental set up is shown in **Figure 2** and the circuital diagram is shown in **Figure 3**.

In **Figure 3**, we show a schematic diagram of the circuit used to measure the induced voltage/current on the DBS. The circuit consists of two main parts A and B. Part A represents the equivalent impedance Z_{eq} of the brain phantom. In a real patient, this impedance would be the impedance of the neighboring regions of the inserted DBS leads. Part B represents the DBS probe and DBS pulse generator's internal resistance and it is typically about 100 Ω (Deng et al., 2010). The resultant voltage waveform is shown in **Figure 4** and the voltage values corresponding to coils' intensities 50–100% are shown in **Figure 5**.

RESULTS

Figure 4 shows the bi-phasic waveforms obtained during the measurements. The waveform shown here corresponds to the

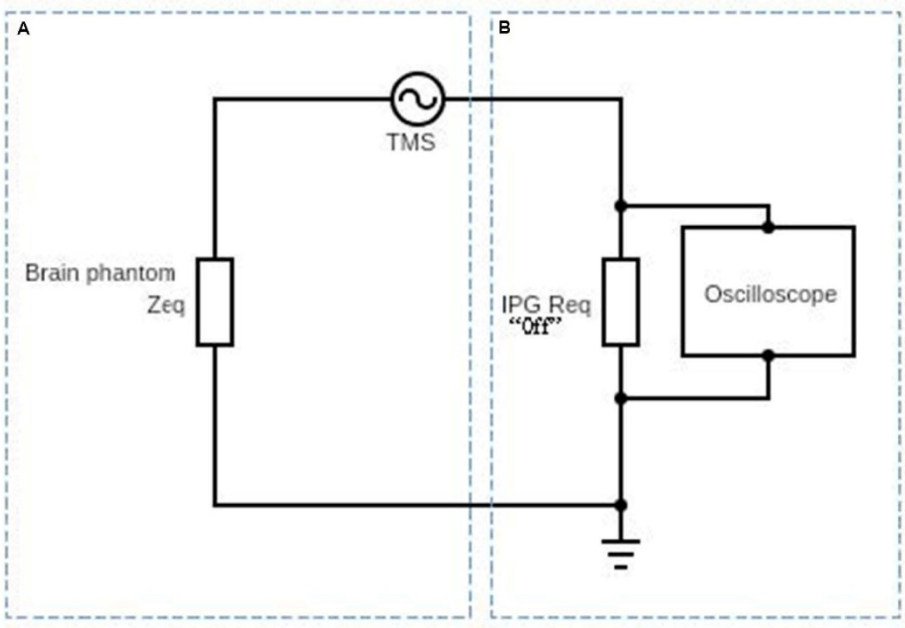

FIGURE 3 | Schematic diagram af the circuit used to obtain the induced electric current on the DBS probe in the presence of the time-varyingmagnetic field. Part (**A**) represents the equivalent impedance Z_{eq} of the brain phantom. Part (**B**) represents the DBS probe and DBS pulse generator's internal resistance and it is typically about 100 Ω (Deng et al., 2010).

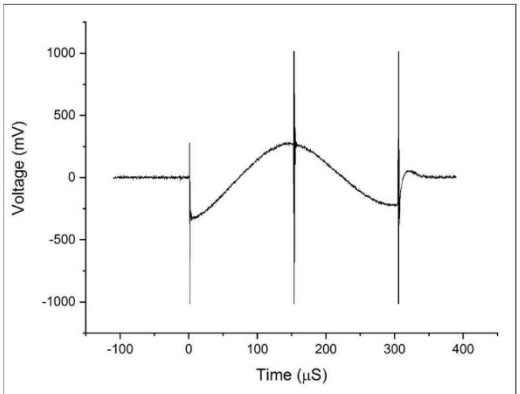

FIGURE 4 | The waveforms obtained from the voltage measurements on the DBS probe during transcranial magnetic stimulation (TMS).

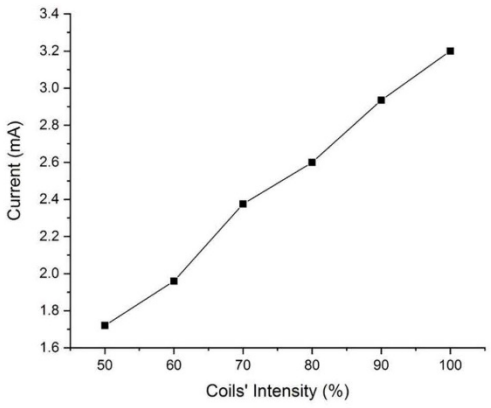

FIGURE 5 | Induced currents with respect to TMS coil's intensities.

measured induced voltage at 100% coils intensity. The waveform obtained with minor artifacts at the ends potentially due to an abrupt transition of the original pulse of the magnetic field and the artifact in the middle is a result of minor variations

in the electric field due to switching off power transistor inside the TMS stimulator. **Figure 5** shows the currents induced concerning changing the magnetic field strength produced by the TMS coils. The induced voltages are converted directly to induced current by dividing the voltage drop by the value of Req = 100 Ω.

DISCUSSION

From the results of the experiments on the physical head phantom, the induced current values are of the order of mA (1.71–3.20 mA), which are in the range of current values used in DBS (3.2–4.5 mA; Ramirez de Noriega et al., 2015). They are higher than values reported by Kumar et al. (1999) where they reported induced current in the range of 70–120 μA. Kühn and Huebl (2011) reported voltages in the rage of 0.2-2.8 V but indicated that the induced current duration was very short and did not reach the stimulation amplitude by the DBS therapy. However, Deng et al. (2010) reported higher values, in the range of 12.75–83 mA and (Shimojima et al., 2010) reported current density of 20 $\mu C/cm^2$/phase which considered to be exceeding the safety threshold. Therefore, our measured values are consistent with Deng et al. (2010) and Shimojima et al. (2010). We theorize that the variation in the results may be due to several factors, the accuracy of the real DBS probe geometry, the medium in which the DBS probe is implanted, and the design and values of the electrical components of the complete circuit. We have experimentally measured the induced voltages and currents in the widely used Medtronic DBS lead. We accounted for the complexity of the brain anatomy and geometry. In our experimental model, we used our novel anatomically accurate brain and head phantom that mimics the impedance/conductivity of the brain as well as the CFS. Previous studies either lack geometrical accuracy of the medium in which the DBS probes were inserted in, DBS probe and lead design, or accurate impedance values. The geometry and impedance of the medium are important because they determine the magnitude of the electric field produced and in turn contribute to the current induced in the DBS probe. Such considerations will help to expand the study to include other DBS configurations and TMS coil orientations and placement. Thus, considering the prior work in the literature of TMS and DBS safety, our study is an improved analysis considering a more accurate brain phantom, actual DBS probe with accurate impedance. Previous studies showed that with the increased number of loops, induced current will increase promotionally. In this work we show that even with single loop, the current induced is on the range of unsafe limits. Moreover, **Figure 4** shows that even at lower coil intensities, the induced current are noticeable and are in the mA range.

There are other sources of risk form such combination techniques like Lorentz forces. However, previous work by Shimojima et al. (2010) showed that there are no detectable movements on the DBS lead inserted in a gelatin phantom and therefore the risk from Lorentz forces is negligible. For that reason, and since our results show that it might be unsafe to combine DBS with TMS, we did not investigate other possible risks such as Lorentz forces in our study.

CONCLUSION

In this work, we investigated the safety of combining DBS with TMS treatments. We developed an accurate physical model with commercially used DBS lead. Our measurements show that using a time-varying magnetic field applied by 100% TMS intensity in the presence of DBS will induce currents that are higher than the safe limits (3.2–4.5 mA) which may result in over-stimulation. These results are in an agreement with previous studies that considered the safety of the combination of TMS with DBS. We attempted to minimize the sources of errors that might result in higher variation in the result. We only used a simple configuration with one loop on the wire and used an accurate brain and head phantom that match the geometry and an averaged electrical conductivity. Our results suggest that even with the simplified setup, the level of induction is above the unsafe limits. Therefore, we recommend that the TMS should not be applied at 100% intensity directly over the implanted DBS leads in the STN area.

DATA AVAILABILITY STATEMENT

The datasets generated for this study are available on request to the corresponding author.

AUTHOR CONTRIBUTIONS

HM: manuscript drafting, created accurate and complex computational head models as well as the novel anatomically realistic brain and head phantom, and performed the experimental side of the research. FS: helped in manuscript drafting and evaluation. IC: assisted in the experiment and designed the circuit to acquire the induced current. KH: helped to conceive the research ideas and gave insightful inputs for the simulation and experimental parameters. RH: principal investigator, conceived the research idea, manuscript drafting, and evaluation.

FUNDING

This study was partly funded by Virginia Commonwealth University (VCU)—College of Engineering start-up funds and from the Saudi Arabian Ministry of Higher Education Scholarship Program.

ACKNOWLEDGMENTS

We are thankful to Dr. Deepak Kumbhare for helpful comments and consultation.

REFERENCES

Akhtari, M., Emin, D., Ellingson, B. M., Woodworth, D., Frew, A., and Mathern, G. W. (2016). Measuring the local electrical conductivity of human brain tissue. *J. Appl. Phys.* 119:064701. doi: 10.1063/1.4941556

Blank, S. C., Scott, S. K., Murphy, K., Warburton, E., and Wise, R. J. (2002). Speech production: wernicke, broca and beyond. *Brain* 125, 1829–1838. doi: 10.1093/brain/awf191

Butson, C. R., and McIntyre, C. C. (2005). Role of electrode design on the volume of tissue activated during deep brain stimulation. *J. Neural Eng.* 3, 1–8. doi: 10.1088/17412-560/3/1/001

Chapman, S. J., Hewett, D. P., and Trefethen, L. N. (2015). Mathematics of the faraday cage. *SIAM Rev.* 57, 398–417. doi: 10.1137/140984452

Chaudhuri, K. R., Healy, D. G., and Schapira, A. H. V. (2006). Non-motor symptoms of Parkinson's disease: diagnosis and management. *Lancet Neurol.* 5, 235–245. doi: 10.1016/S1474-4422(06)70373-8

Chen, R., Classen, J., Gerloff, C., Celnik, P., Wassermann, E. M., Hallett, M., et al. (1997). Depression of motor cortex excitability by low-frequency transcranial magnetic stimulation. *Neurology* 48, 1398–1403. doi: 10.1212/wnl.48.5.1398

Coffey, R. J. (2009). Deep brain stimulation devices: a brief technical history and review. *Artif. Organs* 33, 208–220. doi: 10.1111/j.1525-1594.2008.00620.x

Crary, M., Sura, L., Madhavan, A., and Carnaby-Mann, G. (2012). Dysphagia in the elderly: management and nutritional considerations. *Clin. Interv. Aging* 7, 287–298. doi: 10.2147/cia.s23404

Deng, Z. D., Lisanby, S. H., and Peterchev, A. V. (2010). Transcranial magnetic stimulation in the presence of deep brain stimulation implants: induced electrode currents. *Conf. Proc. IEEE Eng. Med. Biol. Soc.* 2010, 6821–6824. doi: 10.1109/IEMBS.2010.5625958

FDA. (2013). *Class 1 Device Recall Deep Brain Stimulation Lead Kit*. Available online at: https://www.accessdata.fda.gov/scripts/cdrh/cfdocs/cfres/res.cfm?id=116147.

Fox, P. T., Huang, A., Parsons, L. M., Xiong, J.-H., Zamarippa, F., Rainey, L., et al. (2001). Location-probability profiles for the mouth region of human primary motor-sensory cortex: model and validation. *NeuroImage* 13, 196–209. doi: 10.1006/nimg.2000.0659

Gabriel, S., Lau, R. W., and Gabriel, C. (1996). The dielectric properties of biological tissues: II. Measurements in the frequency range 10 Hz to 20 GHz. *Phys. Med. Biol.* 41, 2251–2269. doi: 10.1088/0031-9155/41/11/002

Gabriel, C., Peyman, A., and Grant, E. H. (2009). Electrical conductivity of tissue at frequencies below 1 MHz. *Phys. Med. Biol.* 54, 4863–4878. doi: 10.1088/0031-9155/54/16/002

George, M. S., Lisanby, S. H., and Sackeim, H. A. (1999). Transcranial magnetic stimulation: applications in neuropsychiatry. *JAMA Psychiatry* 56, 300–311. doi: 10.1001/archpsyc.56.4.300

George, M. S., Nahas, Z., Molloy, M., Speer, A. M., Oliver, N. C., Li, X.-B., et al. (2000). A controlled trial of daily left prefrontal cortex TMS for treating depression. *Biol. Psychiatry* 48, 962–970. doi: 10.1016/s0006-3223(00)01048-9

Hartelius, L., and Svensson, P. (1994). Speech and swallowing symptoms associated with Parkinson's disease and multiple sclerosis: a survey. *Folia Phoniatr. Logop.* 46, 9–17. doi: 10.1159/000266286

Hidding, U., Bäumer, T., Siebner, H. R., Demiralay, C., Buhmann, C., Weyh, T., et al. (2006). MEP latency shift after implantation of deep brain stimulation systems in the subthalamic nucleus in patients with advanced Parkinson's disease. *Mov. Disord.* 21, 1471–1476. doi: 10.1002/mds.20951

Human Connectome Project HCP. (2018). *Parkinson's Progression Marker Initiative*. Available online at: https://ida.loni.usc.edu/login.jsp?project=PPMI.

Jankovic, J. (2008). Parkinson's disease: clinical features and diagnosis. *J. Neurol. Neurosurg. Psychiatry* 79, 368–376. doi: 10.1136/jnnp.2007.131045

Khedr, E. M., Ahmed, M. A., Fathy, N., and Rothwell, J. C. (2005). Therapeutic trial of repetitive transcranial magnetic stimulation after acute ischemic stroke. *Neurology* 65, 466–468. doi: 10.1212/01.wnl.0000173067.84247.36

Klein, E., Kreinin, I., Chistyakov, A., Koren, D., Mecz, L., Marmur, S., et al. (1999). Therapeutic efficacy of right prefrontal slow repetitive transcranial magnetic stimulation in major depression. *Arch. Gen. Psychiatry* 56, 315–320. doi: 10.1001/archpsyc.56.4.315

Kobayashi, M., and Pascual-Leone, A. (2003). Transcranial magnetic stimulation in neurology. *Lancet Neurol.* 2, 145–156. doi: 10.1016/s1474-4422(03)00321-1

Koller, W. C., Lyons, K. E., Wilkinson, S. B., Troster, A. I., and Pahwa, R. (2001). Long-term safety and efficacy of unilateral deep brain stimulation of the thalamus in essential tremor. *Mov. Disord.* 16, 464–468. doi: 10.1136/jnnp.71.5.682

Kühn, A. A., and Huebl, J. (2011). Safety of transcranial magnetic stimulation for the newer generation of deep brain stimulators. *Parkinsonism Relat. Disord.* 17, 647–648. doi: 10.1016/j.parkreldis.2011.05.007

Kühn, A. A., Trottenberg, T., Kupsch, A., and Meyer, B. U. (2002). Pseudo-bilateral hand motor responses evoked by transcranial magnetic stimulation in patients with deep brain stimulators. *Clin. Neurophysiol.* 113, 341–345. doi: 10.1016/s1388-2457(01)00731-3

Kumar, R., Chen, R., and Ashby, P. (1999). Safety of transcranial magnetic stimulation in patients with implanted deep brain stimulators. *Mov. Disord.* 14, 157–158. doi: 10.1002/1531-8257(199901)14:1<157::aid-mds1027>3.0.co;2-u

Latikka, J. A., Hyttinen, J. A., Kuurne, T. A., Eskola, H. J., and Malmivuo, J. A. (2001). "The conductivity of brain tissues: comparison of results *in vivo* and *in vitro* measurements," in *2001 Conference Proceedings of the Annual Reports of the Research Reactor Institute* (Istanbul, Kyoto University: IEEE), 910–912.

Lozano, A., and Lipsman, N. (2013). Probing and regulating dysfunctional circuits using deep brain stimulation. *Neuron* 77, 406–424. doi: 10.1016/j.neuron.2013.01.020

Magsood, H., Serrate, C. H. A., El-Gendy, A. A., and Hadimani, M. L. R. (2019). *Anatomically Accurate Brain Phantoms and Methods for Making and Using the Same*. Google Patents.

Marsden, C. D., and Parkes, J. D. (1976). "On-off" effects in patients with Parkinson's disease on chronic levodopa therapy. *Lancet* 307, 292–296. doi: 10.1016/s0140-6736(76)91416-1

Marsden, C. D., and Parkes, J. D. (1977). Success and problems of long-term levodopa therapy in Parkinson's disease. *Lancet* 309, 345–349. doi: 10.1016/s0140-6736(77)91146-1

McIntyre, C. C., Mori, S., Sherman, D. L., Thakor, N. V. and Vitek, J. L. (2004). Electric field and stimulating influence generated by deep brain stimulation of the subthalamic nucleus. *Clin. Neurophysiol.* 115, 589–595. doi: 10.1016/j.clinph.2003.10.033

Medtronic Lead Kit for DBS Stimulation. (2016). *Biomedical Safety and Standards*. New York, NY: Ovid Technologies. doi: 10.1097/01.bmsas.0000508150.05478.86

Melamed, E. (1979). Early-morning dystonia. *Arch. Neurol.* 36, 308–310. doi: 10.1001/archneur.1979.00500410086014

Michel, E., Hernandez, D., and Lee, S. Y. (2017). Electrical conductivity and permittivity maps of brain tissues derived from water content based on T1-weighted acquisition. *Magn. Reson. Med.* 77, 1094–1103. doi: 10.1002/mrm.26193

Pascual-Leone, A., Nguyet, D., Cohen, L. G., Brasil-Neto, J. P., Cammarota, A., and Hallett, M. (1995). Modulation of muscle responses evoked by transcranial magnetic stimulation during the acquisition of new fine motor skills. *J. Neurophysiol.* 74, 1037–1045. doi: 10.1152/jn.1995.74.3.1037

Pascual-Leone, A., Valls-Solé, J., Wassermann, E. M., and Hallett, M. (1994). Responses to rapid-rate transcranial magnetic stimulation of the human motor cortex. *Brain* 117, 847–858. doi: 10.1093/brain/117.4.847

Perlmutter, J. S., and Mink, J. W. (2006). Deep brain stimulation. *Ann. Rev. Neurosci.* 29, 229–257. doi: 10.1146/annurev.neuro.29.051605.112824

Plowman-Prine, E. K., Sapienza, C. M., Okun, M. S., Pollock, S. L., Jacobson, C., Wu, S. S., et al. (2009). The relationship between quality of life and swallowing in Parkinson's disease. *Mov. Disord.* 24, 1352–1358. doi: 10.1002/mds.22617

Ramirez de Noriega, F., Eitan, R., Marmor, O., Lavi, A., Linetzky, E., Bergman, H., et al. (2015). Constant current versus constant voltage subthalamic nucleus deep brain stimulation in Parkinson's disease. *Stereotact. Funct. Neurosurg.* 93, 114–121. doi: 10.1159/000368443

Schrag, A., Jahanshahi, M., and Quinn, N. (2000). What contributes to quality of life in patients with Parkinson's disease? *J. Neurol. Neurosurg. Psychiatry* 69, 308–312. doi: 10.1136/jnnp.69.3.308

Shimojima, Y., Morita, H., Nishikawa, N., Kodaira, M., Hashimoto, T., and Ikeda, S. (2010). The safety of transcranial magnetic stimulation with deep brain stimulation instruments. *Parkinsonism Relat. Disord.* 16, 127–131. doi: 10.1016/j.parkreldis.2009.09.006

Syeda, F., Holloway, K., El-Gendy, A. A., and Hadimani, R. L. (2017). Computational analysis of transcranial magnetic stimulation in the presence of deep brain stimulation probes. *AIP Adv.* 7:56709. doi: 10.1063/1.4974062

Wassermann, E. M., and Lisanby, S. H. (2001). Therapeutic application of repetitive transcranial magnetic stimulation: a review. *Clin. Neurophysiol.* 112, 1367–1377. doi: 10.1016/s1388-2457(01)00585-5

Wei, X. F., and Grill, W. M. (2005). Current density distributions, field distributions and impedance analysis of segmented deep brain stimulation electrodes. *J. Neural Eng.* 2, 139–147. doi: 10.1088/1741-2560/2/4/010

Conflict of Interest: The authors declare that the research was conducted in the absence of any commercial or financial relationships that could be construed as a potential conflict of interest.

8.3 Appendix II: Patent:

US 20190057623A1

(19) **United States**

(12) **Patent Application Publication** (10) **Pub. No.: US 2019/0057623 A1**

Magsood et al. (43) **Pub. Date: Feb. 21, 2019**

(54) **ANATOMICALLY ACCURATE BRAIN PHANTOMS AND METHODS FOR MAKING AND USING THE SAME**

(71) Applicant: **Virginia Commonwealth University**, Richmond, VA (US)

(72) Inventors: **Hamza Magsood**, Henrico, VA (US); **Ciro H. Alcoba Serrate**, Richmond, VA (US); **Ahmed A. El-Gendy**, Richmond, VA (US); **Magundappa L. Ravi Hadimani**, Glen Allen, VA (US)

(21) Appl. No.: **16/104,217**

(22) Filed: **Aug. 17, 2018**

Related U.S. Application Data

(60) Provisional application No. 62/546,810, filed on Aug. 17, 2017.

Publication Classification

(51) **Int. Cl.**

G09B 23/28	(2006.01)
G09B 23/30	(2006.01)
A61N 2/00	(2006.01)
A61L 31/06	(2006.01)
A61L 31/02	(2006.01)
B29C 64/10	(2006.01)
B29C 33/38	(2006.01)
B29C 39/00	(2006.01)
G01R 33/58	(2006.01)

(52) **U.S. Cl.**

CPC ***G09B 23/286*** (2013.01); ***G09B 23/30*** (2013.01); ***A61N 2/006*** (2013.01); ***A61L 31/06*** (2013.01); *B33Y 80/00* (2014.12); ***B29C 64/10*** (2017.08); ***B29C 33/3842*** (2013.01); ***B29C 39/003*** (2013.01); ***G01R 33/58*** (2013.01); ***A61L 31/024*** (2013.01)

(57) **ABSTRACT**

Anatomically accurate brain phantoms are disclosed which may be patient specific and used for experimentally testing neuromodulation and neuroimaging procedures.

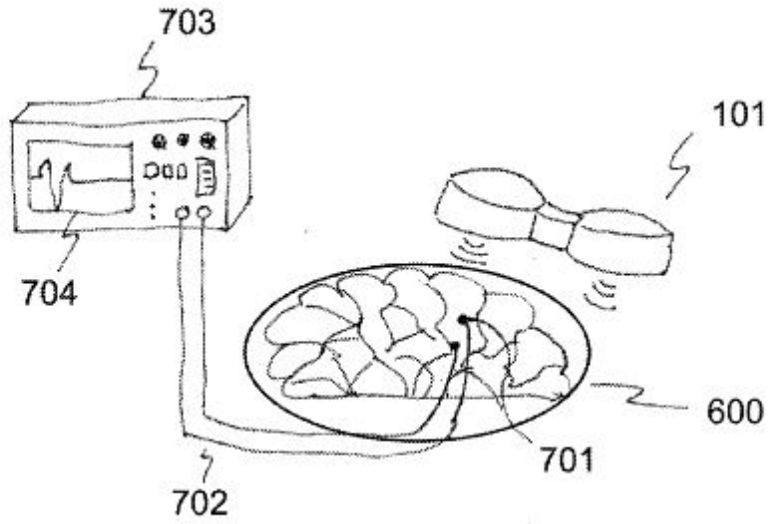

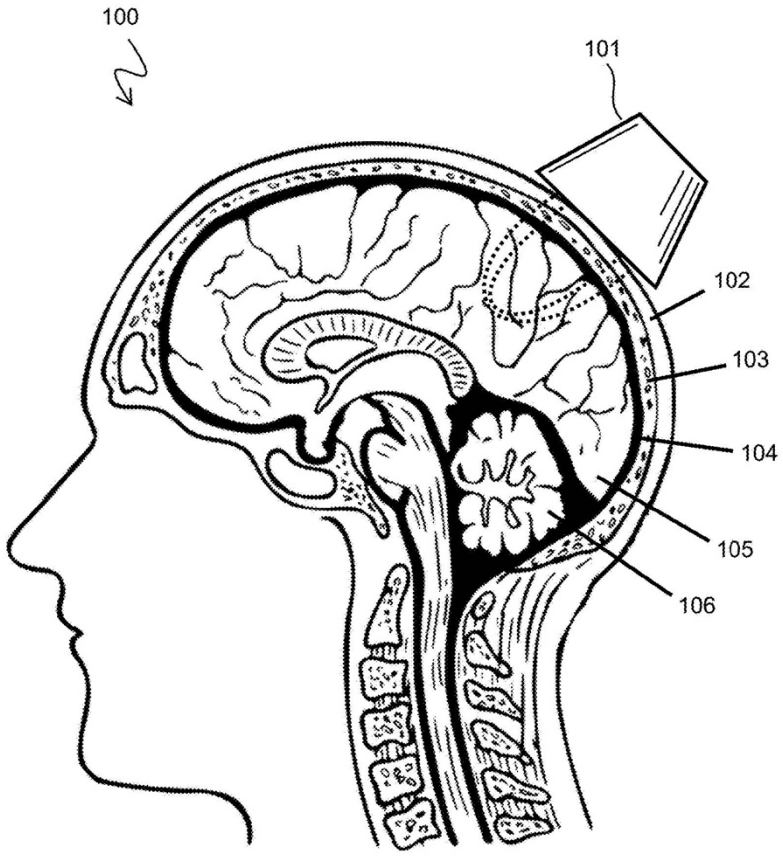

Figure 1

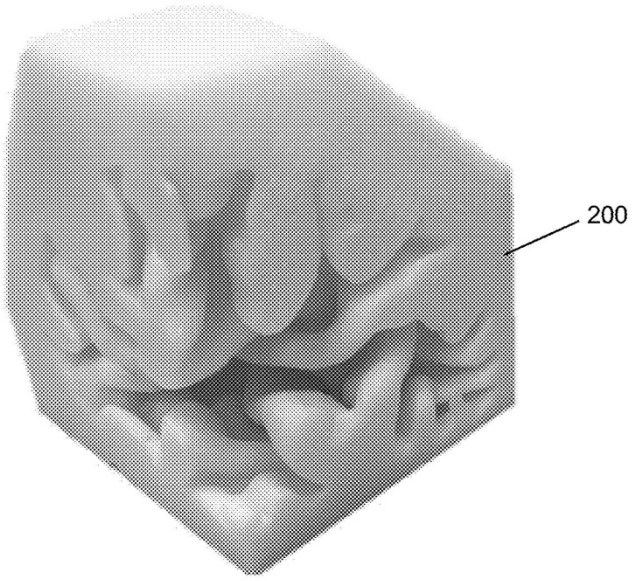

Figure 2A

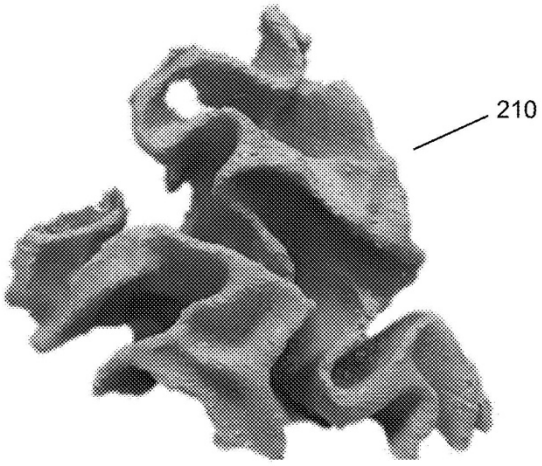

Figure 2B

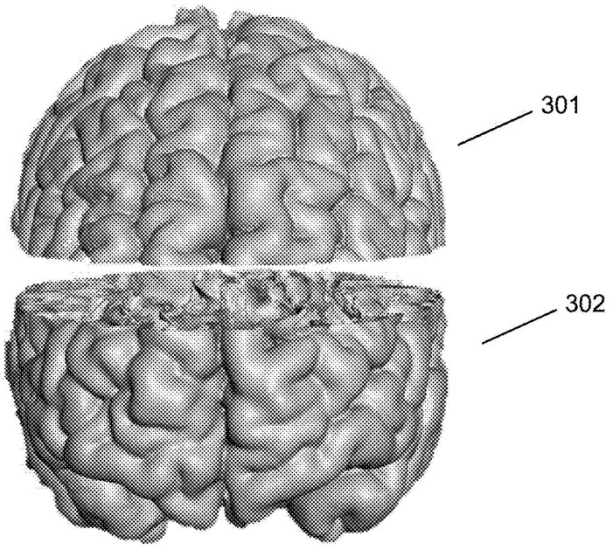

Figure 3A

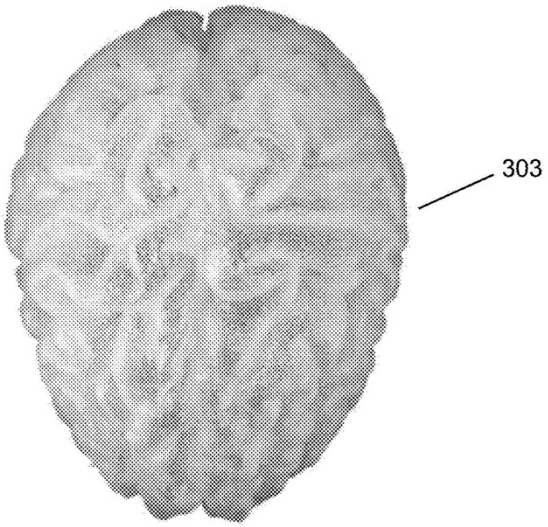

Figure 3B

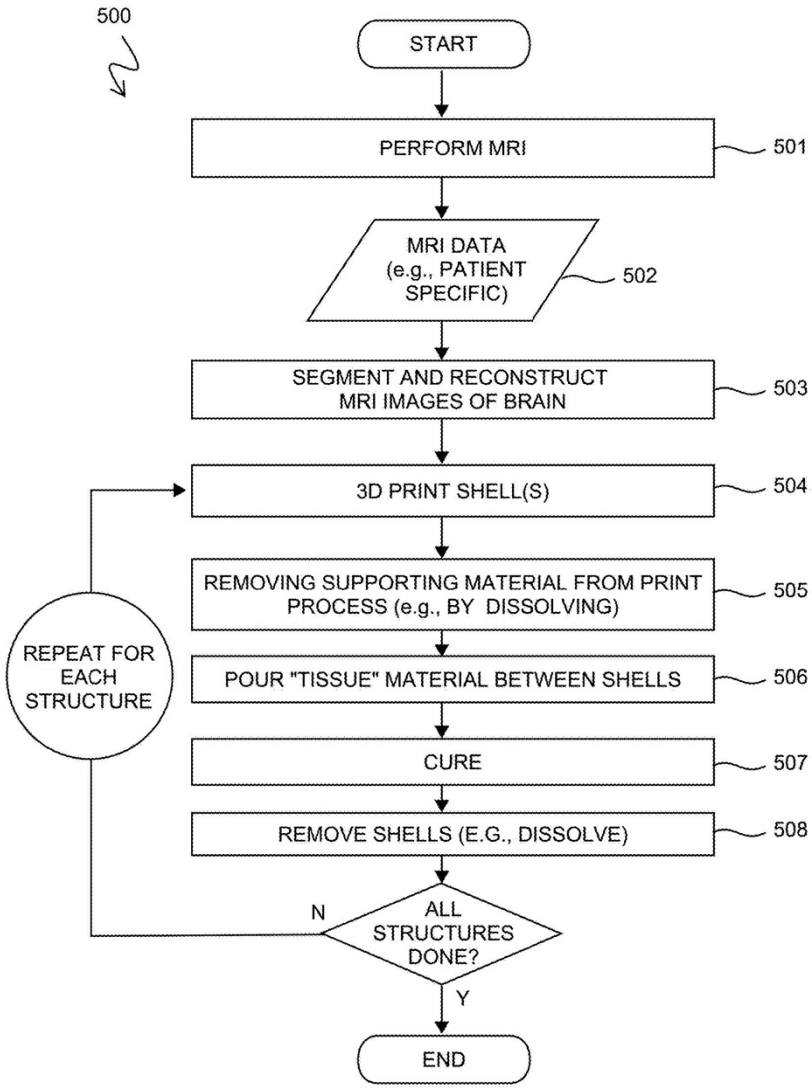
500
START
PERFORM MRI
501
MRI DATA (e.g., PATIENT SPECIFIC)
502
SEGMENT AND RECONSTRUCT MRI IMAGES OF BRAIN
503
3D PRINT SHELL(S)
504
REMOVING SUPPORTING MATERIAL FROM PRINT PROCESS (e.g., BY DISSOLVING)
505
POUR "TISSUE" MATERIAL BETWEEN SHELLS
506
CURE
507
REMOVE SHELLS (E.G., DISSOLVE)
508
ALL STRUCTURES DONE?
N
Y
REPEAT FOR EACH STRUCTURE
END

Figure 5

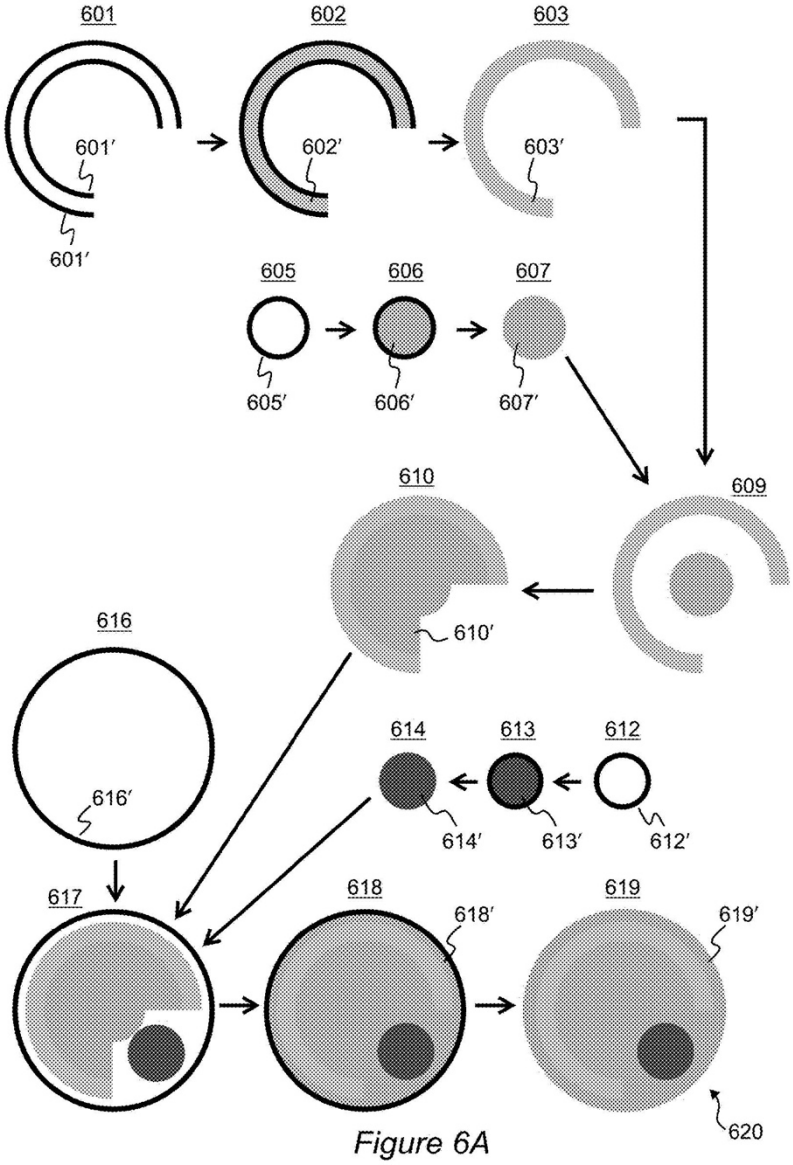
601
602
603
601′
602′
603′
601′
605
606
607
605′
606′
607′
610
609
610′
616
616′
614
613
612
614′
613′
612′
617
618
619
618′
619′
620

Figure 6A

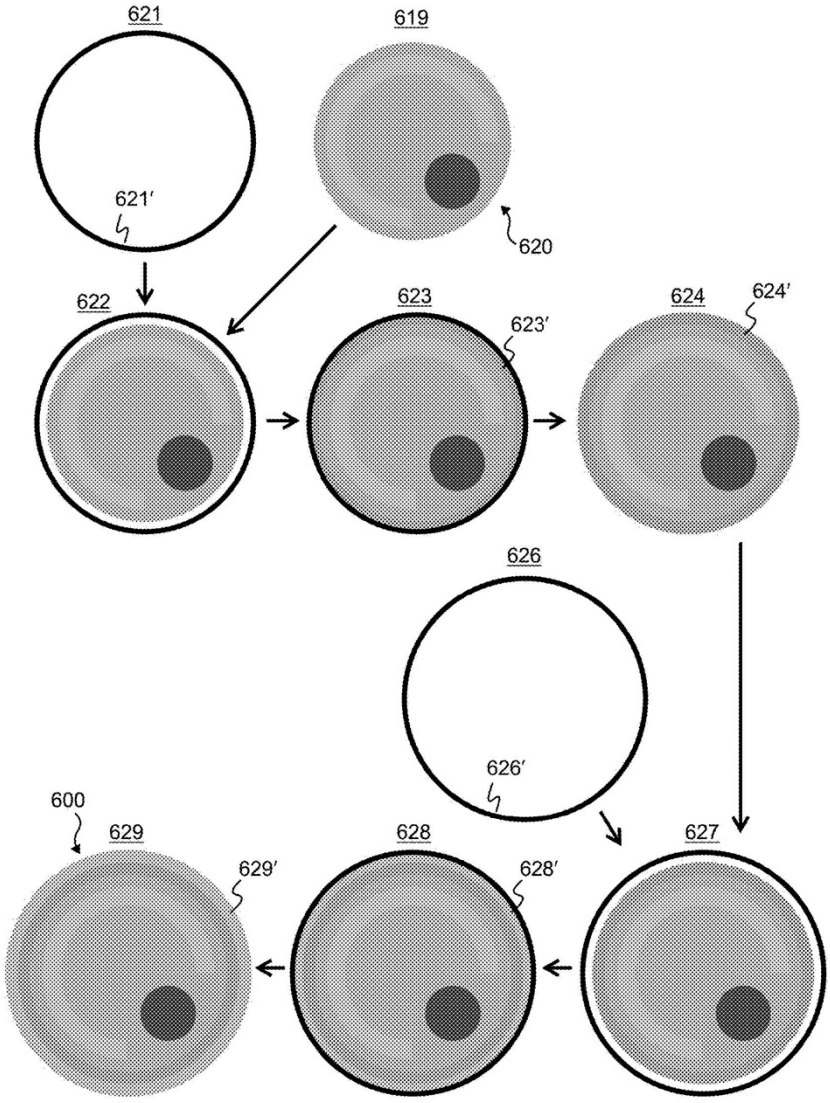
621
619
621′
620
622
623
623′
624
624′
626
626′
600
629
629′
628
628′
627

Figure 6B

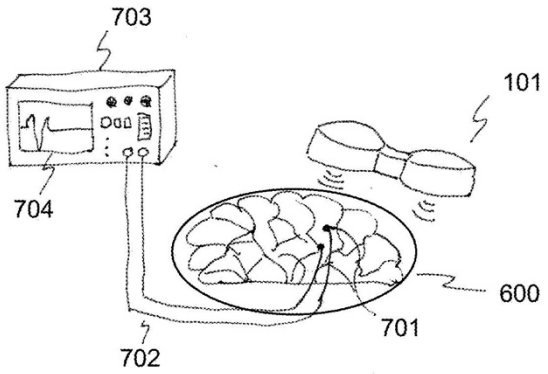

Figure 7

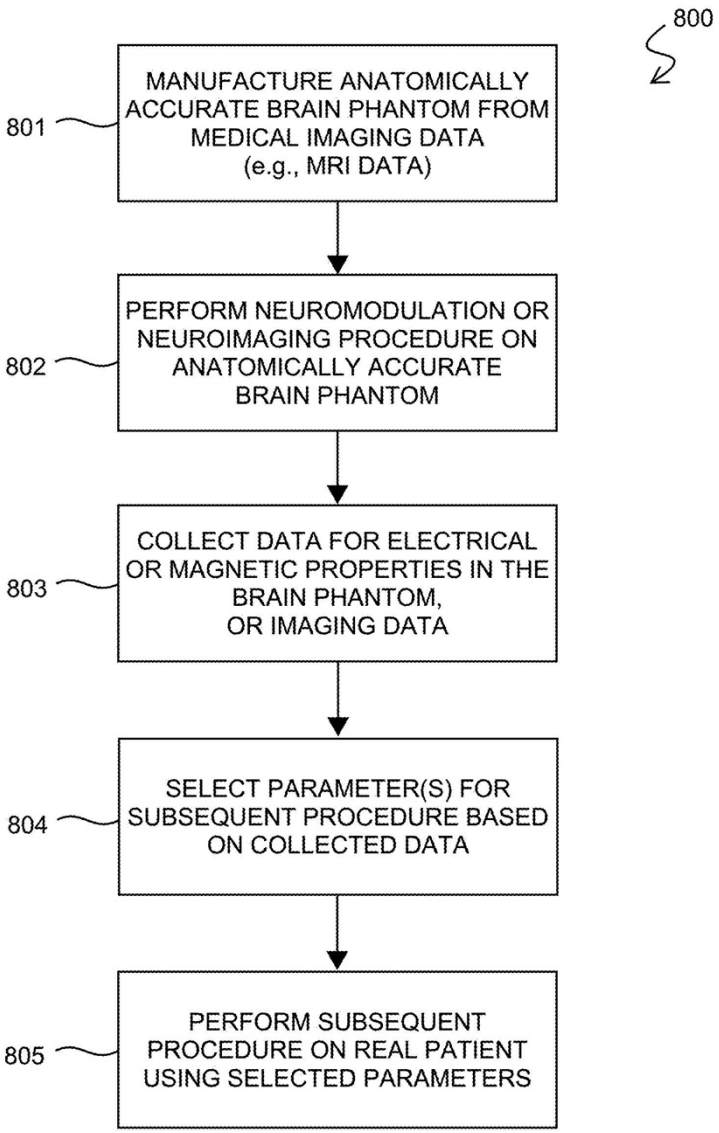
800
MANUFACTURE ANATOMICALLY ACCURATE BRAIN PHANTOM FROM MEDICAL IMAGING DATA (e.g., MRI DATA)
801
PERFORM NEUROMODULATION OR NEUROIMAGING PROCEDURE ON ANATOMICALLY ACCURATE BRAIN PHANTOM
802
COLLECT DATA FOR ELECTRICAL OR MAGNETIC PROPERTIES IN THE BRAIN PHANTOM, OR IMAGING DATA
803
SELECT PARAMETER(S) FOR SUBSEQUENT PROCEDURE BASED ON COLLECTED DATA
804
PERFORM SUBSEQUENT PROCEDURE ON REAL PATIENT USING SELECTED PARAMETERS
805

Figure 8

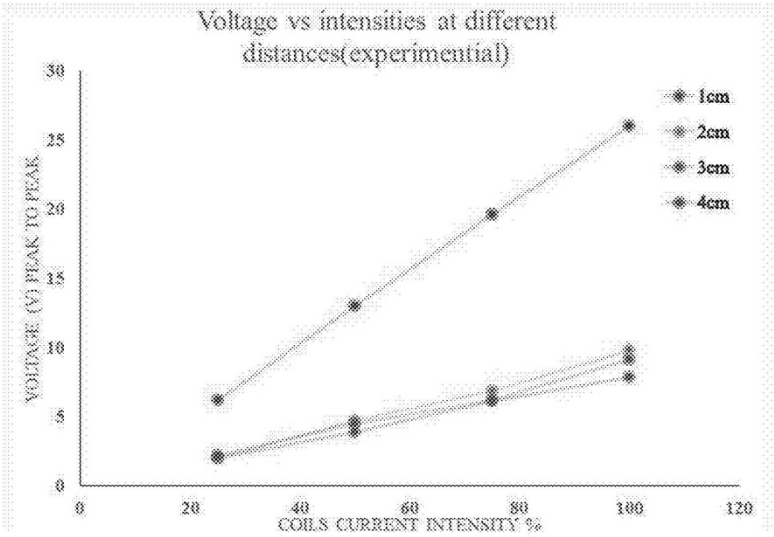
Voltage vs intensities at different distances(experimental)
VOLTAGE (V) PEAK TO PEAK
COILS CURRENT INTENSITY %
1cm
2cm
3cm
4cm
0
5
10
15
20
25
30
0
20
40
60
80
100
120

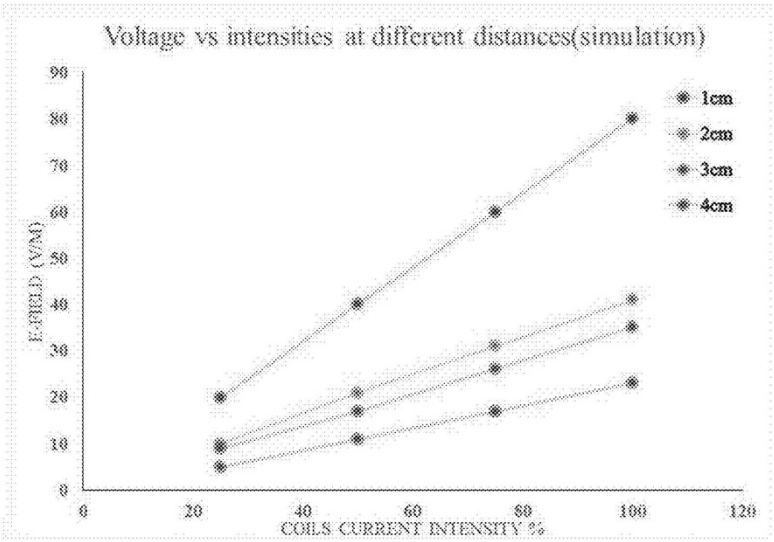
Voltage vs intensities at different distances(simulation)
E-FIELD (V/M)
COILS CURRENT INTENSITY %
1cm
2cm
3cm
4cm
0
10
20
30
40
50
60
70
80
90
0
20
40
60
80
100
120

Figure 9

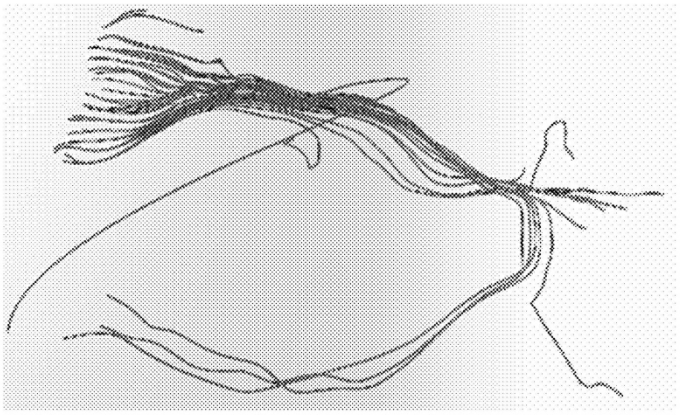

Figure 11

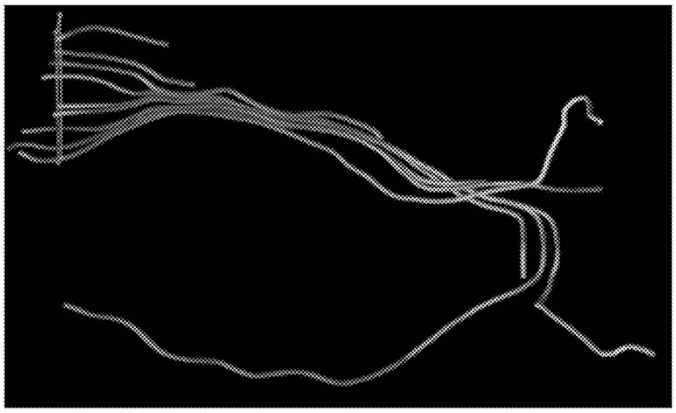

Figure 10

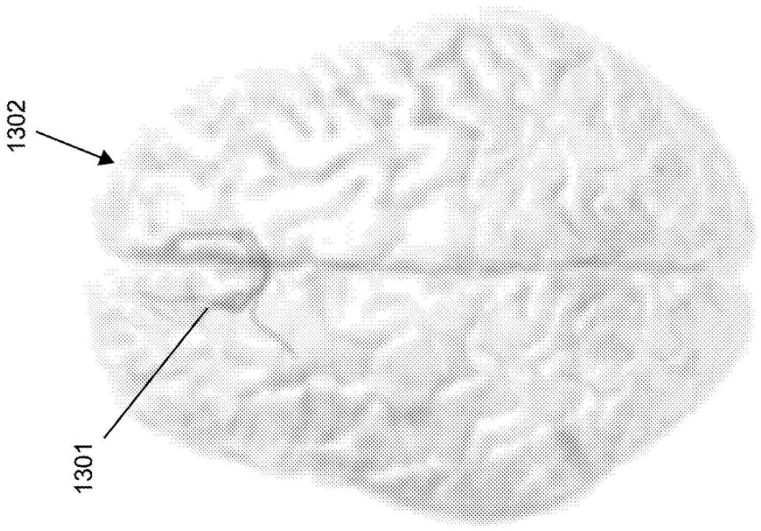

Figure 13

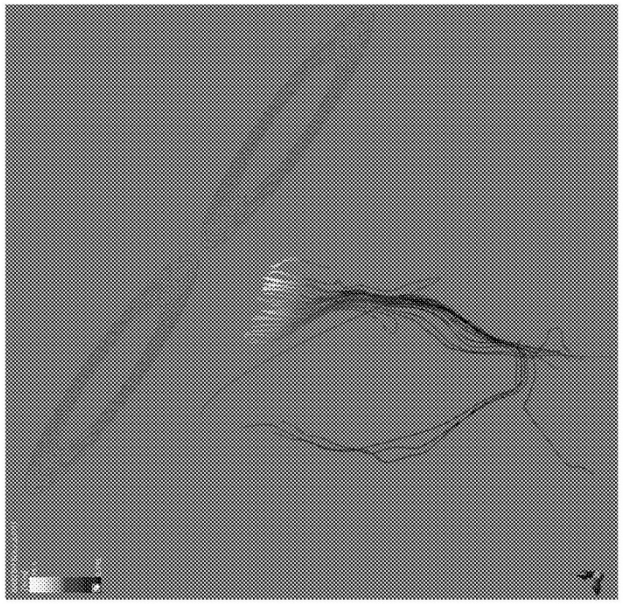

Figure 12

ANATOMICALLY ACCURATE BRAIN PHANTOMS AND METHODS FOR MAKING AND USING THE SAME

CROSS-REFERENCE TO RELATED APPLICATIONS

[0001] This application claims the benefit of U.S. Provisional Patent Application No. 62/546,810, filed Aug. 17, 2017, the complete contents of which are herein incorporated by reference.

FIELD OF THE INVENTION

[0002] The invention generally relates to anatomically accurate brain phantoms and, more particularly, unique brain phantoms, methods of making brain phantoms, and methods of using brain phantoms. In some embodiments brain phantoms are tailored for transcranial magnetic stimulation (TMS) simulation or other non-invasive neuromodulation techniques such as transcranial direct current stimulation (tDCS) or invasive neuromodulation techniques such as deep brain stimulation (DBS) or combination of invasive and non-invasive neuromodulation techniques.

BACKGROUND

[0003] Transcranial Magnetic Stimulation (TMS) is a non-invasive technique used for treatment and diagnosis of many neurological conditions and diseases. However, the experimental measurement of induced electric fields in the brain tissues is not well established or understood due to non-availability of anatomically realistic head/brain phantoms. The lack of anatomically realistic brain phantoms has made the experimental verification of induced electric fields in the brain tissues an impediment to the development of new treatment protocols.

[0004] Transcranial magnetic stimulation (TMS) is a non-invasive treatment for neurological and psychiatric disorders, but the strength of the induced electric field decreases with distance from the TMS coil and the precise nature of induced electrical and magnetic fields may not be safely measured in living patients being treated with TMS. Deep brain effects of TMS are still unclear and not well-studied.

SUMMARY

[0005] An aspect of some embodiments is a 3-D anatomically realistic brain phantom developed using segmentation of MRIs, construction of volumetric brain models, 3-D printing, casting using composite polymer that mimic the brain conductivities, or a combination thereof. Exemplary phantoms may be used for the purpose of evaluation of neuromodulation techniques such as Transcranial Magnetic Stimulation (TMS) or other non-invasive neuromodulation techniques such as transcranial direct current stimulation (tDCS) or invasive neuromodulation techniques such as DBS or combination of invasive and non-invasive neuromodulation techniques. The phantoms may also be used in the evaluation of quality assurance and quality control (QA/QT) of neuroimaging modalities like magnetic resonance imaging (MRI).

[0006] An aspect of some embodiments is the enablement of the professional in the field of brain modulation and treatment to test and preform actual brain stimulations that are accurate and matches the clinical setting of the of the treatments of TMS, tDCS, DBS or combination of them. There are currently no brain heterogenous phantoms that can experimentally verify TMS and tDCS parameters. Embodiments herein comprise brain phantoms and experimental verification of TMS, tDCS, DBS or combination treatment parameters with such brain phantoms.

[0007] An exemplary method is capable of producing patient specific three dimensional anatomically realistic head and brain models from MRI data. It may be used to test the safety of neuroimaging and invasive and non-invasive neuromodulation procedures prior to them being performed on the actual patient.

[0008] Exemplary embodiments may involve a 3-D anatomically realistic brain phantom that mimics the electrical conduction and mechanical stiffness of the brain. An exemplary phantom is producible using MRI images, software for brain tissue segmentation and image reconstruction, a 3-D printer, and polymer with conductive fillers. Varied loading of fillers may be used to differentiate different types of tissue in the brain or in the head.

[0009] In some embodiments, brain tissues of phantoms are divided into cerebrospinal fluid (CSF), white matter (WM), grey matter (GM), ventricles (containing CSF), and cerebellum. In an exemplary phantom according to the present invention, shells are printed for each tissue layer/structure of the brain and head. After printing the shells are filled with a conductive material (e.g., polydimethyl-siloxane (PDMS) or silicon with nanoparticles) that is capable of mimicking the conductive properties of different brain tissues.

[0010] In contrast to commercially available concentric spherical phantoms, exemplary embodiments disclosed herein involve producing anatomically accurate phantoms quickly and economically through 3D printing. These phantoms can also be 3D printed for specific patients using their MRI data which can be valuable for complex brain stimulation procedures such as deep brain stimulation (DBS).

[0011] In some embodiments, diffusion tensor imaging (DTI) is used to construct 3D fiber tract models usable for either finite element analysis for TMS simulation as well as for integration with physical brain phantoms for real world experimentation (as opposed to a computer simulation). The induced electric field throughout a fiber tract can be assessed, and parts of the deep brain are identifiable as receiving stimulation when the outer cortex of the brain is stimulated.

BRIEF DESCRIPTION OF THE DRAWINGS

[0012] The patent or application file contains at least one drawing executed in color. Copies of this patent or patent application publication with color drawing(s) will be provided by the Office upon request and payment of the necessary fee.

[0013] FIG. **1** shows anatomy within a human head undergoing transcranial magnetic stimulation (TMS).

[0014] FIG. **2**A shows a portion of a 3D-printed shell which defines the boundary geometry of a region of grey matter.

[0015] FIG. **2**B shows cast material after it has been cured and the shell removed.

[0016] FIG. **3**A shows two shells which together form a pair for casting grey matter.

[0017] FIG. **3**B shows the (unitary) grey matter casting produced from the shells of FIG. **3**A.

[0018] FIGS. **4**A and **4**B depict multiple shells in a software program (prior to 3D printing) arranged together in a manner consistent with human anatomy.

[0019] FIG. **5** is a process **500** for manufacturing a brain phantom according to combined manufacturing techniques of 3D-printing and casting.

[0020] FIGS. **6**A and **6**B illustrate an exemplary process for manufacturing a brain phantom configured to mimic a brain or one or more structures thereof.

[0021] FIG. **7** is a diagram of an exemplary experimental setup in which transcranial magnetic stimulation (TMS) may be tested on a brain phantom.

[0022] FIG. **8** is a flowchart of an exemplary method of performing a neuromodulation or neuroimaging procedure.

[0023] FIG. **9** is experimental and simulation data for TMS.

[0024] FIG. **10** shows modeled fiber tracts as constructed within the graphical toolbox ExploreDTI.

[0025] FIG. **11** shows modeled fiber tracts constructed with CAD software.

[0026] FIG. **12** shows modeled fibers in a simulation of TMS using simulation program, Sim4Life.

[0027] FIG. **13** shows 3D fibers integrated within a brain phantom.

DETAILED DESCRIPTION

[0028] FIG. **1** shows anatomy within a human head undergoing transcranial magnetic stimulation (TMS). The TMS device **101** is a non-invasive tool. It may be placed against the outside surface (e.g., skin) of the head **100** and produces one or more magnetic fields (shown with dotted lines in FIG. **1**). The magnetic fields penetrate into the underlying brain tissue and act as a stimulus to a region of the brain. The treatment may be used to stimulate regions associated with mood disorders, for example. To reach the target tissue site, the stimulatory signal (e.g., the magnetic field) must traverse skin tissue **102**, bone tissue (skull) **103**, cerebrospinal fluid (**104**), and some amount of neural tissue (brain) **105**. The stimulus may also reach the cerebellum **106** to some extent. In order to improve the effectiveness of TMS, it is desirable if not essential to understand how the parameters of the TMS device **101** affect different areas or parts of the patient's anatomy. Some exemplary embodiments meet this need by the provision of a 3-D anatomically realistic brain phantom ("phantom" for short) developed using 3-D printing.

[0029] For some exemplary phantoms according to the present invention, shells are 3D printed for each tissue layer of the brain. After printing, these shells are filled with a conductive material (e.g., silicon or PDMS with nanoparticles) that is configured to mimic the conductive properties of brain tissue. Different conductive material compositions may be used for different tissues (e.g., white matter vs. grey matter vs. CNF; brain matter vs. bone vs. skin).

[0030] FIGS. **2**A and **2**B show samples from a prototype using 3D printing combined with casting. FIG. **2**A shows a portion **200** of a 3D-printed shell which defines the boundary geometry of a region of grey matter. Suitable materials for shells are those which are 3D printable, shape resilient, and cable of being dissolved by subsequent chemical treatment. An exemplary material meeting these criteria may be a thermoplastic polymer such as Acrylonitrile butadiene styrene (ABS). The shell **200** may be used as mold for casting the conductive material which belongs in the phantom at the end of the manufacturing process. FIG. **2**B shows cast material **210** after it has been cured and the shell **200** removed.

[0031] FIG. **3**A shows two shells **301** and **302** which together form a pair for casting grey matter. FIG. **3**B shows the (unitary) grey matter casting **303** produced from the shells **301** and **302**. Generally, casting of a brain phantom may be facilitated by making pairs of shells for respective parts of the brain, each pair having a top part (i.e., upper part) and a bottom part (i.e., lower part). This approach may be used for some elements of the brain phantom and not for others. For instance, using a pair of shells (one upper part and one lower part) may be especially well suited for casting grey matter, cerebrospinal fluid (CSF), bone, and skin. For parts such as the ventricles and cerebellum, a single shell may be used.

[0032] FIGS. **4**A and **4**B depict multiple shells arranged together in a manner consistent with human anatomy. The images were produced by the program, Meshmixer, the output of which may be sent to a 3D printer. As discussed above, shells for the skin, skull, and grey matter may be 3D printed in pairs comprising both upper and lower parts. The ventricles, however, may be cast using a single shell. In some instances, a shell (be it upper or lower) may technically consist of two shells, respectively referred to as an inner shell and outer shell. As will be discussed below, for example, grey matter may be cast using inner and outer upper shells as well as inner and outer lower shells.

[0033] FIG. **5** is a process **500** for manufacturing a brain phantom according to combined manufacturing techniques of 3D-printing and casting. A high level of anatomical correctness may be achieved by using MRI data from an actual human head and brain as the basis for what the phantom should mimic. Accordingly, at block **501** an MRI procedure is performed to generate MRI data **502**. Because some of the manufacturing approaches described herein are especially cost effective, it may be that different phantoms are made for different respective patients. Patient specific MRI data may be used in each case for producing the phantom.

[0034] At block **503** the MRI brain images are segmented and reconstructed using computer program tools. At the time of this application MRI data may have .nii file extensions, for example, and require conversion for 3D modeling prior to supplying the data to a 3D printer. Software suitable for block **503** at the time includes FreeSurfer, FSL, and simNIBS. The output of such programs may be imported to another program (e.g., Meshmixer) to actually make the shells.

[0035] Blocks **503** to **508** walk through the production, use, and disposal of shells. In other words, these steps detail both mold making, casting, and mold removal. At block **503** shells are actually manufactured in a tangible form. 3D printing is an exemplary means for producing the shells in a cost effective manner. An exemplary material for the 3D printing process is an ABS (Acrylonitrile butadiene styrene) material. 3D printing may require the printing of supporting structures which do not actually have any anatomical analog. In such case these supporting structures may be removed at block **505** by, for example, chemically dissolving the parts (e.g., with acetone for ABS). Next the conductive "tissue" material is poured between shells (e.g., between and upper and lower shell pair, and/or between an inner and outer shell pair) at block **506**, and permitted to cure at block

507. The curing process may involve time during which the chemical composition of the "tissue" material reacts and sets. The curing process may involve exposing the "tissue" material to some form of electromagnetic radiation that triggers curing or just keeping the material at environmental conditions for a finite duration of time.

[0036] After the conductive "tissue" material cures, the shells and the conductive material are placed in an appropriate chemical bath (e.g., Acetone) to dissolve all remaining shell material (e.g., ABS) at block **508**, leaving only the cast "tissue" material for the phantom behind. The mold-making and casting of blocks **504** to **508** are repeated for subsequent parts. As will be discussed in greater detail below, for some tissue structures a prior casting may be used in place of one or more shells. As a result some tissue structures of the phantom are produced using two or more shells, some with only one shell, and some without any shells. Advantages of this approach are many. Fewer shells means less 3D printing which means lower costs of production. Using a prior casting of an existing part as the "mold" for the next part also means the two tissues will intimately share a boundary and reduce or avoid the possibility of gaps between phantom layers which could negatively affect the conductive behavior across the material-to-material boundary. At the conclusion of process **500** all shells have been removed and a multi-layered brain phantom remains and is ready for use.

[0037] FIGS. **6**A and **6**B illustrate an exemplary process for manufacturing an anatomically accurate brain phantom **600** configured to mimic a brain or one or more structures thereof. Generally, the illustrated process corresponds with process **500** of FIG. **5**, in particular block **504** and after. For ease of illustration, the dimensions and surface geometries of individual layers of material are oversimplified into basic geometric shapes (e.g., circles). In addition, the distinctions among upper vs. lower shells and inner vs. outer shells may be omitted to avoid overcomplicating the figures. It will be appreciated by ones of skill in the art that reference to "a shell" in the singular may be understood as indicative of multiple shells, for example a pair or two pairs of shells. Similarly, single shells may be used in some instances where a plurality is described. The details on shell pairing are already described above.

[0038] The end result of the process illustrated by FIGS. **6**A and **6**B is a complete brain phantom **600** containing one or more "tissue" structures, preferably at least six differentiated "tissues". These are grey matter, white matter, cerebrospinal fluid (CSF, including that which surrounds the brain and that which is contained in the ventricles), cerebellum, bone, and skin. Note that CSF may be referred to as a tissue or structure herein despite technically being a fluid in living organisms. Note also the ventricles may be referred to as a tissue or structure despite technically being cavities in living organisms. In the context of brain phantoms, both CSF and ventricles (which in living organisms are filled with CSF) may be simulated with solid or semisolid materials.

[0039] At stage **601**, inner and outer shells **601'** for grey matter (GM) are 3D printed and any supporting structures related to the printing process (and not anatomy) are removed. At stage **602** conductive material **602'** is poured in between the inner and outer shells. The conductive material cures. At stage **603** the shells are removed. For example, the shells and conductive material are bathed in acetone (or other suitable dissolving agent) to dissolve the shell material, leaving only the cured grey matter material **603'** remaining. The cured grey matter material is configured to be anatomically accurate with (e.g., mimic) grey matter found in naturally occurring grey matter of the brain.

[0040] At stage **605**, a shell **605'** is 3D printed for the ventricles and any supporting structures related to the printing process removed. At stage **606** conductive material **606'** is poured inside the shell. The conductive material cures. At stage **607** the shell and conductive material are bathed in dissolving agent to dissolve the shell material, leaving only the cured ventricle material **607'**. The cured ventricle material is configured to be anatomically accurate with (e.g., mimic) CSF ordinarily found in naturally occurring ventricles of the brain.

[0041] At stage **609**, the cured and shell-less grey matter material from stage **603** and ventricle material from stage **607** are arranged together with anatomically correct three-dimensional spacing and orientation. The ventricle material is placed in the proper position inside the grey matter (GM) material. At stage **610** conductive material **610'** simulating white matter (WM) is poured in the gaps between the ventricle material and GM and cured. Stage **610** differs notably from stages **602** and **606** in that no shells are necessary or indeed used according to some exemplary embodiments. Instead, the existing ventricle and GM castings serve as the mold for defining the boundaries of the WM, just as in real anatomy. The elimination of any shells to make the WM reduces both time and money costs involved in 3D printing and provides excellent interfaces among the grey matter, white matter, and ventricle material.

[0042] At stage **612** a shell **612'** is 3D printed for the cerebellum and any supporting structures related to the printing process removed. At stage **613** conductive material **613'** is poured inside the shell. The conductive material cures. At stage **614** the shell and conductive material are bathed in dissolving agent to dissolve the shell material, leaving only the cured cerebellum material **614'**. The cured cerebellum material is configured to be anatomically accurate with (e.g., mimic) a cerebellum found in a naturally occurring brain.

[0043] At stage **616** a shell **616'** is 3D printed for the cerebrospinal fluid (CSF) layer that envelopes the brain. At stage **617**, the shell, the cerebellum, and the already assembled ventricle/WM/GM pieces are arranged together with anatomically correct three-dimensional spacing and orientation. One or more reference frames may be used to position the cerebellum in the assembly with the right location and orientation. For example, a 3D Cartesian table may be used to accurately assembly the brain regions. At stage **618** conductive material **618'** which mimics CSF properties is poured into the spaces within the shell and cured. At stage **619** the shell is dissolved, leaving a fully cured and assembled unitary brain phantom **620** from the CSF layer and deeper. The cured CSF material **619'** is configured to be anatomically accurate with (e.g., mimic) CSF ordinarily found in a naturally occurring brain. In some embodiments the brain phantom **620** produced at stage **619** may serve as an end product of the manufacturing process. The phantom **620** is suitable for use in simulations, tests, and experimentation relating to open surgery on the brain (e.g., where the skin and bone are removed).

[0044] FIG. **6**B continues the manufacturing process for producing brain phantoms used or usable in connection with transcranial procedures. Two additional layers of material are still to be added: bone and skin. At stage **621** a shell **621'**

is 3D printed to define the outer boundary of the skull. At stage **622** the CSF-and-deeper brain phantom **620** of stage **619** is arranged within the shell. At stage **623** the remaining space within the shell is filled with conductive material **623'** configured to mimic the skull bone tissue. The fluid is cured. At stage **624** the shell is removed. The cured bone material **624'** is configured to be anatomically accurate with (e.g., mimic) skull bone ordinarily found in a naturally occurring head.

[0045] At stage **626** a shell **626'** is 3D printed which defines the outer boundary of the skin surrounding the skull. At stage **627** the phantom from stage **624** is arranged within the shell **626'**. At stage **628** the space between the shell and bone layer is filled with material **628'** configured to mimic skin tissue and cured. At stage **629** the shell is removed. The cured skin material **629'** is configured to be anatomically accurate with (e.g., mimic) skin ordinarily found on a naturally occurring head. The final result is a unitary brain phantom **600** which resembles the brain of the original MRI data and has distinguishable parts including skin, bone, CSF, cerebellum, grey matter, white matter, and ventricles (containing CSF).

[0046] In the preceding descriptions, removal of shells after material cast within the shell is cured has generally been described as performed via dissolving in a chemical bath. Alternative shell removal techniques may also be used in embodiments. For instance, shells may in some cases be broken and the resulting fragments removed (without any dissolving necessary).

[0047] FIG. **7** is a diagram of an exemplary experimental setup in which transcranial magnetic stimulation (TMS) may be tested on a brain phantom **600**. Such a setup advantageously permits TMS trials on a phantom made to mimic the actual brain of a patient who is to be treated with TMS. A TMS device **101** is used or usable to subject to the phantom **600** to simulation, and the stimulatory signal may be measured by one or more electrodes **701** (e.g., microelectrodes) inserted or imbedded at different locations inside the phantom **600**. Such electrodes **701** would not necessarily be implantable in the actual patient, at least not without an increased risk of harm to the patient. The phantom **600** which is configured to mimic the patient's brain serves as a ready substitute in which electrodes **701** can be inserted without any risk to the patient. The signals detected by the electrodes **701** may be transmitted, e.g. by wires **702**, to a recording and/or display device **703** with an output (e.g., display **704**) for study or processing. Parameters of the TMS device **101** may then be selected, adjusted and/or set based on the signals received from the electrodes **701**.

[0048] An exemplary phantom is usable for the purpose of evaluation of the neuromodulation such as transcranial magnetic stimulation (TMS). It enables the professional in the field of the brain modulation and treatment to test and perform actual brain stimulations on the phantom that are accurate and match the clinical setting of the of TMS treatment. Prior to the instant invention, no brain phantoms existed to the knowledge of the inventor which were capable of experimentally verifying TMS parameters. An exemplary phantom is examinable under different TMS parameters and suitable for comparison with FEM modelling of induced electric field and magnetic fields in different tissues of the brain. Microelectrodes may be placed at different locations/depths on the phantom to measure the current I and resistance Ω. Since the phantom exhibits same electrical properties of the brain, close readings to actual TMS procedures may be achieved.

[0049] FIG. **8** presents an exemplary method **800** for performing a neuromodulation or neuroimaging procedure. The method **800** may be employed for providing personalized medicine. At block **801** an anatomically accurate brain phantom is manufactured. This process may be as described above. The process at block **801** may use patient-specific MRI data that is specific to the patient for which a future medical procedure is planned. At block **802**, a neuromodulation or neuroimaging procedure is actually performed on the anatomically accurate brain phantom. The procedure may be invasive, non-invasive, or some combination thereof. Multiple procedures (e.g., a series of procedures) may be performed on the same brain phantom. Neuromodulation procedures may include one or more of transcranial magnetic stimulation (TMS), transcranial direct current stimulation (tDCS), or deep brain stimulation (DBS). Neuroimaging procedures may include magnetic resonance imaging, for example. Other procedures may also or alternatively be performed.

[0050] At block **803**, data is collected as the medical procedure is performed. If the procedure is a neuromodulation procedure, electrical or magnetic properties in the brain phantom may be obtained during the neuromodulation procedure (e.g., see FIG. **7** and accompany description). If the procedure is a neuroimaging procedure, image data may be obtained during the neuroimaging procedure (e.g., MRI data). From the collected data, medical software and/or practitioners (e.g., doctors) may select parameters for a subsequent procedure at block **804**, where the parameters are customized for the patient whose MRI data was used to construct the brain phantom. The parameters may be, for example, one or more of power settings, intensity settings, wavelength or frequency settings, duration settings, interval settings, and impulse settings, among others. Indeed, any setting which may be adjusted on existing or future medical devices like TMS devices or MRI machines may be calibrated or customized for a particular patient using the method **800**.

[0051] In connection with the selection process in block **804**, the data collected at block **803** may be compared to reference data, and the selection may be based on the comparison. For example, particular stimulatory conditions may be desired at a particular location within a patient's brain. The desired stimulatory conditions may be saved as reference data. TMS may then be performed using initial settings and the stimulatory response measured. The TMS device settings can be adjusted until the desired stimulatory conditions within the brain phantom are reached. The final TMS settings may then be used for actually treating the patient.

[0052] At block **805** the subsequent neuromodulation or neuroimaging procedure is actually performed on the patient using the selected parameters.

[0053] Exemplary methods like method **800** may be useful for personalized medicine for any patient, human or animal. Method **800** is especially advantageous for patients with unique or abnormal conditions which set them apart from the anatomy typical of most patients. For example, some patients may already have a brain implant such as a DBS device. In such a case any effects of the presence of the existing implant on neuroimaging or neuromodulation may

be unknown or uncertain. Method **800** permits a safe and reliable means for assessing how such a procedure may go using an anatomically accurate phantom mimicking the patient's brain and containing a copy of the patient's implant to select the parameters of performing the procedure. The procedure may then be performed on the actual patient with a greater degree of certainty and safety.

[0054] In the above descriptions for manufacturing brain phantoms, the materials used for the phantom layers are generally described as conductive materials. Addressing the materials directly, an exemplary conductive material is a silicon or silicone based compound (a compound containing silicon, Si) or PDMS with one or more of graphite, multi walled or single walled carbon nanotubes (MWCNT/SWCNT), and silver nanoparticles and nanowires that is capable of mimicking the electrical conductive properties of different brain tissues based on the respective amounts of these constituents. Some embodiments use specific ratios of all three additives in the silicon base. The silicon base may be, for example, silicon polymer polydimethylsiloxane PDM. The conductivity of layers of an exemplary phantom may be in the range between 0.2-3.0 Sm^{-1}. For the skin layer the conductivity range may be lower, e.g., as low as 0.1 Sm^{-1}. In some other embodiments the layers may each be in the range of 0.2-1.8 Sm^{-1}. In a particular example, the electrical conductivity of different brain tissue that was matched in a phantom was as follows: ventricles & CSF=1.77 Sm^{-1}, GM=0.23 Sm^{-1}, WM=0.24 Sm^{-1}, and cerebellum=0.65 Sm^{-1}.

[0055] An "anatomically accurate" brain phantom mimics the brain of a living organism, e.g. a mammalian brain (e.g., a human brain). Anatomically accurate may mean the three dimensional geometry (e.g., sizes, relative sizes, dimensions, relative dimensions, locations or positions, relative locations or positions, etc.) of the phantom matches or substantially matches the three dimensional geometry of a real brain (e.g., an actual mammalian brain). Anatomically accurate may mean one or more electrical properties (e.g., electrical conductivity) of the brain phantom match or substantially match one or more electrical properties of a real brain (e.g., an actual mammalian brain). Anatomically accurate may mean one or more material properties (e.g., mass density, viscosity, etc.) of the brain phantom match or substantially match one or more material properties of a real brain (e.g., an actual mammalian brain). A brain phantom may match or substantially match a real brain if at least one layer/structure of the brain phantom matches or substantially matches the corresponding real brain structure. A brain phantom may match or substantially match a real brain only if all the layers/structures of the brain phantom match or substantially match the real brain. Table 1 below presents exemplary but non-limiting material properties which may be used in a computer simulation or physical brain phantom which is anatomically accurate.

TABLE 1

Material properties for simulation or physical brain phantoms

Structure	Mass Density (kg/m^3)	Electrical Conductivity (S/m)	Relative Permittivity
Skin	1109	0.17	1
Skull	1908	0.32	1
CSF/Ventricles	1007	1.7765	1

TABLE 1-continued

Material properties for simulation or physical brain phantoms

Structure	Mass Density (kg/m^3)	Electrical Conductivity (S/m)	Relative Permittivity
Grey Matter	1044.5	0.239149	1
White Matter	1041	0.26507	1
Cerebellum	1045	0.659667	1

The published literature on the conductivity of healthy adult brain's white matter, grey matter, CSF, skull and skin varies significantly. However, the most trusted values of conductivities for grey and white matter fall in the range of 0.1 to 0.5 S/m. Therefore an anatomically accurate brain phantom may be produced with the conductivities of the grey matter and white matter in the range of 0.1 to 0.5 Sm^{-1}. Different conductivities may be used for different structures/layers/regions of the brain phantom. To achieve different conductivities, different composite polymers may be prepared and used. For example, exemplary brain phantoms or structures/layers thereof may comprise a composite polymer of a silicon-based compound (e.g., PDMS) and carbon nanotubes (in particular multi-walled carbon nanotubes, MWCNTs) with the conductivity/resistivity varied among the structures/layers by variable wt % of the MWCNTs. Table 2 presents the relationship between resistivity and composition of MWCNTs in PDMS.

TABLE 2

Relationship between resistivity and composition of MWCNTs

wt % of CNT in PDMS	Resistivity (ohm/cm)
10.5	1000
11.5	500
12.5	300
15.3	35

Resistivity of 300-400 ohms/cm corresponds to 0.3-0.5 S/m (an exemplary target value range for WM and GM). An exemplary composition used for Example 1 below is 11.5 wt % of MWCNTs composition for GM and WM.

[0056] Layers or structures of exemplary brain phantoms may have electrical conductivities varied with respect to one another by varying one or more of the materials or compositional ratios with respect to the other layers/structures. For example, different layers or structures may be configured to have different electrical conductivities based on nanotubes of different lengths in one layer versus another layer (e.g., shorter in one layer versus longer in another layer). Different layers or structures may be configured to have different electrical conductivities based on different materials for the nanotubes in one layer versus another layer (e.g., carbon versus silver). Different layers or structures may be configured to have different electrical conductivities based on different types of nanotubes in one layer versus another layer (e.g., single walled versus multi walled nanotubes). In some exemplary embodiments which use a combination of PDMS with MWCNTs, the wt % of CNT in PDMS may be between 10.5 and 15.3 with a resistivity between 1000 and 35 ohm/cm. In some exemplary embodiments which use a combination of PDMS with MWCNTs, the wt % of CNT in PDMS may be 10.5 to 12.5 with a resistivity between 1000 and 300 ohm/cm. In some exemplary embodiments which

use a combination of PDMS with MWCNTs, the wt % of CNT in PDMS may be about 11.5 (e.g., 11.5±0.5) with a resistivity of or about 500 ohm/cm. Other exemplary specifications may be used in other embodiments.

[0057] In some embodiments, brain phantoms may comprise integrated fiber tracts. An important feature in the brain that is normally (and disadvantageously) ignored by researchers while calculating induced electric fields is fiber tracts due to their anatomical complexities and small dimensions. The fiber tracts are part of the white matter with high conductivity and impart anisotropy to the white matter. In some embodiments, fiber tracts may be made an integral part of a brain phantom.

[0058] Following is an example approach for integrating one or more fiber tracts into a brain phantom. High resolution diffusion tensor imaging (DTI) data is collected. Then fiber tracts are extracted from the DTI data using, for example, a graphical toolbox ExploreDTI. Then fiber tracts are constructed using whole brain tractography. Tracts are drawn from a seed region of interest (ROI) such as M**1** with parameters such as the following: a seed fractional anisotropy threshold of 0.2, minimum fiber length of 50 mm, and angle threshold of 30 degrees. FIG. **10** shows the resulting fiber tracts originating from the ROI of M**1** within an ExploreDTI interface. Next coordinates of tracts are imported into a CAD modeling software such as SolidWorks to form curved paths, and then each path is extruded to a solid, 3D object. FIG. **11** shows the 3D fiber objects within a SolidWorks interface.

[0059] The 3D fiber (CAD) models can be exported (e.g., as .STL files) for finite element analysis in a simulation program such as Sim4Life. FIG. **12** shows fibers being stimulated by a Figure-Eight TMS coil.

[0060] The 3D fiber (CAD) models may also be integrated directly into a brain phantom. FIG. **13** shows the 3D fibers **1301** integrated within the brain phantom **1302**. The fiber models may be embedded into a 3D head/brain models to experimentally calculate induced electric field during TMS in different regions of the brain. The brain phantoms may be used in testing of various coil configurations to tune the electric field strengths in the targeted regions of the brain.

[0061] Integration of fiber tracts to a brain phantom may involve different or modified manufacturing processes than described above. Integration of fiber tracts in brain phantom needs conductive polymers that have less viscosity. Preparation of soft polymers with high conductivity is a complex process with many variables. The volume fraction/loading factor of conductive materials in a polymer composite increases the viscosity of the polymer and makes it difficult to conform to complex structures, such as fiber tracts, for white and grey matter of the brain. The conductivity of the polymer composite is sensitive to the length of carbon nanotubes or the nanowires used. In some embodiments, carbon nanotubes longer than 50 μm are used to make the hardness of the polymer composite a suitable level. Phantoms may be fabricated using the PDMS/CNT composite in a 3D Bioplotter® which is a multi-nozzle, 3D printer of UV curable soft materials. With a 3D printer like the 3D Bioplotter®, the use of shells and casting may be avoided (although the cost of production may be substantially increased). A 3D printer like the Bioplotter® is used or usable to print complex shapes to simultaneously fabricate all the regions of the phantom (e.g., the parts described above), including the fiber tracts. Electrical and magnetic fields may be induced in the resulting brain phantom as previously described in connection with FIG. **7**.

[0062] Where computer software is discussed herein, it should be understood that such software may be embodied in computer readable instructions which may be provided to one or more processors of a general purpose computer, special purpose computer, or other programmable data processing apparatus to produce a machine, such that the instructions, which execute via the processor of the computer or other programmable data processing apparatus, create means for implementing the functions/acts specified in the description above, in one of the flowcharts, and/or in one or more block diagram blocks. These computer readable program instructions may also be stored in a computer readable storage medium that can direct a computer, a programmable data processing apparatus, and/or other devices to function in a particular manner, such that the computer readable storage medium having instructions stored therein comprises an article of manufacture including instructions which implement aspects of the function/act specified in the flowcharts and/or block diagrams. Embodiments herein may comprise one or more computers, one or more processors, one or more computer readable storage media, and/or appropriate input/output devices therefore, as well as additional supporting hardware as necessary.

[0063] Unless the context indicates otherwise, block diagrams and flowcharts are exemplary and may involve fewer or greater number of blocks and/or a different order of items or steps. In some embodiments elements or steps may be concurrent, combined, or otherwise organized differently than is depicted or described.

EXAMPLES

Example 1. Experimental Verification of Transcranial Magnetic Stimulation Using Anatomically Accurate Brain Phantom

[0064] A phantom was produced by 3-D printed shells for each tissue layer of the brain. Brain tissues were divided into cerebrospinal fluid (CSF), white matter (WM), grey matter (GM), ventricles, and cerebellum. These layers were made into shells defining their geometric spatial boundaries and 3D printed. The shells were then filled with a conductive material (silicon polymer polydimethylsiloxane PDM with electrically conductive filler multi walled carbon nanotubes MWCNT) to impart electrical conduction to the brain phantom. Then, the shells were broken or dissolved to finally produce the brain phantom. The electrical conductivity of the brain phantom tissue was is in the range of 0.4-1.0 Sm^{-1}. The phantom was then examined under different TMS parameters and compared with FEM modelling of induced electric and magnetic fields in the brain.

[0065] TMS device coils were positioned on the brain phantom and an oscilloscope probe was placed just underneath the surface of the phantom in order to measure the voltage (phantom probe). Another probe was placed at the same distance (from the coils) as the first probe but outside the phantom so as to measure the voltage induced on the probe just from the TMS coils (reference probe). Then, the magnetic field from the coils was applied. The process was repeated for four distances total: 1, 2, 3, and 4 cm. At each distance measurements were repeated at four different power intensities: 25, 50, 75, and 100%. The brain phantom and experimental set up corresponds with FIG. **7**. The same

settings were replicated with an FEM simulation (i.e., the virtual coils in the software were places at four distances 1, 2, 3, and 4 cm form the surface of the brain model and with four intensities 25, 50, 75, and 100% at each distance). The voltage readings for both the phantom experimental and computer simulation cases are shown in FIG. **9**. Voltage readings of the experimental work shown in the upper graph of FIG. **9** represent the difference between the voltages induced on the phantom probe and the reference probe. The results indicate that there is a noticeable induced electric field in the phantom due to the applied magnetic field from the TMS coils.

[0066] Next comparing both graphs, experimental (FIG. **9**, top) and simulation (FIG. **9**, bottom), it can be seen that there is an overall similar behavior. The voltage and e-field readings are linearly dependent with intensity in both graphs. Also, the induced voltage decreases almost exponentially with the distance.

Example 2. 3D Modeling of Diffusion Tensor Imaging Tractography Data for Finite Element Analysis

[0067] DTI data was collected from a single subject, healthy 30 year old male patient on a GE 3T HDx scanner with 60 directions. This data was visualized in the graphical toolbox ExploreDTI. Fiber tracts were constructed using whole brain tractography with the following parameters: seed fractional anisotropy threshold of 0.2, minimum fiber length of 50 mm, angle threshold of 30 degrees, and a step size of 1. Tracts were calculated and drawn from a seed ROI drawn on the z-plane around the M1 region. The coordinates of each individual tract were imported into SolidWorks as a curve which could then be extruded to a solid, 3D object with a diameter of 0.25 mm. These 3D fiber models were exported as STL files for finite element analysis to simulate TMS alongside 3D brain tissue models.

[0068] FIG. **10** shows the tracts drawn from the M1 region. Thirty-four tracts were found with an average length of 87.09 mm. Note that while the data shows 34 distinct tracts, all 34 are not apparent in FIG. **10**. The paths of some of these fibers appear to follow the corticospinal tract. Finite element analysis of the fiber tracts alongside a brain tissue model and a FIG. **9** TMS coil produced high currents at tract points by the cortex which gradually decreased towards the deep brain.

[0069] The ability to 3D model fiber tracts allows for a more comprehensive study of the deep brain effects of cortical stimulation. Tractography constructs the pathways of fiber tracts, allowing for visualization of connecting regions of the brain. Finite element analysis calculates the magnitude of the electric field at any point on the tract. Knowing this can help determine if and where TMS can be used to stimulate the deep parts of the brain by stimulating the cortical regions and improve therapies for disorders affecting the deep brain.

[0070] While exemplary embodiments of the present invention have been disclosed herein, one skilled in the art will recognize that various changes and modifications may be made without departing from the scope of the invention as defined by the following claims.

We claim:

1. An anatomically accurate brain phantom, comprising at least one layer that mimics a brain structure formed from a conductive material comprising polydimethyl-siloxane (PDMS) and carbon nanotubes (CNTs).

2. The anatomically accurate brain phantom of claim **1**, further comprising a plurality of layers configured to mimic respective brain structures including cerebrospinal fluid (CSF), white matter (WM), grey matter (GM), ventricles, and cerebellum.

3. The anatomically accurate brain phantom of claim **2**, wherein at least some of the plurality of layers are configured to have different electric conductivities by having different wt % of CNTs with respect to one another.

4. The anatomically accurate brain phantom of claim **1**, wherein the brain phantom further comprises one or more integrated fiber tracts.

5. The anatomically accurate brain phantom of claim **1**, wherein three-dimensional geometry of the brain phantom is based on medical imaging data of a mammalian brain.

6. The anatomically accurate brain phantom of claim **1**, wherein the at least one layer is configured to have an electric conductivity of 0.2 to 3.0 S/m to mimic an electrical conductivity of a brain structure.

7. A method of producing an anatomically accurate brain phantom, comprising

forming an anatomically accurate inner shell and an outer shell that mimic an inner surface and an outer surface of a brain structure;

pouring a conductive material comprising polydimethyl-siloxane (PDMS) and carbon nanotubes in between the inner shell and the outer shell;

curing the conductive material; and

removing the inner shell and the outer shell to provide a brain phantom of said brain structure.

8. The method of claim **7**, further comprising forming a plurality of additional layers which are part of the brain phantom by

pouring conductive material comprising polydimethyl-siloxane (PDMS) and carbon nanotubes between either at least one additional anatomically accurate shell and an existing layer of the brain phantom, or two existing layers of the brain phantom;

curing the conductive material; and

removing the at least one additional shell if an additional shell was used in the pouring step.

9. The method of claim **8**, wherein the plurality of additional layers are configured to mimic respective brain structures including cerebrospinal fluid (CSF), white matter (WM), grey matter (GM), ventricles, and cerebellum.

10. The method of claim **8**, further comprising configuring the plurality of layers to have different conductivities with respect to one another by varying the wt % of CNTs from one layer to the next.

11. The method of claim **7**, wherein the forming step comprises 3D printing the anatomically accurate inner and outer shells.

12. The method of claim **7**, wherein the forming step uses medical imaging data of a mammalian brain to determine three dimensional geometry of the anatomically accurate inner and outer shells.

13. The method of claim **12**, further comprising segmenting and reconstructing MRI brain images with a computer program to produce segmented brain tissues corresponding to separate shells to be formed.

14. A method of neuromodulation or neuroimaging, comprising

performing a neuromodulation or neuroimaging procedure on an anatomically accurate brain phantom;

collecting data which characterizes either

electrical or magnetic properties in the brain phantom during the neuromodulation procedure, or

one or more images of the brain phantom during the neuroimaging procedure; and

selecting one or more parameters for a subsequent neuromodulation or neuroimaging procedure for performing on a patient based on the collected data.

15. The method of claim **14**, further comprising a step of manufacturing the anatomically accurate brain phantom to be used in the performing step using patient-specific MRI data that is specific to the patient for which parameters are selected in the selecting step.

16. The method of claim **15**, further comprising a step of performing the subsequent neuromodulation or neuroimaging procedure on the patient using the selected one or more parameters.

17. The method of claim **14**, wherein the performing step comprises performing a neuromodulation procedure, and wherein the collecting step comprises collecting data with one or more electrodes inside the brain phantom.

18. The method of claim **17**, further comprising comparing the data collected with the one or more electrodes with reference data, and wherein the selecting step comprises selecting at least one parameter of the one or more parameters based on the comparison.

19. The method of claim **14**, wherein the performing step comprises performing transcranial magnetic stimulation (TMS), transcranial direct current stimulation (tDCS), or deep brain stimulation (DBS).

20. The method of claim **14**, wherein the performing step comprises conducting a magnetic resonance imaging (MRI) procedure.

* * * * *